

**IN SITU INFRARED SPECTROSCOPY STUDY OF ATOMIC
LAYER DEPOSITION OF HIGH-K METAL OXIDE AND
METAL ON PASSIVATED SILICON SURFACES**

by

MIN DAI

**A dissertation submitted to the
Graduate School-New Brunswick
Rutgers, The State University of New Jersey**

In partial fulfillment of the requirements

**For the degree of
Doctor of Philosophy
Graduate Program in
Physics and Astronomy**

**Written under the direction of
Prof. Yves J. Chabal**

And approved by

New Brunswick, New Jersey

October, 2008

© 2008

Min Dai

ALL RIGHTS RESERVED

ABSTRACT OF THE DISSERTATION

IN SITU INFRARED SPECTROSCOPY STUDY OF ATOMIC LAYER DEPOSITION OF HIGH-K METAL OXIDE AND METAL ON PASSIVATED SILICON SURFACES

By MIN DAI

Dissertation Director:

Prof. Yves J. Chabal

Atomic layer deposition (ALD) is a novel and promising film deposition method for microelectronics and many other areas with documented commercial success. Notable advantages include accurate thickness control and high conformality, all of which are particularly important for deep trenches, porous materials and nanoparticles.

The key elements of ALD including starting surfaces and precursors are investigated with *in situ* Fourier transform infrared spectroscopy, using a variety of starting surfaces: hydrogen-terminated Si (H/Si), oxidized Si, nitrided Si, and self-assembled monolayers (SAMs) grafted on H/Si surfaces. In particular, the formation of nitrided surfaces using thermal NH₃ reaction with flat and vicinal H/Si(111) is studied and a mechanistic understanding is achieved with the aid of density functional theory calculation. An unexpected NH incorporated bridging structure is found at the dihydride step edge. The properties and stability of methyl and carboxylic groups terminated alkene-based SAMs grafted to H/Si(111) surface via direct Si-C bonds are also addressed. The carboxylic

groups terminated SAM can be grafted without formation of interfacial SiO₂. Moreover, the use of SiN_x and SAM successfully minimizes the interfacial SiO₂ during ALD process.

With a thorough understanding of the starting surfaces, the nature of ALD grown high-κ metal oxides and metal is studied. Water- and ozone-based ALD of HfO₂ and Al₂O₃ are investigated mechanistically. Unexpected intermediate species and reaction pathways are found to depend on ozone partial pressure, such as formate intermediate for Al₂O₃ deposition.

La₂O₃ and Cu deposited by novel precursors, La(ⁱPr-MeAMD)₃/D₂O and [Cu(^sBu-amd)]₂/H₂ respectively, are explored in many aspects such as the nature of precursor gas phase, the ALD temperature window, the film properties, and so on. In all cases, a mechanistic picture of the surface interaction and film growth is unraveled using infrared spectroscopy and other complementary techniques, such as Rutherford back scattering spectroscopy and X-ray photoelectron spectroscopy. Gas phase studies show that the two precursors are both readily hydrolyzed and highly reactive. ALD-deposited La₂O₃ films are of poor quality due to the hygroscopic nature of La₂O₃, and Cu diffusion and agglomeration are inferred from the evolution of IR vibrational modes.

Acknowledgements

First and foremost, I would like to express my gratitude to my advisor Prof. Yves J. Chabal for his invaluable guidance, advice and stimulating discussions as well as providing great opportunities for me to finish my PhD studies. He is always paying great attention to my thesis project and actively involved in all my experiments. I learned a lot from him from his knowledge, patience, consideration and inspiration both in research and daily life. His enthusiasm for science and work encourages me and shows a great example for me to continue my studies. I feel really grateful and lucky to have had him as my advisor.

I would like to thank Dr. Yu Wang and Dr. Ming-Tsung Ho who introduced and helped me to initiate my thesis project for nitridation and ALD of HfO_2 . I learned many experimental skills and FTIR knowledge from them. They are always ready to help. I would also like to thank Dr. Jinhee Kwon with whom I carried out lots of *long* experiments for ALD of La_2O_3 and ozone based Al_2O_3 , and initiated the study of Cu ALD and trenched Si. We had many pleasant discussions about our research. She is an excellent researcher whom I learned a lot from.

I want to thank Dr. Meng Li and Dr. Oliver Seitz. We worked closely together. They prepared many SAMs samples for me. I learned a lot of interesting chemical knowledge from them. Oliver also helped me a lot in research and many others things when I was visiting UTD for 3 months. Also I would like to thank Dr. Mathew Halls for all DFT theoretical calculations and Dr. Leszek S. Wielunski for RBS Measurements. Thanks Prof. Roy Gordon for providing La and Cu precursors and insightful information, and Dr. Uwe Schroeder for trenched samples and SEM pictures. I would thank Dr. Jean-Francois

Veyan also. He is extraordinarily helpful in mechanics and many other technical stuffs making my study much easier. His optimistic attitude towards all things affects me very much. And thanks Dr. SunKyung Park for her helps at UTD.

There are many other people who helped me very much and I really appreciate. Dr. David Michalak taught me how to prepare the stepped H/Si and Irinder Chopra told me how to use AFM. Thanks Norman Lapin, Melissa Stokes, and Nour Nijem, we spent a lot of time together in the lab. Also thanks Erik Langereis for his excellent 3-month work with Jinhee and me, and thanks for the help of all my committee members.

Table of Contents

ABSTRACT OF THE DISSERTATION	ii
Acknowledgements	iv
Table of Contents	vi
List of Tables	ix
List of Illustrations	x
List of Frequently Used Abbreviations and Acronyms	xv
Chapter 1: Introduction	1
1.1 Atomic layer deposition	1
1.2 ALD of high- κ metal oxide	5
1.3 ALD of metal	6
1.4 Overview of the dissertation	7
Bibliography	10
Chapter 2: Experiment Setup, Substrate Preparation, and Data Analysis	14
2.1 Home made atomic layer deposition system	14
2.2 Sample preparation and FTIR data analysis	17
2.3 Summary	24
Bibliography	24
Chapter 3: Thermal Nitridation of H/Si for ALD	26
3.1 Thermal NH_3 nitridation of flat H/Si(111)	27
3.2 Thermal NH_3 nitridation of vicinal H/Si(111)	31
3.3 HfO_2 deposition on nitrided Si(111) surface	42
3.4 Summary	47

Bibliography	48
Chapter 4: ALD of Al ₂ O ₃ and HfO ₂ with Ozone	52
4.1 TMA gas phase and gas phase reaction	53
4.2 Al ₂ O ₃ deposition on H/Si(111) using TMA/ozone.....	57
4.3 HfO ₂ deposition using TEMAH/ozone	72
4.4 Summary	79
Bibliography	81
Chapter 5: La ₂ O ₃ and La _x Al _y O Growth on H/Si by ALD	85
5.1 Lanthanum precursor gas phase.....	85
5.2 ALD of La ₂ O ₃ on H/Si(111) surface	89
5.3 Miscellany of La(ⁱ Pr-MeAMD) ₃ ALD temperature window	98
5.4 ALD of La _x Al _y O on H/Si(111) surface	100
5.5 Summary	103
Bibliography	104
Chapter 6: ALD of Cu on Si Surfaces.....	107
6.1 Precursor properties and the gas phase IR spectrum	108
6.2 ALD of Cu on H/Si surface.....	109
6.3 ALD of Cu on SiO ₂	113
6.4 ALD of Cu on SiN _x and Al ₂ O ₃	130
6.5 Other application: deposition of Cu ₃ N.....	136
6.6 Summary	140
Bibliography	141
Chapter 7: SAMs Modification of H/Si, and ALD of Al ₂ O ₃ , HfO ₂ and Cu on SAMs ...	145
7.1 Stability of the -CH ₃ and -COOH SAMs.....	147

7.2 ALD of Al ₂ O ₃ on -COOH SAM	156
7.3 ALD of HfO ₂ on -COOH SAM	166
7.4 ALD of Cu on -COOH SAM	170
7.5 Summary	173
Bibliography	174
Chapter 8: Summary	178
Appendix: ALD of HfO ₂ on Trenched H/Si.....	183
A.1 Thermal stability of H/Si surfaces	184
A.2 HfO ₂ deposition on trenched H/Si(100).....	190
A.3 Summary	193
Bibliography	194
Acknowledgment of Previous Publications.....	196
Curriculum Vita.....	197

List of Tables

Table 2.1	The elements concentration of SiO ₂ /Si(100) surface after RCA cleaning	18
Table 2.2	The elements concentration of H/Si(100)	18
Table 2.3	Relation between the thickness of SiO ₂ and integrated area of SiO ₂ IR TO/LO modes	23
Table 3.1	Calculated PBE/DNP wavenumbers and mode assignments corresponding to the observed infrared (IR) bands	42
Table 4.1	The IR band assignment of TMA gas phase	55
Table 5.1	Calculated PBE/DNP wavenumbers and mode assignments corresponding to the observed infrared (IR) bands based on calculations for the intact La precursor	74
Table 6.1	The thickness of 10 cycles Cu on SiO ₂ at different temperatures by RBS	125
Table 6.2	The summary XPS results for 10 cycles of Cu on SiO ₂ at different temperatures.	128
Table 6.3	The summary of element concentration by XPS results for 10 cycles of Cu on SiO ₂ at 140°C for the fresh sample	128
Table 6.4	The relative O concentration for three fitted O 1s peaks for 10 cycles of Cu on SiO ₂ at different temperatures	130
Table 6.5	The estimation of pure Cu (Cu ⁰) concentration in all elements for 10 cycles of Cu on SiO ₂ at different temperatures	130
Table 6.6	The summary of element concentration by XPS results for 10 cycles of Cu on SiN _x at 185°C	133
Table 6.7	The summary of element concentration by XPS results for 10 cycles of Cu on Al ₂ O ₃ at 185°C	136
Table 6.8	The summary of element concentration by XPS results for 20 cycles of reduced Cu ₃ N	140

List of Illustrations

Fig 1.1	Ideal ALD process based on self-terminating mechanism	2
Fig 1.2	Examples of typical ALD metal precursors	3
Fig 1.3	ALD temperature window	4
Fig 2.1	Schematic diagram of home made ALD system	14
Fig 2.2	Diagram of Nicolet FTIR spectrometer	16
Fig 2.3	The absorption spectrum of H/Si(111) referenced to the SiO ₂	20
Fig 2.4	The absorption spectrum of H/Si(100) referenced to the SiO ₂	22
Fig 3.1	Nitridation of flat H/Si (111) referenced to oxide surface	28
Fig 3.2	Nitridation of flat H/Si (111) (Spectra are referenced to H/Si (111) surface)	29
Fig 3.3	(a) Opposed NH ₂ +H ₂ on Si (100) and (b) nitrogen insertion into Si-Si to form N _x -Si-H	30
Fig 3.4	The schematic of (a) monohydride and (b) dihydride stepped H/Si (111) surfaces	31
Fig 3.5	Nitridation of monohydride stepped H/Si(111)	33
Fig 3.6	The fitting results of the Si-H stretching modes of monohydride H/Si(111)	34
Fig 3.7	Nitridation of dihydride stepped H/Si(111)	36
Fig 3.8	The schematic of H-Si-NH-Si bridging structure due to NH ₃ interaction with dihydride	37
Fig 3.9	The fitting results of the Si-H stretching modes of dihydride H/Si(111)	38
Fig 3.10	Reaction scheme for NH ₃ reacting at the dihydride H/Si(111) step edge. Reaction site structures are fully optimized at the PBE/DNP level of theory	39
Fig 3.11	PBE/DNP calculated reaction energy profile for the reaction of NH ₃ at the dihydride-H/Si(111) surface leading to the NH incorporated step-edge structure	40
Fig 3.12	The structure of TEMA	43
Fig 3.13	ALD reaction scheme of TEMA and D ₂ O	44
Fig 3.14	Differential spectra of first 3 cycles TEMA/D ₂ O on nitride surface	45
Fig 3.15	Absorption spectra up to 20 cycles TEMA/D ₂ O on nitride surface	46
Fig 4.1	Structure of TMA monomer (left) and dimer (right)	53
Fig 4.2	The TMA gas phase spectrum and the spectrum after reaction with D ₂ O	54
Fig 4.3	The TMA gas phase spectrum and the spectrum after reaction with ozone	56
Fig 4.4	The schematic of adsorbed species on the H/Si after TMA exposure	57
Fig 4.5	IR absorption spectrum of H/Si(111) exposed by TMA referenced to H/Si(111) at 300°C	58

Fig 4.6	Differential FTIR absorption spectra of 10 cycles Al_2O_3 on H/Si(111) at 300°C	59
Fig 4.7	Absorption spectra of 10 cycles Al_2O_3 on H/Si(111) at 300°C	60
Fig 4.8	Differential FTIR spectra of 20 cycles TMA and ozone deposition on H/Si(111) at 300°C	62
Fig 4.9	(a) Periodic model vibrational density of states (VDOS); and (b) cluster model IR calculations of each surface structure.	64
Fig 4.10	Reaction scheme of formate formation after ozone	66
Fig 4.11	A possible pathway to form formate after ozone exposure	67
Fig 4.12	Absorption spectra of 20 cycles Al_2O_3 at 300°C referenced to H/Si(111)	67
Fig 4.13	Differential FTIR spectra of 20 cycles TMA and ozone deposition on H/Si(111) at 300°C with reduced ozone	69
Fig 4.14	A possible pathway to form Al-OH after ozone exposure with alcohol species on the surface	70
Fig 4.15	Absorption spectra of 20 cycles Al_2O_3 at 300°C with reduced ozone referenced to H/Si(111)	71
Fig 4.16	Differential FTIR spectra of 20 cycles TEMAH and ozone deposition on H/Si(100)	73
Fig 4.17	Absorption spectra of 20 cycles HfO_2 on and referenced to H/Si(100) at 100°C	74
Fig 4.18	Differential FTIR spectra of 20 cycles TEMAH and ozone deposition on SiN_x at 100°C	76
Fig 4.19	Absorption spectra of 20 cycles HfO_2 on SiN_x and referenced to $\text{SiN}_x(100)$ at 100°C	77
Fig 4.20	Absorption spectra show the annealing of 20 cycles HfO_2 on SiN_x referenced to SiN_x	78
Fig 5.1	Chemical structure of $\text{La}(\text{}^i\text{Pr-MeAMD})_3$ precursor and its ball-stick three dimensional view	86
Fig 5.2	FTIR absorption spectrum of gas phase $\text{La}(\text{}^i\text{Pr-MeAMD})_3$ and reaction with D_2O	86
Fig 5.3	FTIR absorption spectrum of 1st $\text{La}(\text{}^i\text{Pr-MeAMD})_3$ on and referenced to H/Si(111) at 200°C	90
Fig 5.4	(a) Absorption spectra of first 3 cycles $\text{La}(\text{}^i\text{Pr-MeAMD})_3+\text{D}_2\text{O}$ on H/Si(111) referenced to oxide; (b) Difference spectra of first 3 cycles $\text{La}(\text{}^i\text{Pr-MeAMD})_3+\text{D}_2\text{O}$ on H/Si(111)	91
Fig 5.5	FTIR absorption spectra of 20 cycles of La precursor and D_2O on H/Si(111) at 200°C	92
Fig 5.6	(a) Differential spectra of 19 th cycle and 20 th cycle La_2O_3 deposition in the carbonate range; (b) the absorption spectra showing the post annealing of 20 cycles La_2O_3 in N_2 which are reference to the H/Si(111)	94
Fig 5.7	FTIR absorption spectra of 20 cycles of La precursor and D_2O on	

	H/Si(111) at 300°C	96
Fig 5.8	Differential spectra of the first 3 cycles of La precursor and D ₂ O on H/Si(111) at 300°C	97
Fig 5.9	Possible decomposition pathways from intact precursor ligand to cyanamide	98
Fig 5.10	Differential spectra of continuous multiple dosing of La precursor on H/Si(111) at 300°C	99
Fig 5.11	Differential spectra of first 4 cycles of La _x Al _y O nanolaminate on H/Si(111) at 300°C	101
Fig 5.12	FTIR absorption spectra of 20 cycles of La _x Al _y O nanolaminate on H/Si(111) at 300°C referenced to H/Si(111)	102
Fig 6.1	Gas phase FTIR absorption spectrum of the copper precursor [Cu(^s Bu-amd)] ₂	109
Fig 6.2	Differential FTIR absorption spectra of [Cu(^s Bu-amd)] ₂ on H/Si (100) surface	110
Fig 6.3	(a) Absorption spectra of 10 cycles Cu on H/Si(111) reference to oxide (left) and (b) the plot of the loss of Si-H vs number cycles (right)	111
Fig 6.4	Differential spectra of 10 cycles Cu on H/Si(111)	112
Fig 6.5	Differential spectra of the first 3 cycles Cu on oxide	114
Fig 6.6	Schematic of Cu precursor and H ₂ interaction on the SiO ₂ surface	115
Fig 6.7	Absorption spectra of the first 3 cycles Cu on Si oxide	116
Fig 6.8	Fitted integrated area of 1010 cm ⁻¹ mode	117
Fig 6.9	(a) Differential spectra of the first cycle Cu on oxide at different temperatures. The Cu is referenced to the oxide and the H ₂ is referenced to the Cu. (b) The absorption spectra of Cu precursor on oxide at different temperatures referenced to oxide	118
Fig 6.10	Schematic of ligand rearrangement on the surface	119
Fig 6.11	The ligand behavior after multiple dosing at different temperatures	120
Fig 6.12	The differential spectra of the 10 th cycle of Cu deposited on SiO ₂ at 185°C	121
Fig 6.13	Results of 10 cycles Cu growth at 140°C	122
Fig 6.14	Results of 10 cycles Cu growth at 125°C	124
Fig 6.15	The relation between thickness of 1 cycle of Cu and growth temperature	125
Fig 6.16	XPS results (Cu 2p and C 1s) of 10 cycles Cu on SiO ₂ at different temperatures	127
Fig 6.17	XPS results (Cu 2p and C 1s) of 10 cycles Cu on SiO ₂ at 140°C for the fresh sample	128
Fig 6.18	XPS results (O 1s) of 10 cycles Cu on SiO ₂ at different temperatures	129
Fig 6.19	Differential FTIR absorption spectra of 10 cycles	131
Fig 6.20	FTIR absorption spectra of 10 cycles Cu on SiN _x at 185°C	132
Fig 6.21	XPS results (C 1s) of 10 cycles Cu on SiN _x at 185°C	133

Fig 6.22	Differential FTIR absorption spectra of 10 cycles copper ALD on Al_2O_3 at 185°C	134
Fig 6.23	XPS results (C 1s) of 10 cycles Cu on Al_2O_3 at 185°C	136
Fig 6.24	Differential FTIR absorption spectra of 20 cycles Cu_3N on SiO_2 at 160°C	137
Fig 6.25	FTIR absorption spectra of 20 cycles Cu_3N on SiO_2 at 160°C	138
Fig 6.26	FTIR absorption spectra of 20 cycles Cu_3N reduced by forming gas	139
Fig 7.1	Area-selective growth of HfO_2	146
Fig 7.2	The schematic of $-\text{CH}_3$ SAM and $-\text{COOH}$ SAM	147
Fig 7.3	Absorption spectra of (a) $-\text{CH}_3$ SAM and (b)- COOH SAM referenced to H/Si(111)	148
Fig 7.4	The annealing results of (a) $-\text{CH}_3$ SAM and (b)- COOH SAM in N_2 referenced to the fresh SAM surface	151
Fig 7.5	The schematic for transformation of carboxyl group to anhydride group	152
Fig 7.6	The absorption spectra of (a) $-\text{CH}_3$ SAM and (b)- COOH SAM which are exposed to ozone and referenced to the fresh SAM surface	154
Fig 7.7	Differential FTIR absorption spectra of TMA on $-\text{COOH}$ SAM surface at 100°C	156
Fig 7.8	Scheme of TMA reacting with the $-\text{COOH}$ SAM surface	157
Fig 7.9	Differential FTIR absorption spectra of 10 cycles Al_2O_3 on $-\text{COOH}$ SAM surface deposited at 100°C	158
Fig 7.10	Absorption spectra of 10 cycles Al_2O_3 on SAM deposited at 100°C	160
Fig 7.11	Annealing of 10 cycles Al_2O_3 on $-\text{COOH}$ SAM surface in N_2	162
Fig 7.12	Differential FTIR absorption spectra of 20 cycles Al_2O_3 by ozone at 100°C on $-\text{COOH}$ SAM surface	163
Fig 7.13	Absorption spectra of 20 cycles Al_2O_3 by ozone on SAM	164
Fig 7.14	Annealing of 20 cycles Al_2O_3 by ozone on $-\text{COOH}$ SAM surface	165
Fig 7.15	Differential FTIR absorption spectra of 10 cycles HfO_2 on $-\text{COOH}$ SAM surface at 100°C	167
Fig 7.16	Absorption spectra of 10 cycles HfO_2 on SAM at 100°C	169
Fig 7.17	Annealing of 10 cycles HfO_2 on $-\text{COOH}$ SAM surface	169
Fig 7.18	Differential FTIR absorption spectra of 10 cycles Cu on $-\text{COOH}$ SAM surface at 185°C	171
Fig 7.19	Absorption spectra of 10 cycles Cu on SAM referenced to the SAM surface at 185°C	171
Fig 7.20	XP S Cu 2p of 10 cycles Cu on SAM	172
Fig A.1	Diagram of a trench capacitor in silicon.	183
Fig A.2	Absorption spectra of annealing of flat H/Si(111) at 300°C	184
Fig A.3	Absorption spectra of annealing of flat H/Si(100)	185
Fig A.4	The structure of trenched sample	186
Fig A.5	The absorption spectrum of hydrogen terminated trenched Si(100)	188

Fig A.6	Absorption spectra of annealing of H-terminated trenched Si surface	189
Fig A.7	Absorption spectra of trenched H/Si(100) exposed to TEMAH at 100°C	190
Fig A.8	Absorption spectra of trenched H/Si(100) exposed to TEMAH at various temperatures	191
Fig A.9	Absorption spectra of 10 cycles HfO ₂ on trenched H/Si(100) at 300°C	192
Fig A.10	RBS spectrum of 10 cycles HfO ₂ on trenched H/Si(100) at 300°C	193

List of Frequently Used Abbreviations and Acronyms

ALD	Atomic layer deposition
ATR	Attenuated total reflectance
[Cu(^s Bu-amd)] ₂	Copper (I) di-sec-butylacetamidinate
CVD	Chemical vapor deposition
DI water	De-ionized water
DFT	Density functional theory
FTIR	Fourier transform infrared spectroscopy
H/Si	Hydrogen-terminated silicon
IR	Infrared
La(ⁱ Pr-MeAMD) ₃	Lanthanum tris (N,N' - diisopropylacetamidinate)
MBE	Molecular-beam epitaxy
RBS	Rutherford backscattering spectroscopy
SAMs	Self-assembled monolayers
SEM	Scanning electron microscopy
TEMAH	Tetrakis(ethylmethylamino) hafnium
TMA	Tri-methyl aluminum
UHV	Ultra-high vacuum
UTD	University of Texas at Dallas
XPS	X-ray photoelectron spectroscopy

Chapter 1: Introduction

1.1 Atomic layer deposition

Deposition of thin films has great significance in every field with numerous applications such as in optics, optoelectronics, microelectronics, superconductors, catalysts, solar energy, and so on. Particularly, the demand of continuous shrinking of devices for nanotechnology such as in microelectronics and micro-electromechanical systems (MEMS) requires various thin film deposition methods suitable for different applications and conditions. Among them, atomic layer deposition (ALD) as a novel deposition method is attracting more and more attention of both academic and industrial researchers due to its great advantages in depositing high quality thin films.

ALD was first introduced and realized in 1970s by T. Suntola and co-workers in Finland to deposit ZnS [1] referred as atomic layer epitaxy at that time. After 30 years of development, it has become one of the most important methods to deposit thin films. Compared with other deposition techniques such as CVD, sputtering, MBE, evaporation, and so on, ALD can be initiated at lower temperature and with more flexible growth parameters without damaging the surface.

The advantages of ALD include excellent thickness control, high quality (e.g. pin-hole free films), and highly conformal deposition [2, 3, 4, 5, 6]. Thus, it is a very good deposition tool for various rough surfaces such as trenches [7, 8], nanowires [9, 10], nanoporous materials [11, 12], and so on due to its excellent step coverage [13, 14]. For example, trenches are commonly used for trench capacitor in DRAM to achieved high capacitance. How to deposit high quality and uniform high- κ insulator/metal gate into those deep trenches is challenging. For this purpose, ALD is becoming the best choice because of its good step coverage.

ALD has already been utilized to deposit various materials such as metal oxides [6], metals [15], organic films [16] and nitrides [6] with commercial success. Its applications include in microelectronic, photonics, MEMS, 3D optoelectronics, photovoltaics, catalysts, electrolyte fuel cells, and so on [17].

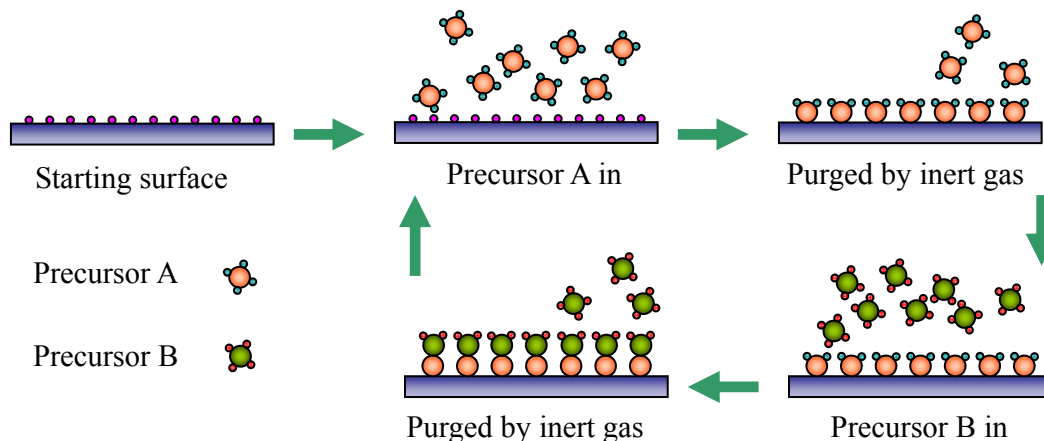


Fig 1.1 Ideal ALD process based on self-terminating mechanism. Precursor A exposure followed by Precursor B exposure is one cycle. The rest of the precursor is purged away.

ALD is based on self-terminating reaction mechanism [18, 19]. Two precursors, A and B, are individually and alternatively introduced into the reactor. Each precursor will not react with itself but react with each other. Thus, the film could be deposited layer by layer. The thickness of the film is naturally controlled by the number of growth cycles (one dosing of precursor A with one dosing of B is called one cycle). In this way, a uniform, pin-hole-free film could be obtained. The schematic procedure of ALD growth is shown in Fig. 1.1. Starting from a reactive surface, precursor A is carried in and reacts with the surface until saturating it. Then the rest of the precursor and byproducts are purged away by inert gas. After that, precursor B is carried in and reacts with the first layer of adsorbed precursor A on the substrate until saturating the surface, and then again the rest of the precursor and byproducts are purged away so that one cycle of film is deposited. By repeating this process, we can deposit the film layer by layer. The thickness

of the film can be easily controlled by the number of cycles. The typical growth rate is about 1 Å/cycle. Most ALD processes are thermally activated and plasma has been used as well to increase the precursor reactivity [20, 21].

In the ideal case, compared with CVD process, the temperature, pressure, and the precursor pulse length will not affect the ALD growth. So ALD is able to deposit high quality film at lower temperature with higher parameter tolerance, which is a great improvement.

However, the real ALD has many critical issues. They can be briefly summarized as follows:

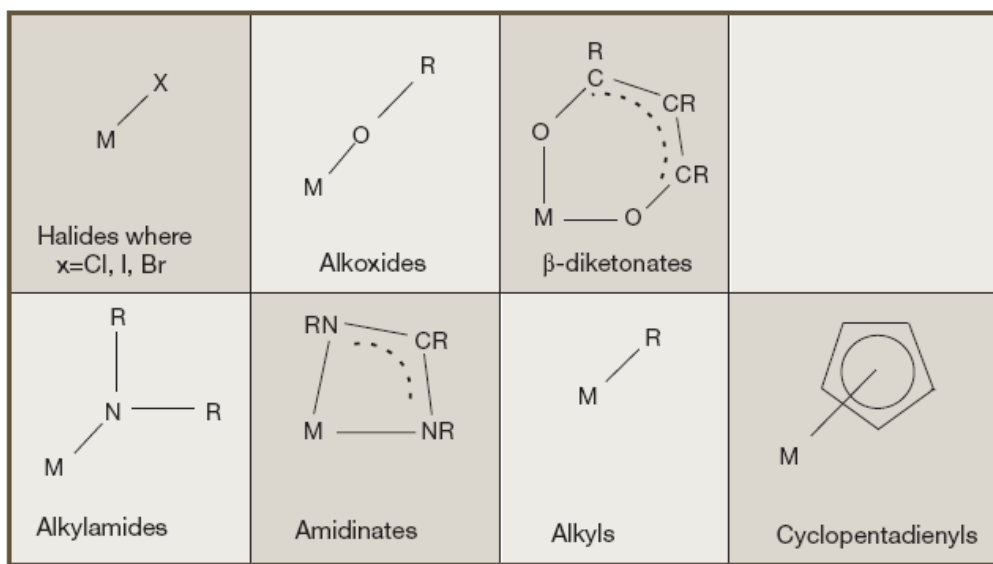


Fig 1.2 Examples of typical ALD metal precursors [22], including metal halides, metal-N, metal-O, metal-C bonding types and so on.

1) The precursor—precursor is the key element for all ALD process. Several basic requirements must be satisfied for acceptable ALD precursors [22]. First the precursor must be highly reactive with both the starting surface and the other precursor previously attached to the surface but not self-reacting. At the same time, they must be sufficiently

volatile at a temperature at which they are thermally stable. A reasonable and reproducible evaporation rate for the precursors is desired as well. On the other hand, the byproducts after reaction should not be reactive to or etch the surface and can be easily purged away. Also, they should not contaminate or damage the ALD reactor.

As for the structures, most ALD metal and metal oxide precursors are halides or metal organic compounds. Fig 1.2 shows the structures of typical ALD precursors having been utilized. There are also some pure organic precursors used to deposit organic films [23]. Usually water or ozone is used as oxidant for metal oxides [24], and H_2 [15] or oxygen [25] is used as reductant for metals. NH_3 is also used for nitride deposition [26].

2) The growth temperature—only within the ALD temperature window can we have real ALD process with a constant growth rate [19]. If the temperature is too low, it may not initiate the reactions for ALD or may cause insufficient reactions. The physisorption of the precursor on the surface could also occur, resulting in higher growth rate than normal. If the temperature is too high, the precursor may decompose to give CVD growth or may desorb from the surface resulting in lower growth rate. Fig 1.3 shows the relation between the ALD deposition rate and temperature.

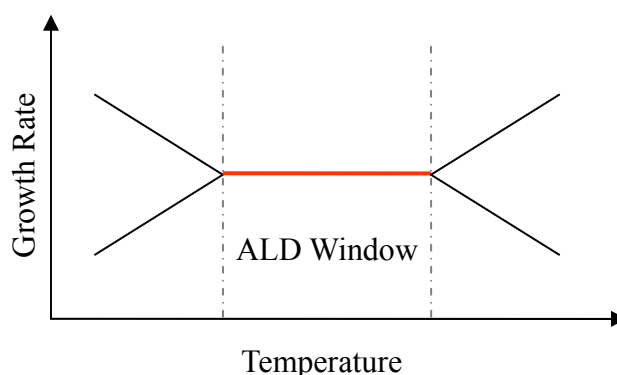


Fig 1.3 ALD temperature window. Only within the ALD window, the growth rate is constant. Higher or lower temperature will cause unexpected growth rate.

3) The starting surface—ALD cannot deposit the film on any surface. The surface

must be chemically reactive enough with the precursor enabling the precursor to chemically bond to the surface. Otherwise the growth will not take place. If the reactivity is too low to have saturated growth, it will result in rough film [27]. On the other hand, the surface must be stable during the transportation and pretreatment before the ALD process. Various surfaces have been used for different purposes, such as SiO₂, H/Si, nitride, SAMs, graphene, and so on [28, 29, 30, 31, 32].

1.2 ALD of high- κ metal oxide

The transistor--the basic of modern integrated circuit devices, is becoming smaller and smaller defined as scaling [33]. In transistors, silicon dioxide has been used for decades as a gate insulator material due to its excellent quality on silicon. Scaling includes reducing the oxide thickness, junction depth, and depletion width to achieve high-speed and low-power consumption. It requires the SiO₂ gate insulator layer as thin as possible. However, there is a physical limit for such kind of scaling. When the SiO₂ thickness goes down to 10-12 Å, there is no full band-gap structure and it results in significant leakage current [34, 35]. Thus, alternative insulator materials replacing SiO₂ are necessary [36]. High- κ ($\kappa > 3.9$, κ is the dielectric constant) materials, such as HfO₂, Al₂O₃, and La₂O₃, are good candidates to replace SiO₂. By using high- κ , the physically thickness of the high- κ insulator ($t_{high-\kappa}$) would be thicker than that of SiO₂ (t_{eq}) with equivalent capacitance, as shown in Eq. 1.1. Therefore, the leakage current is decreased without impairing the performance of devices. Although high- κ materials can replace the SiO₂, many important issues need to be addressed before the application including band alignment to silicon, film morphology, thermal stability, mobility of charge carriers, electrical defects, and so on [36].

$$t_{high-\kappa} = \frac{\kappa_{high-\kappa}}{\kappa_{SiO_2}} t_{eq} = \frac{\kappa_{high-\kappa}}{3.9} t_{eq} \quad (1.1)$$

Several methods are used to deposit high- κ insulators, such as ALD [36], MBE [37], CVD [38] and PVD [39]. Among them, ALD is the most promising and widely used method due to its many advantages as we mentioned in the previous section.

For each high- κ material there are several types of precursors, and for each precursor before its industrial application, we must have a fundamental understanding of its every aspect during the ALD process, such as the quality of the deposited film, the reaction mechanism during the ALD process, the properties in the gas phase and on surfaces, and so on. The interface between the substrate and the high- κ insulator is also crucial because the interfacial SiO_2 significantly decreases the effective dielectric constant value of high- κ materials [36]. So, the formation of interfacial SiO_2 must be examined during the ALD process for each new precursor due to its individual physical and chemical properties.

1.3 ALD of metal

No doubt that pure metal deposition has plenty of applications almost in every field. Considering the great advantages of ALD, it is promising to deposit pure metal film by ALD, such as to deposit metal gate on high- κ insulator. However, only a few pure metals such as tungsten, ruthenium and platinum have been deposited by ALD due to lack of good metal precursors [15], which makes the deposition of metal the least understood among all ALD systems. Thus, many potential applications of ALD are hindered. The major difficulty is that most of the precursors either have very low vapor pressure or have very low reactivity [15, 40].

With the great effort of chemists, more and more new metal precursors have been synthesized for ALD recently, which make it possible to deposit copper, iridium palladium, rhodium, titanium, tantalum, and so on [15, 40, 41, 42]. Although the deposition by these precursors is successful, the detailed picture of the ALD process, such as the reaction mechanism, the ALD temperature window, and the film quality, is not clear yet. It makes the mechanistic study of metal ALD process, the evaluation of the precursor properties and the quality of the films by those new precursors become urgent. On the other hand, metal diffusion and agglomeration are well known issues for metal deposition such as copper [40, 42]. So the study of metal thermal dynamic behavior on surfaces during ALD is also critical.

1.4 Overview of the dissertation

Despite the great success of ALD, many physical and chemical processes during the ALD growth have not been not well understood yet. Since different precursors have different physical and chemical properties, a case-by-case study is necessary for each precursor. However, the mechanistic study of ALD is far behind the experimental applications of ALD due to the lack of efficient mechanistic study tools. Only a few precursors have been studied in detail while with the fast inventions of more ALD precursors. The actual understanding of reactions during ALD processes is significantly important because it could greatly assist the design and optimization of the ALD processes.

Most of ALD issues are related to surface chemistry and it is well known that Fourier transform infrared (FTIR) spectroscopy is a powerful tool to study surface chemistry. Further, there is no doubt that an ideal method to study the ALD processes is

in situ observation, Combining those two factors, we developed a home-made ALD reactor with capability of *in situ* FTIR spectroscopy measurement to mechanistically study the ALD process. By using this unique method, the reactions of the precursor on different surfaces and the formation of interfaces are monitored without interference from the external world. The species on the surfaces are identified and thereby the reaction mechanism of ALD can be inferred. With these understandings, we are able to improve the ALD process.

By using *in situ* FTIR and other techniques, this dissertation will cover the following topics:

Chapter 1 is the introduction of the dissertation. It briefly reviews the fundamentals of ALD including the ideal mechanism, the advantages, the critical issues of ALD, and the applications of ALD for high- κ materials and metals.

Chapter 2 introduces the instruments used for the studies, the configuration of our home-made ALD with the *in situ* transmission FTIR setup, typical ALD growth conditions, sample preparations, and some details about data analysis.

Chapter 3 will show the silicon surface preparation by thermal NH_3 nitridation with *in situ* FTIR study. Nitridation is used to minimize the formation of interfacial SiO_2 between the high- κ insulator and the silicon substrate. Three types of hydrogen-terminated Si(111) surfaces (H/Si) including flat, monohydride stepped and dihydride stepped surfaces are used to study the initial interaction between NH_3 and the surface Si-H by varying the temperature from 150°C to 600°C. Density functional theory calculation is used to confirm our experimental observations. As an example, HfO_2 by ALD of TEMAH/ D_2O is deposited on this nitride.

Chapter 4 focuses on the ozone based ALD. Instead of using water as the oxidant,

ozone is used to grow high- κ metal oxides to eliminate trapped water (-OH) inside the film during the growth. This chapter will show the Al_2O_3 deposition by TMA and ozone on H/Si. The gas phase reactions of TMA/ H_2O and TMA/ozone will be presented. As another example, HfO_2 deposition by TEMA and ozone on thin silicon nitride as an oxidation barrier is studied as well.

Chapter 5 will cover the IR mechanistic study of ALD of La_2O_3 on H/Si surface by a new precursor-- $\text{La}(\text{}^i\text{Pr-MeAMD})_3$ [43] and D_2O at different temperatures. The precursor gas phase IR spectra, reactivity, ALD window, and impurities in the film are discussed. With these understandings, alternating TMA/ D_2O ALD cycle and La/ D_2O cycle are used to deposit $\text{La}_x\text{Al}_y\text{O}$ nano-laminate to improve the film quality. *Ex situ* Rutherford backscattering spectroscopy (RBS) is used to check the growth rate and film uniformity.

Chapter 6 will show the example of pure copper deposition on various substrates including H/Si, SiO_2 , SiN_x and Al_2O_3 by using a new precursor $[\text{Cu}(\text{}^s\text{Bu-amd})]_2$ [44] reduced by H_2 . Precursor gas phase and the deposition temperature dependence on SiO_2 are also studied. The *in situ* FTIR spectra clearly indicate the copper agglomeration and diffusion on SiO_2 surface, and X-ray photoelectron spectroscopy (XPS) is used to investigate the contents in the film as well.

Chapter 7 explores the ALD on self-assembled monolayer (SAM) [45] grafted on H/Si(111) due to its extraordinary electrical properties [46] and potential application for area-selective ALD growth [47, 48]. As examples, the stability of two kinds of SAMs including -COOH and - CH_3 terminated H/Si(111) is studied. HfO_2 , Al_2O_3 , and copper are deposited on -COOH terminated surface which demonstrates that it is a promising starting surface for ALD.

The appendix chapter presents the preliminary *in situ* FTIR study of HfO_2 deposited

on hydrogen-terminated trenched Si(100) surface. The preliminary results of thermal stability and reactivity of the trenched H/Si surface are shown in this chapter. Then HfO₂ deposition is examined by IR spectra and RBS.

Bibliography

1. T. Suntola and J. Antson, *Method for producing compound thin films*, US Patent (1977), 4, 058, 430.
2. L. Niinistö, M. Nieminen, J. Päiväsäari, J. Niinistö, M. Putkonen and M. Nieminen, *Advanced electronic and optoelectronic materials by atomic layer deposition: An overview with special emphasis on recent progress in processing of high-k dielectrics and other oxide materials*, Physica Status Solidi (A) **201** (2004), 1443.
3. M. Leskel and R. Mikko, *Atomic layer deposition chemistry: Recent developments and future challenges*, Angewandte Chemie International Edition **42** (2003), no. 45, 5548.
4. M. Ritala and M. Leskela, *Atomic layer epitaxy-a valuable tool for nanotechnology?*, Nanotechnology **10** (1999), 19.
5. K.-E. Elers, T. Blomberg, M. Peussa, B. Aitchison, S. Haukka and S. Marcus, *Film uniformity in atomic layer deposition*, Chemical Vapor Deposition **12** (2006), no. 1, 13.
6. R. L. Puurunen, *Surface chemistry of atomic layer deposition: A case study for the trimethylaluminum/water process*, Journal of Applied Physics **97** (2005), 121301.
7. R. G. Gordon, D. M. Hausmann, E. Kim and J. Shepard, *A kinetic model for step coverage by atomic layer deposition in narrow holes or trenches*, Chemical Vapor Deposition **9** (2003), 83.
8. D. Hausmann, J. Becker, S. Wang and R. G. Gordon, *Rapid vapor deposition of highly conformal silica nanolaminates*, Science **298** (2002), 402.
9. R. Solanki, J. Huo, J. L. Freeouf and B. Miner, *Atomic layer deposition of ZnSe/CdSe superlattice nanowires*, Applied Physics Letters **81** (2002), no. 20, 3864-3866.
10. Y. Qin, S. M. Lee, A. Pan, U. Gosele and M. Knez, *Rayleigh-instability-induced metal nanoparticle chains encapsulated in nanotubes produced by atomic layer deposition*, Nano Lett. **8** (2008), no. 1, 114-118.
11. S. O. Kucheyev, J. Biener, Y. M. Wang, T. F. Baumann, K. J. Wu, T. v. Buuren, A. V. Hamza, J. H. Satcher, Jr., J. W. Elam and M. J. Pellin, *Atomic layer deposition of ZnO on ultralow-density nanoporous silica aerogel monoliths*, Applied Physics Letters **86** (2005), no. 8, 083108.
12. S. P. Adiga, J. W. Elam, M. J. Pellin, C.-C. Shih, C.-M. Shih, S.-J. Lin, Y.-Y. Su, S. D. Gittard, J. Zhang and R. J. Narayan, *Nanoporous materials for biomedical devices*, Journal of the Minerals, Metals and Materials Society **60** (2008), 26.
13. E. C. John, *Chemical methods of thin film deposition: Chemical vapor deposition*,

- atomic layer deposition, and related technologies*, Journal of Vacuum Science & Technology A: Vacuum, Surfaces, and Films **21** (2003), no. 5, S88-S95.
14. K. Ja-Yong, A. Ji-Hoon, K. Sang-Won and K. Jin-Hyock, *Step coverage modeling of thin films in atomic layer deposition*, Journal of Applied Physics **101** (2007), no. 7, 073502.
 15. B. S. Lim, A. Rahtu and R. G. Gordon, *Atomic layer deposition of transition metals*, Nature Materials **2** (2003), 749-754.
 16. M. Putkonen, J. Harjuoja, T. Sajavaara and L. Niinistö, *Atomic layer deposition of polyimide thin films*, Journal of Materials Chemistry **17** (2007), 664-669.
 17. <http://www.cambridgenanotech.com/ALD-applications.php>, Cambridge NanoTech Inc.
 18. S. M. George, A. W. Ott and J. W. Klaus, *Surface chemistry for atomic layer growth*, Journal of Physical Chemistry **100** (1996), no. 31, 13121-13131.
 19. T. Suntola, *Surface chemistry of materials deposition at atomic layer level*, Applied Surface Science **100-101** (1996), 391-398.
 20. J. L. van Hemmen, S. B. S. Heil, J. H. Klootwijk, F. Roozeboom, C. J. Hodson, v. d. Sanden and W. M. M. Kessels, *Plasma and thermal ALD of Al_2O_3 in a commercial 200 mm ALD reactor*, Journal of the Electrochemical Society **154** (2007), G165-G169.
 21. S. B. S. Heil, P. Kudlacek, E. Langereis, R. Engeln, M. C. M. v. d. Sanden and W. M. M. Kessels, *In situ reaction mechanism studies of plasma-assisted atomic layer deposition of Al_2O_3* , Applied Physics Letters **89** (2006), no. 13, 131505.
 22. C. Musgrave and R. G. Gordon, *Precursors for atomic layer deposition of high-k dielectrics*, Future Fab International **18** (2005), 126-128.
 23. M. Putkonen, J. Harjuoja, T. Sajavaara and L. Niinistö, *Atomic layer deposition of polyimide thin films*, J. Mater. Chem. **17** (2007), 664.
 24. S. K. Kima, C. S. Hwanga, S.-H. K. Parkb and S. J. Yun, *Comparison between zno films grown by atomic layer deposition using H_2O or O_3 as oxidant* Thin Solid Films **478** (2005), 103-108.
 25. T. Aaltonen, P. Alén, M. Ritala and M. Leskelä, *Ruthenium thin films grown by atomic layer deposition*, Chemical Vapor Deposition **9** (2003), 45-49.
 26. J. W. Elama, M. Schuiskya, J. D. Fergusona and S. M. George, *Surface chemistry and film growth during tin atomic layer deposition using TDMAT and NH_3* , Thin Solid Films **436** (2003), 145-156.
 27. M. F. Martin, J. C. Yves, L. G. Martin, D. Annelies, B. Bert, D. W. Glen, H. Mun-Yee, B. O. d. R. Elisa, J. R. B. Israel and C. S. Fernanda, *Enhanced initial growth of atomic-layer-deposited metal oxides on hydrogen-terminated silicon*, Applied Physics Letters **83** (2003), no. 4, 740-742.
 28. X. Wang, S. M. Tabakman and H. Dai, *Atomic layer deposition of metal oxides on pristine and functionalized graphene*, J. Am. Chem. Soc. **130** (2008), no. 26, 8152-8153.
 29. M. T. Ho, Y. Wang, R. T. Brewer, L. S. Wielunski, Y. J. Chabal, N. Moumen and M. Boleslawski, *In situ infrared spectroscopy of hafnium oxide growth on*

- hydrogen-terminated silicon surfaces by atomic layer deposition*, Applied Physics Letters **87** (2005), no. 13, 133103.
30. B. Busch, O. Pluchery, Y. Chabal, D. Muller, R. Opila, J. Kwo and E. Garfunkel, *Materials characterization of alternative gate dielectrics*, MRS Bulletin **27** (2002), no. 206-211.
31. R. T. Brewer, M. T. Ho, K. Z. Zhang, L. V. Goncharova, D. G. Starodub, T. Gustafsson, Y. J. Chabal and N. Moumen, *Ammonia pretreatment for high-kappa dielectric growth on silicon*, Applied Physics Letters **85** (2004), no. 17, 3830-3832.
32. A. S. Killampalli, P. F. Ma and J. R. Engstrom, *The reaction of tetrakis(dimethylamido)titanium with self-assembled Alkyltrichlorosilane monolayers possessing -OH, -NH₂, and -CH₃ terminal groups*, J. Am. Chem. Soc. **127** (2005), no. 17, 6300-6310.
33. P. A. Packan, *Device physics: Pushing the limits*, Science **285** (1999), no. 5436, 2079-2081.
34. D. A. Muller, T. Sorsch, S. Moccio, F. H. Baumann, K. Evans-Lutterodt and G. Timp, *The electronic structure at the atomic scale of ultrathin gate oxides*, Nature **399** (1999), no. 6738, 758-761.
35. J. B. Neaton, D. A. Muller and N. W. Ashcroft, *Electronic properties of the Si/SiO₂ interface from first principles*, Physical Review Letters **85** (2000), no. 6, 1298.
36. G. D. Wilk, R. M. Wallace and J. M. Anthony, *High-k gate dielectrics: Current status and materials properties considerations*, Journal of Applied Physics **89** (2001), 5243.
37. D. H. Triyoso, L. H. R. I. Hegde, Z. Yu, K. Moore, J. Grant, B. E. White and P. J. Tobin, *Lanthanum aluminate by atomic layer deposition and molecular beam epitaxy*, Journal of Vacuum Science & Technology B **23** (2005), 2480.
38. G. Carta, N. El Habra, G. Rossetto, G. Torzo, L. Crociani, M. Natali, P. Zanella, G. Cavinato, V. Matterello, V. Rigato, S. Kaciulis and A. Mezzi, *Growth of hafnium dioxide thin films by MOCVD using a new series of cyclopentadienyl hafnium compounds*, Chemical Vapor Deposition **13** (2007), 626-632.
39. D. Brassard, M. A. E. Khakani and L. Ouellet, *Substrate biasing effect on the electrical properties of magnetron-sputtered high-k titanium silicate thin films*, Journal of Applied Physics **102** (2007), no. 3, 034106.
40. Z. Li, A. Rahtu and R. G. Gordon, *Atomic layer deposition of ultrathin copper metal films from a liquid copper(I) amidinate precursor*, Journal of Electrochemical Society **153** (2006), C787-C794.
41. T. Aaltonen, M. Ritala, Y.-L. Tung, Y. Chi, K. Arstila, K. Meinander and M. Leskelä, *Atomic layer deposition of noble metals: Exploration of the low limit of the deposition temperature*, Journal of Materials Research **19** (2004), 3353-3358.
42. H. Kim, *Atomic layer deposition of metal and nitride thin films: Current research efforts and applications for semiconductor device processing*, Journal of Vacuum Science & Technology B: Microelectronics and Nanometer Structures **21** (2003), no. 6, 2231-2261.

43. B. S. Lim, A. Rahtu, J.-S. Park and R. G. Gordon, *Synthesis and characterization of volatile, thermally stable, reactive transition metal amidinates*, *Inorganic Chemistry* **42** (2003), 7951-7958.
44. Z. Li, S. T. Barry and R. G. Gordon, *Synthesis and characterization of Cu(I) amidinates as precursors for atomic layer deposition (ald) of copper metal*, *Inorganic Chemistry* **44** (2005), 1728-1735.
45. A. Ulman, *Formation and structure of self-assembled monolayers*, *Chemical Reviews* **96** (1996), 1533-1554.
46. O. Seitz, T. Bocking, A. Salomon, J. J. Gooding and D. Cahen, *Importance of monolayer quality for interpreting current transport through organic molecules: Alkyls on oxide-free Si*, *Langmuir* **22** (2006), no. 16, 6915-6922.
47. C. Rong, K. Hyounsub, C. M. Paul, W. P. David and F. B. Stacey, *Achieving area-selective atomic layer deposition on patterned substrates by selective surface modification*, *Applied Physics Letters* **86** (2005), no. 19, 191910.
48. R. Chen and S. Bent, *Chemistry for positive pattern transfer using area-selective atomic layer deposition*, *Advanced Materials* **18** (2006), no. 8, 1086-1090.

Chapter 2: Experiment Setup, Substrate Preparation, and Data Analysis

Having been mentioned in the introduction chapter, the deposition is done in our unique home made atomic layer deposition system. Its most striking feature is that this system enables *in situ* transmission infrared spectroscopy study. The detailed information will be discussed in the following part of this chapter.

2.1 Home made atomic layer deposition system

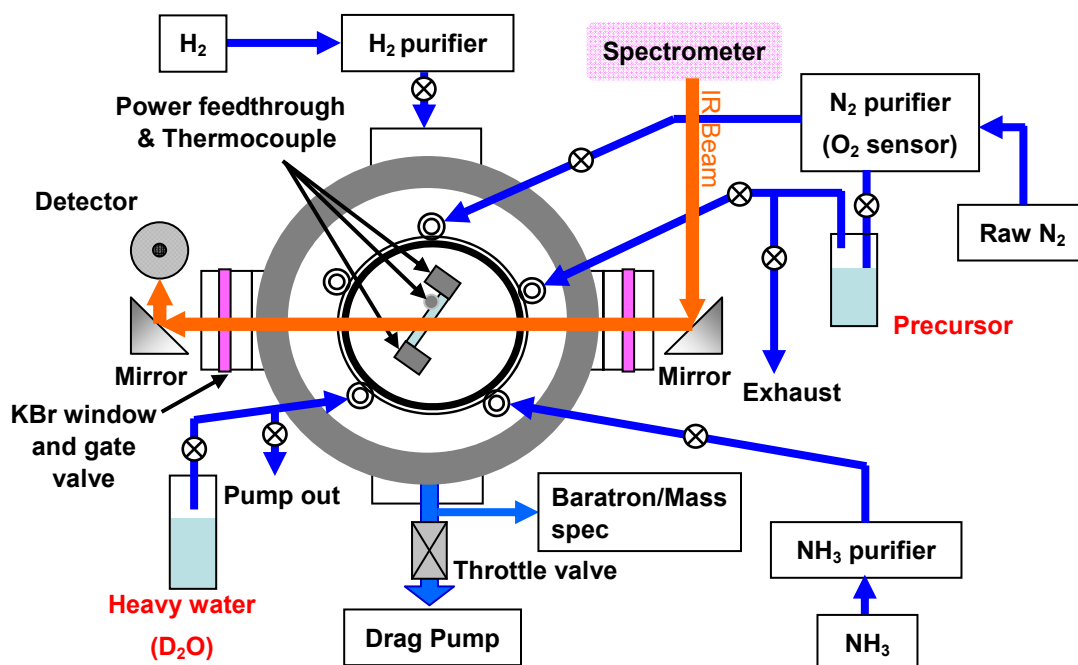


Fig 2.1 Schematic diagram of home made ALD system. The system is equipped with *in situ* FTIR and mass spectrometer. Transmission geometry and resistivity heating are used.

Our home made ALD system is presented by Fig 2.1. We have 3 ALD systems (I, II and III) at Rutgers. ALD I and ALD II were designed and realized by previous group members (Dr. Martin M. Frank, Dr. Rhett Brewer, Dr. Ming-Tsung Ho and Dr. Yu Wang).

I was incorporated to finish ALD III and modified ALD II and III afterwards. I was also involved for the design and realization of the new generation of optimized ALD systems at UTD. As in Fig 2.1, the main reactor is a UHV chamber denoted by the gray circle in the diagram. The sample is placed at the center of the chamber and positioned by tantalum sample holder. DC current passes the sample by applying a DC voltage so that the sample is heated by the resistivity heating method. In this way, the sample is heated without touching anything and remains clean, as well as enabling a transmission IR spectroscopy scheme. The incident angle of the IR can be adjusted by rotating the sample through a manipulator. Sample temperature is monitored by a thermal couple (welded on a tantalum clip) clipped to it, and controlled by Eurotherm 2404 controller with HP 6010 DC power supply.

Thermo Nicolet Nexus 6700 and 670 IR spectrometers are used and equipped with the liquid nitrogen cooled external MCT-B (Mercury Cadmium Telluride) detector which is favorable for the signal below 1000 cm^{-1} . Typical mid-infrared $400\text{-}4000\text{ cm}^{-1}$ with the resolution of 4 cm^{-1} is utilized. The infrared beam comes out from the spectrometer and is aligned to pass through the center of the sample by using an external parabola mirror. Then the transmitted beam is reflected and focused again onto the external MCT-B detector by an ellipsoidal mirror. Transparent KBR windows are mounted to the chamber to let IR beam enter the chamber and protected by gate valves during the sample treatment. The detailed and classical introduction of FTIR technique can be found in many IR books [2, 3, 4, 5, 6]. Fig 2.2 gives a rough idea of the FTIR spectrometer. Note that the mirror on the top right corner of the diagram can rotate to let the IR beam out of the spectrometer and then be introduced into our ALD reactor as shown in Fig 2.1.

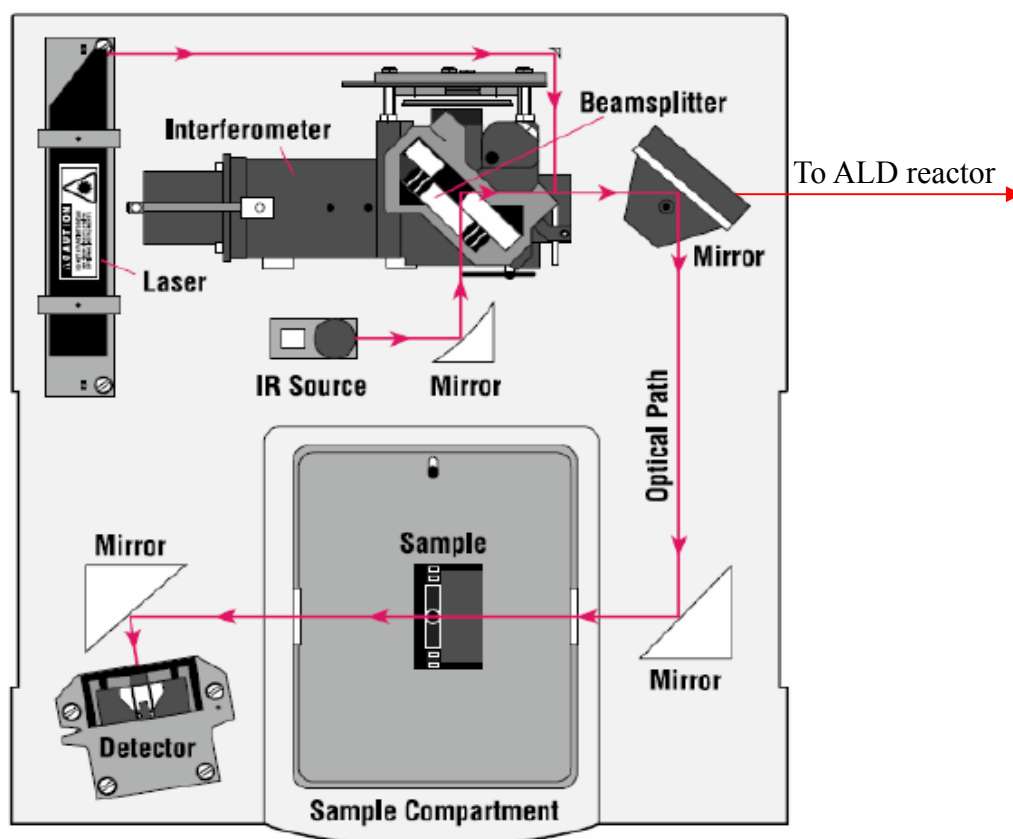


Fig 2.2 Diagram of Nicolet FTIR spectrometer [1]. The mirror at the top left corner can rotate to let the IR beam go out to ALD reactor.

The whole system is pumped by an adixen Drytel 1025 dry pump. The MKS 653B throttle valve is used to control the pumping flow. The base pressure of the system is 10^{-4} to 10^{-7} torr. The pressure is monitored by the Baratron Capacitance Manometer. A mass spectrometer SRS RGA 300 is equipped in the system also. To minimize the adsorbed water inside, the ALD reactor is baked at 60°C all the time. And therefore, **all IR measurements in this dissertation are performed at a substrate temperature of 60°C .** Because at higher temperature, the excitation of Si electron to conduction band will reduce the signal intensity, lowest temperature for IR measurement is desired and 60°C is the lowest temperature in this case.

1/4 inch stainless steel tubings are used for all gaslines. Gas flow is controlled by MKS 1479A series mass flow controllers and Swagelok pneumatic valves. N₂ gas for system purging and precursor carrying gas is purified by the Centorr 2A and Oxygon OG-120M (both with oxygen impurity < 10⁻⁶ ppm) purifiers followed by an additional Aeronex Gate Keeper gas purifier. Ultra high purity (> 99.999%) NH₃, H₂ and D₂ are introduced into the ALD reactor after purified by Aeronex Gate Keeper gas purifiers. Ozone are generated by passing O₂ (> 99.999%) through the INUSA 5000 ozone generator. Most important, the ALD metal or metal oxide precursors are equipped in the system as well, such as D₂O and TMA (for Al₂O₃) which are both kept at room temperature, TEMA^h kept at ~75°C for HfO₂, La(ⁱPr-MeAMD)₃ kept at ~130°C for La₂O₃, [Cu(^sBu-amd)]₂ kept at ~95°C for Cu. They will be discussed in detail in later chapters.

Other instruments are also used in the study, including Rutherford backscattering spectroscopy (RBS), X-ray photoelectron spectroscopy (XPS)--PHI 5600 ESCA (at UTD), Atomic Force Microscopy (AFM)--Veeco Dimension 3100 (at UTD), and Ellipsometry--Horiba Jobin Yvon iHR 320 ellipsometer (at UTD).

2.2 Sample preparation and FTIR data analysis

In our study, double side polished, float-zone grown, and lightly doped (~10 Ω·cm) Si(111) and Si(100) wafers are used. The sample sized is 1.5 cm×3.8 cm. Before any further treatment, the sample is first rinsed by acetone, methanol, and deionized water (DI water, 18.2 MΩ·cm), and then standard RCA [7, 8] (SC1--DI water: H₂O₂: NH₄OH = 4:1:1, SC2--DI water: H₂O₂: HCl = 4:1:1 at 80°C for 10 min) cleaning is performed followed by excessive dionized water rinsing. Hydrogen-terminated Si(100) (H/Si)

surfaces is achieved by a ~ 40 s HF ($\sim 20\%$) etching after RCA cleaning, and for H/Si(111) an additional 2.5 min NH_4F ($\sim 49\%$) etching [9, 10] is used. In the end, the sample is dried by N_2 . Sometimes, instead of RCA cleaning, piranha solution is used for better cleaning by putting the sample into a mixture of concentrated sulfuric acid and hydrogen peroxide at the ratio of 3:1 at 90°C for 45-60 min, followed by thoroughly DI-water rinsing. It has been proven that this method is more efficient than the normal RCA cleaning [7].

Table 2.1 The elements concentration of $\text{SiO}_2/\text{Si}(100)$ surface after RCA cleaning by XPS

Elements	C	O	Si
Concentration (%)	2.4	63.7	33.9

The Si(100) surface is covered by a thin layer of SiO_2 ($\sim 70\text{\AA}$) from Virginia Semiconductor. The constitution of the Si(100) after RCA cleaning is measured by XPS and is shown in table 2.1. The carbon contamination is very low after RCA cleaning and could result from the contamination during the transportation. By fitting of the shifted Si 2p peak due to SiO_2 , the O/Si ratio of this SiO_2 oxide is ~ 2.11 which is very close to the ideal ratio.

Table 2.2 The elements concentration of H/Si(100) by XPS

Elements	C	O	Si	F
Concentration (%)	1.3	0.8	97.6	0.3

H/Si(100) surface is also studied by XPS to verify the quality of Si-H passivation. The elements concentration is shown in table 2.2. Trace amount of carbon contamination is found and accompanied by trivial oxygen amount which may come from the environment as well. Fluorine contamination can be detected due to the HF and NH_4F etching but its concentration is very low. The XPS result confirms that our initial Si surface is very clean.

After the pretreatment, the Si substrate is loaded into the ALD reactor immediately to carry out IR measurements. FTIR technique is a powerful tool to investigate chemical bonds on surface, in gas phase, in solids and even in liquid. The typical IR incident angle used is $\sim 74^\circ$ (Brewster angle) for highest transmission signal intensity, because the p-polarized component completely transmits through the sample without any reflection. Information of both parallel and perpendicular to the surface is achieved at this angle. Normal incidence ($\sim 0^\circ$) or close to normal incidence ($\sim 20^\circ$) is also used to get the information more parallel to the surface in our study. That is, the incident angle dependence can identify the orientation of chemical bonds on the surface. The dipole of the bond perpendicular to the surface can not be observed at normal incidence due to its non-response to the paralleled electrical field, while both parallel and perpendicular components can be observed at 74° [11].

To get the absorption spectrum which shows the change in the interface, surface and film, a reference must be used. The Absorbance (A) can be obtained by using the following equation:

$$A = -\log_{10} \frac{I(\nu)}{I_0(\nu)} \quad (\text{Eq. 2.1})$$

where $I(\nu)$ and $I_0(\nu)$ are the transmission single beam spectrum of the subject and the reference, respectively. Thus, all changes of the subject relative to the reference are exhibited by the absorption spectrum. All positive features in absorbance spectrum correspond to the formation of new chemical bonds and all negative features correspond to the removals of the chemical bonds relative to the reference. The frequency, height, shape, width and integrated area of these peaks contain many information of a specific chemical specie, including the chemical bond, dipole, concentration, absorption response,

surface morphology, and so on. However, in reality, some artifacts may appear due to the systematic change in the IR optical bench such as the temperature fluctuation, vibration, degradation of IR source, strong IR absorption (caused by bulk Si substrate and others), absorbed contaminations, and so on. All these will affect the single beam and introduce unwanted artificial bands in the spectrum or distort the baseline of the spectrum. Furthermore, considering the overlapping of different species' vibrational modes in the same frequency range, all make the analysis of IR data more complicated. Although some effort is needed, IR is a great tool to study surface chemistry.

To reduce some of the systematic error, the spectra in this thesis are taken with a resolution of 4 cm^{-1} for 1000 scans per loop and more than 3-4 loops. Only the last three loops are used and averaged in order to improve signal-to-noise ratio, which is proportional to the square root of the number of total scans.

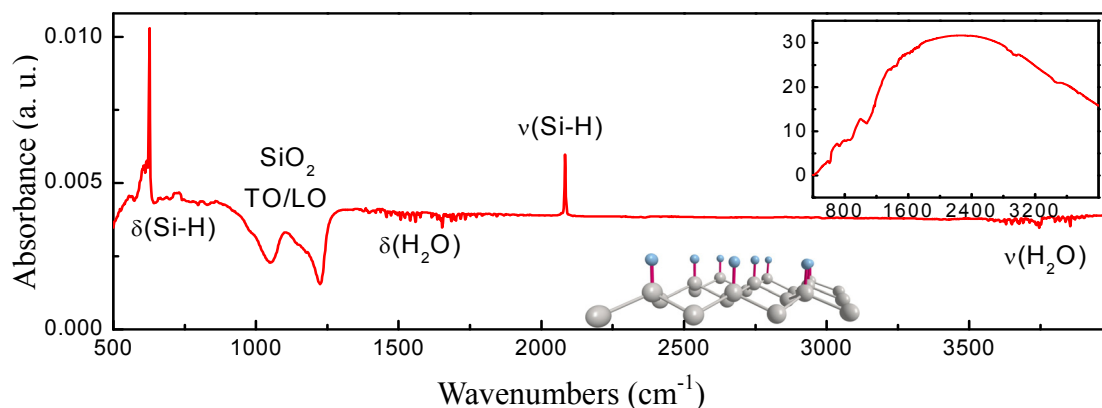


Fig 2.3 The absorption spectrum of H/Si(111) referenced to the SiO_2 at 74° . The inset on the top right shows the single beam of the surface and the inset at the bottom shows the hydrogen terminated Si(111) surface.

Usually two kinds of methods are utilized to present different aspects of the same data. One method is the normal way in which we reference all the data to the same background such as the initial starting surface to show the accumulation of the total

changes relative to the background. The other method is called differential spectra where each spectrum is referenced to the surface after previous treatment. That is, defining B as the background, and C, D, E...as the subsequent treatments on the surface, the normal way is to reference C to B, D to B, E to B ..., while the differential method is to reference C to B, D to C, E to D.... Differential spectra are very useful to show the change of the surface after each treatment.

High sensitivity is achieved by this transmission FTIR geometry. It allows us to measure chemical species on the surface at monolayer level. As an example, the spectrum of H/Si(111) surface is presented in Fig 2.3, which is the absorption spectrum of H/Si(111) referenced to the SiO₂/Si(111) surface at 74°. The small inset on the top right of Fig 2.3 is the single beam of the surface which is used to get the absorption spectrum by Eq. 2.1. The shape of the single beam is the combination of IR source radiation, detector sensitivity, beam splitter and KBR window. H/Si(111) is a simple and nearly perfect flat surface to study the surface chemistry, as shown by the inset at the bottom of Fig 2.3. In Fig 2.3, the sharp peak at 2083 cm⁻¹ is the stretching mode of Si-H and the peak at 627 cm⁻¹ is Si-H bending mode [12, 13]. The two negative bands at 1050 cm⁻¹ and 1225 cm⁻¹ are assigned to SiO₂ TO and LO phonon modes due to the etched SiO₂ [14]. The water from environment outside the ALD chamber along the IR beam path such as in the spectrometer is featured by the stretching band at 3500-4000 cm⁻¹ and the bending band at 1300-1900 cm⁻¹. Since the bending band of the water overlaps with most of C, O and N related modes, water spectrum subtraction is used frequently in the data analysis of this thesis to remove the water effect.

The other most frequently used surface is H/Si(100) surface which has defects and more impurities than H/Si(111) surface. H/Si(100) is less stable in the ALD reactor under

the N₂ purging than the H/Si(111) surface. The thermal stability of these two surfaces will be shown in the Appendix chapter. The study concludes that H/Si(111) surface is stable up to 300°C while H/Si(100) surface is stable up to 250°C due to the environmental -OH group and other oxygen impurities.

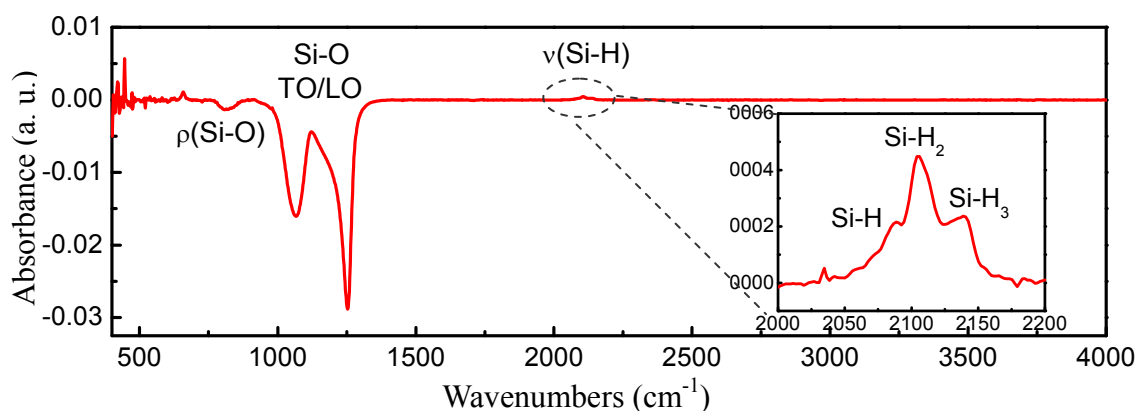


Fig 2.4 The absorption spectrum of H/Si(100) referenced to the SiO₂. The inset shows the detail of the Si-H stretching modes.

The spectrum of H/Si(100) surface which is referenced to oxide at 74° is presented in Fig 2.4 and the inset is the magnified Si-H range. Different from the flat H/Si(111) surface, the Si-H stretch has three modes for H/Si(100), which are due to monohydride (Si-H), dihydride (Si-H₂), and trihydride (Si-H₃), showing a more complicated surface morphology [15]. The etching of SiO₂ is featured by the negative peaks at 1066 cm⁻¹ and 1254 cm⁻¹, the TO/LO phonon modes. The rocking mode of the SiO₂ is observed also around 810 cm⁻¹. Compared with H/Si(111) surface, the SiO₂ TO/LO modes blueshift to higher frequency, due to the thicker SiO₂ layer on the top of silicon [14].

Studies have shown that the SiO₂ TO/LO modes blueshift with SiO₂ thickness increasing, and the shift of LO mode is greater than that of TO mode [14]. What's more, the integrated area of the two bands is correlated with the thickness of the SiO₂ film. In many cases, the integrated area of the TO/LO modes is used to fast estimate the thickness

of the SiO₂. To calibrate it, ellipsometry is used to measure the thickness of SiO₂ film and then the IR integrated area of the corresponding SiO₂ TO/LO modes at 74° (incident angle) is recorded. The ellipsometry is done at the angle of 70°. The results are summarized in table 2.3. Assuming a linear relation, the fitting gives about 0.047 cm⁻¹/Å which will be used as a rough estimation standard for SiO₂ in the following chapters.

Table 2.3 Relation between the thickness of SiO₂ and integrated area of SiO₂ IR TO/LO modes

Integrated area (cm ⁻¹)	0.47	2.79	0.48	0.52
Thickness (Å)	15.8	66.3	16.9	22.0
Substrate type	Si(100)	Si(100)	Si(111)	Si(111)

In addition to the integrated area of SiO₂, the integrated area of Si-H stretching mode is also useful to examine the quality of H/Si after etching. At 74°, the integrated area of Si-H stretching mode for H/Si(111) is 0.010-0.013 cm⁻¹ and for H/Si(100) the area is 0.020-0.024 cm⁻¹. The DTGS detector and MCT-B detect have very similar value in this case.

During all the experiments, after the pretreatment of the surface, the sample is loaded into the ALD reactor immediately and then is heated to 60°C to take the background spectra with a small flow of N₂ purging (~100 sccm). After that, the next treatment is performed such as one precursor dosing or thermal annealing, then the substrate temperature is decreased to 60°C again and spectra are taken at this temperature with N₂ purging. The same process repeats until the whole experiment is done. In addition, after each ALD precursor dosing, excessive amount of N₂ (~500 sccm) is used to purge the chamber for at least 5min.

2.3 Summary

In this chapter, the schematic layout of our home made ALD system is presented. All instruments for the experiments are described, such as the FTIR spectrometer, XPS, RBS, AFM, mass spectrometer, ellipsometer and so on.

The preliminary treatments of the Si surface are discussed including RCA cleaning and acid etching. XPS results show that the Si surface is clean before loaded into chamber. H/Si(111) and H/Si(100) surface are discussed by FTIR as examples to show the basic of IR data analysis.

Bibliography

1. *Introduction to Fourier transform infrared spectrometry*, Thermal Nicolet (2001).
2. R. T. Conley, *Infrared spectroscopy*, Allyn and Bacon, Inc. (1972).
3. J. R. Ferraro and L. J. Basile, *Fourier transform infrared spectroscopy: Applications to chemical systems*, New York: Academic Press (1978).
4. P. R. Griffiths and J. A. D. Haseth, *Fourier transform infrared spectrometry*, Wiley-Interscience (2007).
5. R. G. Messerschmidt and M. A., *Infrared microspectroscopy: Theory and applications*, New York: M. Dekker (1988).
6. B. C. Smith, *Fundamentals of Fourier transform infrared spectroscopy*, CRC Press (1995).
7. G. S. Higashi and Y. J. Chabal, *Silicon surface chemical composition and morphology, chapter in handbook of silicon wafer cleaning technology: Science, technology, and applications* Werner Kern ed, Noyes Pub., (1993).
8. M. K. Weldon, V. E. Marsico, Y. J. Chabal, D. R. Hamann, S. B. Christman and S. S. E. E. Chaban, *Infrared spectroscopy as a probe of fundamental processes in microelectronics: Silicon wafer cleaning and bonding*, , Surface Science **368** (1996), 163.
9. G. S. Higashi, R. S. Becker, Y. J. Chabal and A. J. Becker, *Comparison of Si(111) surface prepared using aqueous solution of NH_4F versus HF* , Appl. Phys. Lett. **58** (1991), 1656.
10. M. A. Hines, *In search of perfection: Understanding the highly defect-selective chemistry of anisotropic etching*, Annu. Rev. Phys. Chem **54** (2003), 29.
11. Y. J. Chabal, *Surface infrared spectroscopy*, Surf. Sci. Reports **8** (1988), 211.
12. V. A. Burrows, Y. J. Chabal, G. S. Higashi, K. Raghavachari and S. B. Christman, *Infrared spectroscopy of Si(111) surfaces after HF treatment: Hydrogen termination and surface morphology*, Appl. Phys. Lett. **53** (1988), 998.

13. G. S. Higashi, Y. J. Chabal, G. W. Trucks and K. Raghavachari, *Ideal hydrogen termination of the Si(111) surface*, Appl. Phys. Lett. **56** (1990), 656.
14. K. T. Queeney, N. Herbots, J. M. Shaw, V. Atluri and Y. J. Chabal, *Infrared spectroscopic analysis of an ordered Si/SiO₂ interface*, Appl. Phys. Lett. **84** (2004), 493.
15. Y. J. Chabal, G. S. Higashi, K. Raghavachari and V. A. Burrows, *Infrared spectroscopy of Si(111) and Si(100) surfaces after HF treatment: Hydrogen termination and surface morphology*, Journal of Vacuum Science & Technology A **7** (1989), 2104.

Chapter 3: Thermal Nitridation of H/Si for ALD

Passivation of semiconductor surface is conveniently realized by terminating surface dangling bonds with a monovalent atom such as hydrogen, often achieved by a simple wet chemical process (HF treatment) [1, 2]. However, the real potential of surface chemical passivation lies in the ability to replace surface hydrogen by multivalent atoms to form surfaces with tailored properties. While some progress has been made to attach organic layers on top of hydrogen-terminated surfaces [3, 4, 5], it has been more challenging to understand and control the incorporation of multivalent atoms, such as oxygen and nitrogen, within the top surface layer of H-terminated surfaces, partly because such processes are dominated by defect sites.

Silicon nitride (Si_3N_4) has been studied for years due to its superior thermal, mechanical and electrical advantages and therefore is utilized in many fields. In microelectronics, it is an excellent diffusion barrier against oxygen, water and sodium ions, which make it a very good material as insulator layer and passivation layer [6, 7]. Recently, since the urgent need of high- κ materials to replace silicon dioxide, it also has been utilized as a barrier to prevent the formation of interfacial silicon oxide between the silicon substrate and high- κ insulator layer, which will significantly decrease the effective dielectric constant [8].

Usually silicon nitride can be obtained by CVD, sputtering or plasma nitridation. However, thermal nitridation by the exposure of silicon to ammonia gas (NH_3) is one of the most promising methods to form the nitride layer because of its high compatibility with ALD, which is the most widely used method to deposit high- κ materials [9, 10]. Since hydrogen-terminated Si (H/Si) is generally used as the starting surface in order to

obtain atomically sharp, oxide free Si and high- κ interface [11], it is also an ideal starting surface for nitridation. Although extensive studies have focused on the dissociation of NH_3 on Si surface in UHV (non-passivated and reconstructed Si surface) or high temperature nitridation (above 600°C), and mostly on Si(100) [12, 13, 14, 15, 16, 17, 18, 19], the detailed studies of the initial reaction of NH_3 with H/Si surface is few, such as the NH_3 dissociation and nitrogen insertion.

In this chapter, we will discuss the thermal NH_3 nitridation of H/Si(111) surface in the home made ALD reactor by utilizing *in situ* FTIR. To study the effect of defect sites, both flat H/Si(111) and vicinal H/Si(111) including monohydride stepped and dihydride stepped surfaces are introduced. Then by varying substrate temperature from 150°C to 600°C at 25°C step in NH_3 , the onset of NH_3 reaction can be established precisely through the unambiguous IR spectra and first principle density functional theory (DFT) calculation.

3.1 Thermal NH_3 nitridation of flat H/Si(111)

The preparation of flat H/Si(111) is performed in the same way as described in Chapter 2, and then the samples are introduced into the ALD chamber immediately. Thermal nitridation is performed by exposing the Si substrate to NH_3 gas [99.999%, with Aeronex hydride gas purifier (oxygen and non-methane hydrocarbons impurity <1 ppb)] from 150°C to 600°C at ~ 7 -9 torr. The nitridation time is 2 min for each temperature. The heating and cooling process are both done in NH_3 ambient. During the *in situ* FTIR measurements, the substrate temperature is kept at 60°C and the incident angle of IR beam is $\sim 74^\circ$ (\sim Brewster angle).

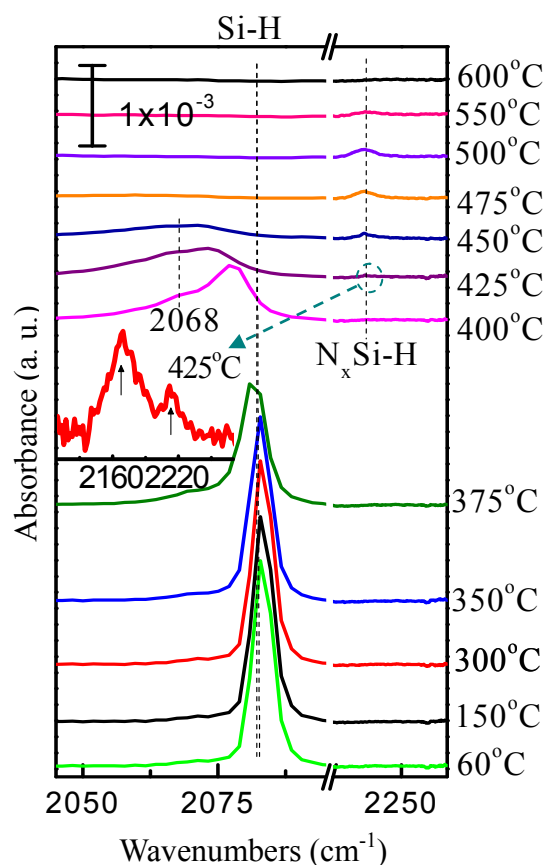


Fig 3.1 Nitridation of flat H/Si (111) (Spectra are referenced to oxide surface.). The inset shows the close view of N_x -Si-H stretching mode at 425°C. The intensity loss of Si-H indicates the onset of the reaction.

Nitridation spectral results of flat H/Si (111) surface at different temperatures are presented in Fig 3.1 and 3.2, where Fig 3.1 shows the absorption spectra referenced to the native oxidized surface and Fig 3.2 shows the spectra referenced to H/Si (111). In Fig 3.1, the very sharp peak at 2083 cm^{-1} assigned to Si-H stretching vibrational mode [$\nu(\text{Si-H})$] indicates the atomically flat, monohydride terminated Si (111) surface formed after HF/ NH_4F etching [20]. Up to 300°C , there is no intensity loss of $\nu(\text{Si-H})$ at 2083 cm^{-1} and no observable feature in the lower frequency range (Fig 3.2), meaning the surface is stable at this temperature. Starting from 350°C , $\nu(\text{Si-H})$ intensity decreases accompanied by the frequency redshift due to Si-H decoupling, and a peak at 1535 cm^{-1} appears which

is assigned the bending mode [scissor mode, $\delta(\text{NH}_2)$] of $-\text{NH}_2$ species on silicon [15, 17, 21]. These two features indicate initial desorption of Si-H and dissociation of NH_3 on the surface. It can be concluded that NH_3 reacting with the H/Si (111) surface is initiated by replacing the surface hydrogen with Si-NH₂, which is in agreement with other experimental and theoretical studies on Si surface in UHV [13, 15, 18, 22].

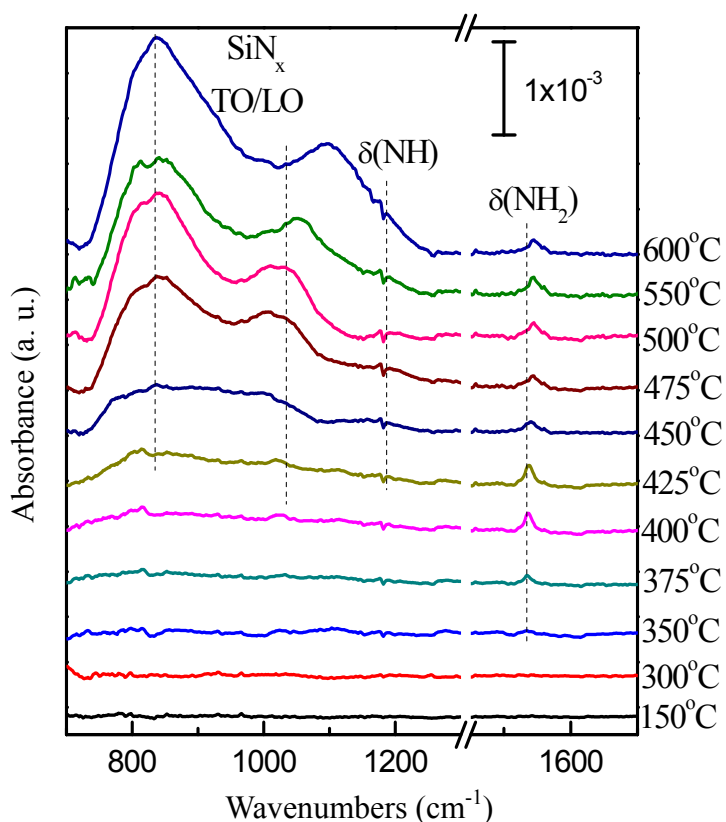
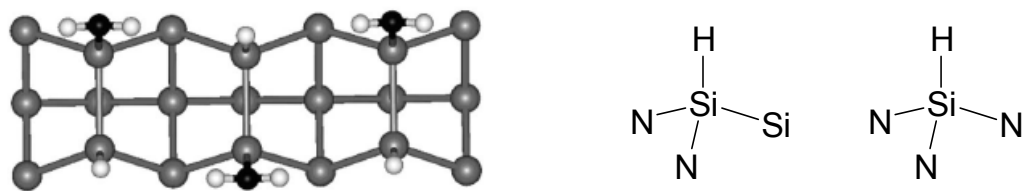


Fig. 3.2 Nitridation of flat H/Si (111) (Spectra are referenced to H/Si (111) surface.). SiN_x, NH and Si-NH₂ species are observed as the feature of nitridation.

At 400°C, the integrated area of $\nu(\text{Si-H})$ decreases by $\sim 18\%$ and the frequency redshifts to 2077 cm^{-1} . This redshift is caused by the decoupling of H/Si (111) stretching mode due to the hydrogen dissolving and formation of surface Si-NH₂ [23]. Meanwhile, in Fig 3.1 for the band of H-Si stretching mode, a shoulder around 2068 cm^{-1} is observed upon 375 °C, which increases at 400°C, decreases and then merges into the other after

425°C. This shoulder has a different origin than the redshift due to decoupling. It may result from the effect of opposed NH_2+H for the $\text{H}_2\text{N-Si-Si-H}$ units which redshifts the $\nu(\text{Si-H})$ as shown in Fig 3.3(a). The $\text{H}_2\text{N-Si}$ structure induces an analogous polarization which weakens the adjacent Si-H bond and this weakening effect is enhanced by the cooperative interaction of two opposed NH_2 groups causing the red shift of Si-H band [15, 18].

Above 400°C, the insertion of N into Si-Si back bonds [$\text{N}_x\text{-Si-H}$ as indicated in Fig 3.3(b)] results in the blueshift of $\nu(\text{Si-H})$ shown as a broad peak around 2167 cm^{-1} in Fig 3.1, implying the formation of nitride. The inset of Fig 3.1 exhibits the detail of $\text{N}_x\text{-Si-H}$ stretching modes. At 425°C, the two peaks observed at 2169 cm^{-1} and 2212 cm^{-1} are corresponded to different number of N atoms inserted to the Si-Si back bonds, $\text{N}_2\text{-Si-H}$ and $\text{N}_3\text{-Si-H}$ respectively [as Fig 3.3(b)] [24, 25]. On the other hand, in Fig 3.2, the very broad band due to Si-N-Si bond at $700\text{-}1100\text{ cm}^{-1}$ is observed and starts from 425°C [26, 27].



(a) (N-black, H-white, Si-gray)

(b) 2 N atoms and 3 N atoms insertion

Fig 3.3 (a) Opposed NH_2+H_2 on Si (100) [18] and (b) nitrogen insertion into Si-Si to form $\text{N}_x\text{-Si-H}$, which can explain the shifted Si-H stretching modes.

Note that as in Fig 3.2, N-H bending mode [$\delta(\text{N-H})$] is observed as well around 1180 cm^{-1} as a small bump [29, 30, 31]. It has been reported that the frequency of Si-N-Si is related to the N-H concentration [30], where the higher N-H concentration, the higher Si-N-Si frequency, with the lower limit at 835 cm^{-1} which is corresponded to

stoichiometry Si_3N_4 structure. If the frequency redshifts, it indicates that the N/Si ratio is lower. In our case, the Si-N-Si TO mode is around 838 cm^{-1} for 600°C which is pretty close to that of the Si_3N_4 structure.

According to above results, thermal NH_3 nitridation is initiated by the dissociation of NH_3 which replaces the surface Si-H by Si- NH_2 at $\sim 350^\circ\text{C}$. Upon 400°C , nitrogen insertion is observed. With these understanding, then we go on to the nitridation of vicinal H/Si(111) surfaces.

3.2 Thermal NH_3 nitridation of vicinal H/Si(111)

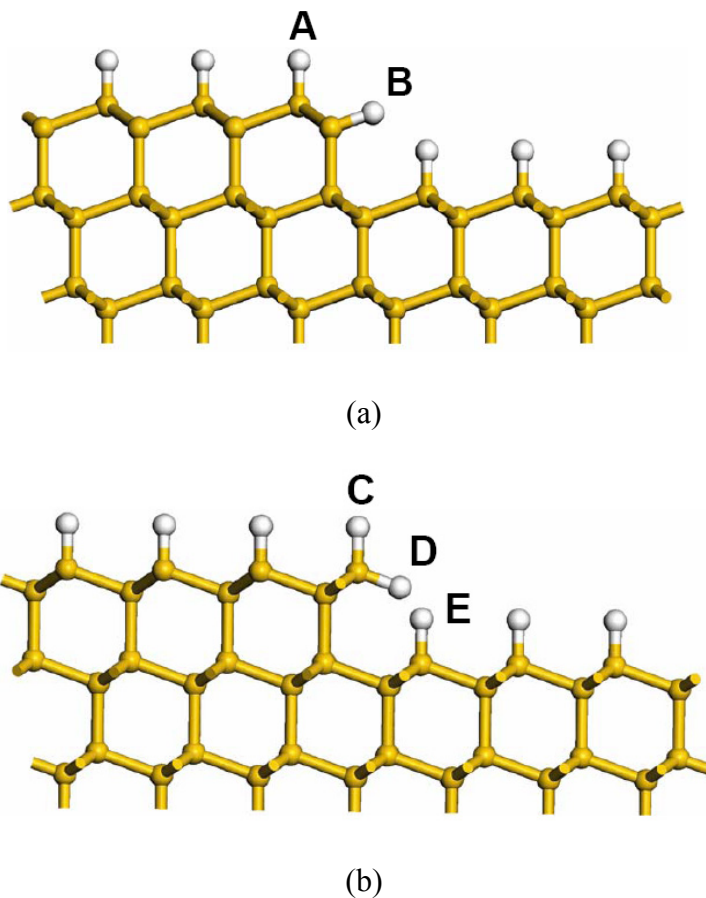


Fig 3.4 The schematic of (a) monohydride and (b) dihydride stepped H/Si (111) surfaces (Si-yellow and H-white). A and B, D and E are coupled surface hydrogen atoms.

Two types of stepped Si (111) wafers with 9° miscut ($[\bar{1}\bar{1}2]$ and $[11\bar{2}]$) are utilized in the nitridation experiments. The stepped hydrogen-terminated Si(111) surfaces are achieved by 30 seconds HF (~20%) etching at room temperature and an additional 3-4 min NH_4F (~49%) etching at $2-4^\circ\text{C}$ [32]. After the samples are immediately introduced into the ALD chamber, the thermal nitridation is performed by exposing the Si substrate to NH_3 gas and *in situ* FTIR measurement is carried out at 60°C with the incident angle of $\sim 70^\circ$ as well, which are the same as flat H/Si(111) surface. Fig 3.4 presents the structural configuration of the monohydride and dihydride Si(111) surfaces. The one along $[11\bar{2}]$ direction gives the step Si atoms with one hydrogen bond (monohydride, B), and the other along $[\bar{1}\bar{1}2]$ direction gives two hydrogen bonds (dihydride, C and D) for the step Si atoms. Note that for the monohydride surface, the stepped Si-H (B) projects to between the two Si atoms of the lower terrace and for the dihydride surface the stepped Si-H (D) projects to the Si-H (E) of the lower terrace.

The nitridation of monohydride surface is show in Fig 3.5(a) and (b), which are reference to oxide and H/Si respectively. Different from the flat H/Si surface, the spectra of monohydride surface show three peaks which are located at 2071 cm^{-1} , 2081 cm^{-1} and 2087 cm^{-1} [Fig 3.5(a)]. The mode at 2081 cm^{-1} (C_1) is assigned to Si-H terrace stretching mode, and the other two modes at 2071 cm^{-1} (C_2) and 2087 cm^{-1} (C_3) are associated with the asymmetric and the symmetric stretching modes resulting from coupled motion of stepped Si-H and the terrace Si-H next to it [33, 34], as the hydrogen atoms denoted by A (H_A) and B (H_B) in Fig 3.4(a).

At 350°C , the total integrated area of Si-H stretching modes slightly decreases accompanied with the observed $\delta(\text{NH}_2)$ at 1535 cm^{-1} , indicating the starting of NH_3 dissociation. Upon 375°C , the Si-H intensity keeps decreasing but due to the overlapping

of the terrace and stepped modes, the evolution of each mode cannot be easily distinguished. To separate those modes, Lorentian curve fitting is carried out for the results from 300°C to 425°C. The fitted integrated area and peak position for each mode are shown in Fig 3.6(a), (b) and (c). It can be seen that the integrated area of Si-H terrace mode is reduced at 350°C and the stepped modes start to vary around 350°C, implying the surface is attacked by NH_3 upon 350°C.

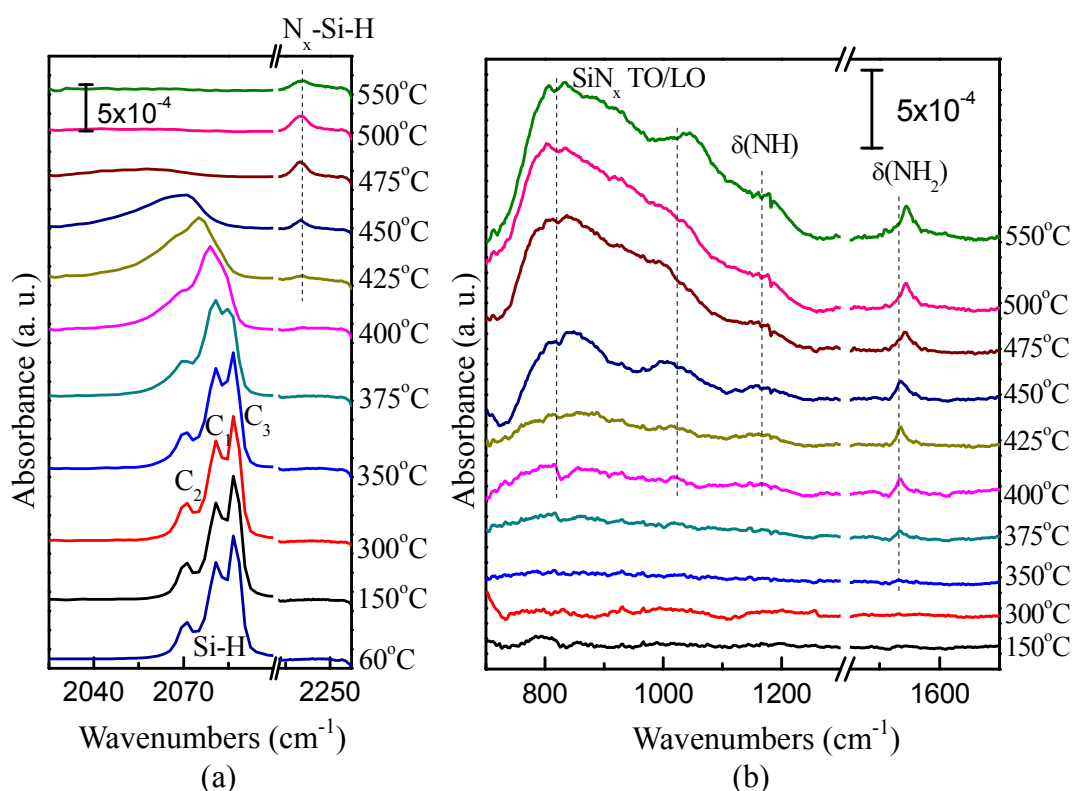


Fig 3.5 Nitridation of monohydride stepped H/Si(111) (a) referenced to oxide surface. C₁, C₂, and C₃ are Si-H terrace, monohydride asymmetric, and monohydride symmetric stretching modes, respectively; (b) referenced to H/Si(111) surface. The intensity loss of Si-H indicates the onset of the reaction.

However, it cannot be distinguished that the terrace Si-H is attacked first or the stepped Si-H reacts first due to their structure similarity. Note that the intensity of terrace Si-H increases slightly at 375°C and then decreases after 400°C. This slightly increase

could result from the contribution of the decoupled terrace Si-H (H_A) due to the loss of stepped Si-H (H_B).

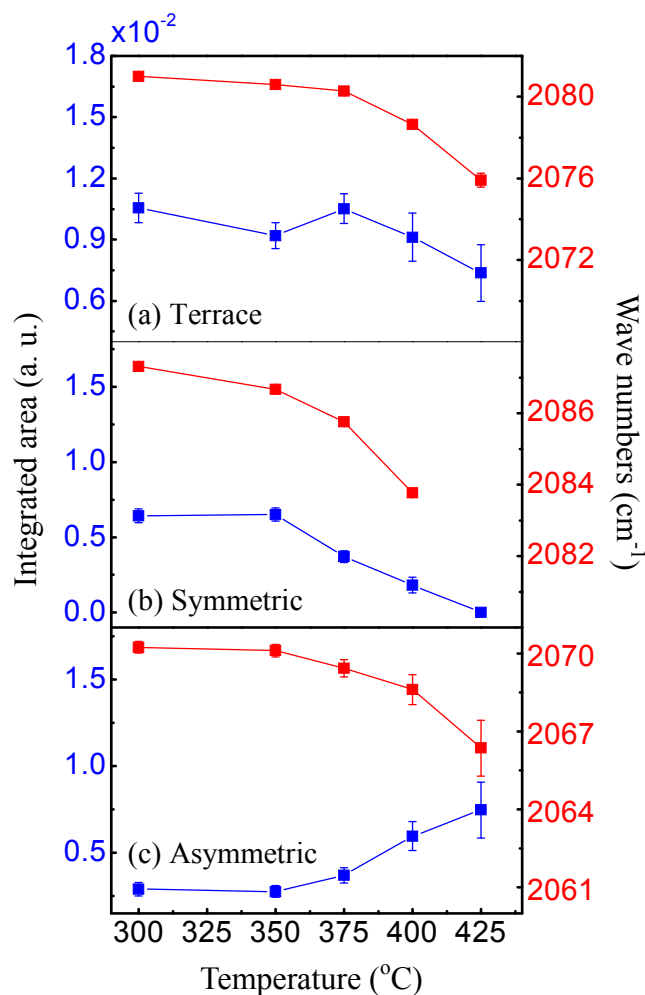


Fig 3.6 The fitting results of the Si-H stretching modes of monohydride H/Si(111): (a) terrace Si-H mode; (b) symmetric stepped Si-H mode; (c) asymmetric stepped Si-H mode. The blue lines are corresponded to the integrated area and red lines are corresponded to the frequency.

It is quite interesting to notice that the intensity of symmetric stepped Si-H mode decreases as the temperature increases until 425°C, while the asymmetric stepped Si-H mode is increasing at the same time. Since the symmetric mode and asymmetric mode must decrease or increase in the same way, it can be inferred that a new mode occurs in

the same frequency range which overlaps with the asymmetric mode. Again, this new mode may be caused by opposed NH_2+H for the $\text{H}_2\text{N-Si-Si-H}$ units which redshifts the terrace stretching mode, as we discussed previously for the nitridation of flat surface in Fig 3.3(a).

Similar to that of the flat surface, upon 350°C , the observed $\delta(\text{NH}_2)$ at 1535 cm^{-1} blueshifts to 1544 cm^{-1} at 550°C as the growing of SiN_x layer. The stretching mode of $\text{N}_x\text{-Si-H}$ appears around 2167 cm^{-1} at 400°C [25], accompanied by the Si-N-Si phonon mode at $700\text{-}1100\text{ cm}^{-1}$ and $\delta(\text{N-H})$ at 1180 cm^{-1} , implying the insertion of N into the Si-Si network. At 550°C , the $\text{N}_x\text{-Si-H}$ survives and its intensity is about twice of that on the flat H/Si(111) surface at the same temperature. The broad TO/LO modes of Si-N-Si centered at 832 cm^{-1} and 1045 cm^{-1} are not as sharp as the flat Si(111) surface, indicating that the nitride on monohydride surface may be rougher and contain more Si than the flat surface.

Therefore, the nitridation process of monohydride stepped H/Si(111) shows no difference compared to the flat surface in spite of the presence of steps. For both cases, the NH_3 dissociation and interaction with Si-H ending with Si- NH_2 start from $\sim 350^\circ\text{C}$, and the nitrogen insertion to Si-Si network is observed at $\sim 400^\circ\text{C}$.

As for the dihydride surface, the nitridation results are presented in Fig 3.7(a) and (b), which are reference to oxide and H/Si respectively. As in Fig 3.7(a), the stretching modes of Si-H are featured by three well separated bands at 2083 cm^{-1} (C_4), 2100 cm^{-1} (C_5) and 2135 cm^{-1} (C_6). The mode at 2083 cm^{-1} is associated to the terrace Si-H bonds, and the modes at 2100 cm^{-1} and 2135 cm^{-1} are associated to the asymmetric and the symmetric stretching modes which result from the coupled motion of the stepped Si-H (H_D) and the terrace Si-H (H_E) next to it [Fig 3.4(b)] due to the strong steric interaction

between them [33, 34, 35].

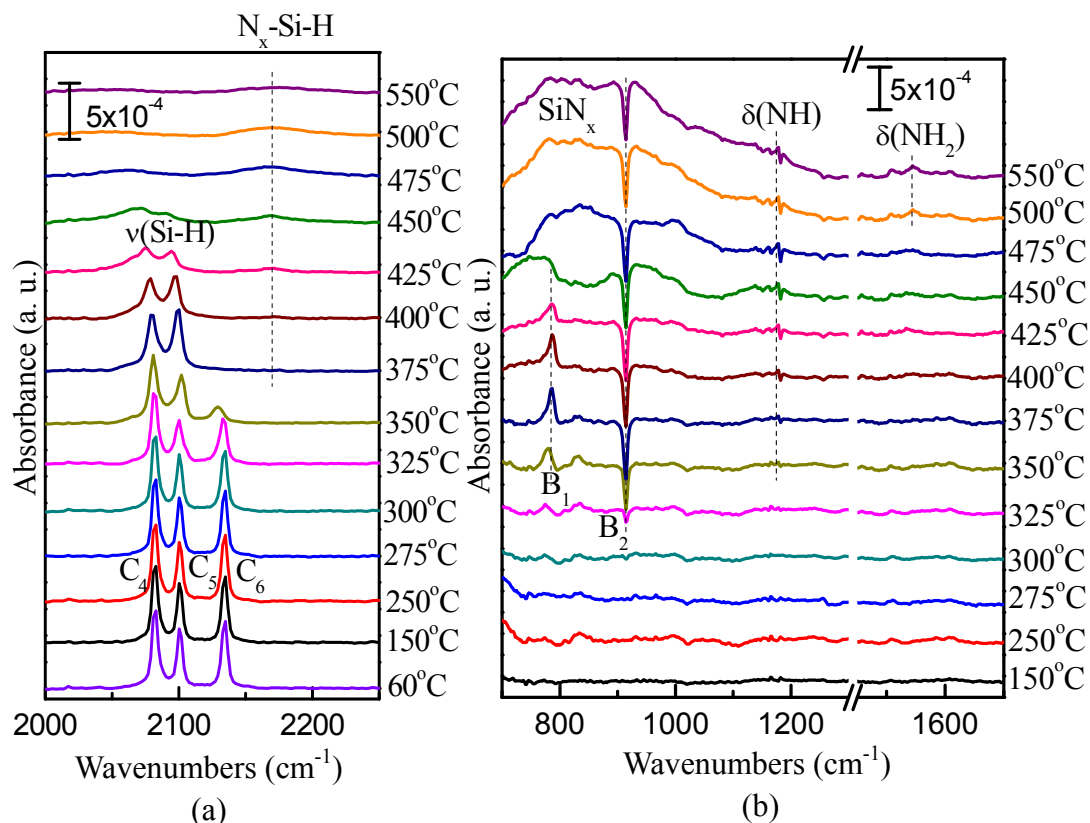


Fig 3.7 Nitridation of dihydride stepped H/Si(111) (a) referenced to oxide surface. C_4 , C_5 , and C_6 are Si-H terrace, dihydride asymmetric, and dihydride symmetric stretching modes, respectively; (b) referenced to H/Si (111) surface. The intensity loss of Si-H indicates the onset of the reaction.

The loss of the Si-H starts at 325°C evidenced by the intensity loss of Si-H stretching modes, which is 25°C lower than that of the flat surface and the mono-hydride surface. At the same temperature, a negative peak is observed at 914 cm^{-1} and assigned to the scissoring deformation mode of dihydride, indicating the loss of Si-H begins with the most reactive stepped dihydride (H_C or H_D). Upon 375°C, only two Si-H stretching modes are left. The symmetric dihydride stretching mode is quenched and the peak at the same position of the asymmetric mode remains, though the asymmetric and symmetric mode must be reduced simultaneously. On the other hand, the strong negative band of

dihydride scissoring deformation mode at 914 cm^{-1} shows that all the surface dihydride is consumed at 375°C . In addition, a peak at 775 cm^{-1} starts to appear at 325°C . All these strongly suggest that a new Si-H mode should be forming during the initial nitridation, with its stretching mode around the same frequency range as the asymmetric dihydride stretching mode and accompanied by a bending mode around 775 cm^{-1} . It should also be noted that no $\delta(\text{NH}_2)$ at 1535 cm^{-1} is observed until 400°C .

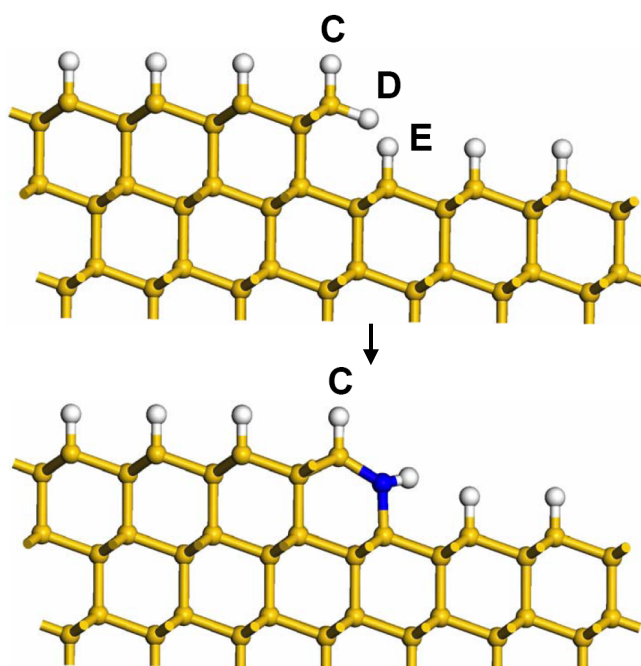


Fig 3.8 The schematic of H-Si-NH-Si bridging structure due to NH_3 interaction with dihydride (N-blue, H-white, and Si-yellow). D and E are reacting with NH_3 , which cause the appearance of new Si-H modes in the spectra: $\sim 2100\text{ cm}^{-1}$ and 775 cm^{-1} .

All above strongly indicates that dihydride surface should be via a different initial nitridation mechanism than the flat surface and monohydride surface. We conclude that NH_3 attacks the H_D and H_E first by forming a H-Si-NH-Si bridging structure due to the strong steric interaction between these two Si-H bonds, as shown by Fig 3.8. The left stepped Si-H (H_C) in this bridging structure results in the new stretching mode around

2100 cm^{-1} and the bending mode around 775 cm^{-1} . The intensity of its bending mode (at 775 cm^{-1}) increases when raising the nitridation temperature, reaching maximum at 375°C due to more reacted H_D and H_E , and then it decreases when the temperature is above 375°C.

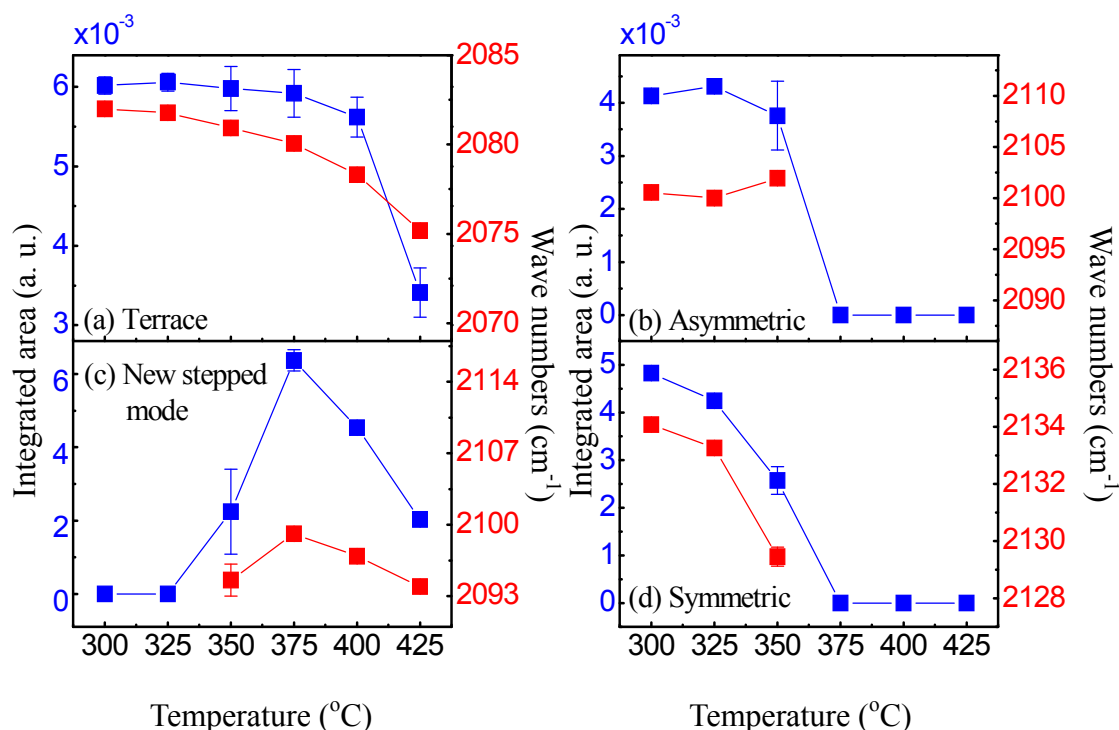


Fig 3.9 The fitting results of the Si-H stretching modes of dihydride H/Si(111): (a) terrace Si-H mode; (b) symmetric stepped Si-H mode; (c) asymmetric stepped Si-H mode. The blue lines are corresponded to the integrated area and red lines are corresponded to the frequency. All the Si-H modes are now separated.

Again we fit the Si-H stretching modes by Lorentian curve fitting to separate different Si-H modes. Fig 3.9(a)-(d) present those fitting results. Clearly observed from the fitting results, the intensity of the new stretching mode due to the H-Si-NH-Si bridging structure achieves the highest value at 375°C and then decreases, which is consistent with the variation of its bending mode. Upon 400 °C and as shown in Fig 3.7(b), NH_3 begins to dramatically interact with terrace Si-H and N is inserted into the

Si-Si network, leading to the rise of $\delta(\text{NH}_2)$ around 1540 cm^{-1} and stretching mode of $\text{N}_x\text{-Si-H}$ around 2167 cm^{-1} in the spectra, along with the growing of Si-N-Si phonon mode at $700\text{-}1100\text{ cm}^{-1}$ and $\delta(\text{N-H})$ at 1180 cm^{-1} . There is no individual TO/LO modes of Si-N-Si as shown for the flat surface, possibly suggesting a rough nitride surface.

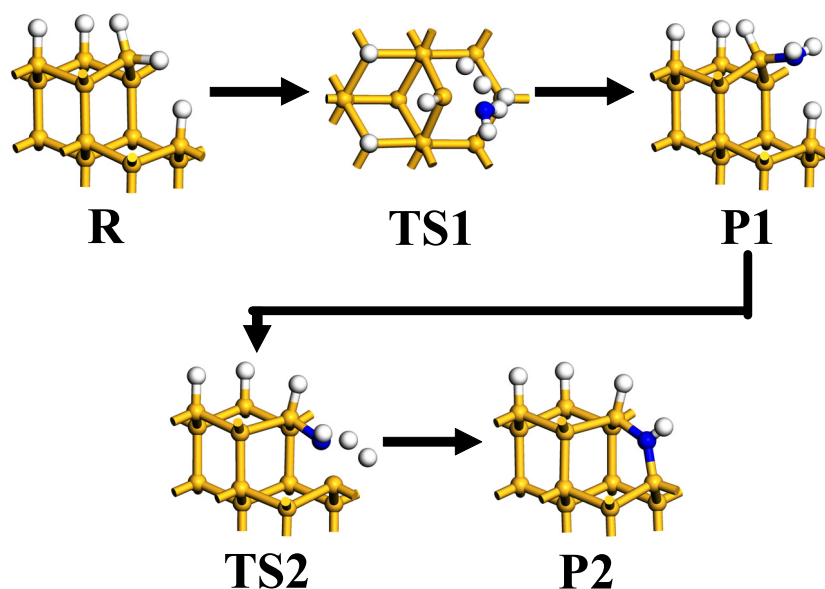


Fig 3.10 Reaction scheme for NH_3 reacting at the dihydride H/Si(111) step edge. Reaction site structures are fully optimized at the PBE/DNP level of theory. The -NH incorporated bridging structure forms as the final state.

To support our conclusion of the nitridation mechanism, fully periodic density functional theory calculations (done by Dr. Mathew Halls) are carried out for dihydride surface using the gradient-corrected PBE functional [36] as implemented in the DMol3 package [37]. A numerical atomic basis set of double- ζ quality, augmented with additional polarization functions (DNP) was employed in this work. The convergence criteria for structural optimizations were 1.0×10^{-5} au and 2.0×10^{-3} au/Å for energy and gradient, respectively. Subsequent vibrational calculations verified the nature of the optimized structures. The stepped surface model was based on a 2×5 supercell/6 layer slab of the hydrogen terminated (111)-Si surface with a 25 Å vacuum slab. A

Monkhorst-Pack k-point mesh with a spacing of 0.04 \AA^{-1} was used to sample the Brillouin zone.

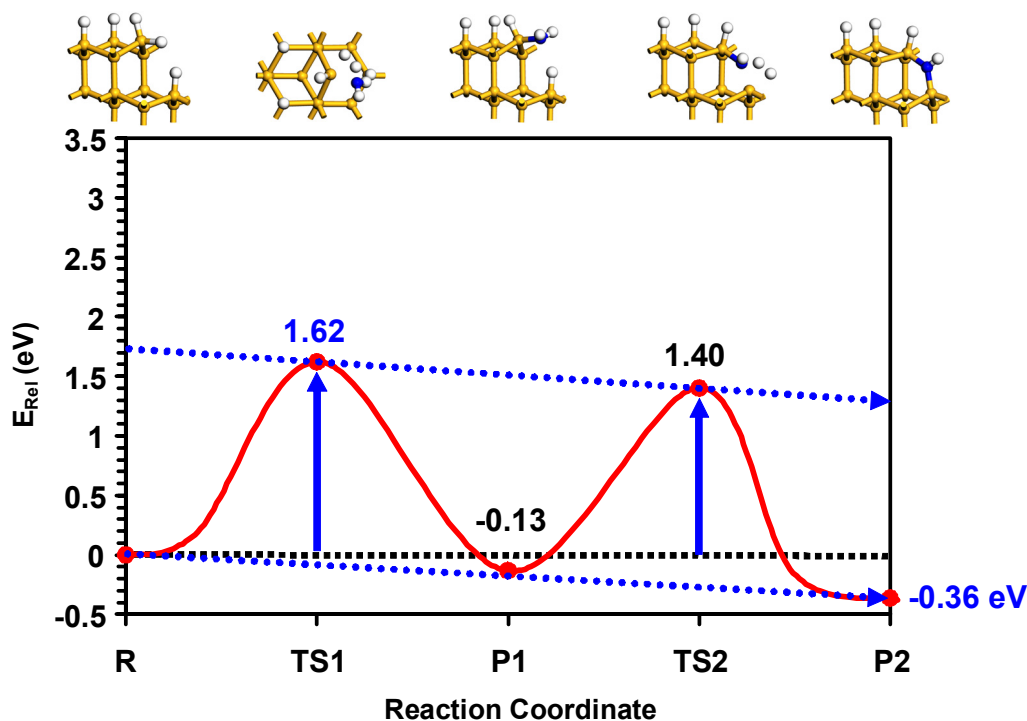


Fig 3.11 PBE/DNP calculated reaction energy profile for the reaction of NH_3 at the dihydride-H/Si(111) surface leading to the NH incorporated step-edge structure.

Thus, the atomistic details of the structure, reaction mechanism and the energetics for the initial reaction of NH_3 at the dihydride H/Si(111) step edge are analyzed theoretically. In addition to providing vital information related to the kinetic and thermodynamic feasibility of the proposed NH-incorporated structure, characteristic vibrational modes are also determined for the final product, allowing comparison to our experimental observations and assisting in the interpretation of unexpected infrared modes. The activation energies and overall reaction enthalpies are calculated for the interaction of NH_3 with the dihydride H/Si surface for the process outlined in Fig 3.10. The overall process for the incorporation of H-Si-NH-Si bridging at the dihydride step

edge involves two reaction steps: 1) the initial reaction of NH_3 at the lower step edge (H_D) Si-H (R) forming a step-edge $-\text{NH}_2$ species (P1), and 2) the subsequent reaction of the step-edge $-\text{NH}_2$ (P1) with the adjacent lower terrace Si-H (H_E), producing the final NH incorporated step-edge product (P2). The critical point structures for this process are labelled and shown in Fig 3.10 and Fig 3.11 (top). Reactant, product and linking transition state structures were fully optimized and verified by subsequent frequency analyses.

The reaction energy profile for the step-edge nitridation is shown in Fig 3.11 (energies denoted by ●). As presented there, as NH_3 interacts with the step-edge Si-H reaction site, the system proceeds through a transition state (TS1) having an energy 1.62 eV higher than the initial separated reactants (R). Structurally, the transition state has elongated Si-H, N-H and Si-N, H-H distances relative to their initial and final values, respectively, consistent with transitional nature of these bonds. From the TS1 state the system evolves forming the step-edge- NH_2 (P1) species, with the loss of H_2 . The formation of the P1 intermediate product is calculated to be exothermic by 0.13 eV. From the $-\text{NH}_2$ P1 structure the system can react further to produce the final NH incorporated step-edge product (P2). As shown in Fig 3.11, the second step-edge reaction step has a classical barrier height of 1.40 eV. The second transition structure has bond lengths consistent with the reaction path linking the P1 and P2 structures. The formation of the final NH bridging structure with loss of H_2 is predicted to be exothermic by 0.36 eV.

The density functional theory results presented here indicate that the initial reaction of NH_3 at the stepped edge of dihydride surface to form the unique NH incorporated step-edge structure is thermodynamically favourable overall. The energies of both the intermediate product (P1) and the final step-edge product (P2) are lower than the starting

reactants, with the final P2 product being most stable. The initial reaction step is found to dominate the kinetics of the process, with the activation energy for the second reaction step being smaller (TS2) than that for the initial reaction (TS1). These results reveal that nitridation of the stepped dihydride surface is energetically favourable and the initial NH_3 step-edge nucleation readily leads to formation of the final products.

Table 3.1 Calculated PBE/DNP wavenumbers and mode assignments corresponding to the observed infrared (IR) bands

Calculated ^a (cm^{-1})	Observed IR (cm^{-1})	Assignment
894	914	Si-H ₂ scissoring deformation
2134	2100	Bridged H-Si-(NH-Si) stretching
772	775	Bridged H-Si-(NH-Si) bending
1165	N/A	N-H bending
856	N/A	Si-N stretching

^a PBE/DNP calculated harmonic frequencies.

Following the analysis of the mechanism and energetics for the proposed initial step-edge nitridation reaction, the theoretically predicted properties of the final P2 structure perfectly match our experimental observations. Both the $\sim 2100 \text{ cm}^{-1}$ and 775 cm^{-1} vibrations are associated with the remaining step-edge Si-H (H_C) after bridging NH incorporation to form the H-Si-NH-Si structure. The remaining Si-H (H_C) stretching mode and its bending mode for the step-edge H-Si-NH-Si structure are in excellent agreement with the observed infrared bands as shown in table 3.1 (calcd (ν/δ): 2134/772 cm^{-1} ; expt (ν/δ): 2100/775 cm^{-1}).

3.3 HfO₂ deposition on nitrided Si(111) surface

Thermal NH_3 nitridation of silicon has shown advantage as an oxygen barrier in ALD of Al_2O_3 [8]. Based on the nitride achieved in the previous discussion, HfO_2 is deposited on it to demonstrate its application for ALD. Known as a high- κ metal oxide

(dielectric constant ~ 25), HfO_2 is the most promising and well studied candidate to replace SiO_2 [38], and has been utilized by Intel for modern chips due to its great performance on silicon substrate [39].

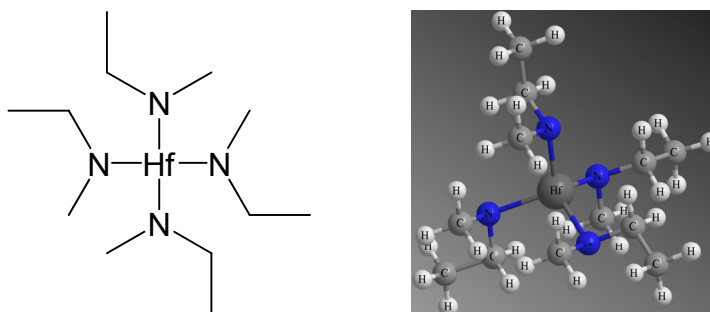


Fig 3.12 The chemical structure of TEMAH for deposition of HfO_2 . The ball-stick 3D view is on the left side.

In our study, HfO_2 is deposited by using Tetrakis (ethylmethylamino) hafnium (TEMAH, $\text{Hf}[\text{N}(\text{CH}_3\text{CH}_2\text{CH}_3)]_4$) [40] and D_2O . TEMAH is one of most popular precursors used in ALD of HfO_2 [41, 42]. The chemical structure is presented in Fig 3.12 along with its ball-stick schematic drawing in 3D view. The Hf-N is the most reactive bond and can be easily hydrolyzed by water to form metal oxide. Here, heavy water D_2O is used to facilitate our IR data analysis since its spectral range is well separated from that of water from environment. Thus spectral variation caused by environmental water fluctuation in the IR spectrometer can be easily distinguished.

Ideally, the reaction mechanism of TEMAH and D_2O is straightforward. As described in Fig 3.13, after the 1st TEMAH dosing on the starting surface, Hf atom is chemically bonded to the surface with unreacted ligands. Due to precursor self-terminating reaction and steric hindrance, the surface will be saturated by one layer of adsorbed TEMAH. Then the subsequent pulse of D_2O will react with the remaining ligand and replace it with -OD specie. When the surface is exposed to TEMAH again, the

precursor will be attached to the surface via Hf-O-Hf bond with unreacted ligands. The same process repeats for the following cycles so that HfO₂ is deposited layer by layer.

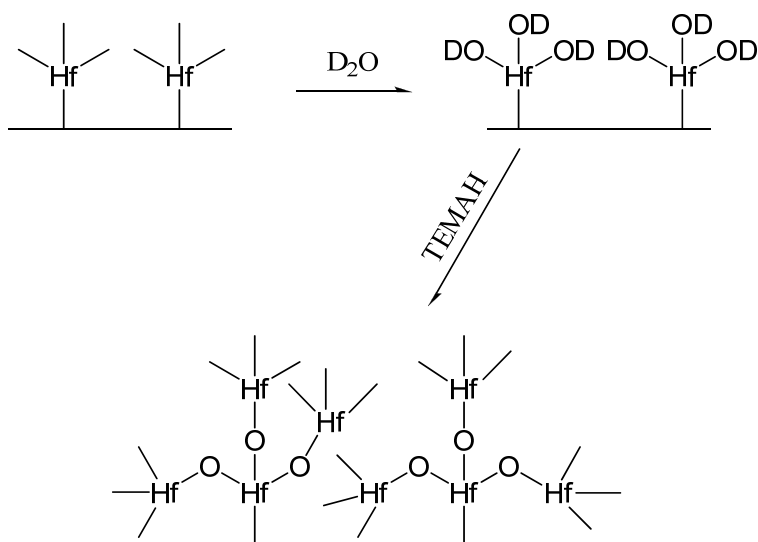


Fig 3.13 ALD reaction scheme of TEMAH and D₂O. The ligand of the Hf precursor is replaced by -OD and -OD can further react with the Hf precursor.

However, the practical scheme is not so simple. Due to the residue water in the reactor, TEMAH could be partially hydrolyzed and the partially hydrolyzed precursor incorporates the surface interaction. For example, on H/Si surface, the partially hydrolyzed precursor competes with the intact precursor to react with the surface Si-H by forming Hf-O-Si featured by a band centered at 1000 cm⁻¹ [23]. Furthermore, the water cannot fully remove the ligands and therefore organic impurities (N, C, O) will exist in the film due to insufficient water reaction. In many cases, trapped water/OH inside the film is observed as well.

After the 500°C thermal NH₃ nitridation of monohydride stepped H/Si(111), 20 cycles of HfO₂ are deposited on it. During the deposition, TEMAH is kept ~75°C to raise its volatility but without thermal decomposition. D₂O is kept at room temperature due to

its high vapor pressure. The deposition is performed at 100°C by alternative exposure of TEMAH and D₂O dosing. For each precursor dosing, saturation pulse length is used. Before each subsequent precursor exposure, the reactor is purged by excessive amount of N₂ for at least 5 min to remove the residue precursor and reaction byproducts. *In situ* IR measurements are carried out at 60°C (substrate temperature) with IR incident angle ~70°.

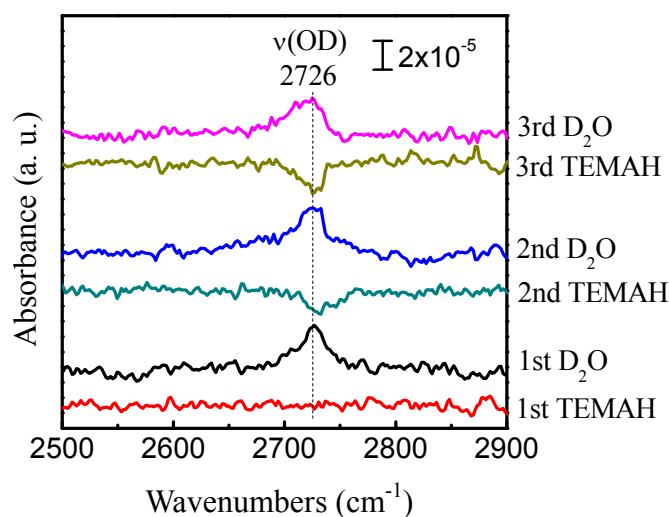


Fig 3.14 Differential spectra of first 3 cycles TEMAH/D₂O on nitride surface which shows the OD exchange with TEMAH. Each spectrum is referenced to the previous one and the 1st TEMAH is reference to the nitride surface.

Fig 3.14 shows the differential spectra of the first 3 cycles TEMAH/D₂O which present the change of surface after each precursor dosing. As expected, after each D₂O exposure, -OD stretching mode is observed at 2726 cm⁻¹ and quenched by the subsequent TEMAH dosing, clearly demonstrating the ALD ligand exchange feature as shown by the ideal ALD scheme in Fig 3.13. Note that the -OD specie is not completely consumed by the next TEMAH pulse, indicating the -OD accumulation inside the film.

Then we reference all the spectra of 20 cycles HfO₂ to the 500°C thermal NH₃ nitride. The spectral results are shown in Fig 3.15. Upon the 1st TEMAH dosing, a broad

band centered around 1072 cm^{-1} appears. According to our previous study of TEMAH on H/Si surface, a similar broad band appears at $\sim 1000\text{ cm}^{-1}$ and is assigned to Hf-O-Si due to partially hydrolyzed TEMAH precursor (Hf-OH) [23]. Therefore, the broad band at $\sim 1072\text{ cm}^{-1}$ is assigned to the Hf-O-SiN_x band. It slowly increases for the subsequent cycles and saturates after 5-10 cycles, confirming that it is an interfacial mode. Direct adsorption of intact TEMAH on the surface via Hf-Si or Hf-N bond cannot be observed because their frequency and intensity is out of our detectable range, but their existence cannot be excluded.

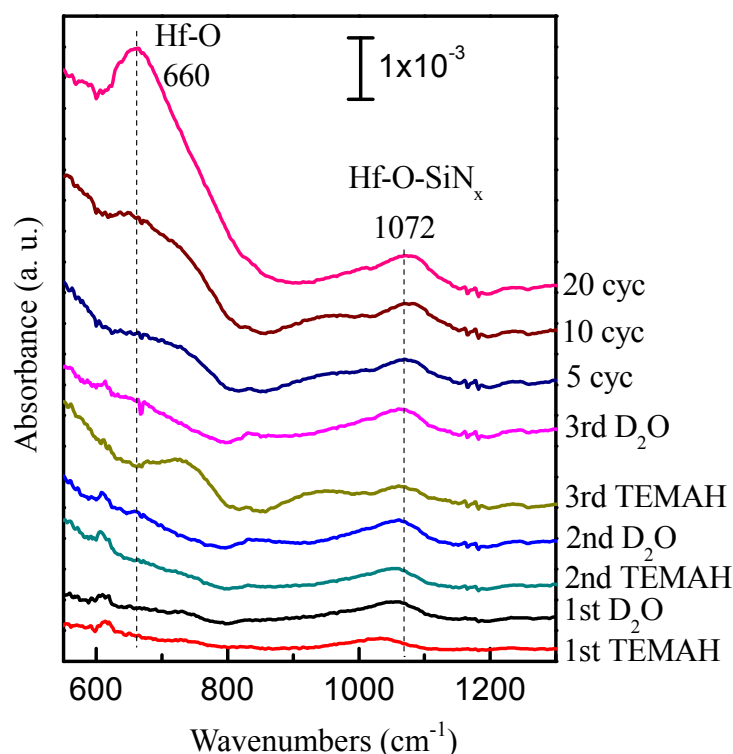


Fig 3.15 Absorption spectra up to 20 cycles TEMAH/D₂O on nitride surface showing the formation of HfO₂ and surface Hf-O-SiN_x. All spectra are referenced to the nitride surface.

As for more ALD cycles, the observation of a broad band around 660 cm^{-1} is attributed to HfO₂ phonon mode, implying the continuous HfO₂ layer on nitride. No

TO/LO SiO_2 modes [43] are evidenced, implying that the interfacial SiO_2 is minimized benefiting from the protection of nitride. Since no substantial amount of SiO_2 is detected as well for the HfO_2 deposited on H/Si(111) at 100°C , the advantage of SiN_x is not as obvious as the Al_2O_3 case. However, our further discussion of ozone based ALD of HfO_2 on nitride will clearly show the advantage of using nitride to minimize the interfacial SiO_2 in the next chapter.

3.4 Summary

In this chapter, we studied the mechanism of thermal nitridation of H/Si(111) by NH_3 for ALD application, with the aid of *in situ* FTIR and first principle DFT calculation. Besides flat H/Si(111) surface, vicinal Si(111) surfaces including monohydride and dihydride stepped H/Si(111) surfaces are used to study the effect of defects during the nitridation process. By varying the temperature from 150°C to 600°C at a small temperature step of 25°C , the surface interaction with NH_3 is investigated to conclude the whole picture of NH_3 nitridation.

Flat H/Si(111) surface and monohydride stepped H/Si(111) surface show the same nitridation behavior due to their structural similarity. Upon 350°C , NH_3 dissociates and replaces the surface Si-H by Si-NH_2 species, which is featured by the observation of scissoring deformation mode of $-\text{NH}_2$ and loss of Si-H stretching modes. The nitrogen atoms start to be inserted into Si-Si network to form SiN_x layer around 400°C featured by the $\text{N}_x\text{-Si-H}$ mode and SiN_x TO/LO modes.

Dihydride stepped H/Si(111) shows a very different nitridation mechanism than the flat and monohydride cases. Desorption of Si-H begins at 325°C without the observation of $-\text{NH}_2$ scissoring deformation mode. The new mode observed at 775 cm^{-1} indicates that

the thermal nitridation is initiated by forming an H-Si-NH-Si bridging structure at the step edge and is therefore attributed to Si-H bending mode of the H-Si-NH-Si structure due to the -NH- bridging process. This process achieves maximum at 375°C. DFT calculation perfectly confirms our vibrational mode assignments and assumed nitridation model. Upon 400°C, nitrogen insertion into Si-Si back bond is evidenced by N_x -Si-H mode and SiN_x phonon modes.

With above understandings, HfO_2 is deposited on this nitride by TEMAH/ D_2O . The precursor structure, properties and ideal reaction mechanism are discussed. Differential spectra of each precursor dosing captured the ALD ligand exchange by showing the periodic variation of -OD stretching mode and the HfO_2 nucleation is confirmed by its phonon mode around 660 cm^{-1} .

Bibliography

1. G. W. Trucks, K. Raghavachari, G. S. Higashi and Y. J. Chabal, *Mechanism of HF etching of silicon surface: A theoretical understanding of hydrogen passivation*, Phys. Rev. Lett. **65** (1990), no. 4, 504.
2. T. Hattori and S. Heusler, *Ultraclean surface processing of silicon wafers*, Springer (1998).
3. A. Ulman, *Formation and structure of self-assembled monolayers*, Chem. Rev. **96** (1996), 1533.
4. A. Faucheux, A. C. Gouget-Laemmel, P. A. llongue, C. H. d. Villeneuve, F. Ozanam and J.-N. Chazalviel, *Mechanisms of thermal decomposition of organic monolayers grafted on (111) silicon*, Langmuir **23** (2007), 1326.
5. J. M. Buriak, *Organometallic chemistry on silicon and germanium surfaces*, Chem. Rev. **102** (2002), 1271.
6. B. F. Hanyaloglu and E. S. Aydil, *Low temperature plasma deposition of silicon nitride from silane and nitrogen plasmas*, J. Vac. Sci. Technol. A **16**(5) (1998), 2794.
7. J. W. Klaus, A. W. Ott, A. C. Dillon and S. M. George, *Atomic layer controlled growth of Si_3N_4 films using sequential surface reactions*, Surface Science **418** (1998), L14.
8. R. T. Brewer, M.-T. Ho, K. Z. Zhang, L. V. Goncharova, D. G. Starodub, T. Gustafsson and Y. J. Chabal, *Ammonia pretreatment for high- κ dielectric growth on*

silicon, Appl. Phys. Lett. **85** (2004), no. 17, 3830.

9. Y. Wang, M. Dai, S. Rivillon, M. T. Ho and Y. J. Chabal, *In situ infrared absorption spectroscopy for thin films growth by atomic layer deposition*, Proc. SPIE **6325** (2006), 63250G.
10. Y. Wang, M.-T. Ho, L. V. Goncharova, L. S. Wielunski, S. Rivillon-Amy, Y. J. Chabal, T. Gustafsson, N. Moumen and M. Boleslawski, *Characterization of ultra-thin hafnium oxide films grown on silicon by atomic layer deposited using tetrakis(ethylmethyl-amino) hafnium and water precursors*, Chem. Mater. **19** (2007), 3127.
11. M. M. Frank, Y. Wang, M.-T. Ho, R. T. Brewer, N. Moumen and Y. J. Chabal, *Hydrogen barrier layer against silicon oxidation during atomic layer deposition of Al_2O_3 and HfO_2* , J. Electrochem. Soc. **154** (2007), no. 2, G44.
12. M. Björkqvist, M. Gothelid and U. O. Karlsson, *Nitride formation and dangling-bond passivation on Si(111)-(7 x 7) with NH_3* , Surface Science **394** (1997), L155-L161.
13. D. R. Bowler and J. H. G. Owen, *Molecular interactions and decomposition pathways of NH_3 on Si(001)*, Phys. Rev. B **75** (2007), 155310.
14. J. L. Bischoff, L. Kubler and D. Bolmont, *Thermal nitridation of Si(100)-2 x 1 surface by NH_3 : XPS results*, Surface Science **209** (1989), no. 1-2, 115.
15. K. T. Queeney, Y. J. Chabal and K. Raghavachari, *Role of interdimer interactions in NH_3 dissociation on Si(100)*, Physical Review Letters **86** (2001), 1046.
16. M. Björkqvist, M. Gothelid, T. M. Grehk and U. O. Karlsson, *NH_3 on Si(111)7x7: Dissociation and surface reaction*, Physical Review B **57** (1998), no. 4, 2327.
17. M. L. Colaiaanni, P. j. Chen and J. J. T. Yates, *The stepwise dissociation of NH_3 on the Si(111)-(7x7) surface: Low-temperature dissociative adsorption and thermal effects*, J. Chem. Phys. **96** (1992), no. 10, 7826.
18. J. C. F. Rodríguez-Reyes and A. V. Teplyakov, *Cooperative nitrogen insertion processes: Thermal transformation of NH_3 on a Si(100) surface*, Phys. Rev. B **76** (2007), 075348.
19. Y. I. S. Ishidzuka, T. Takaoka, I. Kusunoki, *Nitridation of Si(100) surface with NH_3* , Applied Surface Science **130-132** (1997), 107.
20. P. Dumas, Y. J. Chabal and G. S. Higashi, *Coupling of an adsorbate vibration to a substrate surface phonon: H on Si(111)*, Physical Review Letters **65** (1990), 1124.
21. A. C. Dillon, P. Gupta, M. B. Robinson, A. S. Bracher and S. M. George, *Ammonia decomposition on silicon surfaces studied using transmission Fourier transform infrared spectroscopy*, J. Vac. Sci. Technol. A **9(4)** (1991), 2222.
22. J. Yoshinobu, *Physical properties and chemical reactivity of the buckled dimer on Si(100)*, Progress in Surface Science **77** (2004), 37-70.
23. M.-T. Ho, Y. Wang, R. T. Brewer, L. S. Wielunski and Y. J. Chabal, *In situ infrared spectroscopy of hafnium oxide growth on hydrogen-terminated silicon surfaces by atomic layer deposition*, Appl. Phys. Lett. **87** (2005), 133103.
24. G. N. Parsons and G. Lucovsky, *Silicon-hydrogen bond-stretching vibrations in*

- hydrogenated amorphous silicon-nitrogen alloys*, Phys. Rev. B **41** (1990), 1664.
25. D. V. Tsu, G. Lucovsky and B. N. Davidson, *Effects of the nearest neighbors and the alloy matrix on SiH stretching vibrations in the amorphous SiO_xH ($0 < x < 2$) alloy system*, Physical Review B **40** (1989), no. 3, 1795.
 26. G. Dupont, H. Caquineau, B. Despax, R. Berjoan and A. Dollet, *Structural properties of N-rich $\alpha\text{-Si-N:H}$ films with a low electron-trapping rate*, J. Phys. D: Appl. Phys **30** (1997), 1064.
 27. G. Lucovsky and D. V. Tsu, *Plasma enhanced chemical vapor deposition: Differences between direct and remote plasma excitation*, J. Vac. Sci. Technol. A **5**(4) (1986), 2231.
 28. K.-C. Lin and S.-C. Lee, *The structural and optical properties of $\alpha\text{-SiN}_x\text{H}$ prepared by plasma-enhanced chemical-vapor deposition*, J. Appl. Phys. **72** (1992), 5474.
 29. D. V. Tsu and G. Lucovsky, *Silicon nitride and silicon diimide grown by remote plasma enhanced chemical vapor deposition*, J. Vac. Sci. Technol. A **4**(3) (1986), 480.
 30. D. V. Tsu, G. Lucovsky and M. J. Mantini, *Local atomic structure in thin films of silicon nitride and silicon diimide produced by remote plasma-enhanced chemical-vapor deposition*, Physical Review B **33** (1986), 7069.
 31. V. Verlaan, C. H. M., v. d. Werf, W. M. Arnoldbik, H. D. Goldbach and R. E. I. Schropp, *Unambiguous determination of Fourier-transform infrared spectroscopy proportionality factors: The case of silicon nitride*, Physical Review B **73** (2006), 195333.
 32. a. Y. J. C. P. Jakob, *Chemical etching of vicinal Si(111): Dependence of the surface structure and the hydrogen termination on the PH of the etching solutions*, J. chem. Phys. **95**(4) (1991).
 33. X. Zhang, Y. J. Chabal, S. B. Christman, E. E. Chaban and E. Garfunkel, *Oxidation of H-covered flat and vicinal Si(111)-1x1 surfaces*, J. Vac. Sci. Technol. A **19**(4) (2000), 1725.
 34. Y. J. Chabal, G. S. Higashi, K. Raghavachari and V. A. Burrows, *Infrared spectroscopy of Si(111) and Si(100) surfaces after HF treatment: Hydrogen termination and surface morphology*, J. Vac. Sci. Technol. A **7**(3) (1989), 2104.
 35. K. Raghavachari, P. Jakob and Y. J. Chabal, *Step relaxation and surface stress at H-terminated vicinal Si(111)*, Chemical Physics Letters **206** (1993), 156.
 36. J. P. Perdew, K. Burke and M. Ernzerhof, *Generalized gradient approximation made simple*, Phys. Rev. Lett. **77** (1996), 3865.
 37. B. Delley, *From molecules to solids with the Dmol3 approach*, J. Chem. Phys. **113** (2000), 7756.
 38. G. D. Wilk, R. M. Wallace and J. M. Anthony, *High-k gate dielectrics: Current status and materials properties considerations*, Journal of Applied Physics **89** (2001), 5243.
 39. *High-k and metal gate research*, <http://www.intel.com/technology/silicon/high-k.htm>.
 40. S. Yoshihide, P. Seung, C. Hood, B. Lawrence and N. Wesley, *Atomic layer deposition of hafnium oxide and hafnium silicate thin films using liquid precursors and*

ozone, Journal of Vacuum Science & Technology A: Vacuum, Surfaces, and Films **22** (2004), no. 4, 1175-1181.

41. D. M. Hausmann, E. Kim, J. Becker and R. G. Gordon, *Atomic layer deposition of hafnium and zirconium oxides using metal amide precursors*, Chem. Mater. **14** (2002), 4350.

42. K. Kukli, M. Ritala, T. Sajavaara, J. Keinonen and M. Leskelä, *Atomic layer deposition of hafnium dioxide films from hafnium tetrakis(ethylmethanamide) and water*, Chemical Vapor Deposition **8** (2002), no. 5, 199.

43. K. T. Queeney, Y. J. Chabal, M. K. Weldon and K. Raghavachari, *Silicon oxidation and ultra-thin oxide formation on silicon studied by infrared absorption spectroscopy*, Phys. Stat. Sol. (a) **175** (1999), 77.

Chapter 4: ALD of Al_2O_3 and HfO_2 with Ozone

H_2O is most frequently used oxidant for ALD to deposit metal oxides [1]. However, most ALD precursors are extremely sensitive to water, and H_2O or hydroxyl group ($-\text{OH}$) tends to be strongly physisorbed on surfaces or in ALD reactor. The trapped water/ OH may release during the metal precursor dosing and hence increase the growth rate making the deposition more like CVD process. Thus, long purging time is needed to remove the residue water/ OH and hot-wall ALD is necessary to reduce adsorbed water.

Another issue of water based ALD is that the deposited metal oxide film contains hydroxyl groups [2]. These hydroxyl groups make the film oxygen rich and may oxidize the interface during post-annealing treatment by forming interfacial SiO_2 , which greatly minimizes the advantage of using high- κ oxide [3]. In addition, the hydroxyl groups will degrade the electrical property of high- κ oxide film such as increasing the leakage current. Therefore, ozone has been used as the oxidant for ALD growth to prevent those drawbacks caused by water [4, 5, 6, 7, 8]. Studies have shown that ozone based ALD can deposit high- κ oxide film with improved electrical and structural properties including low leakage current [9, 10, 11]. Particularly, ozone has several other advantages over water. It is a strongly-reactive oxidizing agent with high volatility. The concentration and flow of ozone can be easily controlled compared with water vapor. In addition, it is not sticky and can be easily purged away. The decomposed product of ozone is oxygen which is harmless. So it is becoming a promising alternative ALD oxidant. However, the carbon contamination and complicated reaction mechanism are common issues for ozone.

Despite its importance, the mechanistic study of ozone based ALD is rare and the mechanism is not well understood. So, this chapter will discuss the ozone based ALD

compared with water based ALD. Both positive and negative parts of ozone based ALD will be investigated by the examples of high- κ metal oxides, Al_2O_3 (~ 8) and HfO_2 .

4.1 TMA gas phase and gas phase reaction

TMA (tri-methyl aluminum) is a simple and most well studied precursor for long time [12, 13, 14, 15, 16]. Once it was a CVD precursor and now it is widely used for ALD growth. It is very volatile and can be kept at room temperature since its vapor pressure is high enough for ALD application without carrier gas.

Numerous studies [17, 18, 19] of TMA have shown that the monomeric TMA tends to form dimer structure because it has only six electrons in its valence shell which is electron-deficient. The more stable dimer structure with an eight electron configuration is desired and therefore the dimer exists in most cases. It is known that TMA can dimerize in the solid state, in solution (with solvents such as benzene and so on), and in the gas phase. As shown by Fig 4.1, the chemical structure of monomeric TMA is presented on the left and the TMA dimer is on the right, where the dimer structure is formed through the bridging of CH_3 group.

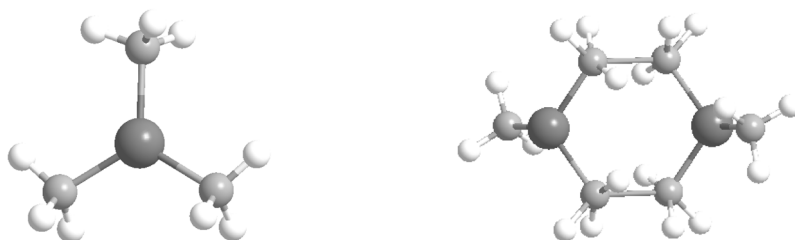


Fig 4.1 Structure of TMA monomer (left) and dimer (right) used for deposition of Al_2O_3

The existence of dimer structure in the TMA gas phase can be easily confirmed by its IR spectrum, which is shown in Fig 4.2 (the spectrum on the top in red). The dimer

and monomer can be identified by the band shift of $-\text{CH}_3$ due to $-\text{CH}_3$ bridging. For example, the stretching modes of $-\text{CH}_3$ at $2800\text{--}3000\text{ cm}^{-1}$ are split into the bridged $-\text{CH}_3$ modes and terminal $-\text{CH}_3$ modes, along with many other bridged modes and terminal modes. The detailed band assignments are shown in table 4.1. Note that in spite of some debates for the assignments [20, 21, 22, 23, 24], there is no doubt that large extent of TMA dimer exists inside the gas phase. The gas phase spectrum is identical to that in other studies and trivial amount of CH_4 is observed, implying little hydrolysis or decomposition of TMA. Thus, it can be concluded that the TMA is quite pure before further ALD reaction.

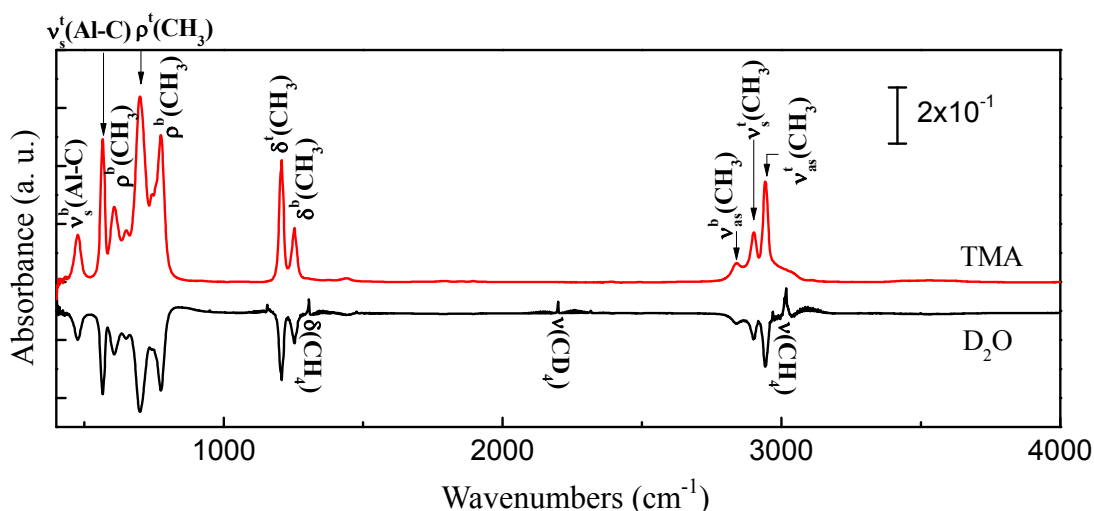


Fig 4.2 The TMA gas phase spectrum and the spectrum after reaction with D_2O . The spectrum on the top in red shows the TMA gas phase (referenced to vacuum) and the spectrum at the bottom in black is after D_2O exposure (referenced to TMA). The superscript 'b' denotes the 'bridged' and 't' denotes 'terminal'. The TMA ligand features disappear after D_2O .

Using TMA and water to deposit Al_2O_3 has been extensively studied. But direct gas phase reaction study is rare. Here, after introducing the gas phase TMA into the ALD reactor and taking the spectrum, D_2O is introduced in to study the reaction byproducts and then the detailed reaction can be concluded. As in Fig 4.2, the spectrum at the bottom

in black is the TMA precursor after D₂O exposure and referenced to TMA. It can be seen that all the TMA related bands such as Al-C and CH₃ vibration modes show as negative peaks implying the strong reaction between TMA and D₂O. The reaction byproducts can be directly detected from the spectra including CD₄, and CH₄, featured by the gas phase peaks centered at ~2199 cm⁻¹ (stretching mode of CD₄), 3017 cm⁻¹ (stretching mode of CH₄), and 1305 cm⁻¹ (deformation mode of CH₄). CH₄ comes from the H₂O impurity inside D₂O and isotope exchange. Thus, the reaction between TMA and water can be easily summarized as the following reaction:

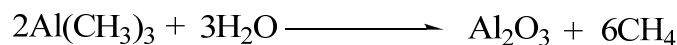


Table 4.1 The IR band assignment of TMA gas phase [20, 21, 22, 23, 24]

Assignments	Wavenumbers (cm ⁻¹)
$\nu_s(\text{Al-C})^b$	477
$\nu_s(\text{Al-C})^t$	567
$\rho(\text{CH}_3)^b$	607
$\nu_{as}(\text{Al-C})^b$	650
$\rho(\text{CH}_3)^t$	700
$\rho(\text{CH}_3)^b$	775
$\delta(\text{CH}_3)^t$	1208
$\delta(\text{CH}_3)^b$	1254
$\nu_{as}(\text{CH}_3)^b$	2840
$\nu_s(\text{CH}_3)^t$	2901
$\nu_{as}(\text{CH}_3)^t$	2941

*The superscript ‘b’ denotes the ‘bridged’ and ‘t’ denotes ‘terminal’

However, ozone shows very different reaction than water and it is more complicated due to ozone’s high reactivity with hydrocarbon species. Fig 4.3 shows the spectra of TMA interaction with ozone, where the spectrum on the top in red shows the TMA gas phase (referenced to vacuum) and the spectrum at the bottom in black is after ozone exposure (referenced to TMA). Compared with the water case, CH₄ is not the only

byproduct after TMA reaction with ozone and only shows small amount in the spectrum. It can also result from the residue water in the ALD reactor instead of ozone gas. A little CO and CO₂ are observed and evidenced by their stretching bands at 2100-2300 cm⁻¹. The loss of the Al-C stretching modes and shift of CH₃ stretching modes (2960 cm⁻¹ and 2856 cm⁻¹) and rocking mode (620 cm⁻¹) indicate the breaking of TMA molecule due to the reaction. The peaks at 998 cm⁻¹, 1024 cm⁻¹, 1068 cm⁻¹ and 1109 cm⁻¹ are tentatively assigned to C-C and C-O related modes [25].

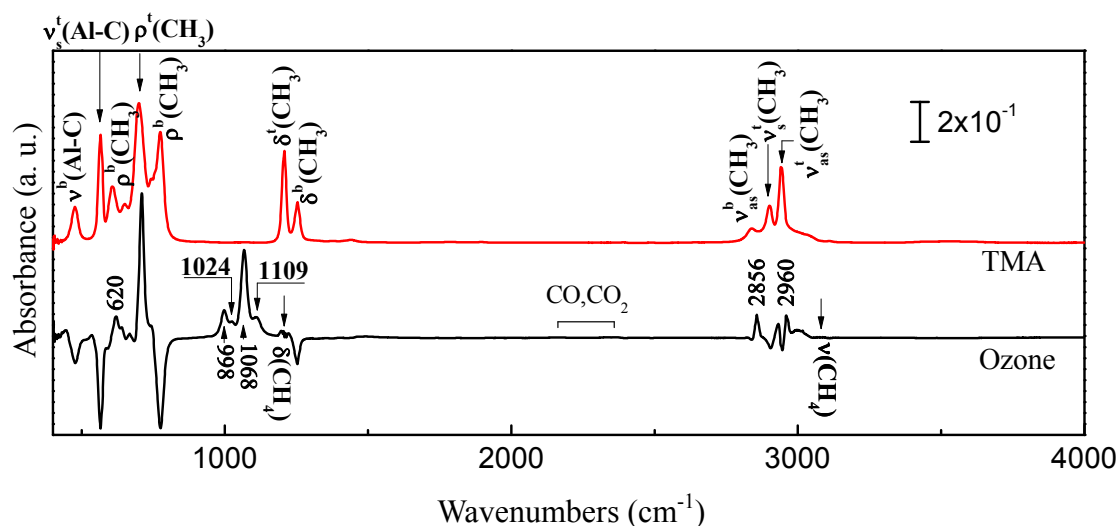
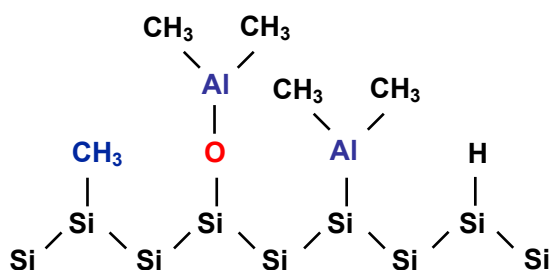


Fig 4.3 The TMA gas phase spectrum and the spectrum after reaction with ozone. The spectrum on the top in red shows the TMA gas phase (referenced to vacuum) and the spectrum at the bottom in black is after ozone exposure (referenced to TMA). The subscript ‘b’ denotes the ‘bridged’ and ‘t’ denotes ‘terminal’.

Some study has shown that the TMA and ozone reaction simply gives $\text{Al}_2(\text{CH}_3)_{6-n}(\text{OH})_n + (n/2)\text{C}_2\text{H}_4$ (gas) [26]. Some other studies assumed the products as Al_2O_3 and H_2O with CO_2 [27]. However, according to our experiment, the dominant IR bands are not from CO_2 or H_2O . The strongest peaks (1000-1200 cm⁻¹) are not gas-phase-like peaks such as C_2H_4 . The real reaction is not as simple as assumed. Unlike the water case, the CH_3 bands are not removed, but shifted. Therefore, the likely reaction

The surface interaction between H/Si(111) and TMA



Before further discussion of Al_2O_3 deposition on H/Si, the interaction between H/Si(111) and TMA is studied as the fundamental of following discussions. Previous studies have shown that the TMA will attack the Si-H bond on the H/Si(111) by forming $\text{Si-O-Al}(\text{CH}_3)_x$, $\text{Si-Al}(\text{CH}_3)_x$, and Si-CH_3 species [28, 29]. The formation of Si-O-Al is due to the residue water partial hydrolyzing TMA to $\text{Al}(\text{OH})_x$, which will compete with intact TMA to be adsorbed on H/Si(111). The interaction is schematically described by Fig 4.4.

It can be experimentally proved by *in situ* FTIR which shows the H/Si(111) exposed to TMA at 300°C. Saturation pulse length is used for the TMA exposure. The IR spectrum is in Fig 4.5 which is referenced to H/Si(111). In the spectra, the Si-CH₃ specie is

confirmed by CH_3 rocking mode at 770 cm^{-1} and deformation mode 1248 cm^{-1} , the $\text{Si-O-Al}(\text{CH}_3)_x$ specie is confirmed by the broad peak at 984 cm^{-1} which is Si-O mode shifted by Al atom, and the Al- CH_3 specie is confirmed by the CH_3 deformation mode at 1217 cm^{-1} . The Al- CH_3 directly attaching Si via Si-Al bond cannot be observed in the spectrum, because it is out of our detection ability. However, the band analysis of Al- CH_3 deformation mode by previous study shows the existence of direct bond of Si-Al [28], where the methyl deformation mode observed at 1217 cm^{-1} with a shoulder at 1206 cm^{-1} is a useful indicator of Si-Al bonding environment. According to our single unit cell cluster DFT calculation, the $-\text{CH}_3$ umbrella deformation mode of Si-O-Al-CH_3 is $\sim 6\text{ cm}^{-1}$ higher than that of Si-Al-CH_3 . This suggests that Al- CH_3 of TMA is attached to Si atoms either directly or through O atoms.

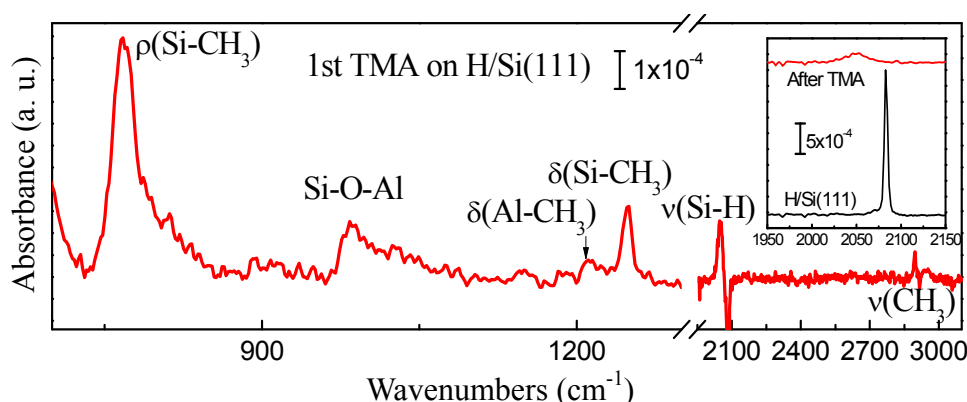


Fig 4.5 IR absorption spectrum of H/Si(111) exposed by TMA at $300\text{ }^{\circ}\text{C}$ which is referenced to H/Si(111) at incident angle $\sim 74^{\circ}$. The inset shows the initial H/Si(111) (spectrum at the bottom in black) and the surface after TMA exposure (spectrum on top and in red) which are all referenced to SiO_2 .

The variation of Si-H at 2083 cm^{-1} indicates the adsorption of TMA on H/Si(111) by replacing Si-H. The coverage can be deduced by the loss of Si-H. As shown by the inset of Fig 4.5 which is referenced to SiO_2 surface, the initial Si-H (bottom spectrum in black) at 2083 cm^{-1} decreases and red shifts to 2050 cm^{-1} due to decoupling of Si-H by the

adsorbed TMA species after TMA exposure (top spectrum in red). The intensity loss of Si-H suggests a $\sim 75\%$ surface coverage. From the intensity of CH_3 stretching modes, it can be concluded that Si- CH_3 is the dominant specie on the surface and it substantially blocks the reaction sites for TMA, resulting in the incubation period for further Al_2O_3 deposition.

Brief review of Al_2O_3 deposited by TMA and D_2O

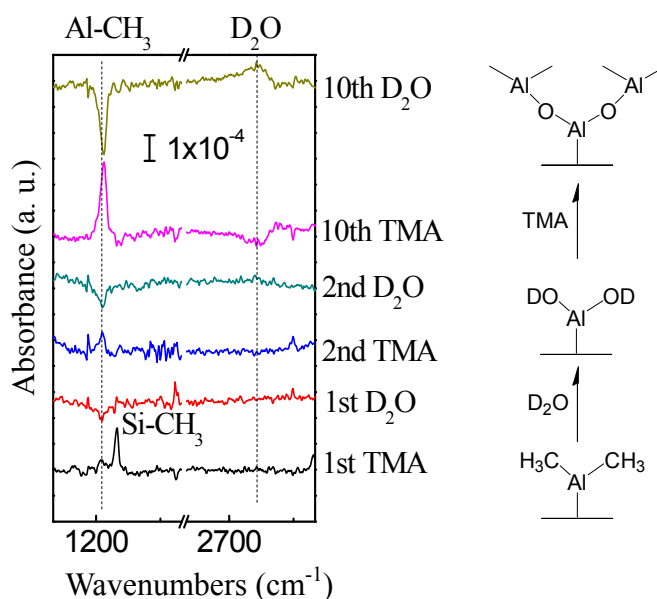


Fig 4.6 Differential FTIR absorption spectra of 10 cycles Al_2O_3 on H/Si(111) at 300°C . Each spectrum is referenced to the previous surface. The 1st TMA is referenced to H/Si starting surface and the 10th TMA is referenced to the 9th cycle (9th D_2O). The inset on the right shows the scheme of ALD reaction.

Before going on to using TMA and ozone to deposit Al_2O_3 , we first briefly review the deposition by TMA and D_2O for comparison with ozone based ALD. For this purpose, 10 cycles Al_2O_3 are deposited on H/Si(111) at 300°C with saturation pulse length for each precursor dosing. Although it has already been studied [28], it is the basic of our later discussions.

Fig 4.6 shows the differential spectra of 10 cycles Al_2O_3 , where each spectrum is referenced to the previous surface and the bottom is referenced to H/Si(111). The 1st TMA on H/Si has been discussed in detail in the previous section. The subsequent D_2O pulse removes the $-\text{CH}_3$ ligands on Al as expected, featured by the negative peak at 1217 cm^{-1} (the deformation mode of $\text{Al}-\text{CH}_3$) and putting $-\text{OD}$ groups onto Al. The next TMA pulse replaces the $-\text{OD}$ groups and is attached to the Al via O-Al bond, evidenced by the positive peak at 1217 cm^{-1} (the deformation mode of $\text{Al}-\text{CH}_3$). This process repeats and Al_2O_3 is deposited monolayer by monolayer. The reaction scheme is described in the inset of Fig 4.6 on the right side. Note that the 10th cycle shows stronger intensity for $\text{Al}-\text{CH}_3$ variation at 1217 cm^{-1} and for the broad $-\text{OD}$ stretching band variation at 2760 cm^{-1} , as the ALD ligand exchange phenomena. It confirms the ALD scheme and indicates the initial incubation period in the Al_2O_3 ALD growth.

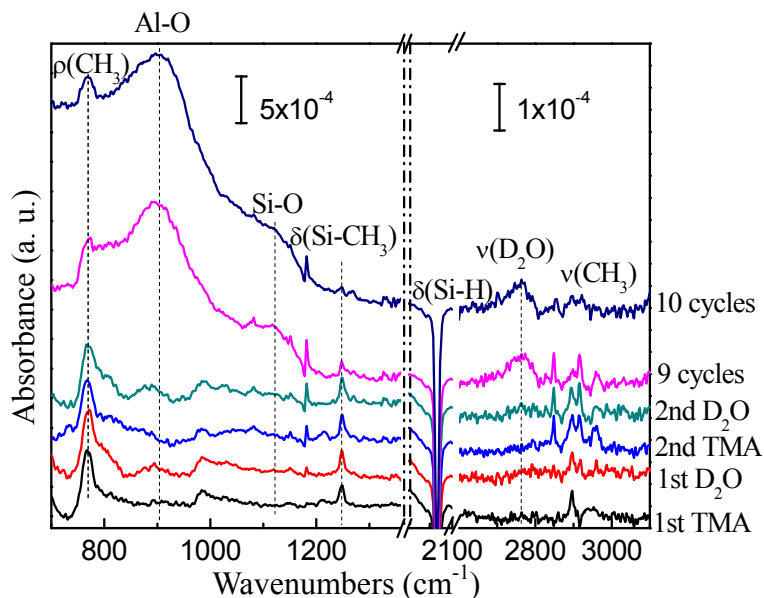


Fig 4.7 Absorption spectra of 10 cycles Al_2O_3 on H/Si(111) at 300°C . All spectra are referenced to the H/Si(111) surface. SiO_x , Al_2O_3 , carbon impurity and trapped water are observed in the spectra.

The spectra in Fig 4.7 are referenced to initial H/Si which are used to examine the

chemical species in the film. The broad band centered at 906 cm^{-1} keeps growing with more cycles. It is assigned to the Al-O phonon mode, confirming the formation of continuous Al_2O_3 film with nearly complete Si-H loss. The shoulder appears at $1000\text{-}1200\text{ cm}^{-1}$ is due to the interfacial Si-O, and the amount is minimal because no individual TO/LO modes are observed. The -OD stretching band at 2760 cm^{-1} indicates the existence of trapped $\text{D}_2\text{O}/\text{OD}$ substance inside the film. The - CH_3 modes at 770 cm^{-1} (Si- CH_3 rocking), 1248 cm^{-1} (Si- CH_3 deformation), 1217 cm^{-1} (Al- CH_3 deformation), and $2800\text{-}3000\text{ cm}^{-1}$ (CH_3 stretching), suggest the detectable amount of hydrocarbon impurities in the film.

With above knowledge, we will discuss ozone based ALD in the following sections. First we will investigate the ozone ALD growth with excessive ozone pulse length, and then the growth with shorter ozone pulse length will be discussed to show the improvement in the film quality.

Al_2O_3 deposited by TMA and ozone(I)-long ozone pulse

The deposition with long ozone pulse length will be discussed first. The ALD of TMA+ozone on H/Si(111) is performed at 300°C for 20 cycles. Saturation pulse length for TMA and excessive pulse length for ozone are used, where the ozone exposure amount is 200sccm for 2s. The differential spectra are shown in Fig 4.8. The H/Si surface after first TMA dosing has been discussed in the previous section. The methyl deformation mode of Al- CH_3 at 1217 cm^{-1} and loss of Si-H at 2083 cm^{-1} indicate adsorbed TMA on the surface. The Si- CH_3 rocking mode (770 cm^{-1}) and deformation mode (1248 cm^{-1}) are observed as well as the Al-O-Si band at 984 cm^{-1} .

After the 1st ozone exposure, the surface is oxidized immediately shown by SiO_2

TO/LO modes at 1027 cm^{-1} and 1154 cm^{-1} , which are the features of continuous SiO_2 layer. Its integrated area implies about 4 \AA SiO_2 which is close to 1 monolayer of SiO_2 . We have exposed the H/Si(111) surface to the same amount of ozone only without TMA. Identical integrated area of LO/TO modes of SiO_2 is obtained (~ 1 monolayer oxide). It suggests that whether the Si surface is hydrogen-terminated or with adsorbed TMA and $-\text{CH}_3$ group, it is same vulnerable to ozone exposure. It is also supported by the variation of Si- CH_3 rocking mode at 770 cm^{-1} and the appearing of the band at 1270 cm^{-1} which is assigned to the methyl deformation mode due to $\text{O}_x\text{-Si-CH}_3$, indicating the oxygen insertion to the Si-Si back bond and the oxidation of the surface [30].

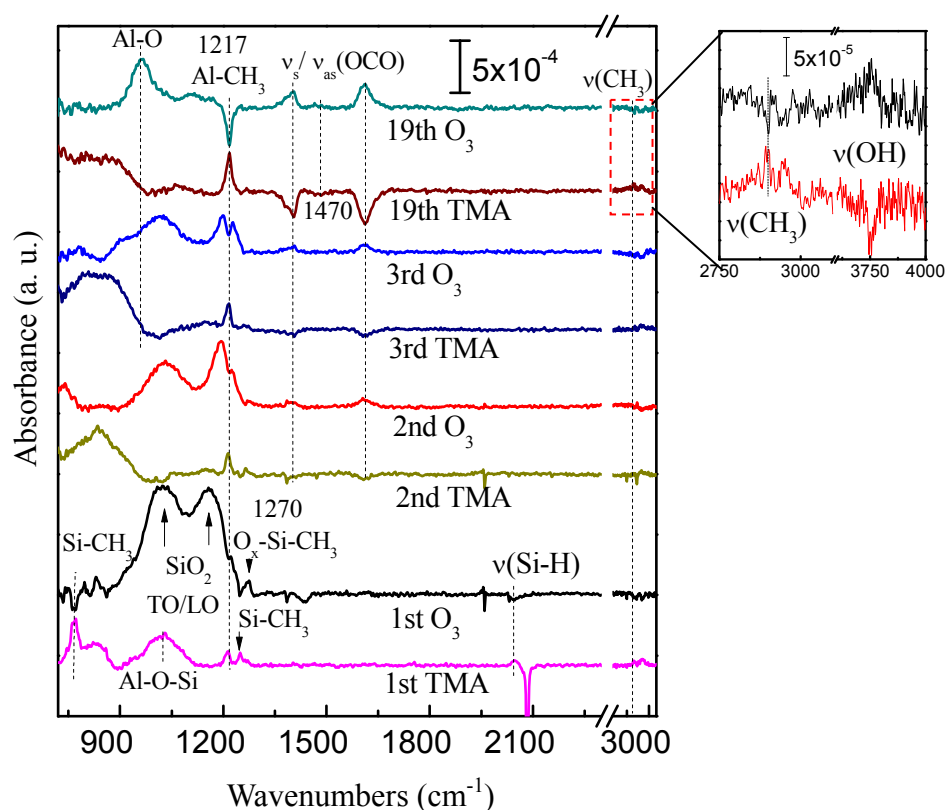


Fig 4.8 Differential FTIR spectra of 20 cycles TMA and ozone deposition on H/Si(111) at 300°C . Each spectrum is referenced to that of the surface subjected to the previous treatment. The 1st TMA is referenced to H/Si starting surface and the 19th TMA is referenced to the 18th cycle (18th O_3). The inset is the detailed spectral feature at $2750\text{--}4000\text{ cm}^{-1}$ to show the $\nu(\text{CH}_3)$ and $\nu(\text{OH})$

The further loss of Si-H confirms the attacking of ozone to the Si surface at later cycles. This oxide phonon band is disrupted after each TMA pulse because of the chemical bonding between the surface Si-O-Si matrix and TMA. The subsequent TMA and ozone pulses show the periodic gain and loss of Al-CH₃ at 1217 cm⁻¹ and -CH₃ stretches at 2800-3000 cm⁻¹, suggesting the ALD ligand exchange and the continuous growth of Al₂O₃. That is, after TMA, the Al-CH₃ is attached to the surface and after ozone, the -CH₃ is attacked. But the actual reaction mechanism is not so simple.

From the second cycle, several new bands have been observed accompanied by the variation of Al-CH₃ deformation mode. The weak band at 1470 cm⁻¹ is assigned to Al-O-CH₃ methyl deformation mode indicating the insertion of oxygen into Al-C bond after ozone exposure. More important, the bands at 1400 cm⁻¹ and 1610 cm⁻¹ are assigned to the formate (OCHO⁻) species on the surface [31, 32]. The 1600 cm⁻¹ band is the asymmetric stretching mode while the 1400 cm⁻¹ band can be deconvoluted to three bands at 1405, 1385 and 1360 cm⁻¹. These bands are attributed to OCO deformation, CH in-plane bending and OCO symmetric stretching modes of the formate species, respectively [31]. At 300°C, the formate species can decompose to gas-phase CO or CO₂, producing OH groups on the surface [33]. These hydroxyl groups out of the formate decomposition are most likely the origin of the -OH stretching band at 3750 cm⁻¹ after each ozone pulse as shown by the inset of Fig 4.8.

To support our band assignments and rule out other possible surface species, periodic and cluster based first principle calculations are carried out (done by Dr. Mathew Halls). The calculations using the density functional theory (DFT) code DMol3 are carried out [34], using all-electron calculations with the gradient corrected PBE [35] functional along with a double numeric polarized basis set (DNP). The vibrational modes

associated with O_3 ALD surface structures are calculated using fully periodic Al_2O_3 surface models, as well as simple cluster models, for comparison with experimental data.

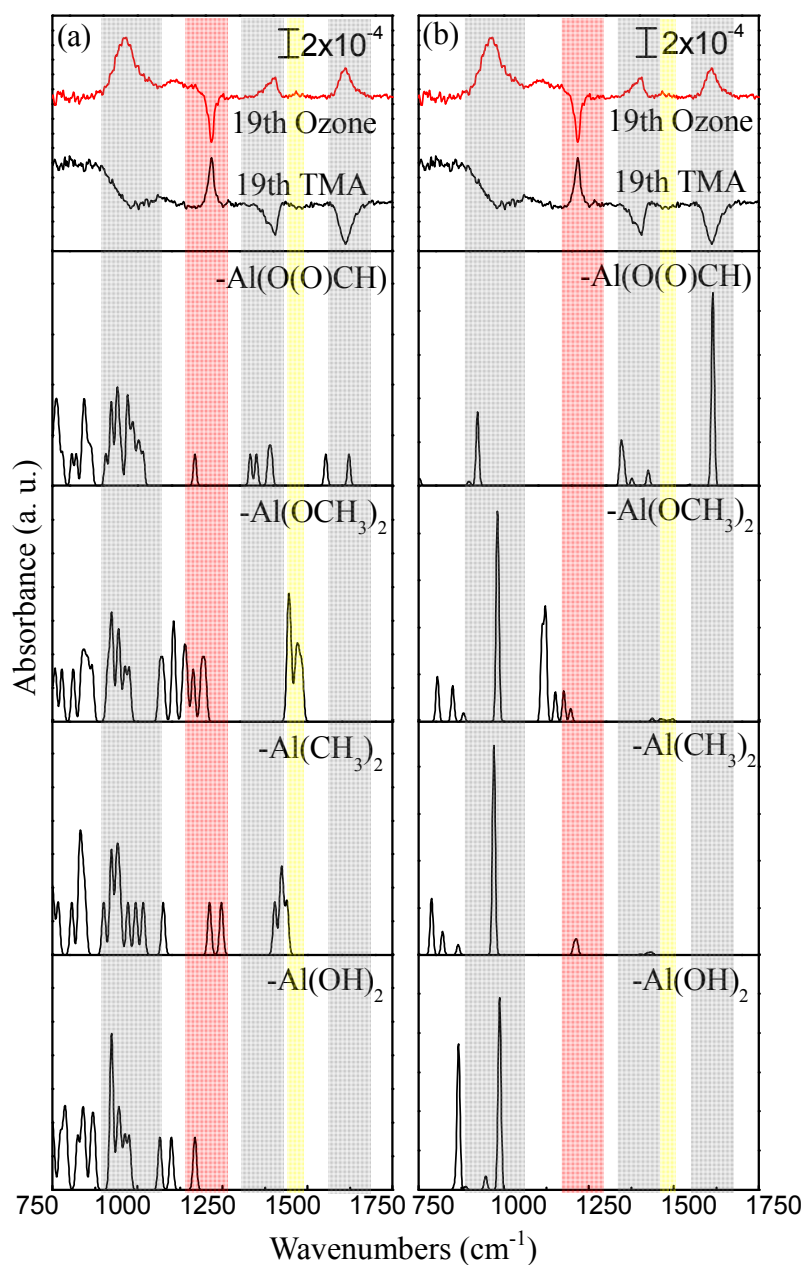


Fig 4.9(a) Periodic model vibrational density of states (VDOS); and (b) cluster model IR calculations of each surface structure done by DFT. The top differential spectra are the same experimental data as in Fig 4.8. The presence of formate species is confirmed.

Periodic atomistic models are based on a 5-layer slab of the (001)- Al_2O_3 surface.

Calculations are carried out for the $-\text{Al}(\text{CH}_3)_2$, $-\text{Al}(\text{OCH}_3)_2$, $-\text{Al}(\text{OH})_2$, and $-\text{Al}(\text{OOCH})$ species using 2×1 and 2×2 supercells, respectively, with a 20 Å vacuum slab. A Monkhorst-Pack k-point mesh with a spacing of 0.04 Å^{-1} was used to sample the Brillouin zone. For the cluster models, cluster stoichiometries of $\text{Al}_2\text{O}_3\text{H}_2-(\text{CH}_3)_2$, $\text{Al}_2\text{O}_3\text{H}_2-(\text{OCH}_3)_2$, $\text{Al}_2\text{O}_3\text{H}_2-(\text{OH})_2$ and $\text{Al}_2\text{O}_3-(\text{OOCH})_2$ were used.

Fig 4.9(a) shows the calculated vibrational density of states from periodic Al_2O_3 surface models and Fig 4.9(b) shows the computed vibrational frequencies with corresponding intensities from cluster adsorbate models, along with the experimental spectra (top panel) for comparison. The shaded vertical areas represent characteristic wavenumber regions are included to facilitate comparison between the experiment and theory. The surface species considered in the calculations include methyl $-\text{Al}(\text{CH}_3)_2$ (red bar), methoxy $-\text{Al}(\text{OCH}_3)_2$ (yellow bar), formate $-\text{Al}(\text{OOCH})$ (gray bars) and hydroxyl $-\text{Al}(\text{OH})_2$. Comparison of the observed IR spectra with the computed spectra for both the periodic (Fig 4.9(a)) and cluster models (Fig 4.9(b)) supports our assignments. The predicted frequencies for the $-\text{Al}(\text{CH}_3)_2$ umbrella modes at $1211\text{--}1240 \text{ cm}^{-1}$ can be compared with the observed frequency at 1217 cm^{-1} . The computed frequencies of $1473\text{--}1483 \text{ cm}^{-1}$ for the methoxy species correspond to the $-\text{Al}(\text{OCH}_3)_2$ deformation seen in the IR at 1470 cm^{-1} .

As shown in Figure 4.9, only the symmetric and asymmetric OCO stretching vibrations are calculated to be at 1350 and 1622 cm^{-1} , respectively, in good agreement with experimental values (1360 cm^{-1} and 1610 cm^{-1}). In general, there are two different formate-aluminum bidentate geometries: a chelating structure, in which each formate binds to a single Al center, and a bridging structure, where a formate bridges between two Al centers. The computed $\nu_{\text{as}}(\text{OCO})$ and $\nu_{\text{s}}(\text{OCO})$ modes are comparable for these two

possibilities. However, the CH in-plane bending vibration for the chelating structure is 100 cm^{-1} lower than for the bridging structure. The $\delta(\text{CH})$ vibration is observed at 1385 cm^{-1} which corresponds to the calculated bridging formate mode at 1393 cm^{-1} . Thus, our analysis conclusively shows that a major intermediate in the O_3 ALD reaction pathway at TMA derived Al_2O_3 interfaces is the bidentate bridging formate species.

Upon O_3 exposure, possible initial surface reaction products include Al-OCH_3 and $\text{Al-CH}_2\text{OH}$ species. Our calculations (done by Dr. Mathew Halls) show that methoxy is the thermodynamically preferred product by 1.54 eV , in agreement with previous work by Elliott [26]. Some previously proposed O_3 ALD reaction mechanism was largely motivated by the detection of a signal of mass 28 u upon O_3 exposure, interpreted to be due to loss of C_2H_4 [36]. However, CO also has a mass of 28 u . Therefore, the reaction mechanism for O_3 ALD is much more complicated than might be assumed.

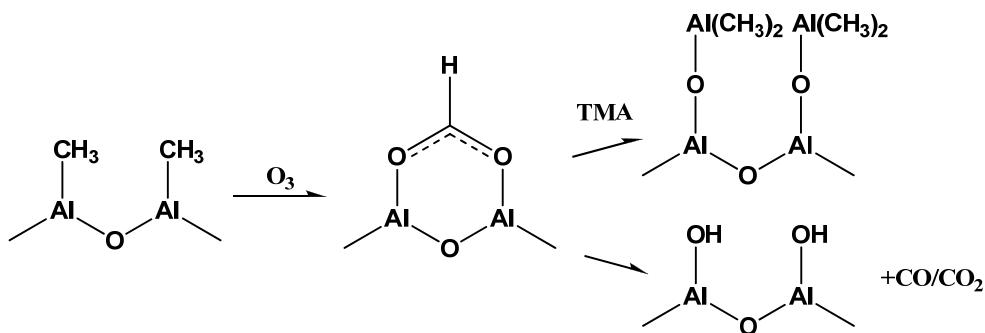


Fig 4.10 Reaction scheme of formate formation after ozone, removal of formate after TMA (top) and self decomposition of formate to Al-OH (bottom).

To simply, the reaction scheme of the formate is shown in Fig. 4.10, which shows the formation of formate and the formate reacting with TMA along with the possible formate decomposition to Al-OH . Most likely, after ozone exposure, the OCO formate is formed following an intermediate stage of Al-O-CH_3 species [32], and then the two

adjacent Al-O-CH₃ is combined to form the formate structure with C₂H₄ as the byproduct, as described by Fig 4.11. It is very possible due to the observation of Al-O-CH₃ in our spectra and is energetically favorable according to our DFT calculation.

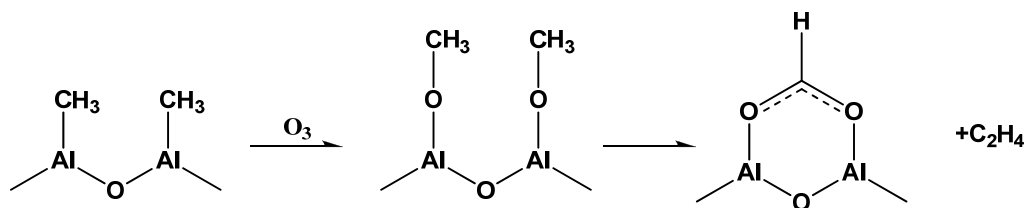


Fig 4.11 A possible pathway to form formate after ozone exposure. Two adjacent methoxy groups can be combined to form formate species.

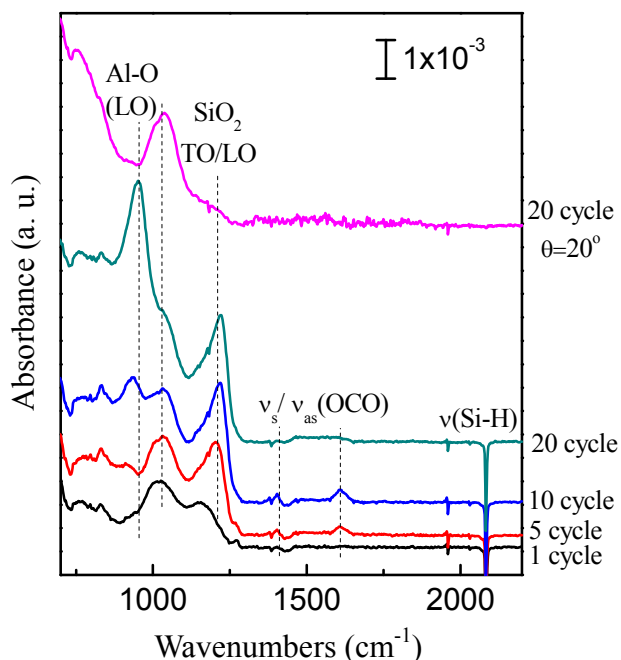


Fig 4.12 Absorption spectra of 20 cycles Al₂O₃ at 300°C referenced to H/Si(111) taken at IR incident angle of 74°, except the spectrum on the top which is taken at 20° to show the angle dependence. Substantial interfacial SiO₂ are observed.

Finally, we referenced all the spectra to the initial starting H/Si (111) surface to study the quality of Al₂O₃ film. As in Fig 4.12, the four spectra at the bottom are taken at ~74° (IR incident angle) and the spectrum on the top is taken at 20°. Strong SiO₂ TO/LO

modes at 1040 cm^{-1} and 1221 cm^{-1} indicate the substantial interfacial SiO_2 interfacial layer. According to the LO position, the thickness of SiO_2 can be estimated as $\sim 8\text{ \AA}$ [37]. The mode at 951 cm^{-1} is attributed to the Al_2O_3 phonon mode implying the formation of continuous film. The spectrum at 20° doesn't show this mode meaning it is an Al-O LO mode. Small amount of residue carbon impurities are observed inside the film due to the formate and methyl species at $1300\text{-}1600\text{ cm}^{-1}$.

Al_2O_3 deposited by TMA and ozone(II)-short ozone pulse

Due to strong oxidation from ozone and the negative effects of interfacial SiO_2 , the method to minimize SiO_2 is desired. It incents us to use shorter ozone pulse to reduce the interfacial silicon oxide while keep enough amount of ozone to have saturation growth. So, we deposit 20 cycles Al_2O_3 by the same saturation pulse length of TMA as the previous experiment, but with shorter ozone pulse length (100 sccm for 1s) now. The result is shown in Fig. 4.13.

As shown by Fig 4. 13(a), the 1st TMA shows the same features as our previous discussion. The observed methyl deformation mode of Al-CH₃ at 1217 cm^{-1} and loss of Si-H at 2083 cm^{-1} indicate adsorbed TMA on the surface. Other modes are observed as well including unwanted Si-CH₃ rocking mode (770 cm^{-1}) and deformation mode (1248 cm^{-1}), and Al-O-Si band at 984 cm^{-1} . The subsequent TMA and ozone pulses show the periodic gain and loss of Al-CH₃ at 1217 cm^{-1} suggesting the ALD ligand exchange and the continuous growth of Al_2O_3 . This disrupted band at $800\text{-}1000\text{ cm}^{-1}$ after each TMA or ozone pulse is because of the chemical bonding between the surface and TMA or ozone to form Al_2O_3 .

However, much different from the long ozone pulse case, after the 1st ozone exposure, no separated SiO_2 TO/LO modes are observed. Only a broad band at $800\text{-}1200$

cm^{-1} appears resulting from the interfacial Al-O-Si. The SiO_2 amount is much less than that of the long ozone pulse case (1 monolayer). No observation of 1270 cm^{-1} due to $\text{O}_x\text{-Si-CH}_3$ or variation of Si-CH₃ rocking modes at 770 cm^{-1} , indicating little oxygen insertion to the Si-Si back bond. It is also confirmed by no further loss of Si-H after the ozone exposure. The negative Si-H band after the 2nd TMA dosing is the result that the previous ozone pulse removes the -CH₃ ligands (Al-CH₃) and recovers the reaction sites (Si-H) which were blocked by the -CH₃ ligands. These strongly suggest that the ozone pulse only removes the methyl ligands from the adsorbed TMA and keeps the Si surface intact.

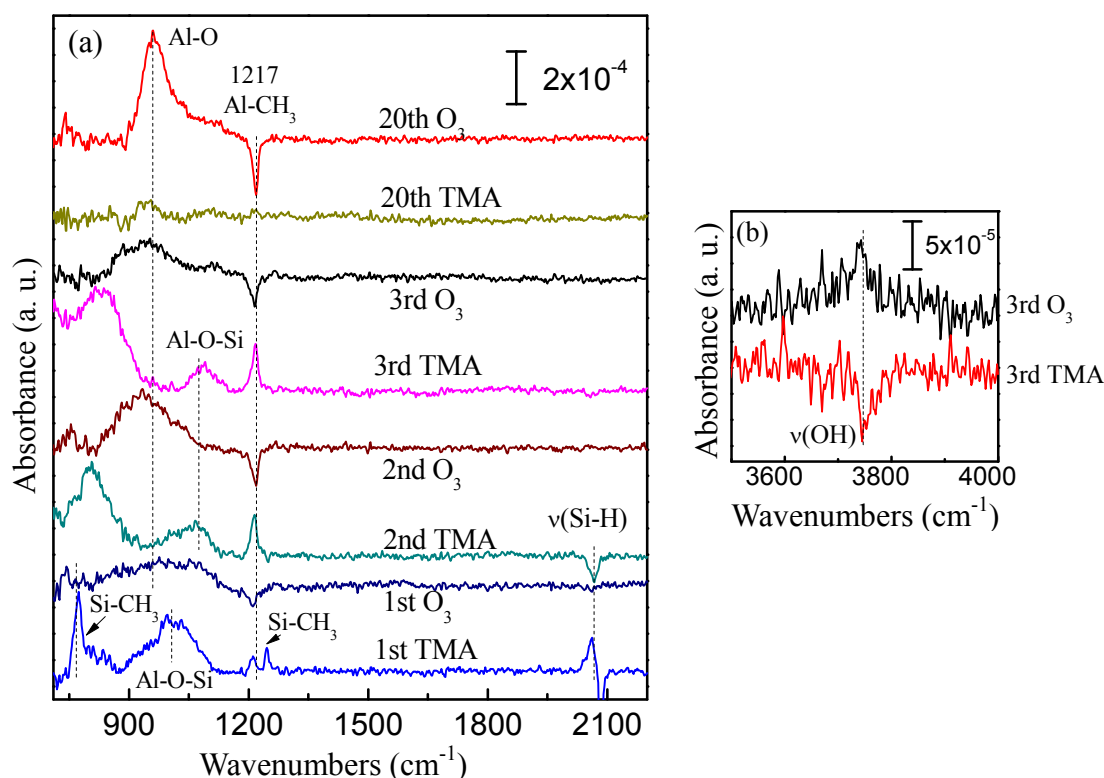


Fig 4.13 Differential FTIR spectra of (a) 20 cycles TMA and ozone deposition on H/Si(111) at 300°C with reduced ozone. Each spectrum is referenced to that of the surface subjected to the previous treatment. . The 1st TMA is referenced to H/Si and the 20th TMA is referenced to the 19th cycle (19th O₃); and (b) the same differential spectra of the 3rd cycle but showing the region of 3500-4000 cm^{-1}

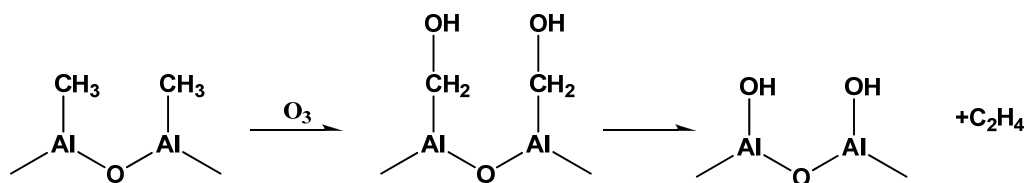


Fig 4.14 A possible pathway to form Al-OH after ozone exposure with alcohol species on the surface. This reaction pathway is not energetically favorable.

More important, no observable formate features around 1400 cm^{-1} and 1610 cm^{-1} in the spectra, indicate a different reaction pathway for the short ozone pulse case. The weak -OH stretch variation at 3742 cm^{-1} shown in Fig 4. 13(b) may suggest the formation of Al-OH specie after each ozone exposure and the Al-OH reacts with TMA to form Al-O-Al after the TMA exposure. It has been proposed that two pathways are possible for the Al_2O_3 deposition based on ozone [27, 38]. The first pathway is through the breaking of Al-C bond of adsorbed TMA on the surface to form Al-O- CH_3 species leading to the formate species as we discussed in the long ozone pulse case. The other pathway is through the oxygen insertion to AlC-H bond to form $\text{AlCH}_2\text{-OH}$ species which will further react to form Al-OH so that the subsequent ALD growth could continue. The latter reaction scheme is shown in Fig 4.14. However, this scheme is not energetically favored according to the DFT calculations done by Elliott [26]. The activation barrier for $\text{AlCH}_2\text{-OH}$ is much higher than that of $\text{Al}_2(\text{CH}_3)_{6-n}(\text{OH})_n$ or Al-O- CH_3 species. Thus the production of $\text{Al}_2(\text{CH}_3)_{6-n}(\text{OH})_n + (n/2)\text{C}_2\text{H}_4$ after the ozone exposure is likely and energetically favorable [26]. However, the pathway initiated with Al-O- CH_3 cannot be excluded due to its comparable low activation energy. As the result of the small ozone amount, Al-O- CH_3 is more isolated on the surface and cannot form formate species with adjacent methoxy groups. Then it may decompose to Al-OH or Al_2O_3 [39, 40] and thereby the subsequent TMA can react with this surface. Conclusively, the reaction

pathway depends on the ozone amount.

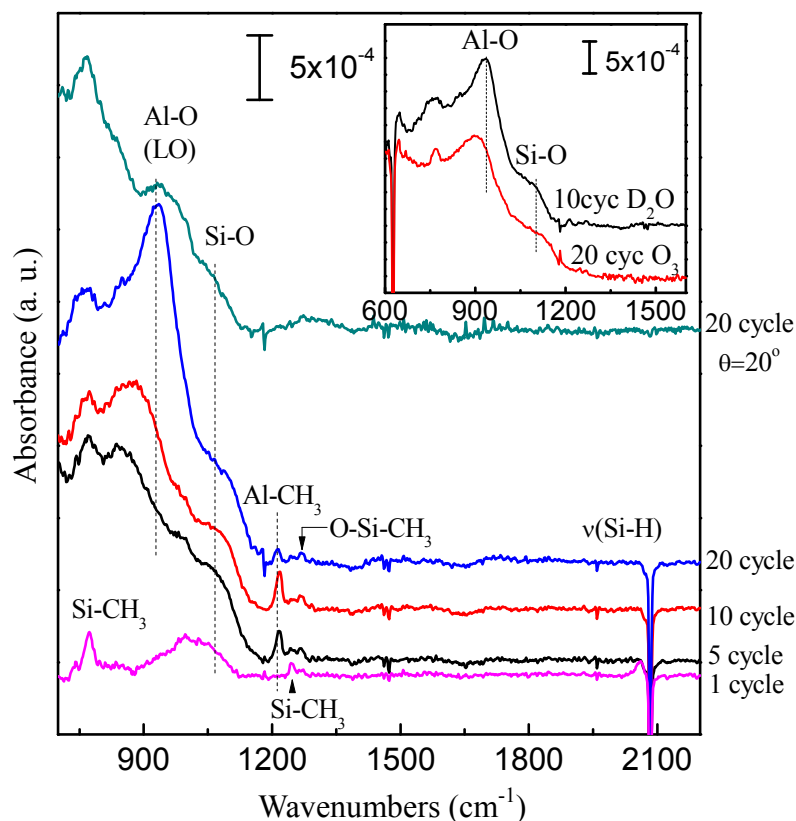


Fig 4.15 Absorption spectra of 20 cycles Al_2O_3 at 300°C with reduced ozone referenced to H/Si(111) taken at IR incident angle of 74° , except the spectrum on the top which is taken at 20° to show the angle dependence. The inset compares the deposition of 10 cycles Al_2O_3 by TMA and D_2O and 20 cycles Al_2O_3 (top in black) by TMA and ozone (bottom in red).

Then all spectra are referenced to the starting H/Si to shown the film contents, as in Fig 4.15. The strong and sharp mode centered at 931cm^{-1} shows the formation of continuous Al_2O_3 and is assigned to the Al_2O_3 LO mode according to the spectrum taken at 20° . Only a shoulder appears around 1060 cm^{-1} which is attributed to the interfacial Si-O, and it does not change after 5 cycles, implying it is mainly due to the interfacial Si-O-Al bond. No SiO_2 LO mode is observed up to 20 cycles. The Si- CH_3 survives after 20 cycles and is only partially changed to $\text{O}_x\text{-Si-CH}_3$ at 1270cm^{-1} . These evidences

confirm that Si-O amount is minimal. The featureless spectra in 1300-2100 cm^{-1} shows no detectable formate species inside the film consisting with our assumption of a different reaction pathway.

By comparing the spectrum with that of 10 cycles Al_2O_3 deposited by TMA and D_2O , as the inset of Fig 4.15, the Al-O and interfacial Si-O modes show similar intensity and shape. According to the intensity of Al-O phonon mode, the growth rate of the ozone based Al_2O_3 is about 1/2 of the water based case, which is in agreement with our ozone based HfO_2 deposition [41] and some studies have shown that the growth rate depends on the amount of ozone [42]. The film has similar quality for both water and ozone ALD but definitely ozone ALD has no trapped water inside the film.

4.3 HfO_2 deposition using TEMAH/ozone

Since HfO_2 has higher dielectric constant than Al_2O_3 and is being used in the industrial, it is necessary to study its deposition based on ozone for future applications. In the following section we will show the deposition HfO_2 on H/Si(100) and SiN_x .

HfO_2 deposited on H/Si(100) by TEMAH/ozone

20 cycles HfO_2 are deposited on H/Si(100) by TEMAH and ozone at 100°C, and for each precursor, saturation exposure time is used. The differential spectra are shown in Fig 4.16. After the first TEMAH dosing, the precursor is chemically adsorbed onto the surface, evidenced by the loss of Si-H stretching modes at 2000-2200 cm^{-1} , the loss of dihydride scissor mode at $\sim 912 \text{ cm}^{-1}$ and the appearance of ligand-related modes including the bands $\sim 1300\text{-}1600 \text{ cm}^{-1}$ and CH_x stretching modes at 2800-3000 cm^{-1} . Through the intensity of $\nu(\text{Si-H})$, it can be concluded that $\sim 17\%$ H is replaced by

TEMAH for the 1st TEMAH dosing. The low H loss is partly due to the bulky ligand which blocks the reaction sites. The formation of Hf-O-Si band centered at 940 cm⁻¹ suggests the precursor is partially hydrolyzed by the residue water as expected [43].

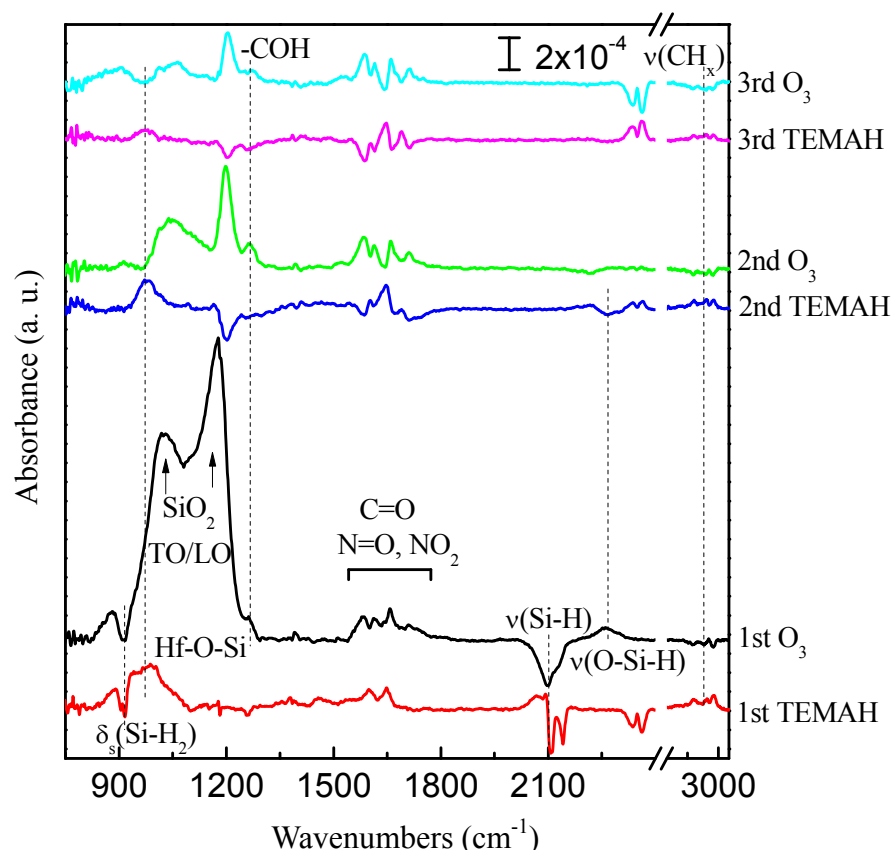


Fig 4.16 Differential FTIR spectra of 20 cycles TEMAH and ozone deposition on H/Si(100) at 100°C. Each spectrum is referenced to that of the surface subjected to the previous treatment. The 1st TEMAH is referenced to H/Si (IR incident angle $\sim 74^\circ$).

After the 1st ozone exposure, the Si-O TO/LO modes at 1025 cm⁻¹ and 1175 cm⁻¹ imply the forming of continuous SiO₂ and the thickness is about 6-7 Å according to the integrated area. Upon the ozone dosing, the further loss of v(Si-H) as well as the formation of O_x-Si-H at 2260 cm⁻¹ consolidates the surface oxidation. The new modes appear at 1500-1750 cm⁻¹ (at 1585, 1614, 1659, and 1710 cm⁻¹) are possibly attributed to the carbonyl/nitro derivatives such as C=O, -NO₂, N=O stretching and -NH bending

modes due to the ligand oxidation by ozone [4]. The band at $\sim 1270\text{ cm}^{-1}$ is tentatively assigned to C-O-H stretching mode [25]. Some studies do have shown that TEMAH/ozone reaction byproducts possibly include CO_2 , H_2O , CH_2O , and NO_2/NO by RGA [4]. The reaction is quite complicate and the detailed mechanism is not clear yet. The variation in the SiO_2 range ($900\text{--}1200\text{ cm}^{-1}$) for subsequent TEMAH/ozone pulses is due to the disruption of SiO_2 by the precursors.

The periodic gain and loss for the CH_x stretching modes at $2800\text{--}3000\text{ cm}^{-1}$ and the carbonyl/nitro derivatives' modes at $1500\text{--}1750\text{ cm}^{-1}$ as well as $\nu(\text{COH})$ at 1270 cm^{-1} , indicate the ALD ligand exchange and layer by layer deposition. In addition, the 2nd TEMAH dosing consumes the $\text{O}_x\text{-Si-H}$ (the loss at 2260 cm^{-1}) as the result that the ligand of TEMAH on the surface is partially removed by the previous ozone dosing so that some reaction sites under it are restored to react with TEMAH.

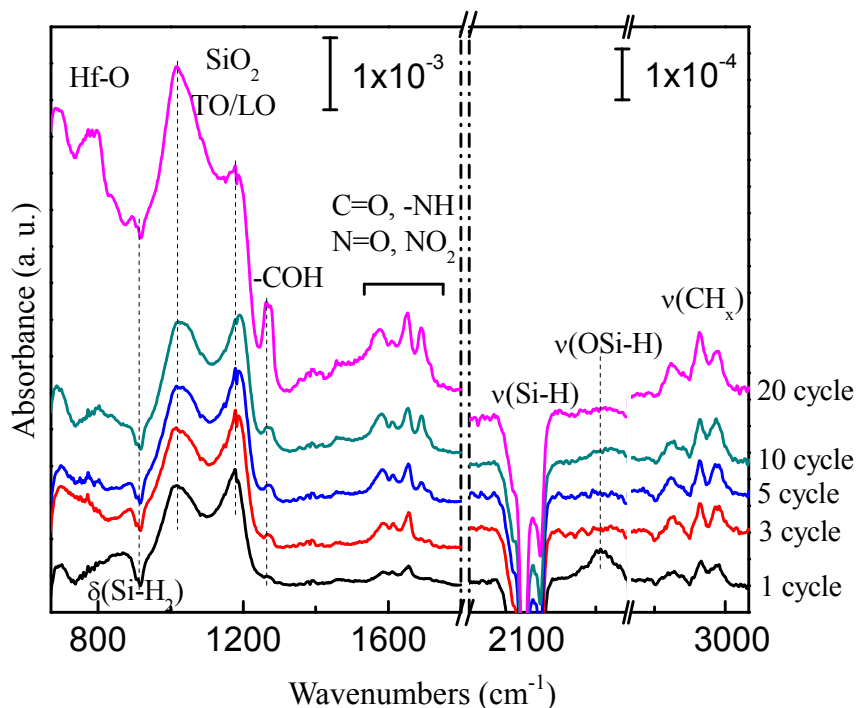


Fig 4.17 Absorption spectra of 20 cycles HfO_2 on and referenced to $\text{H}/\text{Si}(100)$ at 100°C (IR incident angle $\sim 74^\circ$). Substantial SiO_2 and carbon impurities are observed.

Then we reference all the spectra to H/Si(100) as Fig 4. 17. The very broad Hf-O band is observed at 700-900 cm^{-1} , showing the growth of HfO_2 . The SiO_2 increases with more cycles and is estimated to be ~ 1.5 nm for 20 cycles. The COH (1270 cm^{-1}), carbonyl/nitro derivatives (at 1585, 1614, 1659, and 1710 cm^{-1}) and CH_x (2800-3000 cm^{-1}) modes keep increasing with more ALD cycles, indicating the accumulation of impurities inside the film. Our study shows that these contaminants can be partially removed after the post-deposition annealing at a moderate temperature ($\sim 400^\circ\text{C}$) in N_2 without further substantial oxidation. However, higher temperature annealing results in much more oxide.

HfO₂ deposited on SiN_x by TEMAH/ozone

We have demonstrated that significant amount of SiO_2 forms for the ozone based deposition of HfO_2 on H/Si. Since SiN_x is a good barrier to prevent oxidation and has higher dielectric constant than SiO_2 , it motivates us to deposit HfO_2 on nitrided silicon.

Starting from H/Si(100) surface, we thermally anneal the surface in NH_3 at 600°C for 2min. The thickness of the nitride is about 6Å. Then 20 cycles HfO_2 are deposited on it at 100°C by TEMAH and ozone with saturation pulse length for each precursor. The differential spectra of HfO_2 on SiN_x are shown in Fig 4. 18. The inset of Fig 4.18 shows the SiN_x which is referenced to the H/Si(100) surface. The observed SiN_x TO/LO modes (800-1200 cm^{-1}) and the complete loss of Si-H stretching modes (2000-2200 cm^{-1}) indicate the surface is covered by continuous SiN_x layer. The mode at 1545 cm^{-1} is the $-\text{NH}_2$ scissor mode on nitride. The negative peak at 912 cm^{-1} is due to the dihydride scissor mode.

After the first TEMAH dosing, the precursor is chemically adsorbed onto the surface,

featured by the loss of NH_2 scissor mode at 1545 cm^{-1} , and the observation of ligand-related modes including the bands at $\sim 1300\text{--}1600\text{ cm}^{-1}$ and CH_x stretching modes at $2800\text{--}3000\text{ cm}^{-1}$. The band centered at 1020 cm^{-1} is assigned to Hf-O-SiN_x due the partially hydrolyzed TEMAH. Upon the 1st ozone exposure, Si-O mode is observed at 1108 cm^{-1} indicating the oxidation of SiN_x , and the thickness is less than 1 \AA according to the integrated area. No separate SiO_2 TO/LO modes are observed. The SiO_2 amount is much less than that on the H/Si case, so SiN_x successfully minimizes the interfacial SiO_2 .

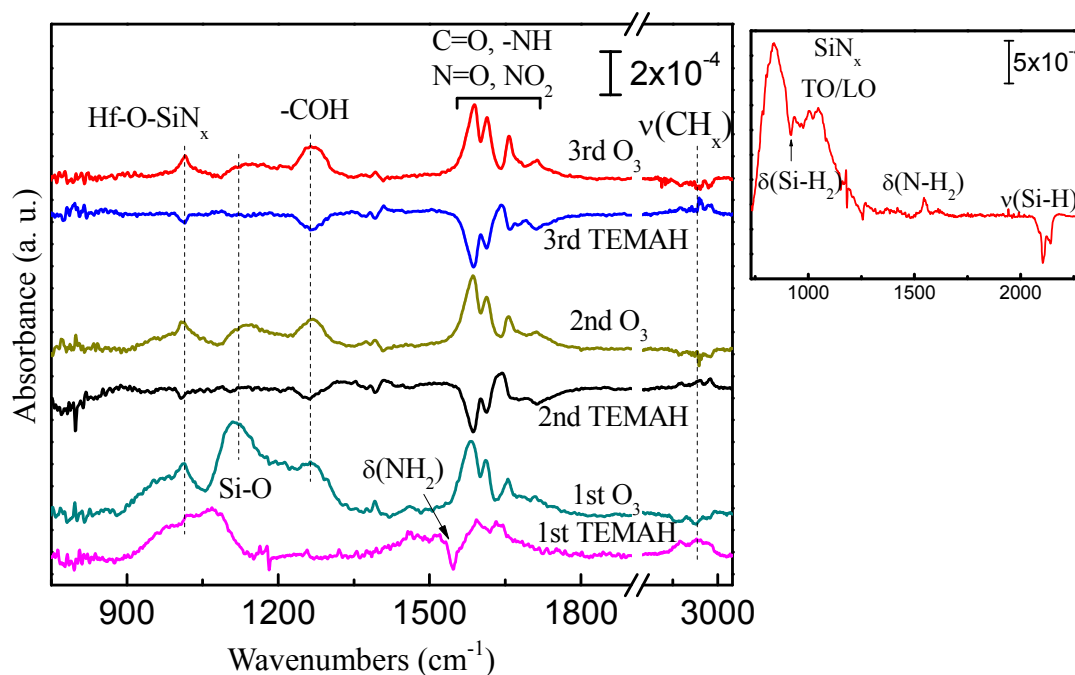


Fig 4.18 Differential FTIR spectra of 20 cycles TEMAH and ozone deposition on SiN_x at 100°C . Each spectrum is referenced to that of the surface subjected to the previous treatment. The 1st TEMAH is referenced to SiN_x (IR incident angle $\sim 74^\circ$). The inset is the spectrum of SiN_x which is referenced to the H/Si(100) surface.

On the other hand, the same bands are observed in Fig 4.18 showing the ligand oxidation by ozone, including the band at 1270 cm^{-1} assigned to $\text{v}(\text{COH})$, and the modes appearing at $1500\text{ cm}^{-1}\text{--}1750\text{ cm}^{-1}$ (1585 , 1614 , 1659 , and 1710 cm^{-1}) which are possibly attributed to the carbonyl/nitro derivatives. Again, the variation in the Si-O range

(900-1200 cm^{-1}) for subsequent TEMAH/ozone is due to the disruption of SiO_2 by precursors. The ALD ligand exchange is confirmed by the periodic gain and loss of the CH_x stretching modes at 2800-3000 cm^{-1} and the carbonyl/nitro derivatives' modes at 1500-1750 cm^{-1} as well as $\nu(\text{COH})$ at 1270 cm^{-1} , indicating and the layer by layer ALD growth.

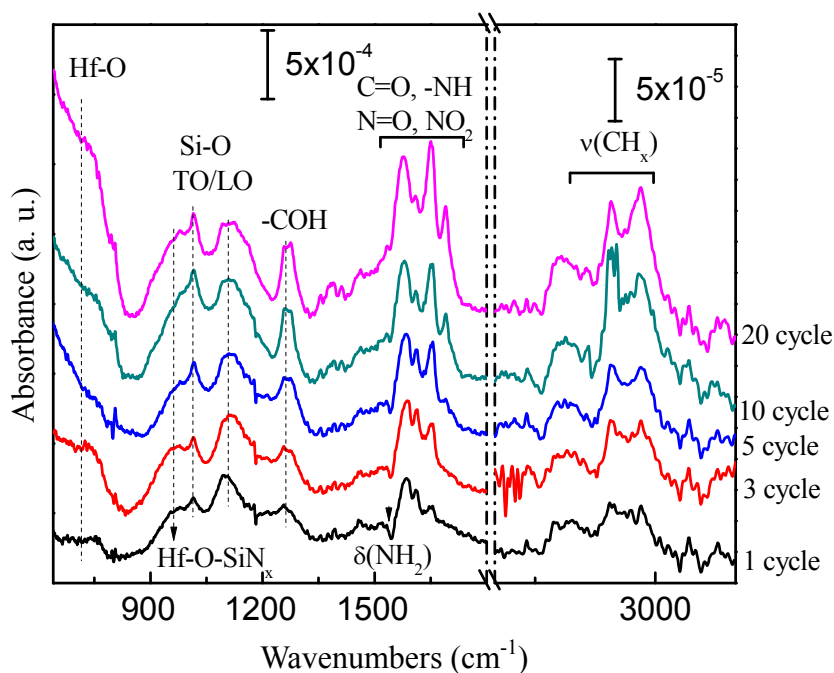


Fig 4.19 Absorption spectra of 20 cycles HfO_2 on SiN_x and referenced to $\text{SiN}_x(100)$ at 100°C (IR incident angle $\sim 74^\circ$). Less interfacial SiO_2 and same carbon impurities are observed in the spectra.

Similarly, we present all the spectra using SiN_x as the reference to show the species accumulated inside the film. The spectra are exhibited in Fig 4.19. With the increasing of cycle number, Hf-O phonon mode is observed at $\sim 680 \text{ cm}^{-1}$, indicating the formation of continuous HfO_2 . Our angle dependent IR measurement shows that it is more like Hf-O LO mode. Our RBS measurement determines the growth rate of ozone base HfO_2 deposition as $\sim 0.49 \text{ \AA}$ which is lower than that of water based deposition ($\sim 1.24 \text{ \AA}$).

The interfacial Si-O modes are observed at 1020 cm^{-1} and 1120 cm^{-1} and may partly

correspond to the Si oxynitride either. The integrated area shows that the thickness of this interfacial layer is only $\sim 3\text{-}4$ Å for 20 cycles which is close to 1 monolayer. It stops growing after 10 cycles indicating it is only an interfacial layer. The $\nu(\text{COH})$ at 1270 cm^{-1} , and the carbonyl/nitro derivatives at $1400\text{-}1750\text{ cm}^{-1}$ as well as the CH_x stretching modes at $2800\text{-}3000\text{ cm}^{-1}$, accumulate in the film due to the insufficient ligand removal by ozone.

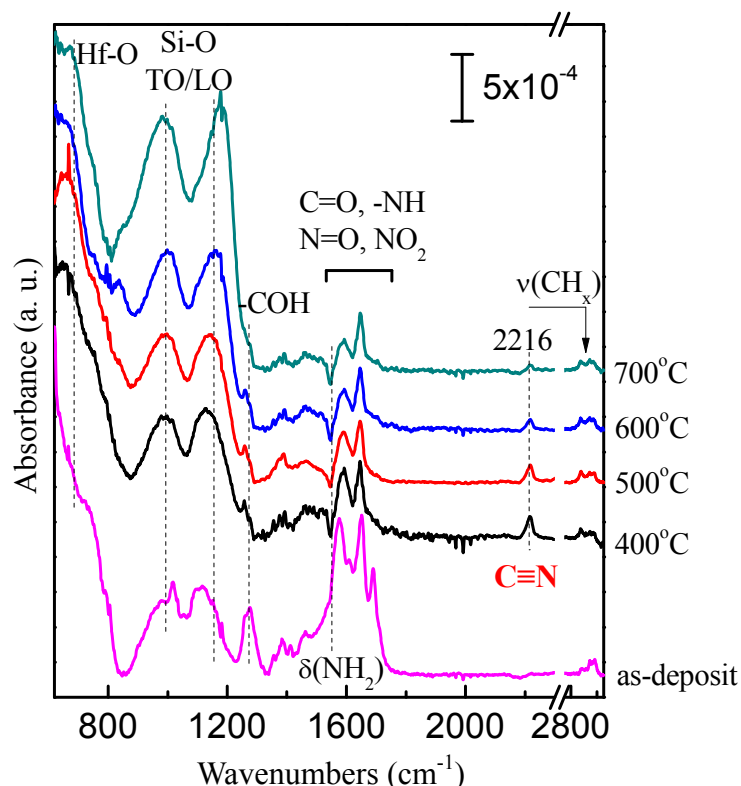


Fig 4.20 Absorption spectra show the annealing of 20 cycles HfO_2 on SiN_x referenced to SiN_x . The bottom spectrum is the as-deposit HfO_2 film. (IR incident angle $\sim 74^\circ$). The carbon impurities can be removed but with increased interfacial SiO_2 .

Post-annealing of the 20 cycles as-deposited HfO_2 film in N_2 (~ 0.4 torr) for 2min is performed. The results are shown in Fig 4.20 and referenced to SiN_x surface. The bottom spectrum shows the as-deposited film. At 400°C , the carbonyl/nitro derivatives are partially decomposed evidenced by the decreased intensity of the COH mode at 1270

cm^{-1} and the carbonyl/nitro derivatives at ($1400\text{-}1750\text{ cm}^{-1}$), and by the partial loss of CH_x stretching modes at $2800\text{-}3000\text{ cm}^{-1}$. However, the bands at 1593 cm^{-1} and 1646 cm^{-1} survive even after 700°C annealing, implying some impurities are strongly bonded in the HfO_2 . The increasing of Si-O TO/LO modes with the raised temperature is expected because of the environmental oxygen contamination and the oxygen from the decomposition of carbonyl/nitro derivatives. The blue shift of SiO_2 LO mode (1177 cm^{-1}) results from the increased SiO_2 amount, but it is still much lower than the typical value ($>1200\text{ cm}^{-1}$). It may indicate that it is not pure SiO_2 .

Interestingly, a new unexpected mode appears at 2217 cm^{-1} at 400°C and decreases upon 600°C annealing. It cannot be attributed to the Si-H stretching mode because our experiments have shown that Si-H nearly completely decomposes at 600°C . The likely assignment is $\nu(\text{C}\equiv\text{N})$ resulting from the rich N content due to the SiN_x layer. The carbon and nitrogen may rearrange and combine to form nitrile groups at $\sim 400^\circ\text{C}$ because of the oxygen consumption by SiN_x oxidation and the decomposition of the ligand-related impurities.

4.4 Summary

In this chapter, the ozone based ALD of Al_2O_3 and HfO_2 are investigated for the future application which can eliminate the trapped water/OH inside the film compared with water based deposition. However, more complicated reaction mechanism of ozone based ALD is found and substantial carbon impurities are incorporated during the deposition, which may affect the final film quality.

For the ozone based Al_2O_3 by TMA/ozone, the gas phase of TMA is first examined by *in situ* FTIR. The TMA in the ALD reactor shows little impurity due to hydrolysis and

is in large extent of dimer structure. Then D_2O is introduced to the reactor to study the gas phase reaction between TMA and D_2O . This reaction is straightforward and CH_4 , CD_4 are observed as the only byproducts. When ozone is introduced into the TMA gas, the reaction is much more complicated. Unexpectedly, C_2H_4 is not the only byproduct and the oxidation of the methyl terminal group/ $Al-O-CH_3$ may prevail which needs further study.

Al_2O_3 deposition with long and short ozone pulse length is studied on $H/Si(111)$ at $300^\circ C$. In the long pulse case, the cleavage of $Al-C$ bond to form formate is observed by two unexpected modes at 1400 cm^{-1} and 1600 cm^{-1} . With the aid of DFT calculation, the assignments of the new modes are confirmed. Substantial SiO_2 interfacial layer is observed in this case. As for the short ozone pulse case, little interfacial $Si-O$ is observed. The carbon impurities are trivial as well, indicating an improved film quality which is comparable to water based deposition. The growth rate is about 1/2 of that of water based deposition. In addition, no observation of formate species for the short ozone pulse case suggests a different reaction pathway. Thus, the reaction pathway depends on the ozone amount.

The ozone based HfO_2 ALD is performed on both $H/Si(100)$ and $600^\circ C$ -thermal- NH_3 nitrided $H/Si(100)$ surface at $100^\circ C$. On $H/Si(100)$ surface, ozone substantially oxidizes the surface. Carbonyl and nitro derivatives are observed as the impurities inside the film, which come from the strong oxidation of ligands by ozone. Then we deposit HfO_2 on SiN_x surface by ozone based ALD. The thin nitride ($\sim 6\text{\AA}$) successfully minimizes the formation of interfacial SiO_2 . However, the film still contains substantial carbonyl and nitro derivatives. The post-annealing experiment shows that a moderate temperature annealing at $\sim 400^\circ C$ can partially eliminate those impurities with

slightly increase of SiO₂ interfacial layer. Some impurities survive even after 700°C annealing. More interesting, an unexpected peak at 2217 cm⁻¹, which is possibly due to the formation of nitrile (-C≡N), is observed after 400°C annealing, indicating the reorganizing of the film contents. All suggest that the ozone based ALD is a much more complex system.

Bibliography

1. C. Musgrave and R. G. Gordon, *Precursors for atomic layer deposition of high-k dielectrics*, Future Fab International **18** (2005), 126-128.
2. J. B. Kim, D. R. Kwon, K. Chakrabarti and C. Lee, *Improvement in Al₂O₃ dielectric behavior by using ozone as an oxidant for the atomic layer deposition technique*, J. Appl. Phys. **92** (2002), 6739.
3. G. D. Wilk, R. M. Wallace and J. M. Anthony, *High-k gate dielectrics: Current status and materials properties considerations*, Journal of Applied Physics **89** (2001), 5243.
4. X. Liu, S. Ramanathan, A. Longdergan, A. Srivastava, E. Lee, T. E. Seidel, J. T. Barton, b. Dawen Pang and R. G. Gordonb, *ALD of hafnium oxide thin films from tetrakis(ethylmethylamino) hafnium and ozone*, J. Electrochem. Soc. (2005), 2005.
5. V. R. Rai and S. Agarwal, *Surface reaction mechanisms during ozone-based atomic layer deposition of titanium dioxide*, J. Phys. Chem. C **112** (2008), 9552.
6. J. Kima, K. Chakrabartia, J. Leeb, K.-Y. Ohc and C. Lee, *Effects of ozone as an oxygen source on the properties of the Al₂O₃ thin films prepared by atomic layer deposition*, Mat. Chem. Phys. **78** (2003), 733.
7. J. Hamalainen, M. Kemell, F. Munnik, U. Kreissig, M. Ritala and M. Leskela, *Atomic layer deposition of iridium oxide thin films from Ir(acac)₃ and ozone* Chem. Mat. **20** (2008), 2903.
8. D. H. Triyoso, R. Gregory, M. Park, K. Wang and S. I. Lee, *Physical and electrical properties of atomic-layer-deposited Hf_xZr_{1-x}O₂ with TEMAHF, TEMAZr, and ozone*, J. Electrochem. Soc. **155** (2008), H43.
9. M. Cho, H. B. Park, J. Park, S. W. Lee, C. S. Hwang, J. Jeong, H. S. Kang and Y. W. Kim, *Comparison of properties of an Al₂O₃ thin layers grown with remote O₂ plasma, H₂O, or O₃ as oxidants in an ald process for HfO₂ gate dielectrics*, J. Electrochem. Soc. **152** (2005), F49.
10. S. K. Kim, S. W. Lee, C. S. Hwang, Y.-S. Min, J. Y. Won and J. Jeong, *Low temperature (<100°C) deposition of aluminum oxide thin films by ALD with O₃ as oxidant*, J. Electrochem. Soc. **153** (2006), F69.
11. S. Kamiyama, T. Miura and Y. Nara, *Electrical properties of ultrathin HfO₂ films for replacement metal gate transistors, fabricated by atomic layer deposition using TEMA*

- and O_3 , Appl. Phys. Lett. **87** (2005), 132904.
12. M. Juppo, P. Alén, M. Ritala and M. Leskelä, *Trimethylaluminum as a reducing agent in the atomic layer deposition of $Ti(Al)_n$ thin films*, Chemical Vapor Deposition **7** (2001), 211.
 13. A. Demchuk, S. Simpson and B. Koplitz, *Exploration of the laser-assisted clustering and reactivity of trimethylaluminum with and without NH_3* , J. Phys. Chem. A **107** (2003), 1727.
 14. H. M. Manasevit, *The use of metal-organics in the preparation of semiconductor materials*, J. Electrochem. Soc. **118** (1971), 647.
 15. R. Anwender, C. Palm, O. Groeger and G. Engelhardt, *Formation of Lewis acidic support materials via chemisorption of trimethylaluminum on mesoporous silicate MCM-41* Organometallics **17** (1998), 2027.
 16. J. Schmidt, T. Risse, H. Hamann and H.-J. Freund, *Characterization of a model ziegler-natta catalyst for ethylene polymerization*, J. Chem. Phys. **116** (2002), 10861.
 17. S. Balasubramanian, C. J. Mundy and M. L. Klein, *Trimethylaluminum: A computer study of the condensed phases and the gas dimer*, J. Phys. Chem. B **102** (1998), 10136.
 18. J. Tanaka and S. R. Smith, *Mass spectra of bridge-bonded aluminum compounds*, Inorganic Chemistry **8** (1968), 265.
 19. A. W. Laubengayer and W. F. Gilliam, *The alkyls of the third-group elements. I. Vapor-phase studies of the alkyls of aluminum, gallium and indium*, J. Am. Chem. Soc. **63** (1941), 477.
 20. T. Shinzawa¹, F. Uesugi, I. Nishiyama, K. Sugai¹, S. Kishida and H. Okabayashi, *New molecular compound precursor for aluminum chemical vapor deposition*, Appl. Organometal. Chem. **14** (2000), 14.
 21. B. G. Willis and K. F. Jensen, *An evaluation of density functional theory and ab initio predictions for bridge-bonded aluminum compounds*, J. Phys. Chem. A **102** (1998), 2613.
 22. R. J. O'Brien and G. A. Ozin, *A gas-phase Raman study of trimethylaluminum and trimethylboron monomers*, J. Chem. Soc. A (1971), 1136.
 23. C. Soto, R. Wu, D. W. Bennett and W. T. Tysoe, *Infrared spectroscopy of trimethylaluminum and dimethylaluminum chloride adsorbed on alumina*, Chem. Mat. **6** (1994), 1705.
 24. M. Sugiyama, H. Itoh, J. Aoyama, H. Komiyama and Y. Shimogaki, *Reaction analysis of aluminum chemical vapor deposition from dimethyl-aluminum-hydride using tubular reactor and Fourier-transform infrared spectroscopy: Theoretical process optimization procedure (I)*, Jpn. J. Appl Phys. **39** (2000), 1074.
 25. G. Socrates, *Infrared and Raman characteristic group frequencies*, 3rd edition, John Wiley & Sons (2006).
 26. S. D. Elliott, G. Scarel, C. Wiemer, M. Fanciulli and G. Pavia, *Ozone-based atomic layer deposition of alumina from TMA: Growth, morphology, and reaction mechanism*, Chem. Mater. **18** (2006), 3764.
 27. R. L. Puurunen, *Growth per cycle in atomic layer deposition: Real application*

- examples of a theoretical model*, Chemical Vapor Deposition **9** (2003), 327.
28. M. M. Frank, Y. J. Chabal and G. D. Wilk, *Nucleation and interface formation mechanisms in atomic layer deposition of gate oxides*, Appl. Phys. Lett. **82** (2003), 4758.
 29. M. D. Halls, K. Raghavachari, M. M. Frank and Y. J. Chabal, *Atomic layer deposition of Al_2O_3 on H-passivated Si: $Al(CH_3)_2OH$ surface reactions with $H/Si(100)-2 \times 1$* , Phys. Rev. B **68** (2003), 161302.
 30. J. Kwon, M. Dai, M. D. Halls and Y. J. Chabal, *Detection of a formate surface intermediate in the atomic layer deposition of high- κ dielectrics using ozone*, Chem. Mat. **20** (2008), 3248.
 31. V. Boiadjev and W. T. Tysoe, *Infrared study of the surface species formed by sequential chemical vapor deposition of trimethylaluminum and methanol on a hydroxylated alumina surface* Chem. Mat. **10** (1998), 334.
 32. D. N. Goldstein and S. M. George, *Conference program of the 6th international conference on atomic layer deposition*, Seoul, South Korea; American Vacuum Society: New York (2006).
 33. G. A. M. Hussein and N. Sheppard, *Infrared spectroscopic studies of the reactions of alcohols over group IVB metal oxide catalysts*, J. Chem. Soc. Faraday Trans. **87** (1991), 2655.
 34. B. Delley, *From molecules to solids with the Dmol3 approach*, J. Chem. Phys. **113** (2000), 7756.
 35. J. P. Perdew, K. Burke and M. Ernzerhof, *Generalized gradient approximation made simple*, Phys. Rev. Lett. **77** (1996), 3865.
 36. G. Precht, A. Kersch, G. S. Icking-Konert, W. Jacobs, T. Hecht, H. Boubekeur and U. Schröder, *A model for Al_2O_3 ALD conformity and deposition rate from oxygen precursor reactivity*, IEEE Int. Electron Devices **9** (2003), 9.6.1.
 37. K. T. Queeney, N. Herbots, J. M. Shaw, V. Atluri and Y. J. Chabal, *Infrared spectroscopic analysis of an ordered Si/SiO₂ interface*, Appl. Phys. Lett. **84** (2004), 493.
 38. D. N. Goldstein, J. A. McCormick and S. M. George, *Al_2O_3 atomic layer deposition using trimethylaluminum and ozone studied by in situ transmission FTIR spectroscopy and quadrupole mass spectrometry*, J. Phys. Chem. C (2008).
 39. G. P. Shulman, M. Trusty and J. H. Vickers, *Thermal decomposition of aluminum alkoxides*, J. Org. Chem. **28** (1963), no. 4, 907-910.
 40. J. A. Aboaf, *Deposition and properties of aluminum oxide obtained by pyrolytic decomposition of an aluminum alkoxide*, Journal of The Electrochemical Society **114** (1967), no. 9, 948-952.
 41. Y. Wang, M. Dai, M.-T. Ho, L. S. Wielunski and Y. J. Chabal, *Infrared characterization of hafnium oxide grown by atomic layer deposition using ozone as the oxygen precursor*, Appl. Phys. Lett. **90** (2007), 022906.
 42. J. Kima, K. Chakrabartia, J. Leeb, K.-Y. Ohc and C. Lee, *Effects of ozone as an oxygen source on the properties of the Al_2O_3 thin films prepared by atomic layer deposition*, Mat. Chem. Phys. **78** (2003), 733.

43. M.-T. Ho, Y. Wang, R. T. Brewer, L. S. Wielunski and Y. J. Chabal, *In situ infrared spectroscopy of hafnium oxide growth on hydrogen-terminated silicon surfaces by atomic layer deposition*, Appl. Phys. Lett. 87 (2005), 133103.

Chapter 5: La_2O_3 and $\text{La}_x\text{Al}_y\text{O}$ Growth on H/Si by ALD

Lanthanum oxide (La_2O_3) is widely used in industry and laboratory. It has been used to make optical glasses to improve the refractive index and chemical durability [1, 2, 3]. It can also be used to develop ferroelectric materials [4, 5]. Since La_2O_3 has the largest band gap among the rare earth oxides (~ 4.3 eV) with the lowest lattice energy, very high dielectric constant (~ 27) and good thermal stability on Si [6, 7, 8], it is also a candidate to replace SiO_2 as an insulator material [6, 9, 10]. La_2O_3 films can be obtained by many different methods, such as chemical vapor deposition, thermal oxidation, sputtering, and so on [1, 2, 3, 11, 12, 13].

Due to its great advantages equivalent to or over other methods such as uniformity and high quality, ALD is being used to deposit La_2O_3 as well. In the following part of this chapter, we will study the ALD of La_2O_3 film by using a brand new precursor [14], lanthanum tris (N,N'- diisopropylacetamidinate) [$\text{La}(\text{}^i\text{Pr-MeAMD})_3$] and heavy water (D_2O). The precursor ALD temperature window, reaction mechanism and film quality will be investigated. The deposition of lanthanum aluminate film on H/Si will be studied also.

5.1 Lanthanum precursor gas phase

$\text{La}(\text{}^i\text{Pr-MeAMD})_3$ precursor has high volatility ($80^\circ\text{C}/0.04$ torr) among most of known lanthanum precursors [15], and has been successfully demonstrated for ALD [16]. The chemical structure of $\text{La}(\text{}^i\text{Pr-MeAMD})_3$ precursor is shown in Fig. 5.1 with its ball-stick three dimensional view. It is thermally stable enough and the metal-N bond has low bond strength compared with metal-Cl and metal-O bonds to make it highly reactive with water [14, 17]. On the other hand, the metal-N bond causes fewer impurities than the

metal-C bond during the deposition. Thus, it is a suitable precursor for ALD. To have as high as possible vapor pressure for ALD, the precursor is kept at $\sim 130^\circ\text{C}$ for all experiments. Purified N_2 (oxygen impurity $<10^{-6}$ ppm) is used as the carrying gas to deliver more precursor to the ALD reactor.

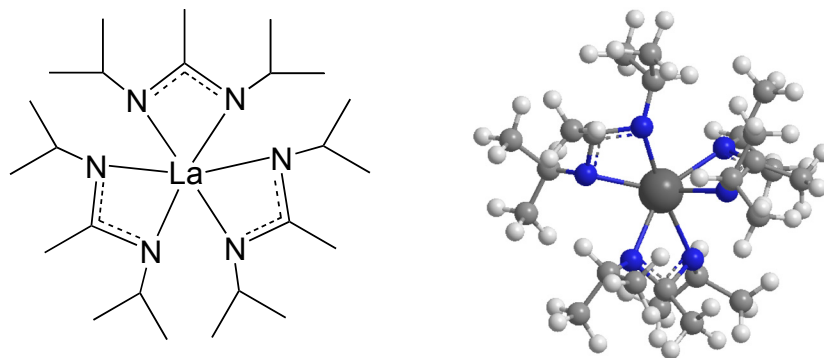


Fig 5.1 Chemical structure of $\text{La}(\text{iPr-MeAMD})_3$ precursor and its ball-stick three dimensional view used to deposit La_2O_3

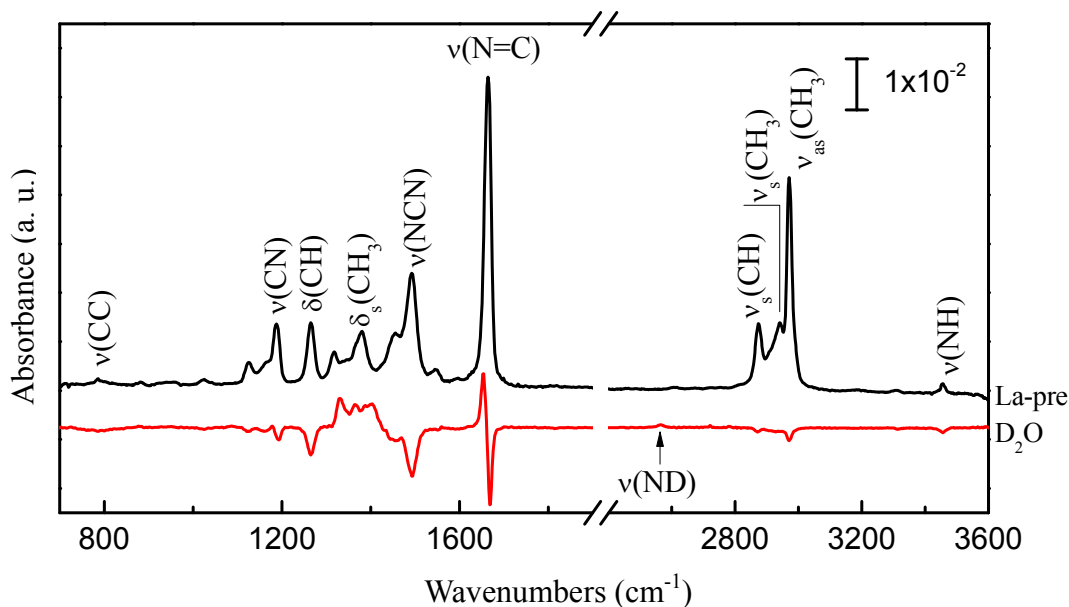


Fig 5.2 FTIR absorption spectrum of gas phase $\text{La}(\text{iPr-MeAMD})_3$ (top in black) referenced to vacuum and the spectrum after exposed to D_2O (bottom in red) referenced to the La precursor showing the gas phase reaction.

Before the ALD of La_2O_3 , the precursor gas phase is first examined to know the

status of the precursor in our chamber before its reaction with the surface, which is crucial for any ALD application. The spectrum on the top (in black) of Fig 5.2 shows the IR absorption spectrum of the La precursor gas phase in our ALD reactor which is reference to vacuum. As in Fig 5.2, all the features associated with the organic -NCN- ligand of the La precursor is observed such as the hydrocarbon bending/stretching modes and the -NCN- stretching mode as well as the C-C stretching mode.

Table 5.1 Calculated PBE/DNP wavenumbers and mode assignments corresponding to the observed infrared (IR) bands based on calculations for the intact La precursor (LaL_3) and the free ligand HL/DL (H-Ligand/D-Ligand).

Observed IR (cm^{-1})	Calculated ^a (cm^{-1})	Species	Assignment
3456/2564	3464/2534	HL/DL	NH(ND) str
2968	3110 (3033)	HL(LaL_3)	CH_3 asym str
2942	2950	LaL_3	CH_3 sym str
2874	2970 (2876)	HL(LaL_3)	CH str
1665/1659	1636/1625	HL/DL	C=N str
1492	1517	LaL_3	NCN str + CH_3 scissor def
1450	1473	LaL_3	NCN str + CH_3 scissor def
1381	1377	HL(LaL_3)	CH_3 umbrella + CH bend
1317	1355	LaL_3	CH wag
1265	1304	LaL_3	CH bend
1188	1185 (1193)	HL(LaL_3)	CN str + CH_3 rock
1126	1159	LaL_3	CH_3 rock + NCN str
1022	1047	LaL_3	CH_3 rock + NCN bend
786	774	LaL_3	CC str

^a PBE/DNP calculated harmonic frequencies. (str-stretching, def-deformation)

The detailed assignments of those key modes are listed in table 5.1. First-principle calculations based on density functional theory (DFT) are carried out to aid in the interpretation of IR features of the intact La precursor with three amidinate ligands (LaL_3) and of an isolated amidine (a hydrogenated ligand, HL), where L represents a ligand (done by Dr. Mathew Halls). Calculations are carried out using the gradient-corrected

PBE functional [18] as implemented in the *DMol3* package [19]. A numerical atomic basis set of double- ζ quality, augmented with additional polarization functions (DNP) with a real-space cutoff of 5.8 Å is employed. For La the core electrons are represented with an effective relativistic semi-core pseudopotential (PSPP) along with the DNP basis for valence electrons [20]. The convergence criteria for structural optimizations are 1.0×10^{-7} au and 1.0×10^{-5} au/Å for energy and gradient, respectively

Note that in the IR spectrum of the La precursor gas phase, the strong mode at 1665 cm^{-1} and the weak mode at 3456 cm^{-1} are assigned to $\nu(\text{C}=\text{N})$ and $\nu(\text{N}-\text{H})$ in the hydrogenated ligand H-Ligand, respectively. However, they are not part of the intact precursor. When the chelated ligand of the precursor is intact, the π -electrons within the bond of the N-C-N linkage are delocalized, leading to a mode at 1492 cm^{-1} . When the precursor is hydrolyzed to form the localized C=N in the HN-C=N bond, the band at 1492 cm^{-1} will be shifted to 1665 cm^{-1} (calc. 1636 cm^{-1}) with the stretching mode of N-H at 3456 cm^{-1} . In addition, our real-time mass spectroscopy of the ALD reactor confirms that a gas phase molecule with atomic mass 142 is observed, which corresponds to the HL species. Since HL is non-reactive, it remains in the gas phase and is preferentially detected by mass spectroscopy. It also does not affect film growth during the ALD process which we will show later.

To further prove this process and study the preliminary of ALD reaction mechanism, D_2O is introduced into the chamber with La precursor to investigate the gas phase reaction. In Fig 5.2, the spectrum at the bottom (in red) shows the spectral changes (referenced to La precursor) occurring after the lanthanum precursor is exposed to water (D_2O). Most of the methyl-related bands of the $\text{La}(\text{Pr-MeAMD})_3$ precursor lose their intensity, and some new bands are observed between 1300 and 1430 cm^{-1} after the D_2O

exposure. The N-H stretching at 3456 cm^{-1} is shifted to 2564 cm^{-1} due to isotope replacement (N-D), predicted by DFT at 3464 cm^{-1} and 2534 cm^{-1} , respectively. The isotope effect is also evident for the C=N stretching of N-C=N from HL to DL as the band shifts from 1665 cm^{-1} to 1659 cm^{-1} . Calculations show a corresponding redshift of $\sim 11\text{ cm}^{-1}$ due to the H/D exchange. These suggest the precursor reacts with D_2O so that the -NCN- ligand bonded to the precursor is detached to form the free ligand as DL molecule containing N-D and C=N bonds.

Thus it can be concluded that the precursor is partially hydrolyzed in the chamber before reacting with the surface. This precursor is very sensitive to the water as expected. In the following part of this chapter, we will study the precursor behavior on hydrogen terminated Si(111) surface.

5.2 ALD of La_2O_3 on H/Si(111) surface

To investigate the interaction of the precursor with the surface, H/Si(111) is used to deposit La_2O_3 by $\text{La}(\text{}^i\text{Pr-MeAMD})_3$ and D_2O . Saturation pulse length is used for each precursor dosing and the IR incident angle is $\sim 74^\circ$. Two deposition temperatures are used to study the temperature dependence including 200°C and 300°C .

Deposition at 200°C

The deposition of 20 cycles La_2O_3 on H/Si(111) at 200°C is studied first. Fig 5.3 shows the spectrum of 1st La precursor exposed to H/Si(111). The decrease of Si-H stretch intensity at 2083 cm^{-1} indicates that the $\text{La}(\text{}^i\text{Pr-MeAMD})_3$ precursor readily reacts with the atomically flat H/Si(111) surface. The first $\text{La}(\text{}^i\text{Pr-MeAMD})_3$ pulse consumes about 40% of surface hydrogen, and more than 80 % of surface H by the end of the 5th

cycle, as presented in Fig 5.4(a) which shows the loss of Si-H for the first 3 cycles deposition (all spectra are referenced to the oxide). Most of this reaction results from the La precursor attacking rather than D₂O. Rutherford backscattering (RBS) measurements show $\sim 3 \times 10^{14} \text{ cm}^{-2}$ La atoms are on the surface after the first ALD cycle, corresponding to $\sim 40\%$ of H density on H/Si(111) ($7.8 \times 10^{14} \text{ cm}^{-2}$). This indicates a one-to-one interaction. That is, after the precursor dosing, each La atom is bonded to one Si by replacing the Si-H. Ideally, the reaction should follow this mechanism:

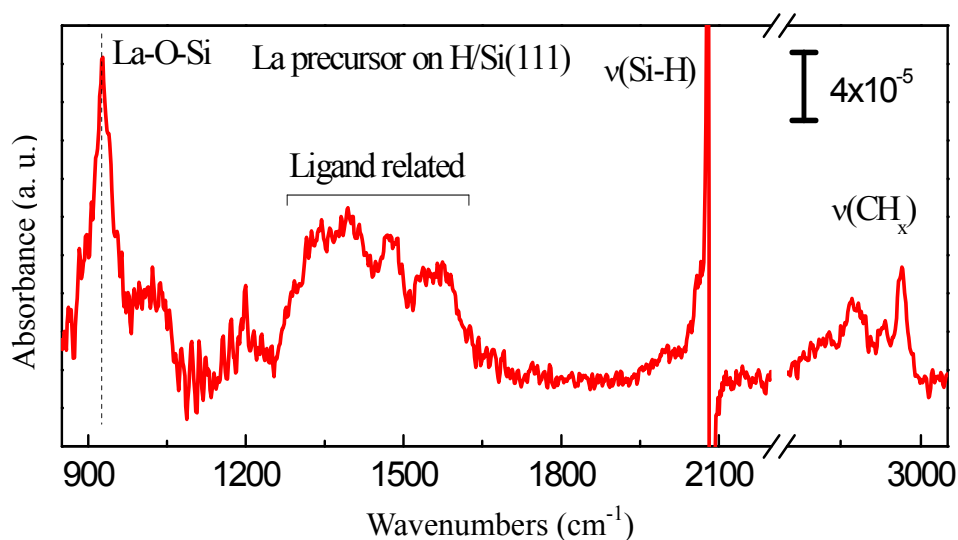
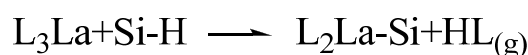


Fig 5.3 FTIR absorption spectrum of 1st La(*i*Pr-MeAMD)₃ on and referenced to H/Si(111) at 200°C. The La-O-Si species and ligand related features are observed at 928 cm⁻¹, 1400-1600 cm⁻¹ and 2800-3000 cm⁻¹. Hydrogenated ligand is not reactive.

However, the mode at 928 cm⁻¹ which is due to the bond of La-O-Si results from the partially hydrolyzed precursor as we have discussed for precursor gas phase [21]. It suggests the coexistence of both La-Si and La-O-Si. Since the Si-La stretching band is below our accessible spectrum range, it is impossible to determine how much of the reaction with the surface is due to the partially hydrolyzed precursor. No observation of

the C=N mode at 1665 cm^{-1} confirms that the free ligand (HL) is volatile and will not affect our ALD deposition. The broad band around $1300\text{-}1600\text{ cm}^{-1}$ is attributed to the surface amidinate ligand, and the band at $2800\text{-}3000\text{ cm}^{-1}$ is due to $\nu(\text{CH}_x)$. Fig 5.4(b) shows the differential spectra of the first 3 cycles $\text{La}(\text{}^i\text{Pr-MeAMD})_3$ and D_2O in order to present the change after each treatment. The periodic intensity gain and loss of the CH_x stretching modes at $2800\text{-}3000\text{ cm}^{-1}$ is due to the ALD ligand exchange. After each La precursor dosing the ligand is added on the surface and after each D_2O exposure, the ligand is hydrolyzed. The enhanced intensity for later cycles may indicate a short incubation period.

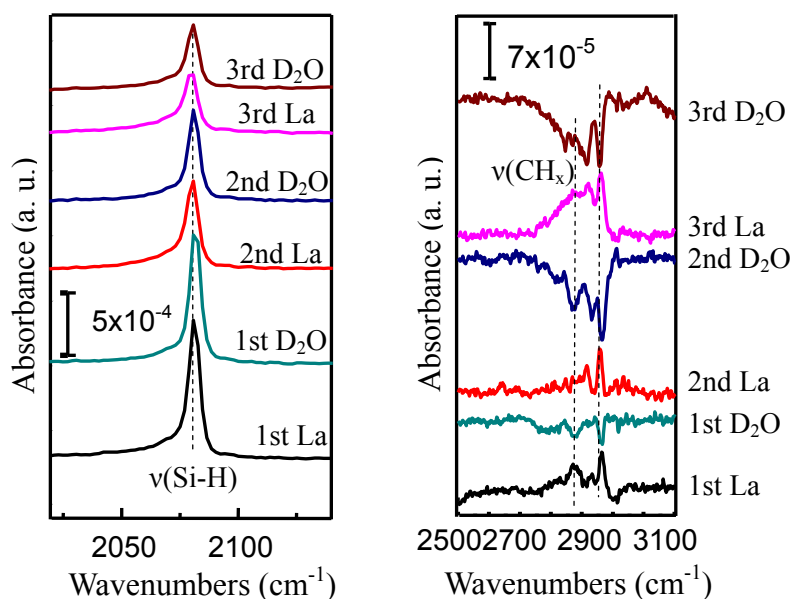


Fig 5.4 (a) Absorption spectra of first 3 cycles $\text{La}(\text{}^i\text{Pr-MeAMD})_3 + \text{D}_2\text{O}$ on $\text{H/Si}(111)$ referenced to oxide; (b) Difference spectra of first 3 cycles $\text{La}(\text{}^i\text{Pr-MeAMD})_3 + \text{D}_2\text{O}$ on $\text{H/Si}(111)$, where each spectrum is referenced to the previous spectrum and the 1st La is referenced to $\text{H/Si}(111)$.

For the subsequent cycles, we reference the spectra to $\text{H/Si}(111)$ surface to show the evolution of La_2O_3 film. The spectra are presented in Fig 5.5. With more ALD cycles, the La_2O_3 phonon modes are observed at $450\text{-}540\text{ cm}^{-1}$ [3, 13]. The broad bands at $800\text{-}1200$

cm^{-1} are assigned to the Si-O stretching modes of lanthanum silicate [22]. The spectral results of normal incidence (electric field parallel to the interface) indicate that the modes at 985 and 1170 cm^{-1} are LO modes which are polarized perpendicular to the surface. All suggests the formation of a thin lanthanum silicate in addition to the Si-O-La interfacial layer during the ALD of La_2O_3 .

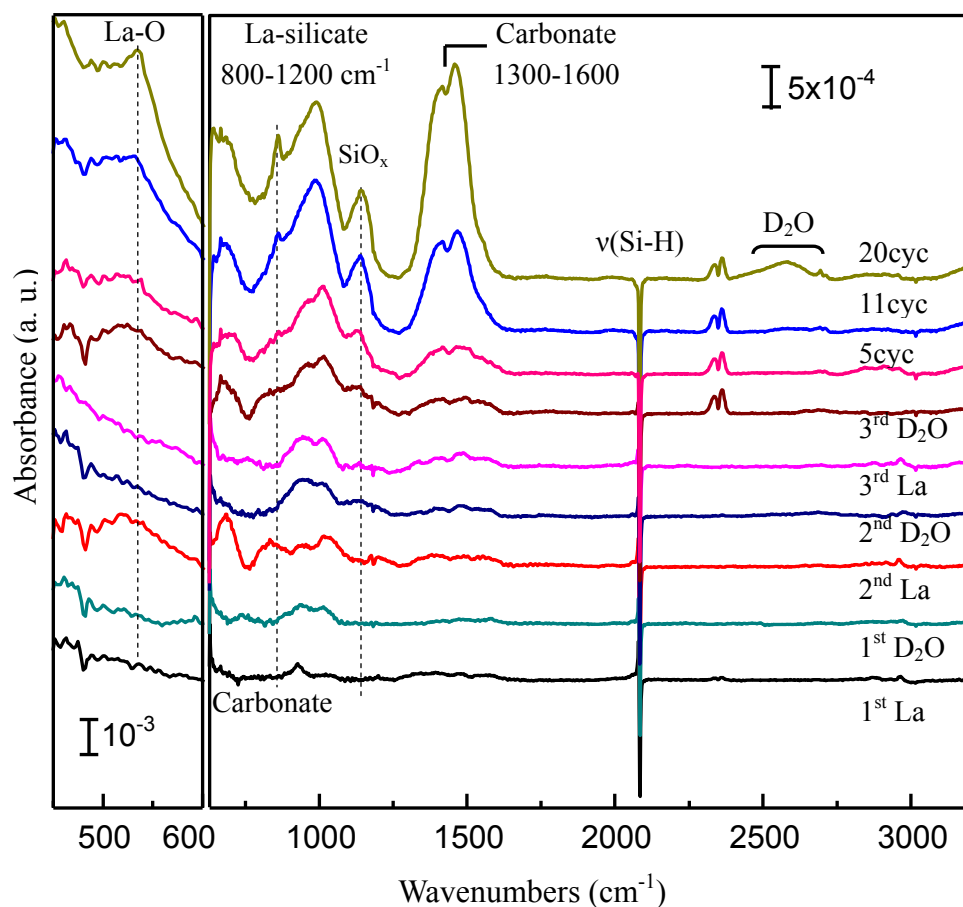
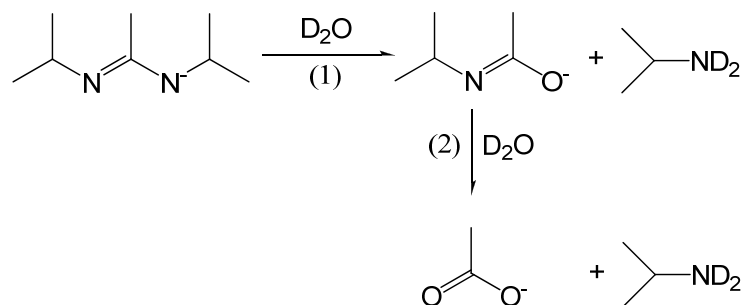


Fig 5.5 FTIR absorption spectra of 20 cycles of La precursor and D_2O on H/Si(111) at 200°C. All spectra are referenced to H/Si(111). Substantial carbonated impurities, interfacial SiO_2 and trapped water are observed.

Besides, carbonate and D_2O are detected in the films evidenced by the broad bands at 1300-1600 cm^{-1} and 2400-2700 cm^{-1} , respectively. The doublet centered at 1460 cm^{-1} , 1415 cm^{-1} together with the band at 860 cm^{-1} are due to carbonate species [23]. It is

known that La_2O_3 can react with ambient CO_2 , resulting in carbonate species [2, 12, 24, 25, 26, 27, 28]. However, since all our ALD process is performed *in situ* in vacuum chamber with N_2 , the observed carbonate present in the film must originate from intrinsic surface reactions. It is likely that lanthanum carbonate is produced through the thermal decomposition of lanthanum acetate. There is in fact possible evidence of some acetate species present on the surface, characterized by the broad bands at $600\text{-}700\text{ cm}^{-1}$ and $2800\text{-}3000\text{ cm}^{-1}$ [29]. The areas under these bands (and the bands between 1300 and 1600 cm^{-1}) grow almost linearly with the number of ALD cycles.

As in Fig 5.6(a), the differential spectra for each half-cycle clearly shows that the intensity of these vibrational modes increases after D_2O pulses rather than after $\text{La}(\text{iPr-MeAMD})_3$ pulses. It suggests that these carbonate bands arise from reactions between D_2O and the remaining amidinate ligand. The possible reaction scheme is described by the following two steps:



Some of the resulting acetate ions are likely to remain in the film as impurities because the lanthanum acetate bond is roughly as strong as a lanthanum-hydroxyl bond. Thus there is little thermodynamic driving force to hydrolyze the acetate ions to acetic acid, which would vaporize off the surface. And then part of lanthanum acetate is thermally decomposed into lanthanum carbonate as the observed strong doublet centered at 1460

cm^{-1} and 1415 cm^{-1} as well as the band at 860 cm^{-1} .

After the deposition, *in situ* post-deposition annealing in N_2 for 5 min from $400\text{--}800^\circ\text{C}$ is performed. The spectral results are shown in Fig 5.6(b) where the spectra are referenced to H/Si and the bottom spectrum is the 20 cycles La_2O_3 as-deposit film. At 500°C , the carbonate species are almost completely removed as evidenced by the loss of carbonate broad bands at $1300\text{--}1600\text{cm}^{-1}$. However, the resulted excessive oxygen from the decomposition of carbonate species and trapped D_2O in La_2O_3 cause the oxidation [30] of Si interface featured by the broad peaks at $900\text{--}1200 \text{ cm}^{-1}$ (TO/LO modes of SiO_2 [31]).

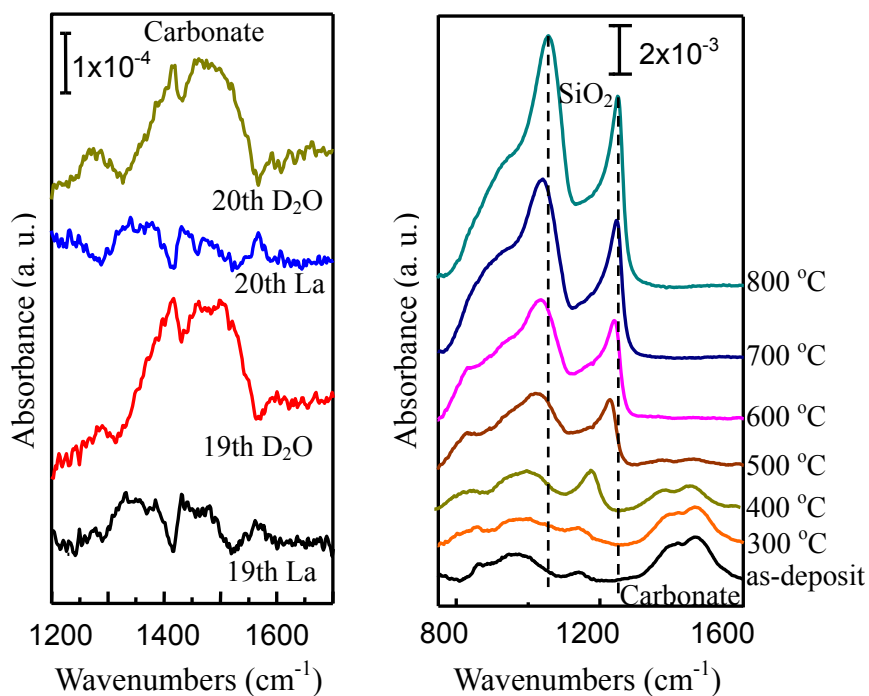


Fig 5.6 (a) Differential spectra of 19th cycle and 20th cycle La_2O_3 deposition in the carbonate range; (b) the absorption spectra showing the post annealing of 20 cycles La_2O_3 in N_2 which are reference to the H/Si(111). The spectra shows ALD ligand exchange and removal of carbonate species.

Deposition at 300°C

The above experiments show that at 200°C the deposited film contains substantial amount of impurities including acetate/carbonate and D₂O. These impurities can be substantially reduced by thermal annealing at a moderate temperature ($\leq 400^\circ\text{C}$) without much increasing the interfacial SiO₂ layer. So a higher deposition temperature, 300°C is used to deposit La₂O₃ with the same condition as 200°C. The results are presented in Fig 5.7.

As in Fig 5.7, at 300°C, the intensities of bands at 1300-1600 cm⁻¹ and 2800-3000 cm⁻¹ for acetate/carbonate, and at 2400-2700 cm⁻¹ for D₂O are suppressed substantially. According to the drastic loss of Si-H stretching mode at 2083 cm⁻¹, Si-H reacts with surface hydrogen very strongly at 300 °C, where almost all Si-H bonds are consumed in 5 ALD cycles. And with more ALD cycles, the observed La₂O₃ phonon modes at 450-540 cm⁻¹ confirm the formation of La₂O₃ layer. Although the amount of interfacial SiO₂ is increased compared to the deposition at 200°C (~ 100% increase), the total amount of that interfacial layer is estimated to be ~ 3 Å according to the integrated area of SiO₂. These observations suggest that 300°C is a better deposition temperature for La₂O₃ growth.

Note that in Fig 5.7 there are two new features at 1990 and 2110 cm⁻¹ observed during the deposition at 300°C. As in Fig 5.8 (differential spectra of the first 3 cycles), their intensities are increased after each La precursor pulse, and then dramatically reduced after each D₂O pulse. Although the frequencies of these two bands are within the range of Si-H stretching mode, but their integrated areas are much greater than that of the initial Si-H stretching mode. Since only C, N, H, D, and O are involved in the film, their origin is very likely related to C and N. They can be either assigned to stretching vibration of the triple bond (C≡N) in the cyanamide (N-C≡N)²⁻, or to the double bond (C=N) in the carbodiimide (N=C=N)²⁻ [32, 33].

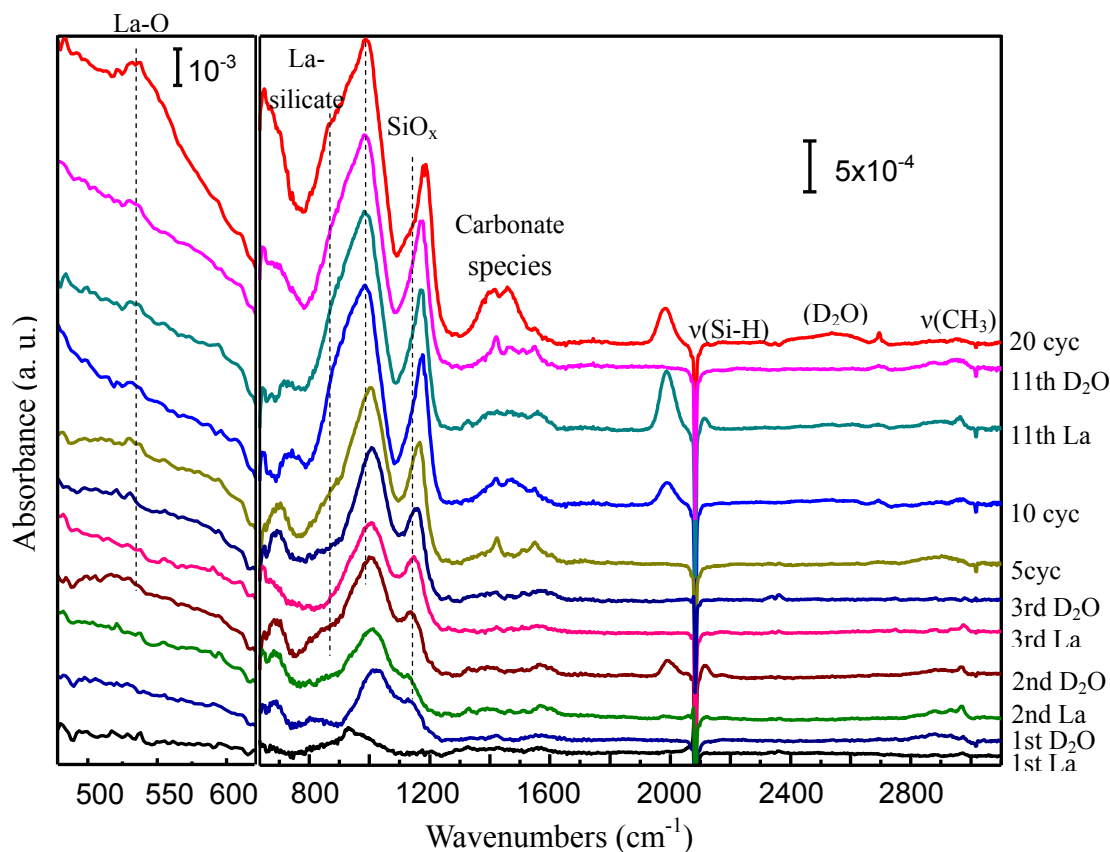


Fig 5.7 FTIR absorption spectra of 20 cycles of La precursor and D₂O on H/Si(111) at 300°C. All spectra are referenced to H/Si(111). Less carbonated species and less D₂O are observed. But the interfacial SiO₂ increases substantially.

The formation of the cyanamide (or carbodiimide) species on the surface may be attributed to precursor ligand decomposition at 300°C and probably through β - or δ -hydrogen transfer within the ligand. Fig 5.9 shows the possible decomposition pathways from intact ligand to cyanamide. β -hydrogen transfers to form NH bonds in the ligand and propene (C₃H₆) is produced as a gas phase byproduct. N \equiv C triple bonds are produced through the second β -hydrogen transfer with methane (CH₄) as a gas phase byproduct. This N \equiv C triple bond can also be formed directly through δ -hydrogen transfers from the intact ligand on the surface. Finally cyanamide is formed through additional β -hydrogen transfers with propene as a byproduct which is pumped off without

further interaction with the surface.

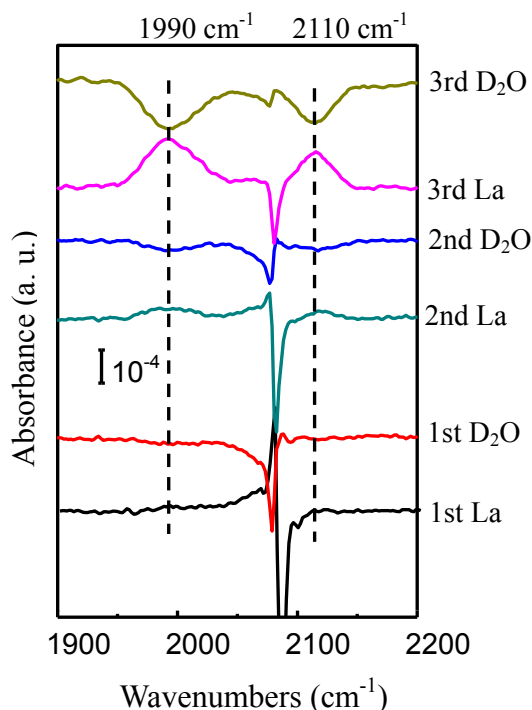


Fig 5.8 Differential spectra of the first 3 cycles of La precursor and D₂O on H/Si(111) at 300°C, where each spectrum is referenced to the previous spectrum and the 1st La is referenced to H/Si(111), and the exchange of the decomposed ligands with D₂O is observed as well.

Generally, the precursor ligand decomposition on the surface leads to further reaction among precursor molecules during the precursor dosing, and thereby destroys the self-limitation of the ALD reaction. However, in this case the La precursor with decomposed ligand is not reactive with other La precursor molecules, and then the decomposed ligand is removed from the surface by the subsequent water pulse, as evidenced by the loss of the intensity at 1990 and 2110 cm⁻¹ as shown by the differential spectra in Fig 5.8. Thus the self-termination property of the precursor will not be affected by the ligand decomposition. In fact, the smaller decomposed ligand facilitates access of more precursor molecules to the surface (smaller steric interactions), speeding up the film growth.

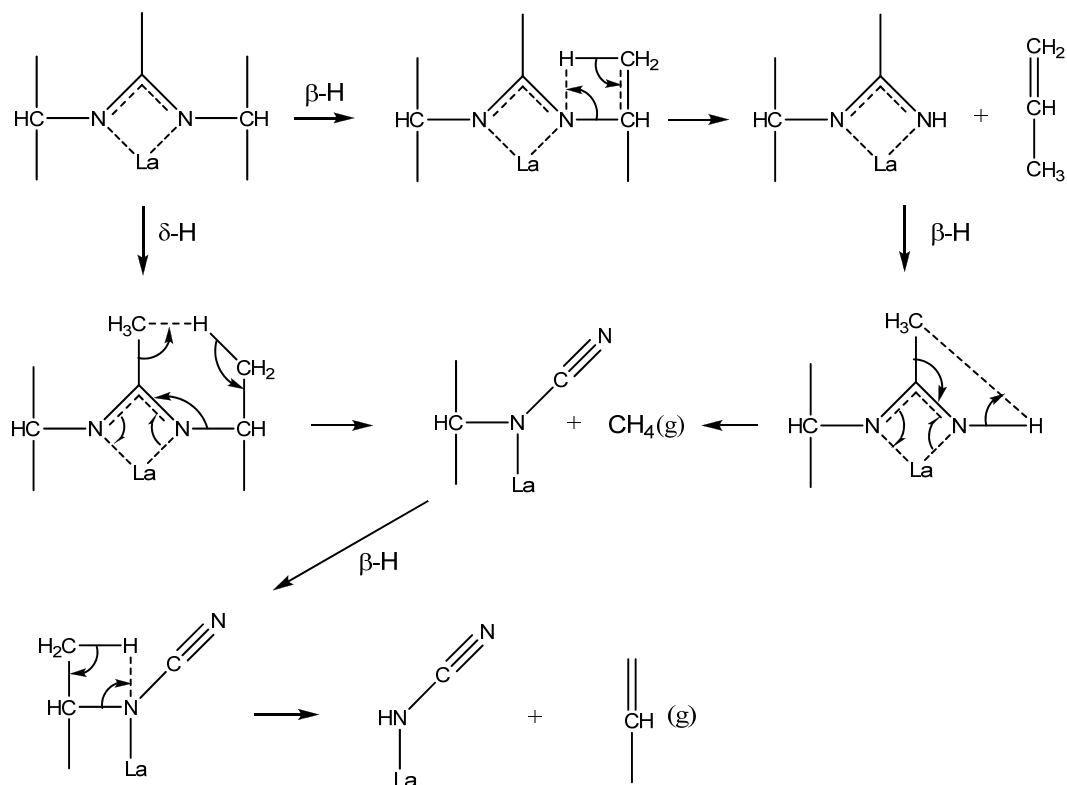


Fig 5.9 Possible decomposition pathways from intact precursor ligand to cyanamide (proposed by Prof. Roy Gordon). The actual pathway is not clear yet.

5.3 Miscellany of $\text{La}(\text{iPr-MeAMD})_3$ ALD temperature window

Lanthanum oxide is known to be highly hygroscopic [25, 34]. During the ALD process, it can slowly absorb water either from the ambient or when exposed to water, forming lanthanum hydroxide. Lanthanum hydroxide then slowly desorbs -OH during lanthanum precursor exposures. CVD-like reaction can thus happen and destroys the ALD self terminating condition [16].

One example is shown in Fig 5.10, where the H/Si(111) surface is exposed to the La precursor several times continuously at 300°C. After each dosing of La precursor at 300°C, we cool down the sample and take IR spectra which will take about 1 hour, and then increase the temperature to expose the surface to La precursor again. This process repeats and Fig 5.10 shows the differential spectra of the effect of multiple dosing. After

the 1st dosing of the La precursor, the subsequent precursor exposures keep consuming the Si-H evidenced by the continuous intensity loss of Si-H stretching mode at 2083 cm⁻¹. Upon the 4th La dosing, the ligand decomposition is observed and featured by the modes at 1990 cm⁻¹ and 2110 cm⁻¹. These findings suggest that the self terminating condition is broken so that the reaction will not stop. Due to the highly hygroscopic nature of La₂O₃ and the extreme sensitivity of the precursor to water, the adsorbed La precursor on the surface is slowly hydrolyzed during the measurement so that further reaction can occur when exposed to the next dosing La precursor without water dosing. Thus, the deposition is more like a CVD process.

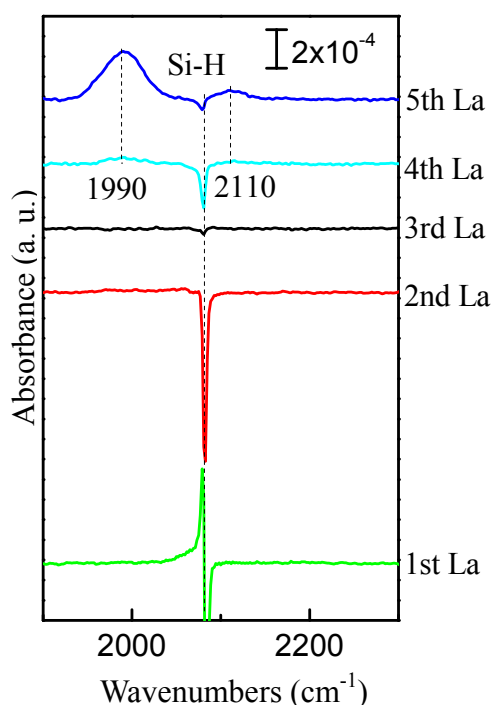


Fig 5.10 Differential spectra of continuous multiple dosing of La precursor on H/Si(111) at 300°C. Each precursor is referenced to the previous one and the 1st La is referenced to H/Si. The ligand decomposition is observed.

Similar results are obtained for 250°C and 400°C. In addition, the RBS result shows that the precursor decomposes at 400°C leading to a CVD process. As for the vibrations

of ligand decomposition at 1990 cm^{-1} and 2110 cm^{-1} , they show the minimum intensity at 300°C . When temperature goes below 200°C , precursor physisorption is observed on the surface frequently. Thereby, the deposition of La_2O_3 is not a well defined ALD process in our ALD reactor. *Ex situ* RBS didn't show a clear relation between the deposition rate and temperatures or between the deposition rate and cycle numbers. The film is not uniform and the growth rate somehow is quite random. 300°C appears to be the best choice for the deposition temperature.

5.4 ALD of $\text{La}_x\text{Al}_y\text{O}$ on H/Si(111) surface

Now we are in dilemma: at low temperature ($< 250\text{-}300^\circ\text{C}$) deposition, substantial amount of carbonate species and D_2O exists inside the film or physisorption occurs; while at $250\text{-}300^\circ\text{C}$ the deposition somehow is more CVD-like due to the trapped water/OH by lanthanum oxide. Study has shown that the water adsorption/desorption problems due to the hygroscopic nature of La_2O_3 can be overcome by deposition of alternating layers of La_2O_3 and Al_2O_3 , which remains the high dielectric constant [9, 16]. Thus, $\text{La}_x\text{Al}_y\text{O}$ nanolaminate is deposited on H/Si(111) in our ALD reactor to have reaction mechanistic study by *in situ* FTIR.

During the deposition of $\text{La}_x\text{Al}_y\text{O}$, a full cycle of TMA/ D_2O is introduced after every $\text{La}(\text{Pr-MeAMD})_3/\text{D}_2\text{O}$ cycle and saturation pulse length is used for each precursor dosing. Fig 5.11 shows the differential spectra of H/Si(111) exposed to alternating $\text{La}_2\text{O}_3/\text{Al}_2\text{O}_3$ ALD cycles at 300°C , where each odd number of cycle is La_2O_3 cycle and each even number of cycle is Al_2O_3 cycle.

The 1st La exposure shows the same features as we have discussed previously. Upon the subsequent 1st D_2O , interfacial SiO_2 is observed at this temperature in addition to the

evidence of lanthanum silicate, featured by the modes centered around 1034 and 1155 cm^{-1} . The slight loss of these modes after the 2nd TMA pulse shows the disruption of the oxide matrix by TMA. The vibrational mode at 1211 cm^{-1} is assigned to $-\text{CH}_3$ deformation mode of Al-CH_3 [35, 36]. Upon D_2O exposure, ALD ligand exchange behavior is presented by the intensity decrease of Al-CH_3 at 1211 cm^{-1} and the increase of $-\text{OD}$ band at 2745 cm^{-1} as expected (from Al-CH_3 to Al-OH).

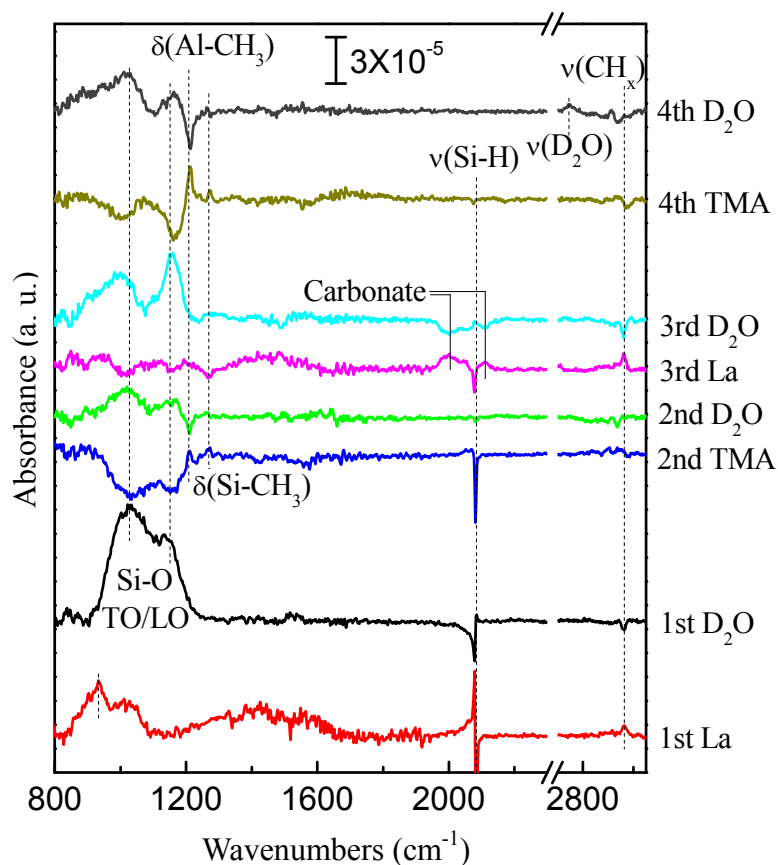


Fig 5.11 Differential spectra of first 4 cycles of $\text{La}_x\text{Al}_y\text{O}$ nanolaminate on H/Si(111) at 300°C , where each spectrum is referenced to the previous spectrum and the 1st La is referenced to H/Si(111) . ALD ligand exchange is observed.

As shown by Fig 5.11, TMA pulses after complete $\text{La}/\text{D}_2\text{O}$ cycles appear to react with residual surface amidinate ligands as evidenced by the loss of the modes around 1300-1600 cm^{-1} (2nd TMA and 4th TMA). In addition, the mode observed after the 2nd

TMA dosing at 1271 cm^{-1} is assigned to the umbrella deformation mode of -CH_3 directly bonded to Si atom (Si-CH_3) [35]. The subsequent $\text{La}(\text{Pr-MeAMD})_3$ pulse appears to react with Si-CH_3 as evidenced by the negative peak at 1271 cm^{-1} (3^{rd} La) and all surface H atoms are consumed by then. The cyanamide (or carbodiimide) species are observed at 1993 and 2115 cm^{-1} due to decomposition of the La precursor ligand, and are reacting with the subsequent water pulse as illustrated in Fig 5.11 (3^{rd} La and 3^{rd} D_2O). The periodic intensity gain and loss of CH_3 stretching modes at $2800\text{-}3000\text{ cm}^{-1}$ indicate the ALD ligand exchange behavior as well.

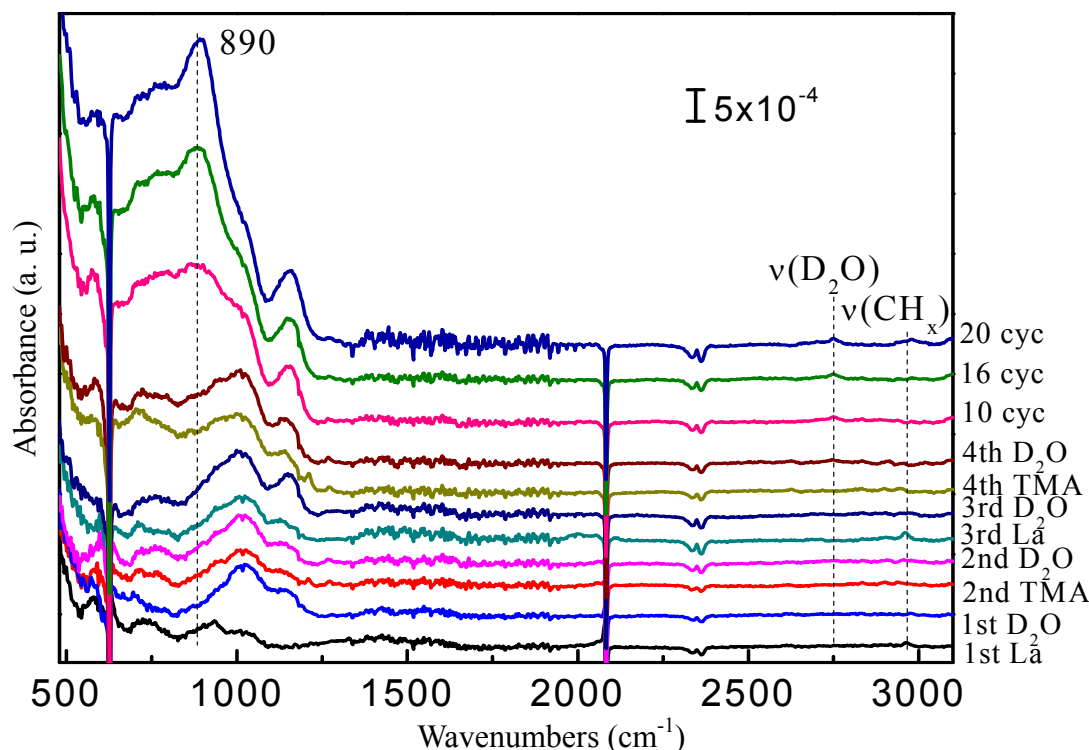


Fig 5.12 FTIR absorption spectra of 20 cycles of $\text{La}_x\text{Al}_y\text{O}$ nanolaminate on H/Si(111) at 300°C . All spectra are referenced to H/Si(111) . The film quality is improved featured by reduced interfacial SiO_2 , carbonated species trapped D_2O , and decomposed ligand byproducts.

Again, all the spectra of 20 cycles $\text{La}_x\text{Al}_y\text{O}$ are referenced to H/Si(111) surface to

study the contents accumulated in the film as in Fig 5.12. Compared to the similar cycles La_2O_3 as in Fig 5.5 and 5.7, the vibrational signature of acetate/carbonate impurities in the $1300\text{-}1600\text{ cm}^{-1}$ region is almost completely absent. It can be concluded that the suppression of impurity incorporation is mainly due to the interaction of TMA with the surface amidinate ligand as described above. However, the interfacial SiO_2 amount is comparable to the pure La_2O_3 deposition at 300°C because the TMA/ D_2O ALD cycle produces interfacial oxide at this temperature as well. The strong peak centered at 890 cm^{-1} can be attributed to La-O-Al phonon absorption [9]. In addition, little ligand decomposition residue is observed after 20 cycles. The La atom surface density measured by Rutherford backscattering confirms that the lanthanum aluminate film thickness is uniform and the CVD like deposition is minimized.

5.5 Summary

In this chapter, we discussed the deposition of La_2O_3 and lanthanum aluminate by using a new precursor, $\text{La}(\text{}^i\text{Pr-MeAMD})_3$, and heavy water (D_2O).

With the aid of first principle DFT calculation, the precursor gas phase is checked first by FTIR and all ligand features are observed. Partial hydroxylation of the precursor is discovered by the unexpected stretching modes resulting from C=N and N-H in free hydrogenated ligands. Then D_2O is introduced into the La precursor to study the precursor gas phase reaction. Free ligand is observed as the byproduct of the reaction which is proved to be unreactive with the surface.

The growth of La_2O_3 on H/Si(111) surface shows that, due to the precursor reaction with residual water vapor, the initial interaction of $\text{La}(\text{}^i\text{Pr-MeAMD})_3$ with H/Si involves the formation of a Si-O-La bond at the interface. Despite the large size of the precursor (i.e.

potential steric hindrance), there is a complete reaction of all surface Si-H bonds within a few ALD cycles (~10 cycles at 200°C and 5 cycles at 300°C). This reaction is facilitated at 300°C by the fact that the adsorbed precursor ligand readily dissociates to form much smaller cyanamide (or carbodiimide) species which readily react with water pulses. The size and partial reactivity of the precursor contribute to the observation of trapped acetate and carbonate impurities, which are produced upon water interaction with adsorbed ligands during the growth. The concentration of these impurities decreases at higher growth temperatures or upon post annealing. In general, the ALD of pure La_2O_3 films is difficult because they are highly hygroscopic, resulting in thickness non-uniformities on a macroscopic scale. Introducing alternating TMA/ D_2O and $\text{La}(\text{}^i\text{Pr-MeAMD})_3/\text{D}_2\text{O}$ ALD cycles suppresses CVD-like reactions and minimizes the acetate/carbonate incorporation.

Bibliography

1. S. S. Kale, K. R. Jadhav, P. S. Patil, T. P. Gujar and C. D. Lokhande, *Characterizations of spray-deposited lanthanum oxide (La_2O_3) thin films* Materials Letters **59** (2005), 3007.
2. O. V. Manoilova, S. G. Podkolzin, B. Tope, J. Lercher, E. E. Stangland, J. M. Goupil and B. M. Weckhuysen, *Surface acidity and basicity of La_2O_3 , LaOCl , and LaCl_3 characterized by IR spectroscopy, TPD, and DFT calculations*, J. Phys. Chem. B **108** (2004), no. 40, 15770-15781.
3. M. Nieminen, M. Putkonen and L. Niinisto, *Formation and stability of lanthanum oxide thin films deposited from beta-diketonate precursor*, Applied Surface Science **174** (2001), 155.
4. D.-J. Won, C.-H. Wang and D.-J. Choi, *Characteristics of metal/ ferroelectric/ insulator/ semiconductor using La_2O_3 thin film as an insulator*, Jpn. J. Appl. Phys. **40** (2001), L1235.
5. D. C. Lupascu, *Fatigue in ferroelectric ceramics and related issues*, Springer (2004).
6. G. D. Wilk, R. M. Wallace and J. M. Anthony, *High-k gate dielectrics: Current status and materials properties considerations*, Journal of Applied Physics **89** (2001), 5243.
7. J. H. Jun, D. J. Choi, K. H. Kim, K. Y. Oh and C. J. Hwang, *Effect of structural properties on electrical properties of lanthanum oxide thin film as a gate dielectric*, Jpn. J. Appl. Phys. **42** (2002), 3519.

8. S. Guha, E. Cartier, M. A. Gribelyuk, N. A. Bojarczuk and M. C. Copel, *Atomic beam deposition of lanthanum- and yttrium-based oxide thin films for gate dielectrics*, Appl. Phys. Lett. **77** (2000), 2710.
9. R. A. B. Devine, *Infrared and electrical properties of amorphous sputtered $(La_xAl_{1-x})_2O_3$ films*, J. Appl. Phys. **93** (2003), 9938.
10. H. Yamada, T. Shimizu, A. Kurokawa, K. Ishii and E. Suzuki, *Mocvd of high-dielectric-constant lanthanum oxide thin films*, J. Electrochem. Soc. **150** (2003), G429.
11. G. A. H. Mekhemer and B. A. A. Balboul, *Thermal genesis course and characterization of lanthanum oxide*, Colloids and Surfaces **181** (2001), 19.
12. C. Bedoya, G. G. Condorelli, S. T. Finocchiario, A. D. Mauro, D. Atanasio, I. L. Fragalà, L. Cattaneo and S. Carella, *Mocvd of lanthanum oxides from $La(tmhd)_3$ and $La(tmod)_3$ precursors: A thermal and kinetic investigation*, Chemical Vapor Deposition **12** (2006), 46.
13. N. Imanaka, T. Masui and Y. Kato, *Preparation of the cubic-type La_2O_3 phase by thermal decomposition of LaI_3* , Journal of Solid State Chemistry **178** (2005), 395.
14. B. S. Lim, A. Rahtu, J.-S. Park and R. G. Gordon, *Synthesis and characterization of volatile, thermally stable, reactive transition metal amidinates* Inorg. Chem. **42** (2003), 7951.
15. R. G. Gordon, J.-S. Lehn, Y. Liu, K. K. H., Z. Li, M. Coulter, H. Li, P. R. and D. Shenai, AVS 75th International Conference on Atomic Layer Deposition, San Jose (2007).
16. B. S. Lim, A. Rahtu, P. d. Rouffignac and R. G. Gordon, *Atomic layer deposition of lanthanum aluminum oxide nano-laminates for electrical applications*, Appl. Phys. Lett. **84** (2004), 3957.
17. S. Dagorne, I. A. Guzei, M. P. Coles and R. F. Jordan, *Synthesis and structures of cationic aluminum and gallium amidinate complexes* J. Am. Chem. Soc. **122** (2000), 274.
18. J. P. Perdew, K. Burke and M. Ernzerhof, *Generalized gradient approximation made simple*, Phys. Rev. Lett. **77** (1996), 3865.
19. B. Delley, *From molecules to solids with the Dmol3 approach*, J. Chem. Phys. **113** (2000), 7756.
20. ---, *Hardness conserving semilocal pseudopotentials*, Phys. Rev. B **66** (2002), 155125.
21. H. Ono and T. Katsumata, *Interfacial reactions between thin rare-earth-metal oxide films and Si substrates*, Appl. Phys. Lett. **78** (2001), 1832.
22. Y. I. Takashi Yamamoto, Hideki Hashimoto, Masanori Oosawa and Yoshihiro Sugita, *Structural changes of Y_2O_3 and La_2O_3 films by heat treatment*, Jpn. J. Appl. Phys. **45** (2006), 6196.
23. B. Klingenberg and M. A. Vannice, *Influence of pretreatment on lanthanum nitrate, carbonate, and oxide powders*, Chem. Mater. **8** (1996), 2755.
24. M. Suzuki, M. Kagawa, Y. Syono and T. Hirai, *Thin films of rare-earth (Y, La, Ce, Pr,*

- Nd, Sm*) oxides formed by the spray-icp technique *Journal of Crystal Growth* **112** (1991), 621.
25. W. He, S. Schuetz, R. Solanki, J. Belot and J. McAndrewc, *Atomic layer deposition of lanthanum oxide films for high-kappa gate dielectrics*, *Electrochem. and Solid-State Lett.* **7** (2004), G131.
26. A. M. D. Asha, J. T. S. Critchley and R. M. Nix, *Molecular adsorption characteristics of lanthanum oxide surfaces: The interaction of water with oxide overlayers grown on Cu(111)*, *Surface Science* **405** (1998), 201.
27. T. Gougousi, D. Niu, R. W. Ashcraft and G. N. Parsons, *Carbonate formation during post-deposition ambient exposure of high-k dielectrics*, *Appl. Phys. Lett.* **83** (2003), 3543.
28. J. B. Cheng, A. D. Li, Q. Y. Shao, H. Q. Ling, D. Wu, Y. Yang, Y. J. Bao, M. Wang, Z. G. Liu and N. B. Ming, *Growth and characteristics of La₂O₃ gate dielectric prepared by low pressure metalorganic chemical vapor deposition* *Appl. Surf. Sci.* **233** (2004), 91.
29. S. M. R. da Rocha, C. A. da Silva Queiroz and A. Abrao, *Synthesis and characterization of lanthanum acetate for application as a catalyst*, *Journal of Alloys and Compounds* **344** (2002), 389.
30. M. Leskelä and L. Ninistö, *Handbook on the physics and chemistry of rare earths, chapter 56*, Elsevier, Amsterdam **8** (1986).
31. K. T. Queeney, Y. J. Chabal, M. K. Weldon and K. Raghavachari, *Silicon oxidation and ultra-thin oxide formation on silicon studied by infrared absorption spectroscopy*, *Phys. Stat. Sol. (a)* **175** (1999), 77.
32. G. Socrates, *Infrared and Raman characteristic group frequencies, 3rd edition*, John Wiley & Sons (2006).
33. O. Reckeweg and A. Simon, *Azides and cyanamides - similar and yet different (in german)*, *Z. Naturforsch B* **58B** (2003), 1097.
34. Y. Zhao, M. Toyama, K. Kita, K. Kyuno and A. Toriumi, *Moisture-absorption-induced permittivity deterioration and surface roughness enhancement of lanthanum oxide films on silicon*, *Appl. Phys. Lett.* **88** (2006), 072904.
35. J. Kwon, M. Dai, M. D. Halls and Y. J. Chabal, *Detection of a formate surface intermediate in the atomic layer deposition of high-k dielectrics using ozone*, *Chem. Mater.* **20** (2008), 3248.
36. M. M. Frank, Y. J. Chabal and G. D. Wilk, *Nucleation and interface formation mechanisms in atomic layer deposition of gate oxides*, *Appl. Phys. Lett.* **82** (2003), 4758.

Chapter 6: ALD of Cu on Si Surfaces

ALD is advantageous to deposit highly uniform thin film with high aspect ratio [1], and quite a number of compounds, such as high- κ metal oxides including high-quality thin films of Al_2O_3 , ZrO_2 and HfO_2 , have been successfully grown by ALD. ALD of pure metals, however, is sparse and shows limited success [2, 3]. Recently, more and more researches have been underway to produce suitable precursors which satisfy stringent requirements for ALD [4], and this should be paralleled with mechanistic *in situ* studies of ALD of metals for practical applications.

Due to its lower resistivity, lower electromigration and higher melting point, copper ($1.72 \times 10^{-6} \Omega \cdot \text{cm}$, 1083°C) is replacing aluminum ($2.82 \times 10^{-6} \Omega \cdot \text{cm}$, 659°C) as an interconnect material in integrated circuits [5]. In such application, a highly conformal and continuous copper seed layer is needed before subsequent electrochemical deposition of copper film with high growth rate [6]. Considering the great advantages, ALD of copper is becoming a good choice.

However, ALD of copper is challenging. Several copper (I) and copper (II) precursors were commonly used in the past, such as CuCl [3, 7], $\text{Cu(II)-2,2,6,6-tetramethyl-3,5-heptanedionate}$ [Cu(thd)_2] [8, 9], $\text{Cu(II)-1,1,1,5,5,5-hexafluoro-2,4-pentanedionate}$ [Cu(hfac)_2] [10, 11], and $\text{Cu(II) acetylacetonate}$ [Cu(acac)_2] [12, 13], but all suffered from undesirable properties as ALD precursors [14]. For example, CuCl has very low vapor pressure, and the Cu film deposited by Cu(hfac)_2 contains fluorine which reduces the Cu adhesion on the substrate. They all have very low reactivity with low growth rate, so that either high temperature ($> 200^\circ\text{C}$), which is not preferable for smooth Cu growth due to Cu agglomeration and diffusion [14, 15, 16], or plasma is needed to

enhance the reactivity.

In this chapter, we will discuss ALD of Cu by a new copper(I) amidinate precursor. By using *in situ* FTIR, *ex situ* RBS, and XPS, the interaction mechanism and film properties are explored for the initial Cu ALD cycles.

6.1 Precursor properties and the gas phase IR spectrum

Recently, Gordon et al. reported ALD grown Cu films with high conformality, high conductivity and aspect ratio over 35:1 by using a novel liquid precursor copper (I) di-sec-butylacetamidinate ($[\text{Cu}(\text{}^s\text{Bu-amd})]_2$) [17]. $\text{Cu}(\text{}^s\text{Bu-amd})_2$ has equilibrium vapor pressure as high as 0.23 torr at 95°C, low melting point (77 °C) and fast vaporization rate (38.8 nmol/cm²·min at 100°C). It is very stable with a half-life around 33 days at 190°C in benzene-d₆ solution. Most of all, this precursor is highly reactive and can be reduced by molecular H₂ at relatively low temperature (<200°C) which is more favorable to deposit smooth and continuous pure thin copper layer. It also readily reacts with water and NH₃, producing copper oxide and copper nitride, respectively. The chemical structure of the copper precursor $[\text{Cu}(\text{}^s\text{Bu-amd})]_2$ is shown by the inset of Fig 6.1.

Before depositing copper, the $[\text{Cu}(\text{}^s\text{Bu-amd})]_2$ gas phase IR spectrum is measured to determine the composition and the state of the gas phase precursor prior to reaction. As shown in Fig. 6.1, the spectrum is characterized by $\nu_{\text{as}}(\text{CH}_3)$ at 2971 cm⁻¹, $\nu_{\text{s}}(\text{CH}_3)$ at 2882 cm⁻¹, $\nu_{\text{as}}(\text{CH}_2)$ at 2932 cm⁻¹, $\nu_{\text{s}}(\text{CH}_2)$ at 2861 cm⁻¹, and $\delta_{\text{s}}(\text{CH}_3)$ at 1377 cm⁻¹. The NCN-related ligand modes and the other CH_x bending and deformation modes are in the range of 1000-1600 cm⁻¹, where the band at 1492 cm⁻¹ is assigned to $\nu(\text{N-C-N})$ in the intact ligand. The very strong and sharp feature at 1664 cm⁻¹ cannot be assigned to any mode (e.g. NCN stretch) of the ligand bonded to the metal (Cu) center. Instead, it is the

characteristic of C=N stretching mode in the -HNC=N- molecule (HL, L denotes the ligand) as the La precursor. Along with the $\nu(\text{NH})$ at 3456 cm^{-1} , the observed C=N stretching mode at 1664 cm^{-1} is the result of partial hydrolyzation of the parent precursor, most likely due to a small amount of residual water in the ALD chamber or precursor gas line. This gas phase IR spectrum is useful to interpret some of the surface reactions.

For the following experiments, the precursor is kept at $94\text{--}100^\circ\text{C}$ to generate a high enough vapor pressure. During film deposition, the pressure of the copper precursor is around 2 torr and that of H_2/NH_3 is >11 torr. The thickness of the ALD-grown copper films is measured by *ex situ* RBS, assuming that the copper film density is equal to the density of bulk copper (8.96 g/cm^3 , or $8.49 \times 10^{22}\text{ atoms/cm}^3$).

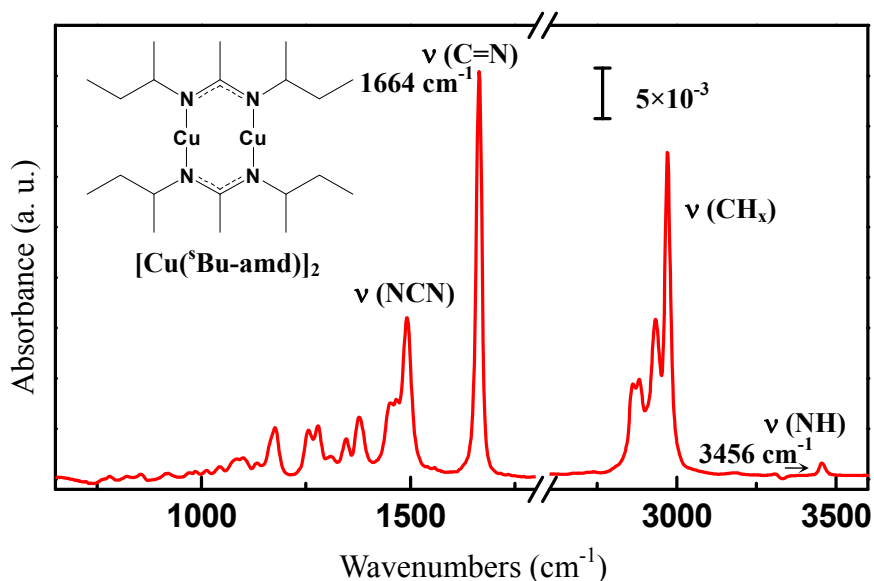


Fig 6.1 Gas phase FTIR absorption spectrum of the copper precursor $[\text{Cu}(\text{sBu-amd})]_2$ used in this study (Partial pressure ~ 0.4 torr, IR path length ~ 6 inch). Its chemical structure is shown on the upper left corner (inset).

6.2 ALD of Cu on H/Si surface

H/Si is the most widely used surface in microelectronics, and the Cu deposition is first examined on H/Si surface. Fig. 6.2 shows the differential absorption spectra of

H/Si(100) exposed to $[\text{Cu}(\text{}^s\text{Bu-amd})]_2$ precursor at 185°C. In total, an integrated exposure of 6s is performed to investigate the surface saturation. The incident angle of IR is 74° with a single transmission configuration as usual. Each spectrum is referenced to that recorded after the previous pulse to highlight changes occurring after each 2s exposure to $\text{Cu}(\text{}^s\text{Bu-amd})$ each time.

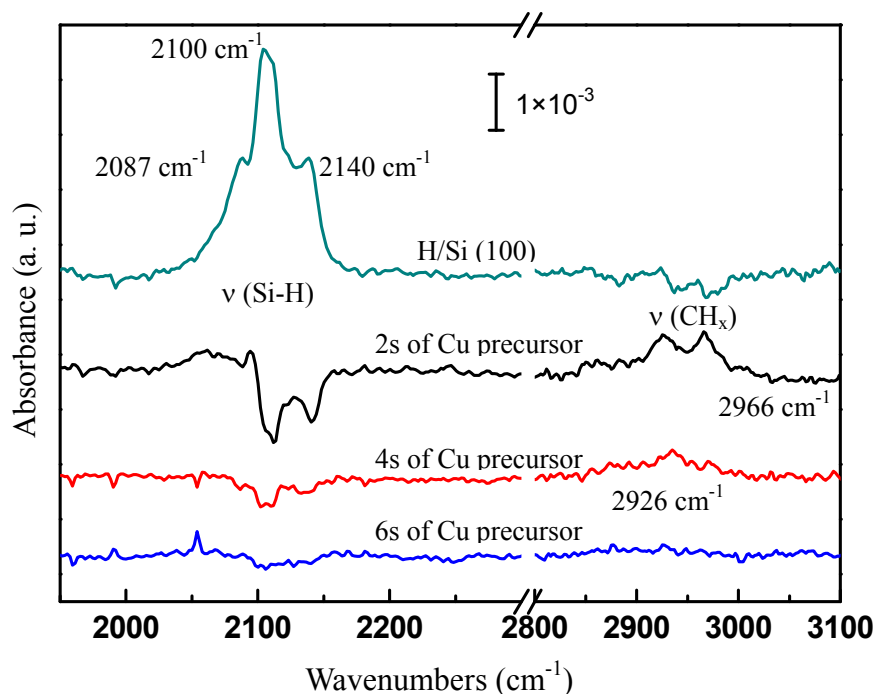


Fig 6.2 Differential FTIR absorption spectra of $[\text{Cu}(\text{}^s\text{Bu-amd})]_2$ on H/Si (100) surface. Each spectrum is referenced to the spectrum recorded for the previous treatment. The spectrum of H/Si is referenced to that of the oxidized surface; the spectrum of 2s Cu precursor exposure is referenced to that of the H/Si(100) surface; the spectrum of 4s Cu precursor exposure is referenced to that of the 2s Cu precursor exposure, and so on. The incident angle of IR is $\sim 74^\circ$

As shown in Fig. 6.2, the initial H/Si (100) surface is characterized by Si-H stretching modes centered at 2087 cm^{-1} , 2104 cm^{-1} and 2140 cm^{-1} , which are attributed to mono-, di- and tri-hydrides, respectively [18]. By monitoring the intensity of the Si-H stretching bands, the reactivity of the copper precursor with the surface can be inferred. After the first 2s dosing, the intensity of the Si-H bands is decreased by $\sim 14\%$, and only

by $\sim 21\%$ and $\sim 22\%$ (relative to the original H/Si surface) after the second (4s) and third exposures (6s), respectively. The change after 4s exposure is negligible according to the differential spectra, suggesting no more chemical bonding formation. These data indicate that the saturation is achieved after ~ 4 s integrated exposure time. Concurrently, the asymmetric stretching modes of CH_3 at 2966 cm^{-1} and CH_2 2926 cm^{-1} are observed after the first dosing of Cu precursor with little intensity increase afterwards. The behavior of Si-H and CH_x stretching modes indicates that most of the surface reaction occurs during the first precursor dosing (2-4s exposure). RBS measurement performed after 2 cycles of $[\text{Cu}(\text{}^s\text{Bu-amd})]_2/\text{H}_2$ on H/Si(100) shows that the Cu thickness is about 0.24 \AA .

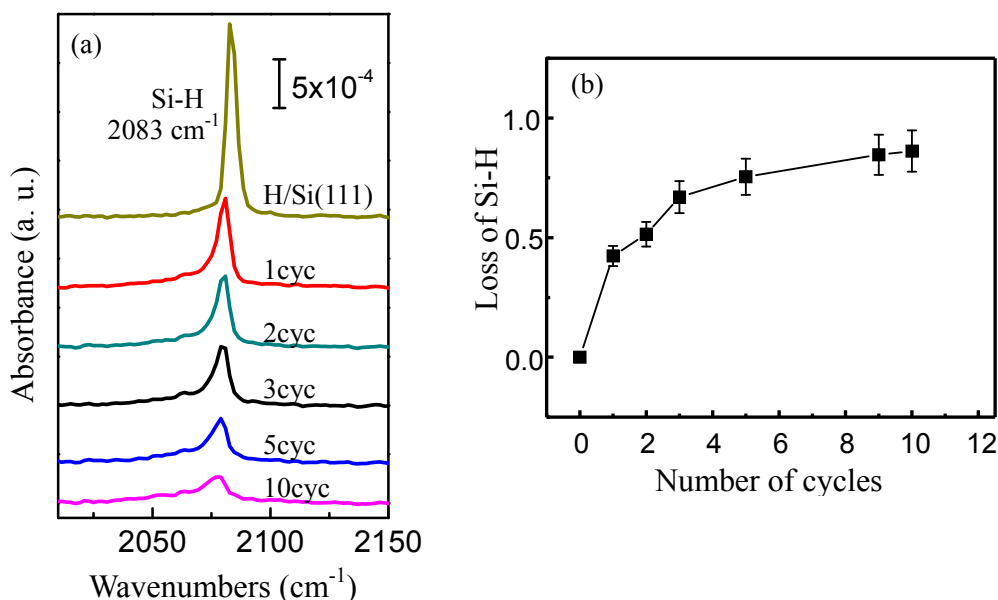


Fig 6.3(a) Absorption spectra of 10 cycles Cu on H/Si(111) reference to oxide (left) and (b) the plot of the loss of Si-H vs number cycles (right). The incident angle of IR is $\sim 74^\circ$. The Cu precursor can react with H/Si.

A study has shown that there is no Cu growth on H/Si surface by this precursor [14] but our spectra clearly show that there are obvious chemical reactions between $[\text{Cu}(\text{}^s\text{Bu-amd})]_2$ and H/Si. To confirm it, atomically flat and almost defect-free

H-terminated silicon (111) is used. The results of 10 cycles of Cu on H/Si(111) at 185°C (incident angle 74°) are shown in Fig 6.3 and Fig 6.4. The Cu precursor pulse length is 35s and H₂ pulse length is 200s to ensure saturation reaction.

As in Fig 6.3(a), the spectra clearly show that after the 1st dosing of Cu precursor exposure, there is ~18% loss of surface hydrogen as well as the red shift of Si-H stretching mode, indicating that the Si-H can react with the Cu precursor. The CH_x stretching modes are observed also as the proof of the reaction. After 10 cycles, the Si-H loss is about 86% [Fig 6.3(b)]. However, the Cu amount on the H/Si(111) is quite low. RBS shows that the Cu thickness is about 0.9 Å for 10 cycles.

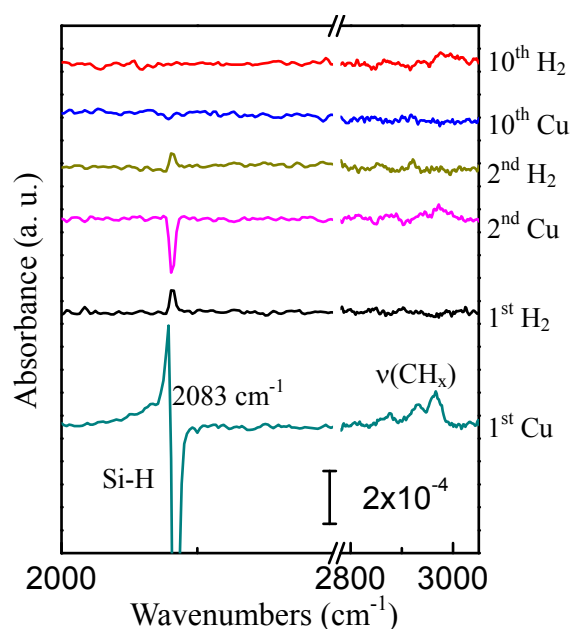


Fig 6.4 Differential spectra of 10 cycles Cu on H/Si(111). Each spectrum is referenced to the spectrum recorded for the previous treatment and the 1st Cu spectrum is referenced to H/Si(111). The 10th Cu is referenced to the 9th H₂ (9 cycles). The incident angle of IR is ~74°. Most of the reaction occurs for the first cycle.

From the differential spectra in Fig 6.4, it can be concluded that most of the reaction takes place at the first several cycles (~5 cycles) and little change is observed for the 10th cycle. One interesting feature in Fig 6.4 is that after the H₂ dosing, the Si-H is recovered

partially. It may result from the Cu diffusion into Si by forming CuSi_3 [19, 20, 21], where H_2 reduces the Cu precursor attached on the Si surface to Cu atoms and a few Cu atoms diffuse into the Si network to free the surface Si atoms, which are passivated again by H.

6.3 ALD of Cu on SiO_2

In general, oxidized Si surface is much more reactive to metal precursors than H/Si surface. We therefore studied the reactivity of $[\text{Cu}(\text{}^s\text{Bu-amd})]_2$ with Si(100) covered by thin oxide (60-100 Å). On this surface, Cu is deposited at different temperatures, with 35s dosing of $[\text{Cu}(\text{}^s\text{Bu-amd})]_2$ and 200s dosing of H_2 to study the temperature dependence of ALD.

Deposition at 185°C

The differential absorption spectra for the first 3 cycles Cu deposited on SiO_2 at 185°C are shown in Fig 6.5, where each spectrum is referenced to that of the previous treatment to see the change on the surface after each treatment.

As shown in the spectra, upon the initial dosing of $[\text{Cu}(\text{}^s\text{Bu-amd})]_2$ on the oxide surface, there is a clear intensity decrease of SiO_x phonon absorption evidenced by two negative peaks centered at 1075 cm^{-1} and 1247 cm^{-1} (TO/LO modes of Si-O-Si), along with the loss of isolated -OH stretching/bending modes at 3737 cm^{-1} and 1660 cm^{-1} respectively [22]. Their intensity loss indicates that initially a part of the SiO_2 matrix is chemically involved with the Cu precursor. Concurrently, a broad absorption band centered at 1010 cm^{-1} appears, corresponded to the formation of Si-O-Cu bonds due to the adsorbed Cu precursor on SiO_2 . The reaction scheme is shown in Fig 6.6(a) and (b). Upon the H_2 exposure (1 cycle), there is a partial recovery of SiO_x phonon modes and

-OH stretching mode. This observation suggests that after the H₂ dosing, the Cu precursor on the surface is reduced to pure copper atoms which then migrate and self-agglomerate to form copper particles [14, 23, 24]. As they agglomerate, the chemical bonds between Cu and the underlying SiO_x surface are broken, partially restoring the SiO₂ phonon modes and reactive sites of the surface. This process is schematically illustrated in Fig 6.6 (c)-(e). The same phenomena in the SiO₂ range (900-1250 cm⁻¹) are observed for the 20th cycle implying that the surface is not saturated due to the Cu agglomeration effect. In addition, the removal of ligands on the Cu atom can also open more reaction sites which were initially blocked by the intact ligands.

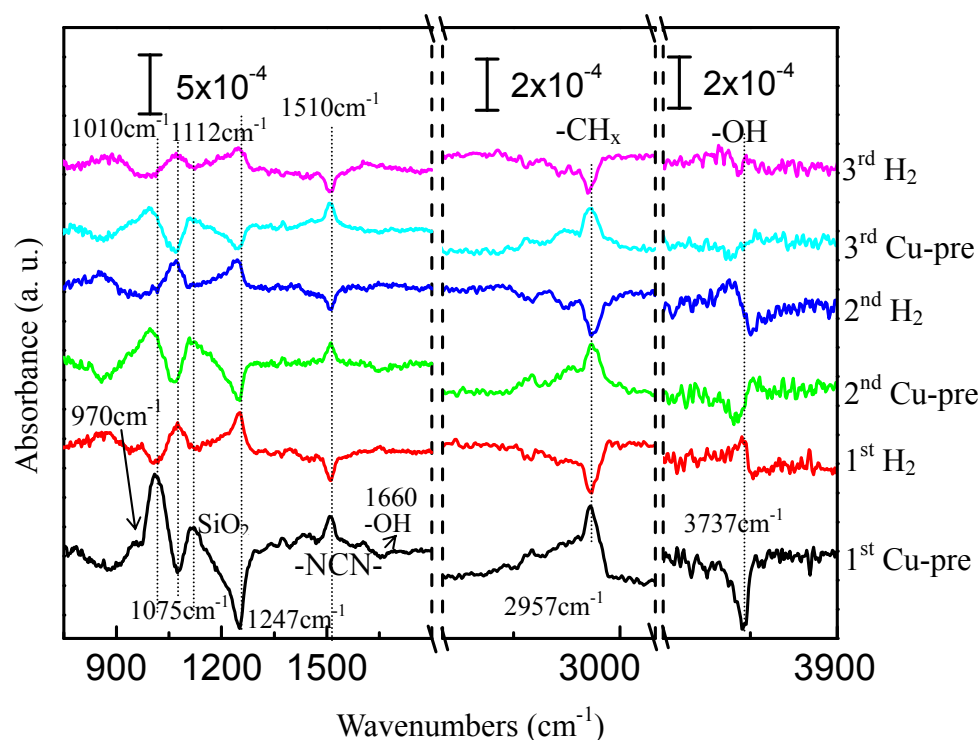
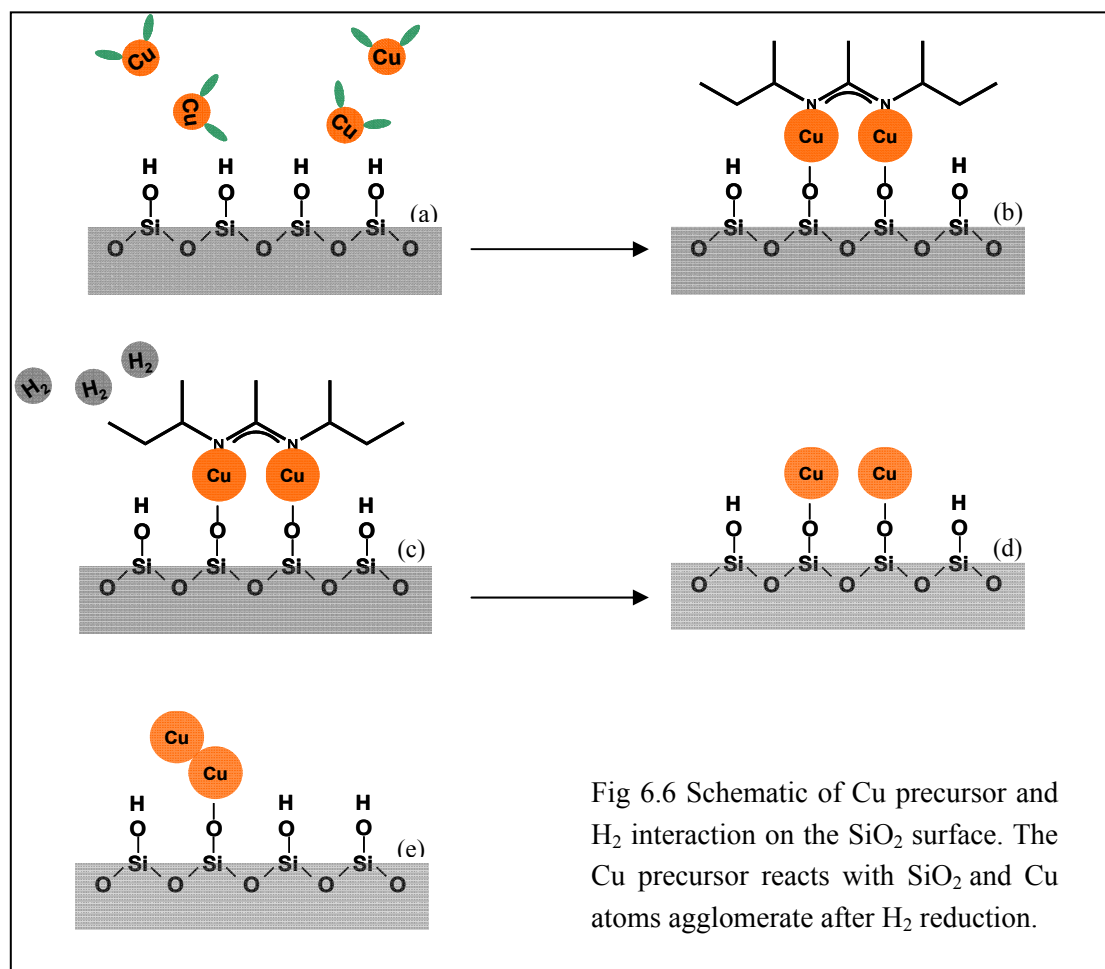


Fig 6.5 Differential spectra of the first 3 cycles Cu on oxide. Each spectrum is referenced to the spectrum recorded for the previous treatment. The bottom is referenced to initial oxide surface. The incident angle of IR is $\sim 74^\circ$. The surface is not saturated and ALD ligand exchange is observed.

In Fig 6.5, the mode appearing at 1510 cm^{-1} is assigned to $\nu(\text{N-C-N})$ in the intact ligand on the Cu atoms (shown in Fig 6.6 (b)). Along with CH_x stretching modes at $2800\text{--}3000\text{ cm}^{-1}$, their intensity increases after each copper precursor dosing, and decreases after each H_2 dosing, confirming that the precursor is adsorbed on the surface with intact ligands after the Cu precursor dosing and the H_2 dosing does react by removing those ligands, as shown in Fig 6.6 (b)-(d). For each cycle, H_2 removes the ligands almost completely, leaving little N and C remnant inside the film for the initial cycles. These spectra show a direct observation of the ALD process through the ligand exchange.



The spectra of subsequent cycles (up to 20 cycles) referenced to the initial SiO₂ surface are presented in Fig 6.7 to show the Cu film on SiO₂. Two incident angles are used, $\sim 74^\circ$ (left) and $\sim 0^\circ$ (right), to see the polarization effect. IR of 74° incidence is sensitive to both parallel and perpendicular components to the surface, while normal incidence is only sensitive to the parallel component. The spectra show that there is no difference between the two angles, indicating that the film is isotropic. Consequently, the strong peaks at 1010 cm^{-1} and 1112 cm^{-1} cannot be assigned to SiO₂ TO/LO modes since the LO mode of SiO₂ is angle dependent and will not appear at normal incidence. Their frequencies are also much lower than that of typical SiO₂ TO/LO modes which are around 1075 cm^{-1} and 1247 cm^{-1} respectively as observed in Fig 6.5.

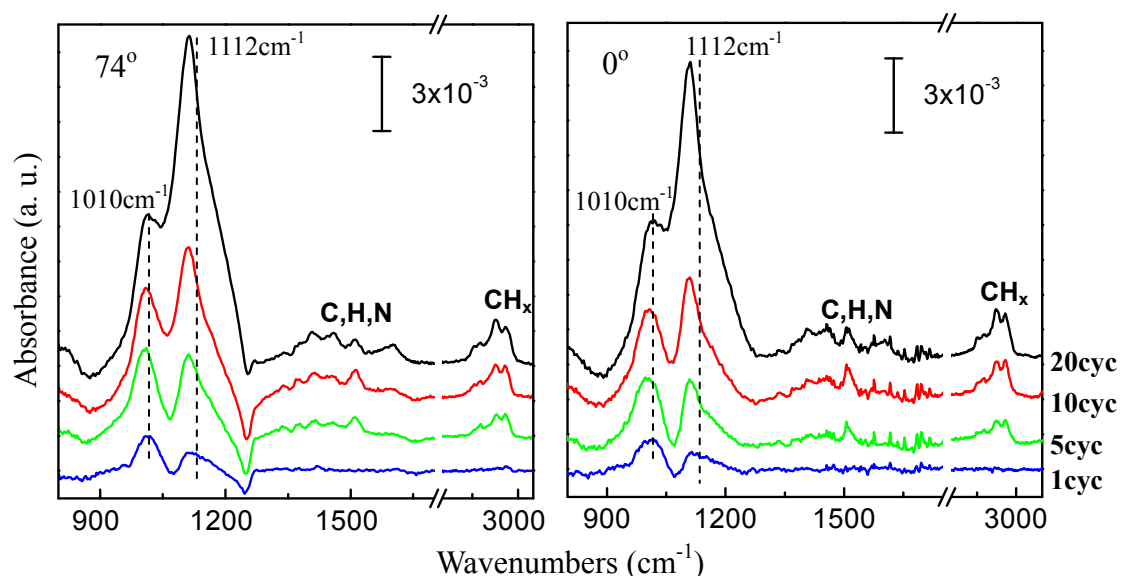


Fig 6.7 Absorption spectra of the first 3 cycles Cu on Si oxide. Each spectrum is referenced to the spectrum recorded for the previous treatment. The bottom one is referenced to initial oxide surface. The left one is taken at 74° and the right one is taken at 0° . Ligand related impurities are observed and spectra show little difference at different angles.

It is most likely that they are related to Cu-incorporated Si oxide as Cu-SiO_x modes [25, 26, 27] because Cu-O stretching modes are all below 700 cm^{-1} [28, 29, 30]. By peak

deconvolution, we find that the intensity of 1010 cm^{-1} band increases much less after 10 cycles as shown by Fig. 6.8, while the intensity of 1112 cm^{-1} band obviously keep increasing. It is well known that copper readily diffuses into SiO_2 [31, 32]. Therefore, we can tentatively assign the 1010 cm^{-1} band to the surface mode of Cu-O-Si while the 1112 cm^{-1} band to the silicon oxide disrupted by Cu diffusion.

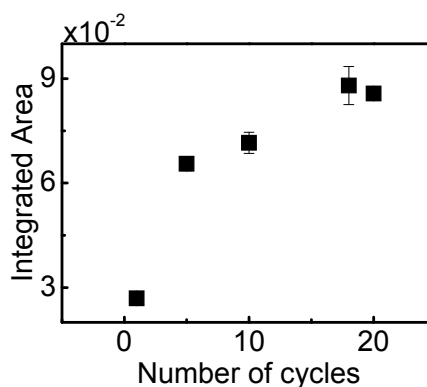


Fig 6.8 Fitted integrated area of 1010 cm^{-1} mode. This mode almost saturates after 10 cycles and is assigned to the surface Si-O-Cu mode

1 cycle Cu deposition at other temperatures

Because temperature has a great effect on Cu agglomeration and diffusion, we varied the growth temperature from $100\text{ }^{\circ}\text{C}$ to $300\text{ }^{\circ}\text{C}$ to study the temperature dependence of the growth. The spectra of 1 cycle of Cu on SiO_2 at different temperatures are shown in Fig. 6.9 (a) with the same growth parameter (35s Cu precursor and 200s H_2).

The Cu precursor reaction with the surface at 100°C is not as strong as that of higher temperatures, and H_2 cannot reduce the absorbed Cu precursor on the surface shown by the featureless spectra after H_2 . At 140°C , H_2 can have the reaction as shown by the loss of -NCN- mode at 1510 cm^{-1} and CH_x stretching modes around 2957 cm^{-1} (all are ligand-related modes), but very little agglomeration is observed by the variation of SiO_2

TO/LO modes after the H_2 dosing. Above 140°C , the agglomeration is clearly observed after the H_2 dosing. On the other hand, as shown in Fig. 6.9 (b), higher temperature gives higher 1112 cm^{-1} band, while the 1010 cm^{-1} band keeps similar, implying that higher temperature possibly causes more Cu diffusion but the surface Si-O-Cu should keep constant once the surface is saturated. This diffusion could be the result that the adsorbed precursor on the surface partly decomposes to Cu atoms due to the increased temperature, and thereby Cu diffusion may occur.

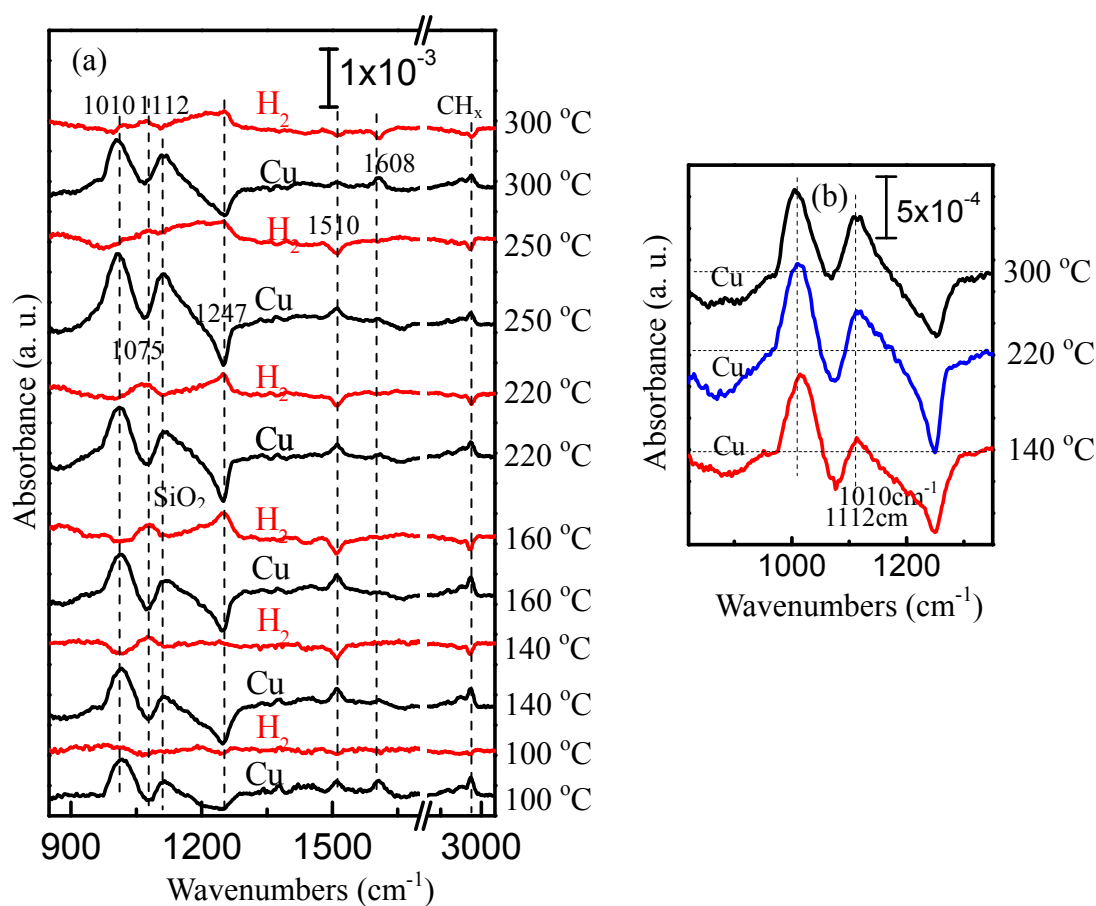


Fig 6.9 (a) Differential spectra of the first cycle Cu on oxide at different temperatures. The Cu is referenced to the oxide and the H_2 is referenced to the Cu. (b) The absorption spectra of Cu precursor on oxide at different temperatures referenced to oxide. The incident angle of IR is $\sim 74^\circ$. The H_2 is less reactive at 100°C .

Carefully looking at the spectral range at $1500\text{--}1600\text{ cm}^{-1}$, actually two modes are

observed: 1510 cm^{-1} and 1608 cm^{-1} , especially at low temperature like 100°C or high temperature like above 250°C . The 1510 cm^{-1} band has been assigned to $\nu(\text{NCN})$ in the intact ligand, while the 1608 cm^{-1} band is possibly due to ligand hydrogenation. As illustrated by Fig 6.10, the Cu precursor reacts with the hydroxyl group on the SiO_2 surface to free one hydrogenated ligand and leave one ligand bonded to the Cu in a bidentate structure featured by the 1510 cm^{-1} band. Then the bidentate ligand rearranges to the monodentate binding featured by the 1608 cm^{-1} band with release of a copper atom. And according to our preliminary DFT calculation (done by Dr. Mathew Halls), the monodentate ligand may have been hydrogenated to have the structure of HL-Cu (L denotes the intact ligand).

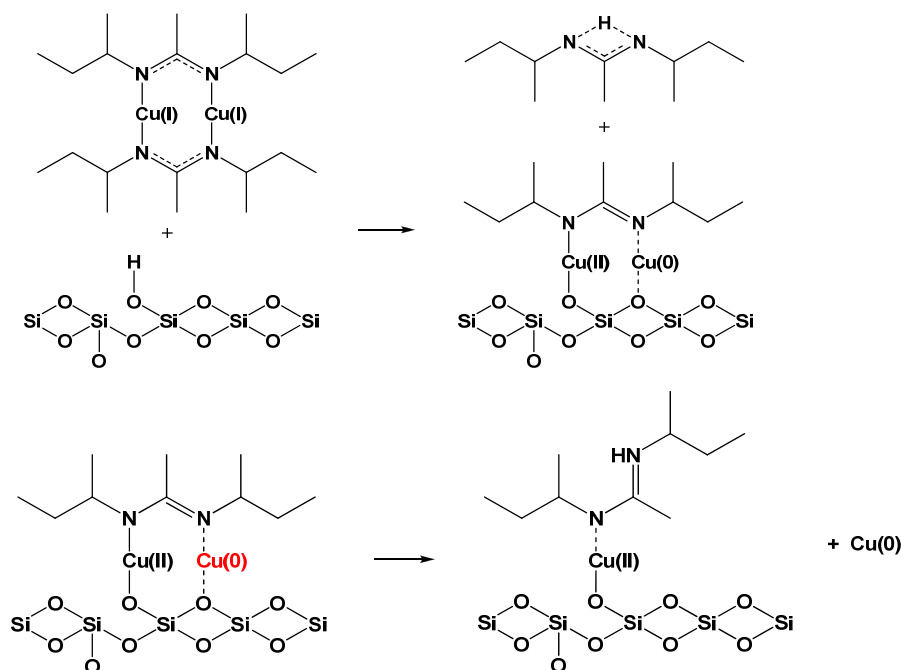


Fig 6.10 Schematic of ligand rearrangement on the surface. The ligand may be hydrogenated on the surface to have the mode at 1608 cm^{-1} (from the discussion with Prof. Roy Gordon and Dr. Mathew Halls).

This reaction can be activated by either temperature or H_2 . The temperature activated rearrangement occurs above 250°C as shown in Fig 6.9. However, the monodentate state also exists at lower temperatures as evidenced by a weak 1608 cm^{-1} band at 140°C - 220°C (Fig 6.5 and Fig 6.9) and a stronger 1608 cm^{-1} band at 100°C , which indicates that this feature may result from either the precursor thermal decomposition on the surface or source hydrolization.

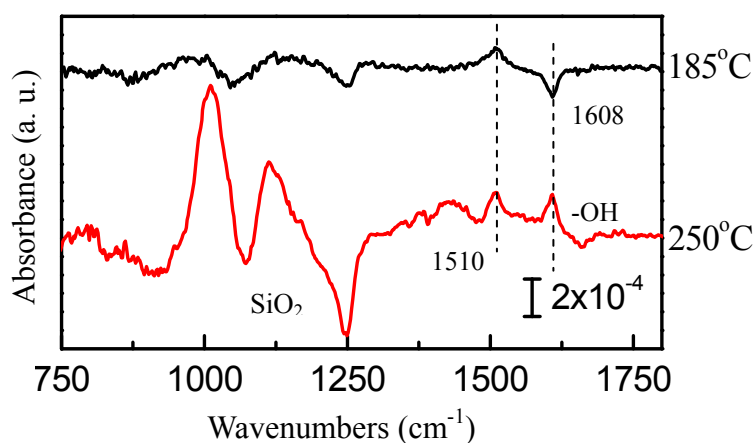


Fig 6.11 The ligand behavior: the Cu precursor is exposed to the SiO_2 at 250°C (the bottom spectrum which is reference to the initial SiO_2) and then is exposed to the precursor again at 185°C (the top spectrum which is reference to the bottom one). The incident angle of IR is $\sim 74^\circ$. It may indicate a competitive reaction.

There are some interesting behaviors of the ligand rearrangement. First, it is a competitive reaction. The rearranged ligand can be removed by the precursor with intact ligands, which can be observed in Fig 6.11. After the oxide surface is exposed to the precursor at 250°C , both bands at 1510 cm^{-1} and 1608 cm^{-1} are observed. After the subsequent Cu precursor dosing at 185°C on it, the 1608 cm^{-1} band is removed and additional 1510 cm^{-1} band is added on the surface, indicating the growth of another layer of Cu. The second feature of the rearranged ligand is that it can occur with the aid of H_2 . Fig 6.12 shows the 10th cycle Cu on SiO_2 at 185°C . Upon H_2 dosing, the 1510 cm^{-1} band

is removed and the 1608 cm^{-1} band appears, implying that a part of the bidentate ligands are rearranged to the hydrogenated monodentate state (HL). At 300°C , both intact (bidentate) and rearranged (monodentate) ligands are removed by H_2 as shown in Fig 6.9(a).

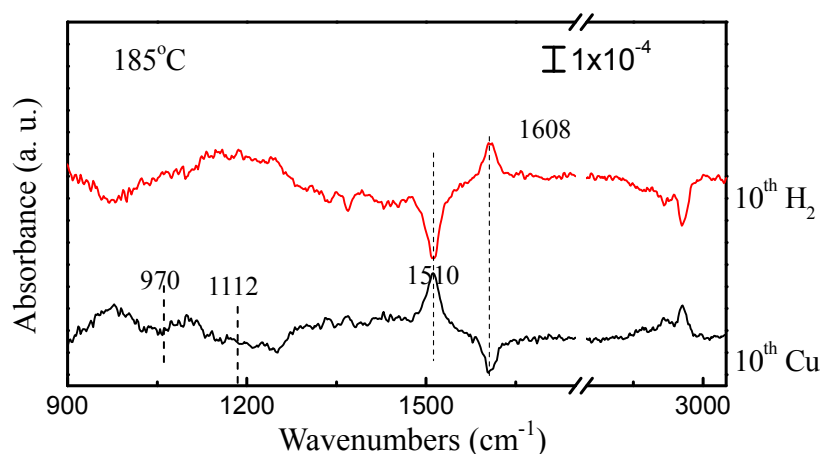


Fig 6.12 The differential spectra of the 10th cycle of Cu deposited on SiO_2 at 185°C : the 10th Cu spectrum is reference to the 9 cycles (9th H_2) and the 10th H_2 is reference to the 10th Cu. The incident angle of IR is $\sim 74^\circ$.

Note that another mode at 970 cm^{-1} appears simultaneously with 1112 cm^{-1} after the 10th Cu precursor dosing (see Fig. 6.12), and it can be possibly assigned to another mode of Cu in SiO_2 [25]. It has no polarization dependence according to the IR angle-dependence study. This mode appears as a shoulder after the 1st Cu precursor dosing as shown in Fig 6.5 and 6.9 but not at 100°C , confirming its assignment. Considering the ligand rearrangement and H_2 reactivity, the appropriate temperature range for the Cu deposition is between 140°C and 220°C ; i.e., monodentate state of hydrogenated ligand at 1608 cm^{-1} is minimal after the Cu precursor dosing and the reactivity of H_2 is high enough.

Cu deposition at 140°C and 125°C

As shown in Fig 6.9, less Cu agglomeration and diffusion is observed below 140°C

according to the variation in SiO_2 TO/LO modes. Thus, the growth temperature is accordingly lowered to 140°C and 125°C in order to study the dynamics of Cu atoms during the deposition.

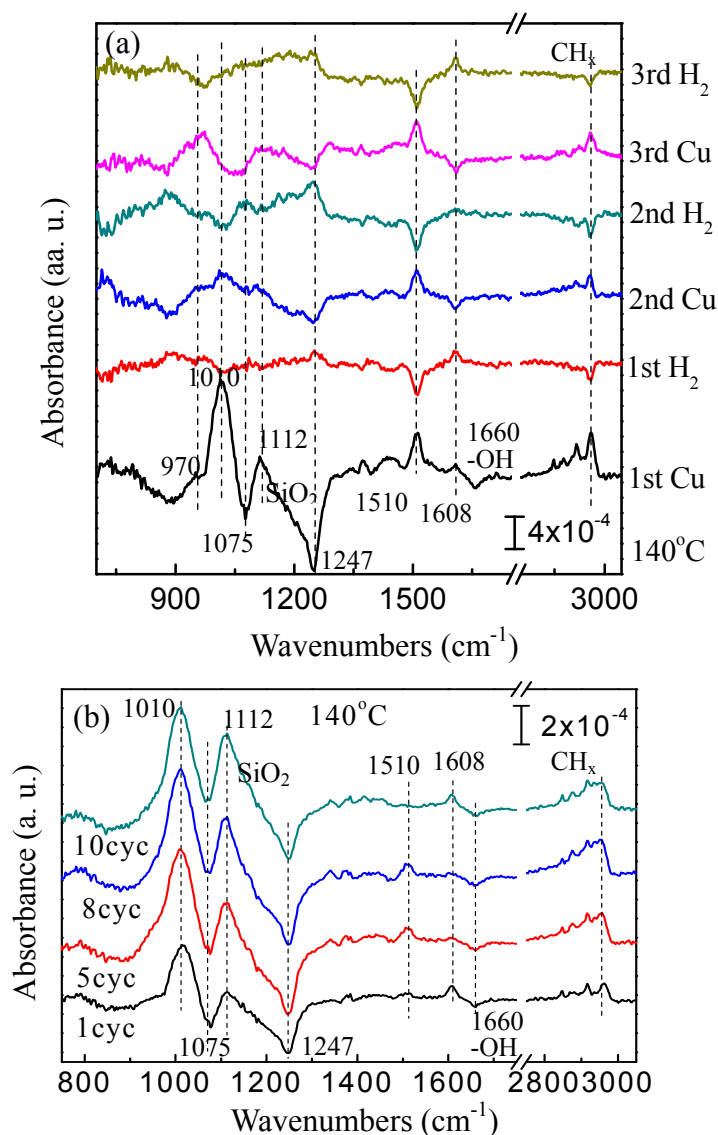


Fig 6.13 Results of 10 cycles Cu growth at 140°C . The incident angle of IR is $\sim 74^\circ$. (a) Differential spectra of the first 3 cycles Cu on oxide. Each spectrum is referenced to the spectrum recorded for the previous treatment. The bottom is referenced to initial oxide surface. (b) The absorption spectra up to 10 cycles Cu on SiO_2 , all the spectra are referenced to SiO_2 .

Figure 6.13 shows spectra of 10 cycles of Cu ALD at 140°C . The 1st Cu precursor

dosing shows similar reactivity as 185°C. But, upon the 1st H₂ dosing, almost no change in the SiO₂ phonon modes around 1000-1300 cm⁻¹ is observed, implying less Cu agglomeration due to the lowered temperature. The 1608 cm⁻¹ mode after the 1st H₂ dosing indicates that the intact ligand (1510 cm⁻¹) is rearranged to hydrogenated monodentate state by H₂ because of the low reactivity of H₂ at low temperature. The intensity of the 1608 cm⁻¹ band is about 60% of the 1510 cm⁻¹ band, indicating that most ligands may just be rearranged on the surface. Thus, the growth rate will be much lower than that of 185°C because of insufficient reaction of H₂ to remove the ligand.

Although the Cu agglomeration is absent for the 1st cycle, it occurs for the 2nd cycle. Upon the 2nd H₂ dosing, SiO₂ TO/LO modes are partially recovered again. Therefore, it can be concluded that the agglomeration only takes place when Cu reaches a critical thickness on the surface [33, 34]. The minimized diffusion of Cu is also seen in Fig 6.13(b) which shows different cycles Cu referenced to the oxide. The intensity of Cu-SiO_x band at 1112 cm⁻¹ is much less than that at 185°C, but it may also be caused by much less Cu deposition at lower temperature.

For the deposition at 125°C, as in Fig 6.14(a), the first cycle shows the same feature as at 140°C. But the agglomeration doesn't occur for the initial cycles until the 10th cycle where the agglomeration is observed after the H₂ dosing. The ligand related bands also show less change after H₂ exposures. All indicate that the growth rate is lower and more cycles are needed to reach the critical thickness for Cu agglomeration than that at 140°C. Fig 6.14(b) shows absorption spectra of up to 10 cycles Cu referenced to the oxide where even less Cu diffusion is observed. Note that remnant ligand impurities (according to the bands at 1510/1608 cm⁻¹ and 2800-3000 cm⁻¹) are observed in the for all cases (125°C-185°C).

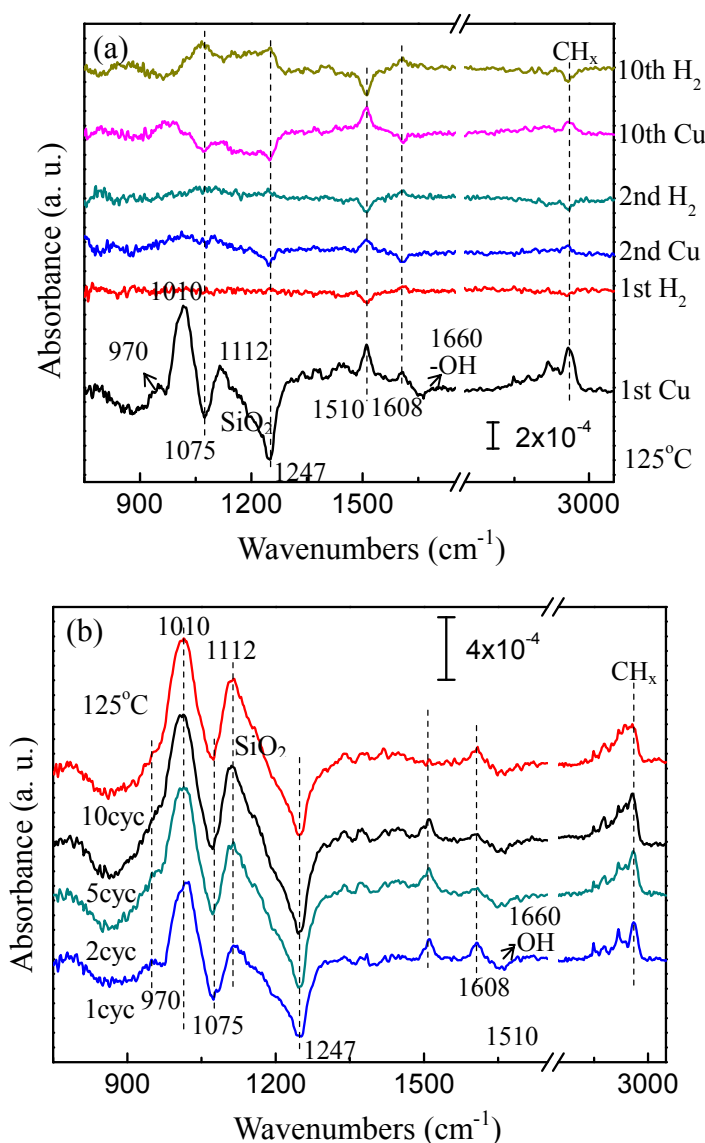


Fig 6.14 Results of 10 cycles Cu growth at 125°C. The incident angle of IR is $\sim 74^\circ$. (a) Differential spectra of the first 2 cycles Cu and 10th cycle on oxide. Each spectrum is referenced to the spectrum recorded for the previous treatment. The bottom is referenced to initial oxide surface and the 10th Cu is referenced to 9 cycles (9th H₂). (b) The absorption spectra up to 10 cycles Cu on SiO₂, all the spectra are referenced to SiO₂.

RBS and XPS analysis of Cu on SiO₂

The areal density of Cu atoms is measured by *ex situ* RBS. Table 6.1 shows the RBS results of 10 ALD cycles of Cu on SiO₂ at 125°C, 140°C, and 185°C with the accuracy

within 6%.

Table 6.1 The thickness of 10 cycles Cu on SiO₂ at different temperatures by RBS

Temperature (°C)	125	140	185
Thickness (nm)	0.29	0.64	1.18-1.04*

* According to the results of 2 identical experiments

At 185°C the growth rate is about 1.1 Å per cycle which is a typical ALD growth rate, while the growth rate decreases with the temperature. The decrease of the growth rate is caused by combined effects of diffusion, agglomeration and H₂ reactivity due to the temperature. Cu diffusion and agglomeration at higher temperature make more reactive sites available on the surface. Different positions on the sample for the growth at 185°C are tested by RBS and the same thickness is obtained implying a homogenous growth.

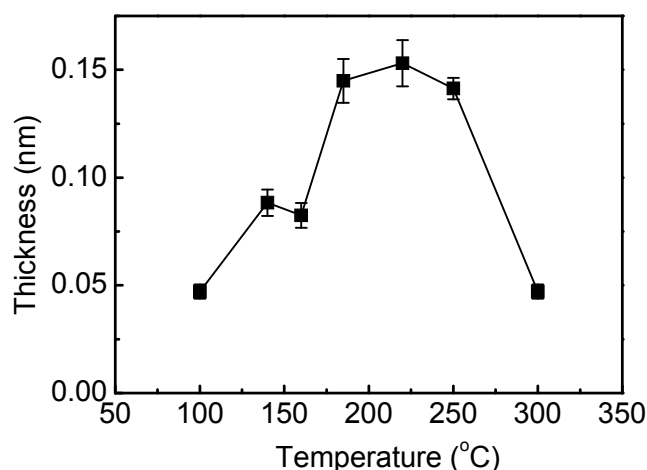


Fig 6.15 The relation between thickness of 1 cycle of Cu and growth temperature. The highest growth rate achieved at 185-250°C

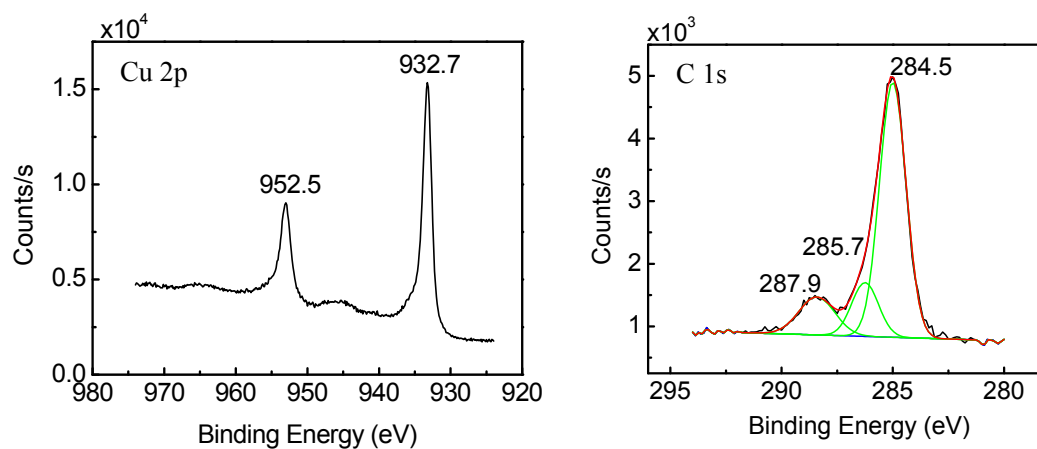
The Cu areal density on SiO₂ after one ALD cycle at different temperatures is summarized in Fig 6.15. The highest growth rate is obtained around 200°C. The low growth rate at below 185°C is due to insufficient surface reactions, and the decreased growth rate at 300°C could be the result of Cu desorption due to the low adhesion of Cu

to SiO₂ surface [35, 36] or system error. At 185°C, the thickness after the first cycle is about 1.4 Å which is higher than the growth rate derived from 10-cycle films (~1.1 Å), confirming that the growth rate decreases when the surface is covered by Cu [14].

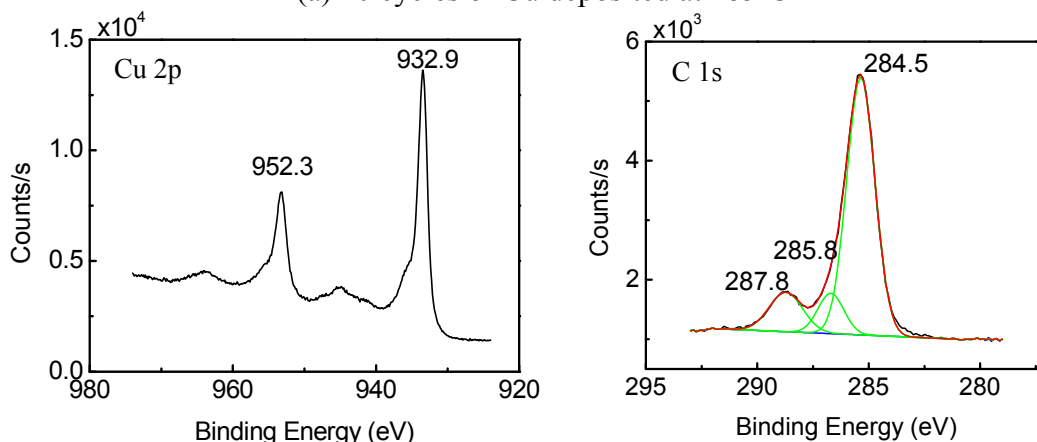
The element composition of the Cu film is analyzed by *ex situ* XPS measurements. All spectra are calibrated by C 1s at 284.5 eV. Fig 6.16(a)-(c) show the spectra of Cu 2p and C 1s of 10-cycle Cu films grown on SiO₂ at different temperatures, and table 6.2(a) summarizes the concentration of each element in the film. The low concentration of N indicates little ligand associated impurities is left in the Cu film. On the other hand, more Si and less Cu are detected with decreasing growth temperature, suggesting the growth rate decreases which is consistent with the RBS results. In addition, C 1s is fitted to three peaks as shown in Fig 6.16, where peak 1 is at 284.5 eV as the calibration, peak 2 is at ~285.8 eV and peak 3 is at ~287.8 eV, and table 6.2(b) shows their concentration relative to the total carbon. Peak 1 could be due to CH_x bonds, and peak 2 and 3 could result from C-N bonds of the residue ligand in the Cu film [37]. In Fig 6.16, the satellite shake-up peaks around 945 eV and 965 eV resulting from CuO become more obvious at low temperature [37, 38, 39]. The fitting results of Cu 2p_{1/2} are shown in table 6.2 (c) to see the CuO percentage relative to the total Cu amount (Cu⁰, Cu¹⁺, and Cu²⁺). It can be clearly observed that CuO concentration increases when we decrease the growth temperature.

The increase of CuO concentration with the decrease the growth temperature is confusing because Cu should be oxidized less and Cu diffusion is suppressed at low temperature. A possible explanation is that due to less Cu diffusion, more Cu atoms are exposed to the environment on the surface and readily oxidized. At high temperature such as 185°C, most of the Cu atoms diffuse into SiO₂ and therefore are prevented from

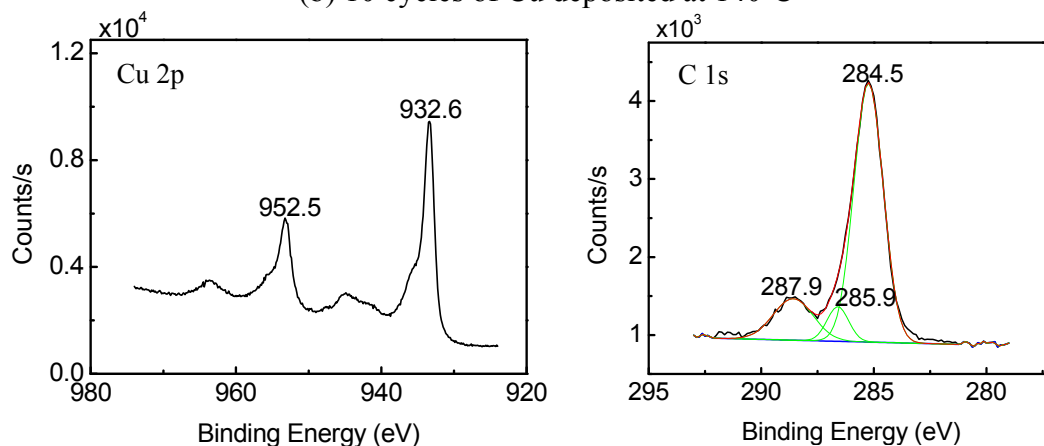
oxidation.



(a) 10 cycles of Cu deposited at 185°C



(b) 10 cycles of Cu deposited at 140°C



(c) 10 cycles of Cu deposited at 125°C

Fig 6.16 XPS results (Cu 2p and C 1s) of 10 cycles Cu on SiO₂ at different temperatures. The spectra are calibrated by C 1s at 284.5 eV. The C 1s is fitted to 3 peaks. The analysis is shown in table 6.2.

Table 6.2(a) The summary of element concentration by XPS results for 10 cycles of Cu on SiO₂ at different temperatures.

Elements		Cu	C	N	O	Si
Concentration (%)	185°C	17.8	47.6	1.8	26.8	6.0
	140°C	13.5	37.8	1.3	35.2	12.2
	125°C	11.2	30.1	0.9	41.8	16.0

Table 6.2 (b) The concentration of different carbons in total C for three fitted C 1s peaks for 10 cycles of Cu on SiO₂ at different temperatures. (Peak 1 ~284.5 eV, Peak 2 ~285.8 eV, and Peak 3 ~287.8 eV)

.C 1s (eV)	Peak 1	Peak 2	Peak 3
185°C	70.7	15.0	14.3
140°C	75.4	10.9	13.7
125°C	76.0	7.5	16.5

Table 6.2 (c) The relative CuO concentration in total Cu

Temperature	185°C	140°C	125°C
CuO (%) in Cu	13% ± 2%	20% ± 5%	26% ± 5%

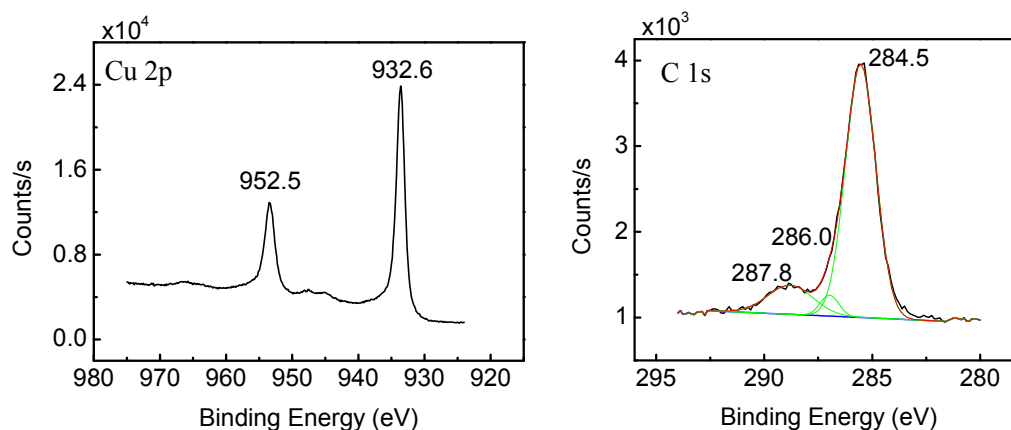


Fig 6.17 XPS results (Cu 2p and C 1s) of 10 cycles Cu on SiO₂ at 140°C (fresh sample transferred to XPS chamber immediately). The spectra are calibrated by C 1s at 284.5 eV. The amount of CuO and C impurities is reduced. Table 6.3 shows the analysis summary.

Table 6.3(a) The summary of element concentration by XPS results for 10 cycles of Cu on SiO₂ at 140°C (fresh sample transferred to XPS chamber immediately).

Elements	Cu	C	N	O	Si
Concentration (%)	20.1	26.3	1.6	38.2	13.8

Table 6.3 (b) The relative carbon concentration for three fitted C 1s peaks for 10 cycles of Cu on SiO₂ at 140°C. (Peak 1 ~284.5 eV, Peak 2 ~286.0 eV, and Peak 3 ~287.8 eV).

C 1s (eV)	284.5 (Peak 1)	286.0 (Peak 2)	287.8 (Peak 3)
Concentration in C (%)	81.8	4.2	14.0

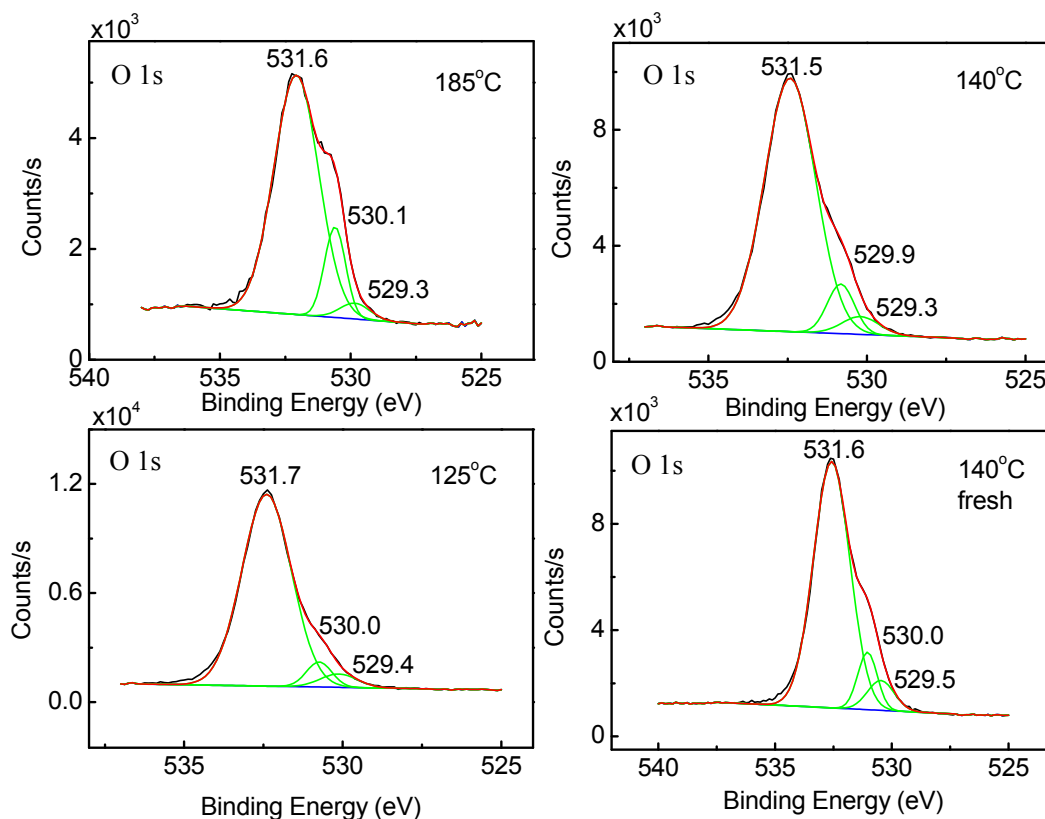


Fig 6.18 XPS results (O 1s) of 10 cycles Cu on SiO₂ at different temperatures (fresh sample transferred to XPS chamber immediately). The spectra are calibrated by C 1s at 284.5 eV. The O 1s is fitted to 3 peaks for SiO₂, CuO and Cu₂O, and the analysis is in table 6.4.

To prove this assumption, 10 cycles of Cu are deposited on SiO₂ at 140°C and then transferred into the XPS chamber immediately to minimize possible oxidation. Fig 6.17 shows the results by the XPS spectra. The shake-up satellite peaks from CuO are suppressed. The CuO is about 12% ± 3% of total Cu according to fitting results of Cu 2p_{1/2}, which is comparable to that of 185°C.

By comparing the concentration of each element in table 6.3(a) for the fresh sample

with table 6.2(a), the decreased C concentration in the fresh sample possibly indicates that carbon contamination is reduced due to the immediate measurement. So, an *in situ* XPS method is much more preferable for future studies.

In the spectra of Cu 2p, since Cu⁰ cannot be distinguished from Cu¹⁺ by XPS, we fit the O 1s to see if a clue can be obtained. Fig 6.18 shows the XPS spectra of O 1s, and table 6.4 summarizes the fitting results of three O 1s peaks possibly assigned to SiO₂ at ~531.6 eV, Cu₂O at ~530.1 eV and CuO at ~529.3 eV [37, 38, 39]. Combining table 6.2, 6.3, and 6.4 and assuming the Cu/O ratio of Cu₂O as 2:1 and CuO as 1:1, we can roughly estimate the percentage of pure Cu (Cu⁰) in all elements as shown in Table 6.5. Thus, we confirm the presence of Cu⁰ indirectly.

Table 6.4 The relative O concentration for three fitted O 1s peaks for 10 cycles of Cu on SiO₂ at different temperatures.

O 1s		Peak 4 (CuO ~529.4 eV)	Peak 5 (Cu ₂ O ~530.0 eV)	Peak 6 (SiO ₂ ~531.6 eV)
Concentration in O (%)	185°C	3.6%	14.5%	81.9%
	140°C	4.4%	8.9%	86.7%
	125°C	4.6%	6.0%	89.4%
	140°C (fresh)	7.3%	10.3%	82.4%

Table 6.5 The estimation of pure Cu (Cu⁰) concentration in all elements for 10 cycles of Cu on SiO₂ at different temperatures.

Concentration	185°C	9.06%
of pure Cu in	140°C	5.68%
all elements	125°C	4.26%
(%)	140°C (fresh)	9.44%

6.4 ALD of Cu on SiN_x and Al₂O₃

The surface reaction of [Cu(^sBu-amd)]₂ with other surfaces are studied including SiN_x and Al₂O₃ surfaces. SiN_x (~6 Å) is achieved by thermal annealing of H/Si(100) at

600°C for 2min as discussed in Chapter 3, and then 10 cycles Cu are deposited on it at 185°C. Al₂O₃ is achieved by 10 cycles TMA+D₂O on H/Si(111) at 300°C (~1 nm). Then Cu is deposited by using the same parameter as on SiO₂ at 185°C.

10 cycles of Cu on SiN_x at 185°C

The spectrum associated with silicon nitride, grown on H/Si (100), is shown in the inset of Fig 6.19, which is referenced to the H/Si (100) surface. The negative band around 2100 cm⁻¹ indicates the loss of all Si-H_x during the nitridation at 600°C. A peak centered at 1545 cm⁻¹ is associated with the scissor mode of -NH₂. SiN_x phonon modes (TO/LO) are observed around 840 cm⁻¹ and 1058 cm⁻¹, showing the formation of a SiN_x layer. A noticeable peak centered at 936 cm⁻¹ is caused by the loss of Si-H₂ (dihydride scissor mode at 914 cm⁻¹) [40].

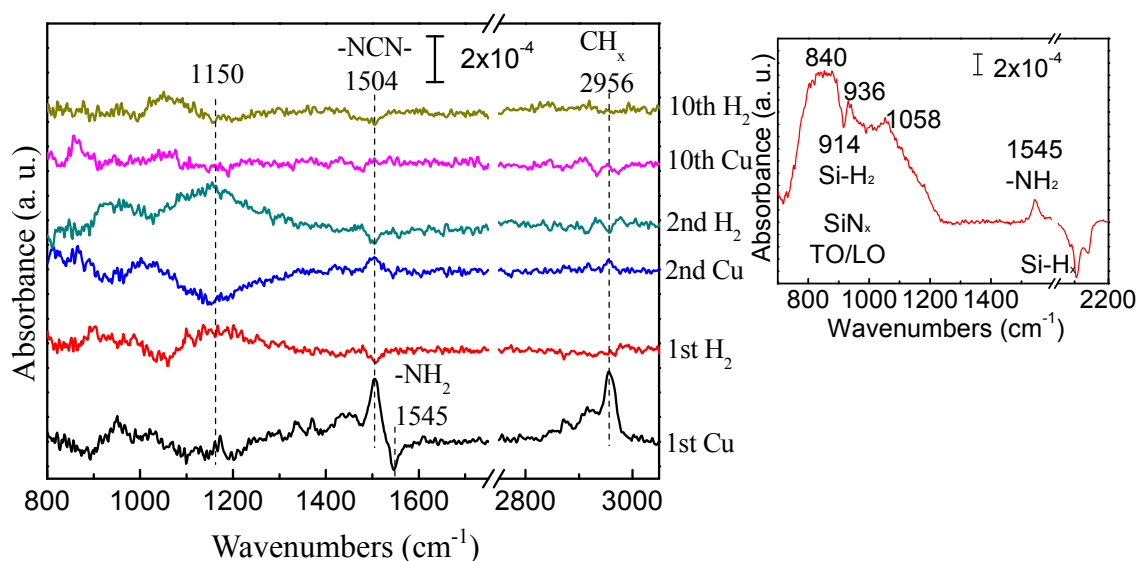


Fig 6.19 Differential FTIR absorption spectra of 10 cycles (H₂ dosing after Cu(^sBu-amd)₂) Cu on SiN_x at 185°C. Each spectrum is referenced to that of the previous surface and the bottom spectrum is referenced to the SiN_x starting surface. The Cu dosing is referenced to H₂ dosing and the 10th Cu is referenced to the 9 cycles (9th H₂). The inset is the spectrum of the SiN_x starting surface referenced to the H/Si (100) surface.

Fig 6.19 summarizes the differential spectra associated with each half cycle for up to 10 cycles of copper deposited on the nitrated surface. The variation of the mode around 1150 cm^{-1} is due to the interaction between the surface and the Cu precursor, which is related to surface $\text{Cu-SiN}_x/\text{Cu-O-SiN}_x$ bonds. It is relatively weak compared to SiO_2 surface as discussed in the previous section. The intensity recovery of the band around 1150 cm^{-1} after H_2 may suggest the agglomeration of Cu on the surface. The intensity loss of $\delta(\text{NH}_2)$ at 1545 cm^{-1} and observation of $\nu(\text{NCN})$ at 1504 cm^{-1} due to intact ligands attached to Cu on the SiN_x surface, imply that the reaction starts by replacing surface $-\text{NH}_2$ with the Cu precursor.

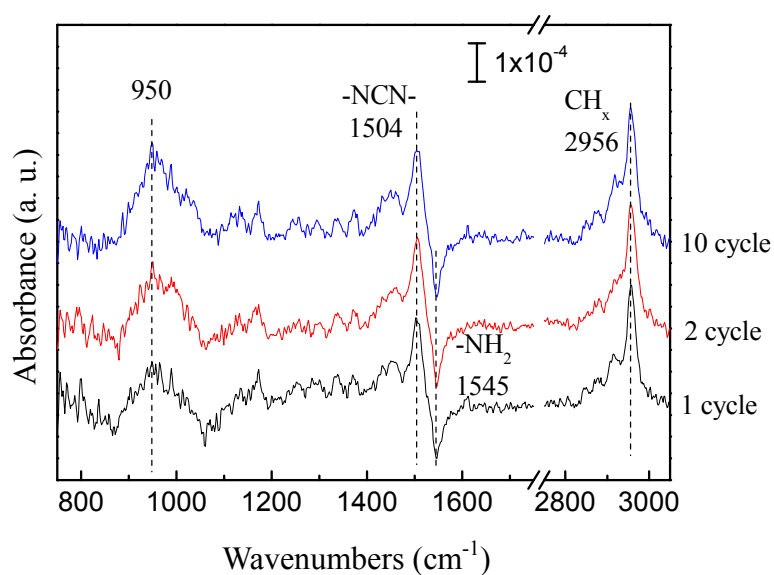


Fig 6.20 FTIR absorption spectra of 10 cycles Cu on SiN_x at 185°C . All spectra are referenced to SiN_x surface. Less Cu agglomeration and low growth rate are found.

The ALD feature of ligand exchange is observed by the variation of CH_x stretching modes at $\sim 2956\text{ cm}^{-1}$ and $\nu(\text{NCN})$ at 1504 cm^{-1} ; i.e., increase upon copper precursor exposures and decrease upon H_2 exposures. Comparing with SiO_2 , the reduced intensity of the ligand exchange and very little change in the spectra of the 10th cycle indicate a much lower growth rate. *Ex situ* RBS confirms that the thickness of 10 cycles Cu on SiN_x

at 185°C is only about 0.14 nm. It indicates that the reactivity of this precursor is very low on the SiN_x obtained by thermal NH₃ nitridation, and is consistent with the IR study. The spectra of up to 10 cycles Cu on SiN_x referenced to the starting SiN_x surface are shown in Fig 6.20. Most of the reaction occurs at the first cycle. No clear Si-O-Cu or Cu in SiO₂ bands as on SiO₂ surface are observed in this case. The peak at 950 cm⁻¹ may be related to thermal effects of IR absorption of the substrate or Cu/SiN_x complex. XPS analysis summarized in table 6.6(a) also confirms that the Cu concentration on this surface is very low.

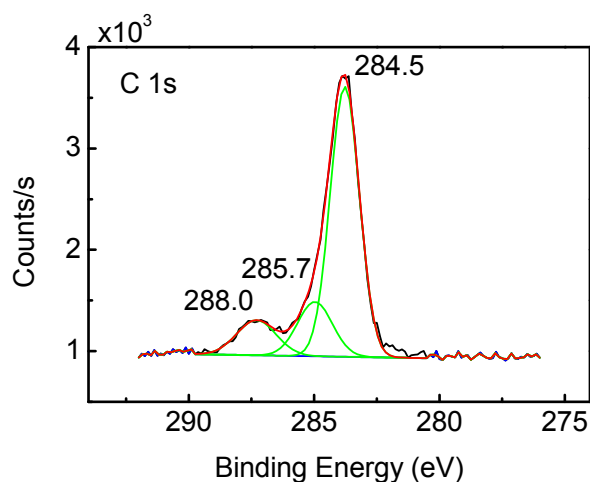


Fig 6.21 XPS results (C 1s) of 10 cycles Cu on SiN_x at 185°C. The spectra are calibrated by C 1s at 284.5 eV. The C 1s is fitted to 3 peaks. The analysis is shown in table 6.6.

Table 6.6(a) The summary of element concentration by XPS results for 10 cycles of Cu on SiN_x at 185°C

Elements	Cu	C	N	O	Si
Concentration (%)	4.5	31.4	10.0	21.4	32.7

Table 6.6(b) The relative carbon concentration for three fitted C 1s peaks for 10 cycles of Cu on SiN_x at 185°C

C 1s (eV)	284.5 (Peak 1)	285.7 (Peak 2)	288.0 (Peak 3)
Concentration in C (%)	70.7	17.0	12.3

The XPS spectrum of C 1s shows the same feature as on the SiO₂ surface and can be fitted to three peaks as in Fig 6.21 and table 6.6(b), where peak 1 (284.5 eV) may be related to CH_x bonds, and peak 2 (285.7 eV) and 3 (288.0 eV) are possibly related to C-N bonds in the residue ligands. By the fitting of Cu 2p_{1/2}, the CuO percentage in total Cu (Cu⁰, Cu¹⁺, and Cu²⁺) is about 57% ± 6%. The relatively high CuO amount may be the result of reduced diffusion so that most Cu atoms are on the surface and oxidized before the measurement.

10 cycles of Cu on Al₂O₃ at 185°C

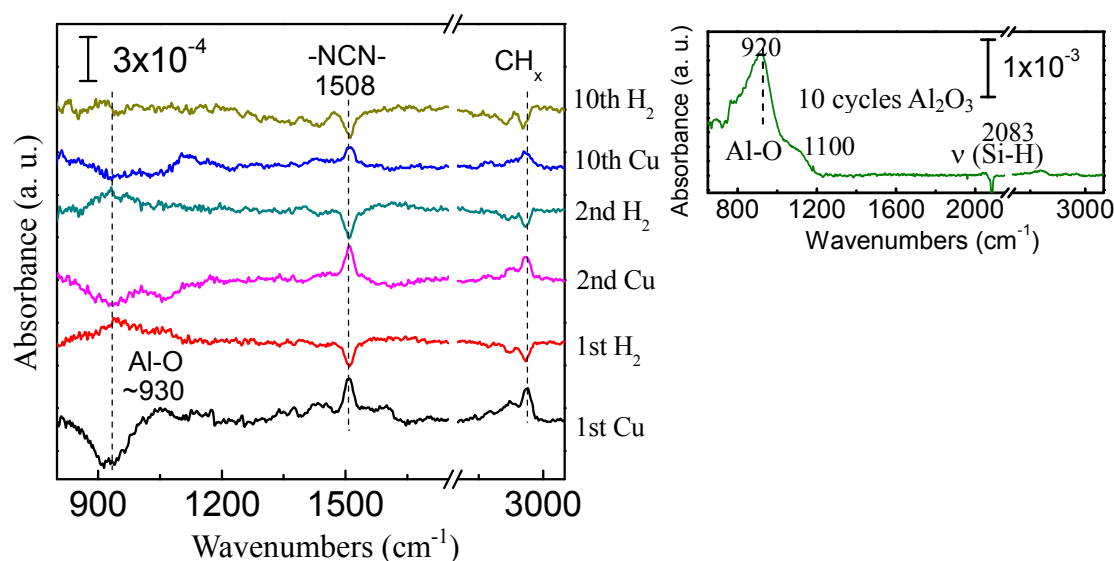


Fig 6.22 Differential FTIR absorption spectra of 10 cycles copper ALD on Al₂O₃ at 185°C. Each spectrum is referenced to the previous surface. The 1st Cu is referenced to Al₂O₃ starting surface and the 10th Cu is referenced to 9th cycle (9th H₂). The inset is the 10 cycles Al₂O₃ starting surface referenced to H/Si (111) surface. ALD ligand exchange is observed.

Al₂O₃ is a typical high-κ oxide, and it is quite interesting to study the Cu growth on it in order to test the application of this precursor to deposit metal on high-κ oxide. Fig 6.22 shows the differential spectra of 10 cycles Cu ALD on Al₂O₃ at 185°C. The Al₂O₃

film is deposited by 10 ALD cycles with TMA/D₂O on H/Si(111) at 300°C. The absorption spectrum of Al₂O₃ film referenced to H/Si (111) is shown in the inset of Fig 6.22. The negative peak at 2083 cm⁻¹ indicates that all the surface hydrogen is removed upon Al₂O₃ deposition. The broad peak centered at 920 cm⁻¹ corresponds to Al₂O₃ phonon mode confirming the formation of an Al₂O₃ thin film. The shoulder at ~1100 cm⁻¹ is due to the interfacial Si-O bonds.

As shown in Fig 6.22, similar to what has been observed on the SiO₂ surface upon the first dose of [Cu(^sBu-amd)]₂, a broad negative peak around 920 cm⁻¹ due to the perturbed Al₂O₃ phonon mode is observed, resulting from chemical interactions of the Cu precursor with the surface. After the 1st H₂ dosing, this absorbance feature is partially recovered as evidenced by a positive band at the same spectral position. The same trend is observed for the subsequent cycles. These observations may suggest the Cu agglomeration on Al₂O₃ as on SiO₂.

The ν(CH_x) intensity increase after Cu precursor exposures and the partial decrease after H₂ exposures in the 2800 cm⁻¹-3000 cm⁻¹ range are observed all the way up to the 10th cycle. Together with the variation of ν(NCN) at 1508 cm⁻¹ (intact ligand on Cu), they are related to the exchange of intact -NCN- ligands on Cu. That is, after the Cu precursor dosing, the Cu precursor with -NCN- ligands is chemically bonded to the surface and after the H₂ dosing, the ligands are removed. According to *ex situ* RBS, the Cu thickness is about 0.44 nm for 10 cycles. XPS analysis in table 6.7(a) also shows the low Cu concentration, confirming the small amount of Cu on this surface.

The XPS C 1s shows the same feature as on the SiO₂ surface. The fitting results of the three peaks are summarized in table 6.7(b), where peak 1 (284.5 eV) may be related to CH_x, and peak 2 (285.8 eV) and 3 (287.9 eV) are possibly related to C-N bonds in the

residue ligands. According to the fitting of Cu 2p_{1/2}, the CuO percentage in total Cu (Cu⁰, Cu¹⁺, and Cu²⁺) is about 22% ± 5%, which is higher than that of Cu on SiO₂ at 185°C and may also imply less Cu diffusion into Al₂O₃.

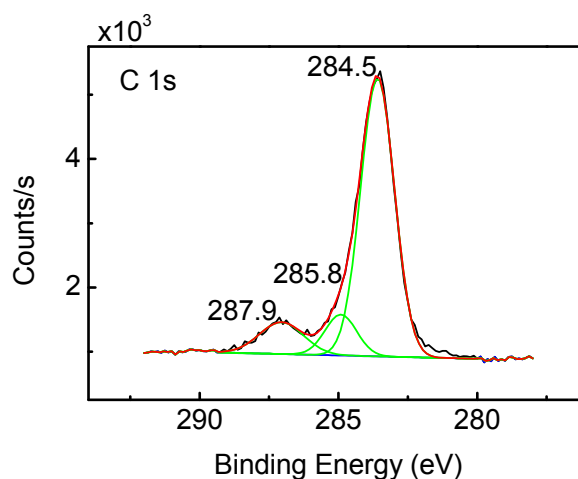


Fig 6.23 XPS results (C 1s) of 10 cycles Cu on Al₂O₃ at 185°C. The spectra are calibrated by C 1s at 284.5 eV. The C1s is fitted to 3 peaks. Table 6.7 shows the XPS analysis summary.

Table 6.7(a) The summary of element concentration by XPS results for 10 cycles of Cu on Al₂O₃ at 185°C

Elements	Cu	C	N	O	Si	Al
Concentration (%)	6.0	38.0	0.8	20.5	8.8	25.9

Table 6.7(b) The relative carbon concentration for three fitted C 1s peaks10 cycles of Cu on Al₂O₃ at 185°C

C 1s (eV)	284.5 (Peak 1)	285.8 (Peak 2)	287.9 (Peak 3)
Concentration (%) in C	77.8	10.6	11.6

6.5 Other application: deposition of Cu₃N

Including deposition of Cu, this Cu precursor can also be used to deposit nitride with NH₃. According to recent studies, Cu₃N has been utilized as a material for optical storage

devices in microelectronics [41]. It is an insulating material with low reflectivity and high resistivity, and is also a promising candidate as an insulating barrier in magnetic tunnel junctions [42]. Moreover, it is metastable that it decomposes to N_2 and Cu above 200°C [43]. This property is useful for write-once optical data storage. Recently, Gordon's group has succeeded to deposit pure, smooth, continuous, and conformal copper films by thermal reduction of Cu_3N using this metastable property [43]. So it is interesting to utilize *in situ* FTIR to study the surface reactions of this process.

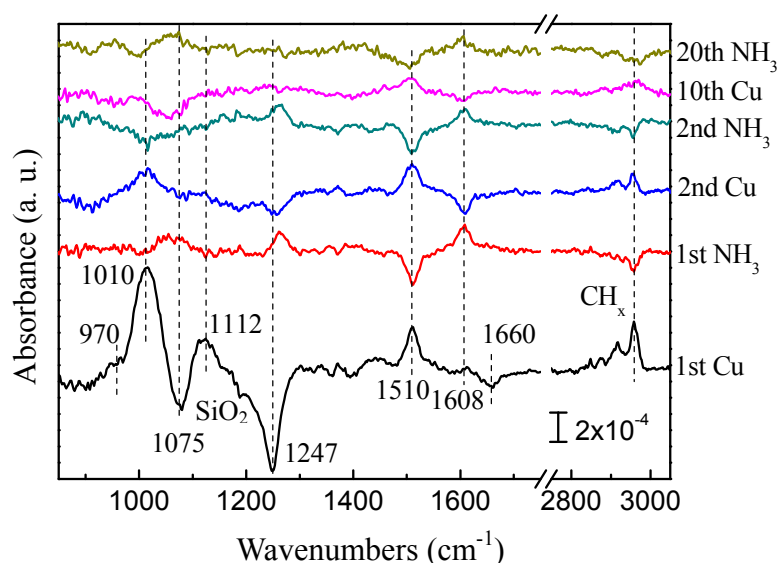


Fig 6.24 Differential FTIR absorption spectra of 20 cycles Cu_3N on SiO_2 at 160°C . Each spectrum is referenced to the previous surface. The 1st Cu is referenced to SiO_2 starting surface and the 20th Cu is referenced to 19th cycle (19th NH_3). ALD ligand exchange is observed.

Cu_3N is deposited by using $[\text{Cu}(\text{sBu-amd})]_2$ and NH_3 at 160°C on a thin silicon oxide surface, which is reported to produce stoichiometrical Cu_3N [43]. The Cu precursor pulse length is 35s and the NH_3 pulse length is 100s to ensure surface saturation. The differential spectra of 20 cycles Cu_3N are shown in Fig 6.24. The 1st Cu dosing on SiO_2 is featured by the loss of SiO_2 phonon modes (1075 cm^{-1} and 1247 cm^{-1}) and the gain of

Si-O-Cu mode (1010 cm^{-1}) as well as the Cu diffusion in SiO_2 modes (970 cm^{-1} and 1112 cm^{-1}). The loss of -OH bending mode at 1660 cm^{-1} indicates the replacement of -OH group by the Cu precursor. The 1st NH_3 exposure reacts with the intact ligand [$\nu(\text{NCN})$ at 1510 cm^{-1}] from the previous Cu precursor dosing. The appearance of the band at 1608 cm^{-1} indicates that a big part of the intact ligands are not removed but rearranged by NH_3 . Therefore, only a part of $\nu(\text{CH}_x)$ around 2956 cm^{-1} is reduced. A little Cu agglomeration is observed by the weak band at 1247 cm^{-1} in the spectrum of the 1st NH_3 dosing.

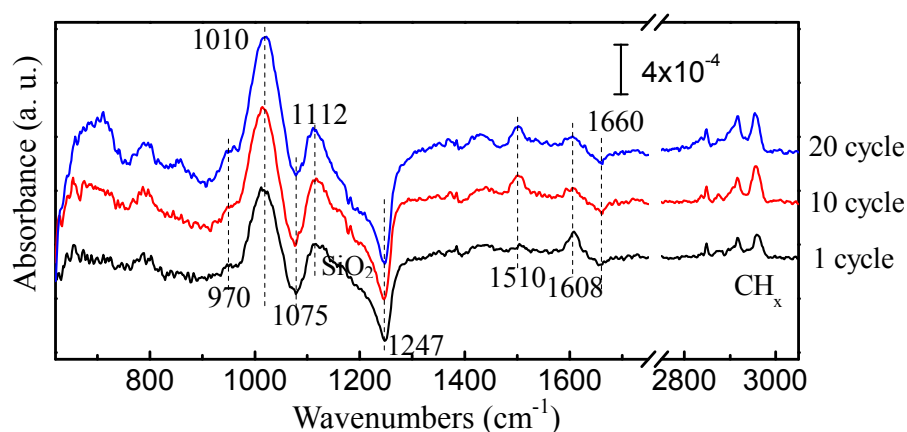


Fig 6.25 FTIR absorption spectra of 20 cycles Cu_3N on SiO_2 at 160°C . All spectra are referenced to SiO_2 surface. Less Cu diffusion and some ligand related impurities are observed in the spectra. The growth rate is low.

There is an increase of the intact ligand upon the 2nd Cu pulse as evidenced by a positive 1510 cm^{-1} peak. This 2nd Cu pulse also removes the rearranged ligand band at 1608 cm^{-1} as shown in the previous section. The variation in the SiO_2 phonon modes suggests that the previous NH_3 dosing reacts with the ligand on the surface, recovering more reaction sites on the SiO_2 surface for the subsequent Cu precursor. For the following cycles, the same scheme continues. The decreased ligand feature for 20th cycle indicates the growth rate decreases with more ALD cycles.

By using the starting SiO_2 surface as the reference, the accumulation of all substances of the film is studied as shown in Fig 6.25. Very little agglomeration and diffusion are observed in this case compared to the Cu deposition on SiO_2 , implying a smooth and uniform growth.

The 20-cycle Cu_3N film is annealed in forming gas [mixture of H_2 (10%) in N_2 , ~ 5.2 torr, 5 min] at 200°C and then at 225°C to reduce the film to Cu. Fig 6.26 shows the FTIR absorption spectra of the annealing which are all referenced to the as-deposited Cu_3N film. A part of the intact and rearranged ligands are removed as evidenced by the negative peaks at 1510 cm^{-1} and 1608 cm^{-1} as well as the loss of CH_x stretching modes. At 225°C , the decomposition of Cu_3N film is more obvious. A broad peak around 1200 cm^{-1} assigned to SiO_2 phonon mode may suggest the agglomeration of Cu. Since the intensity is weak, the Cu agglomeration is not as drastic as on SiO_2 surface.

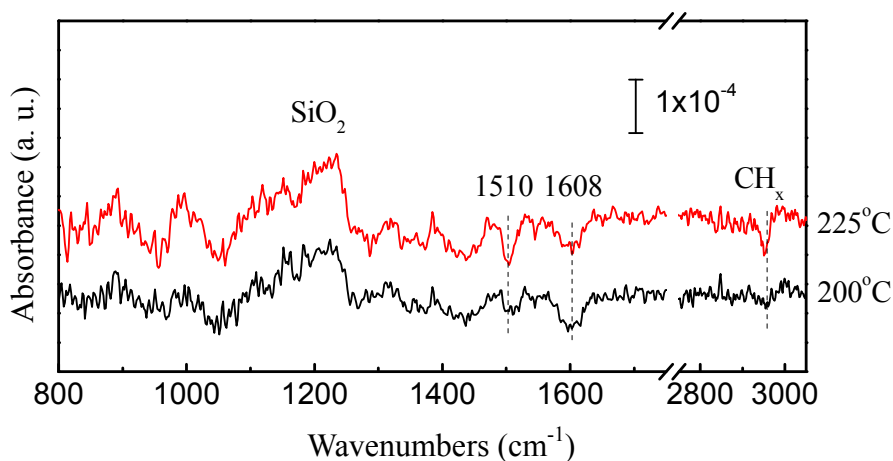


Fig 6.26 FTIR absorption spectra of 20 cycles Cu_3N reduced by forming gas. All spectra are referenced to 20 cycles as-deposited Cu_3N on SiO_2 surface. Only part of the ligand-related modes are reduced.

The XPS analysis is summarized in table 6.8. The Cu concentration suggests a low deposition growth rate. According to RBS measurement, the thickness of the Cu reduced

from 20-cycle Cu_3N is ~ 0.34 nm.

Table 6.8 The summary of element concentration by XPS results for 20 cycles of reduced Cu_3N

Elements	Cu	C	N	O	Si
Concentration (%)	9.8	40.1	2.1	34.2	13.8

6.6 Summary

As a summary of this chapter, we successfully deposited copper using a novel liquid Cu precursor--copper(I) di-sec-butylacetamidinate ($[\text{Cu}(\text{sBu-amd})]_2$) and molecular hydrogen on different substrates. The gas phase IR spectrum shows that the precursor is partially hydrolyzed. *In-situ* FTIR spectroscopy, *ex situ* RBS, and XPS are used to study the ALD processes with the temperature range from 100°C to 300°C . On oxidized Si(100) surfaces ($\sim 6\text{-}10$ nm SiO_2), the evolution of SiO_2 phonon modes in the IR spectra clearly shows the agglomeration and the diffusion of Cu on/into SiO_2 during the initial 10 cycles. Cu agglomeration and diffusion increase when the deposition temperature is raised. The hydrogen reduction of the surface ligand and ligand rearrangement are observed by the modes attributed to CH_x and $-\text{NCN}-$ bonds.

Ex situ XPS results confirm the deposition of copper on the SiO_2 surface. Both FTIR and XPS results show residue ligand impurities inside the Cu film with small amount of N ($< 2\%$) and substantial amount of C for the initial cycles due to incomplete ALD reactions. The Cu growth rate is determined by *ex situ* RBS measurements. The maximum growth rate on SiO_2 is found in the range of $185\text{-}250^\circ\text{C}$ based on one ALD cycle. At 185°C , the thickness of 10 cycles Cu is $1.04\text{-}1.18$ nm, and the film is very uniform.

The Cu deposition at 185°C on other surfaces are studied as well, such as the

hydrogen -terminated Si(111) and Si (100), nitrided Si(100) (SiN_x) and Al_2O_3 surfaces. FTIR and XPS show the similar film contents and growth mechanism as on SiO_2 . However, much lower growth rate is found for all those surfaces than that of SiO_2 surface; i.e., 0.09 nm on H/Si(111), 0.14 nm on SiN_x and 0.44 nm on Al_2O_3 after 10 ALD cycles. This indicates that $[\text{Cu}(\text{sBu-amd})]_2$ has low adhesion on those surfaces.

At last, Cu_3N is deposited on SiO_2 at 160°C successfully. The ligand exchange of the ALD process is observed by FTIR. After annealing at 225°C in forming gas, the Cu_3N is partially reduced to Cu with little Cu agglomeration. FTIR spectra show the incomplete loss of CH_x and ligand bands, and XPS analysis confirms the residue C and N impurities.

Bibliography

1. R. G. Gordon, D. M. Hausmann, E. Kim and J. Shepard, *A kinetic model for step coverage by atomic layer deposition in narrow holes or trenches*, Chemical Vapor Deposition **9** (2003), 83.
2. B. S. Lim, A. Rahtu and R. G. Gordon, *Atomic layer deposition of transition metals*, Nature Materials **2** (2003), 749-754.
3. J. Marika, R. Mikko and L. Markku, *Deposition of copper films by an alternate supply of CuCl and Zn*, Journal of Vacuum Science & Technology A **15** (1997), no. 4, 2330-2333.
4. C. Musgrave and R. G. Gordon, *Precursors for atomic layer deposition of high-k dielectrics*, Future Fab International **18** (2005), 126-128.
5. *The international technology roadmap for semiconductors, semiconductor industry association*, <http://pulic.itrs.net>. (2005).
6. K. Jae Jeong, K. Soo-Kil, L. Chang Hwa and K. Yong Shik, *Investigation of various copper seed layers for copper electrodeposition applicable to ultralarge-scale integration interconnection*, Journal of Vacuum Science & Technology B **21** (2003), no. 1, 33-38.
7. P. Martensson and J.-O. Carlsson, *Atomic layer epitaxy of copper on tantalum*, Chemical Vapor Deposition **3** (1997), no. 1, 45-50.
8. M. Per and C. Jan-Otto, *Atomic layer epitaxy of copper*, Journal of the Electrochemical Society **145** (1998), no. 8, 2926-2931.
9. J. Christopher, W. A. Lanford, J. W. Christopher, J. P. Singh, I. W. Pei, J. S. Jay and L. Toh-Ming, *Inductively coupled hydrogen plasma-assisted Cu ALD on metallic and dielectric surfaces*, Journal of the Electrochemical Society **152** (2005), no. 2, C60-C64.
10. S. Raj and P. Balu, *Atomic layer deposition of copper seed layers*, Electrochemical

and Solid-State Letters **3** (2000), no. 10, 479-480.

11. J. Huo, R. Solanki and J. McAndrew, *Characteristics of copper films produced via atomic layer deposition*, Journal of Materials Research **17** (2002), 2394-2398.

12. M. Utriainen, M. Kröger-Laukkanen, L.-S. Johansson and L. Niinistö, *Studies of metallic thin film growth in an atomic layer epitaxy reactor using $M(acac)_2$ ($M=Mi, Cu, Pt$) precursors*, Applied Surface Science **157** (2000), no. 3, 151-158.

13. N. Antti, R. Antti, S. Timo, A. Kai, R. Mikko and L. Markku, *Radical-enhanced atomic layer deposition of metallic copper thin films*, Journal of the Electrochemical Society **152** (2005), no. 1, G25-G28.

14. Z. Li, A. Rahtu and R. G. Gordon, *Atomic layer deposition of ultrathin copper metal films from a liquid copper(I) amidinate precursor*, Journal of Electrochemical Society **153** (2006), C787-C794.

15. N. Benouattas, A. Mosser, D. Raiser, J. Faerber and A. Bouabellou, *Behaviour of copper atoms in annealed Cu/SiO_x/Si systems*, Applied Surface Science **153** (2000), no. 2-3, 79-84.

16. J. D. McBrayer, R. M. Swanson and T. W. Sigmon, *Diffusion of metals in silicon dioxide*, Journal of the Electrochemical Society **133** (1986), no. 6, 1242-1246.

17. Z. Li, S. T. Barry and R. G. Gordon, *Synthesis and characterization of Cu(I) amidinates as precursors for atomic layer deposition (ALD) of copper metal*, Inorganic Chemistry **44** (2005), 1728-1735.

18. Y. J. Chabal, G. S. Higashi, K. Raghavachari and V. A. Burrows, *Infrared spectroscopy of Si(111) and Si(100) surfaces after HF treatment: Hydrogen termination and surface morphology*, J. Vac. Sci. Technol. A **7**(3) (1989), 2104.

19. L. Stolt and F. M. D'Heurle, *The formation of Cu₃Si: Marker experiments*, Thin Solid Films **189** (1990), no. 2, 269-274.

20. C. Chin-An, *Formation of copper silicides from Cu(100)/Si(100) and Cu(111)/Si(111) structures*, Journal of Applied Physics **67** (1990), no. 1, 566-569.

21. R. R. Chromik, W. K. Neils and E. J. Cotts, *Thermodynamic and kinetic study of solid state reactions in the Cu-Si system*, Journal of Applied Physics **86** (1999), no. 8, 4273-4281.

22. R. T. Conley, *Infrared spectroscopy*, Allyn and Bacon, Inc. (1972).

23. C.-Y. Yang, J. S. Jeng and J. S. Chen, *Grain growth, agglomeration and interfacial reaction of copper interconnects*, Thin Solid Films **420-421** (2002), 398-402.

24. Y. Ching-Yu and J. S. Chen, *Investigation of copper agglomeration at elevated temperatures*, Journal of the Electrochemical Society **150** (2003), no. 12, G826-G830.

25. S. Ishizuka, S. Kato, Y. Okamoto and K. Akimoto, *Control of hole carrier density of polycrystalline Cu₂O thin films by Si doping*, Appl. Phys. Lett. **80** (2002), 950.

26. H. Kim and J. Jand, *Infrared spectroscopic study of SiO_x film formation and decomposition of vinyl silane derivative by heat treatment on copper surface*, J. Appl. Polym. Sci. **68** (1998), 785.

27. X. Su, J. Zhao, X. Zhao, Y. Guo, Y. Zhu and Zichen Wang, *A facile synthesis of*

- Cu₂O/SiO₂ and Cu/SiO₂ core-shell octahedral nanocomposites*, Nanotechnology **19** (2008), 365610.
28. G. Papadimitropoulos, N. Vourdas, V. E. Vamvakas and D. Davazoglou, *Optical and structural properties of copper oxide thin films grown by oxidation of metal layers*, Thin Solid Films **515** (2006), 2428.
 29. B. Balamurugan and B. R. Mehta, *Optical and structural properties of nanocrystalline copper oxide thin films prepared by activated reactive evaporation*, Thin Solid Films **396** (2001), 90.
 30. H. Wu, S. R. Desai and L.-S. Wang, *Two isomers of CuO₂: The Cu(O₂) complex and the copper dioxide*, J. Chem. Phys. **103** (1995), 4363.
 31. J. B. Zhou, T. Gustafsson and E. Garfunkel, *The structure and thermal behavior of Cu on ultrathin films of SiO₂ on Si(111)*, Surface Science **372** (1997), no. 1-3, 21-27.
 32. C. Chin-An, *High-temperature interaction studies of C/Cu/SiO₂/Si and related structures*, Journal of Applied Physics **66** (1989), no. 3, 1163-1169.
 33. S. E. Offerman, N. H. van Dijk, J. Sietsma, S. Grigull, E. M. Lauridsen, L. Margulies, H. F. Poulsen, M. T. Rekveldt and S. van der Zwaag, *Grain nucleation and growth during phase transformations*, Science **298** (2002), no. 5595, 1003-1005.
 34. K.-N. Tu, J. W. Mayer and L. C. Feldman, *Electronic thin film science: For electrical engineering and materials scientist*, Prentice Hall (1996).
 35. K. Nagao, J. B. Neaton and N. W. Ashcroft, *First-principles study of adhesion at Cu/SiO₂ interfaces*, Physical Review B **68** (2003), no. 12, 125403.
 36. C. J. Liu, J. S. Jeng, J. S. Chen and Y. K. Lin, *Effects of Ti addition on the morphology, interfacial reaction, and diffusion of Cu on SiO₂*, Journal of Vacuum Science & Technology B: Microelectronics and Nanometer Structures **20** (2002), no. 6, 2361-2366.
 37. J. F. Moulder, N. F. Stickle, P. E. Sobol and K. D. B. I. J. Chastain, *Handbook of X-ray photoelectron spectroscopy*, Perkin-Elmer Corporation (1995).
 38. J. P. Espinos, J. Morales, A. Barranco, A. Caballero, J. P. Holgado and A. R. Gonzalez-Elipe, *Interface effects for Cu, CuO, and Cu₂O deposited on SiO₂ and ZrO₂. XPS determination of the valence state of copper in Cu/SiO₂ and Cu/ZrO₂ catalysts*, J. Phys. Chem. B **106** (2002), 6921.
 39. C. C. Chusuei, M. A. Brookshier and D. W. Goodman, *Correlation of relative X-ray photoelectron spectroscopy shake-up intensity with CuO particle size*, Langmuir **15** (1999), 2806.
 40. Y. Wang, M. Dai, S. Rivillon, M. T. Ho and Y. J. Chabal, *In situ infrared absorption spectroscopy for thin films growth by atomic layer deposition*, Proc. SPIE **6325** (2006), 63250G.
 41. D. M. Borsa and D. O. Boerma, *Growth, structural and optical properties of Cu₃N films*, Surf. Sci. **548** (2004), 95.
 42. G. H. Yue, P. X. Yan, Z. Liu, M. X. Wang, M. Li and X. M. Yuan, *Copper nitride thin film prepared by reactive radio-frequency magnetron sputtering*, J. Appl. Phys. **98** (2005),

103506.

43. Z. Li and R. G. Gordon, *Thin, continuous, and conformal copper films by reduction of atomic layer deposited copper nitride*, Chem. Vap. Deposition **12** (2006), 435.

Chapter 7: SAMs Modification of H/Si, and ALD of Al_2O_3 , HfO_2 and Cu on SAMs

Self assembled monolayers (SAMs) have been attracting tremendous interest of current researchers since 1980's for its excellent physical and chemical properties and wide applications in many areas [1, 2, 3, 4, 5, 6]. It may show different physical and chemical properties depending on its structure and composition so that it can be used to modify the surface for both the wet-chemical control of surface reactivity and the surface functionalization in molecular growth processes.

Generally, SAMs are prepared by surfactant molecules spontaneously attaching a monomolecular layer onto different surfaces. Without complicate and expensive experimental instruments, SAMs can be prepared simply by the putting the substrate into a solution of the desired molecule and then removing the excess. Typically, the molecules in a SAM are attached to the surfaces via chemical bonds which are dense and well-ordered exhibiting higher stability than normal organic thin films [7].

SAM is an ideal system that allows fundamental studies of interfacial chemistry and self-organization. The examples of the functional head groups of SAMs are -SH, -CN, -COOH, -NH₂, -CH₃, and so on. Alkyl thiols on gold [8] and Alkyl silanes [9] on SiO₂ are the most well studied two SAM systems. It can be used as sensors, transducers, protective layers and has many other applications [1, 5, 10].

Due to the high flexibility of functional head groups of SAMs, they have special meaning in ALD. By varying the functional head groups to reactive or unreactive groups, selective ALD growth is achieved [11, 12], and Fig 7.1 shows an example [11]. In addition, SAMs (alkyl chains) have shown extraordinary electrical properties close to the

ideal insulator on Si via direct Si-C bonds [13]. This Si surface passivated by alkyl chains through Si-C bonds has shown high stability both in the air and in water [7]. These types of SAMs can also serve as diffusion barrier to protect surfaces from oxidation. Another advantage of using SAMs for ALD is that the appropriate functional head group can have higher reactivity than H/Si so that lower reaction temperature can be used which is preferable to minimize the formation of interfacial SiO₂ during the deposition of high- κ metal oxide or the incubation period can be reduced. Thus, SAMs are becoming a promising method to modify surfaces for ALD application [14].

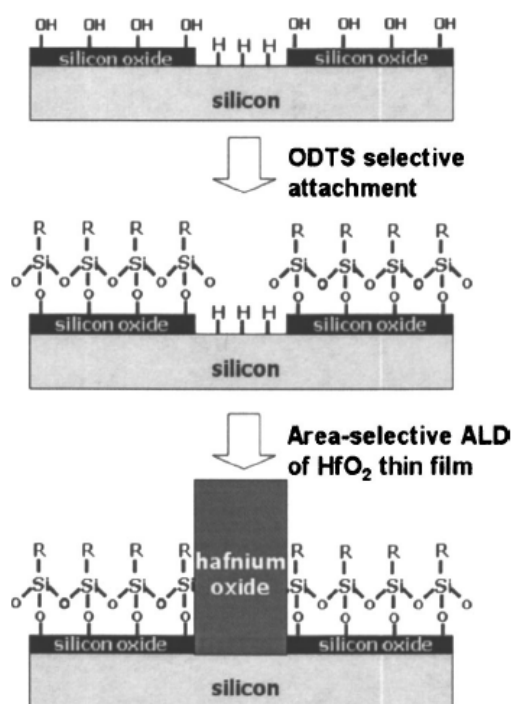
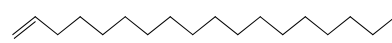


Fig 7.1 Area-selective growth of HfO₂ [11]. On the patterned SiO₂/Si surface, since ODTS can only be grown on SiO₂, so only the SiO₂ area is covered by SAM. The functional head group of the SAM (as “R” in the Figure) is chemically unreactive. Thus the HfO₂ can only be deposited onto the Si-H area. By this method, area-selective growth of ALD is achieved.

In this chapter, we will discuss the application of SAMs passivated Si based on H/Si(111) starting surface. The stability including thermal annealing and ozone exposure

is studied. Then ALD of Al_2O_3 , HfO_2 and Cu are deposited on SAMs to investigate the precursor/surface interaction and film quality for potential applications. Two types of SAMs are studied, the $-\text{CH}_3$ terminated SAM and $-\text{COOH}$ terminated SAM, since one has the chemically unreactive head group and the other has the reactive head group.

7.1 Stability of the $-\text{CH}_3$ and $-\text{COOH}$ SAMs

$-\text{CH}_3$ SAM is prepared as follows: neat 1-octadecene (C_{18} , ) is pre-treated with molecular sieve, and then N_2 gas is bubbled through the solution for at least 1 hour to remove the oxygen and H_2O . H/Si(111) sample is placed into the solution for 2 h at 200°C with N_2 purging. After the reaction, the sample is removed and rinsed with THF, dichloromethane and dionized water, and then dried by N_2 .

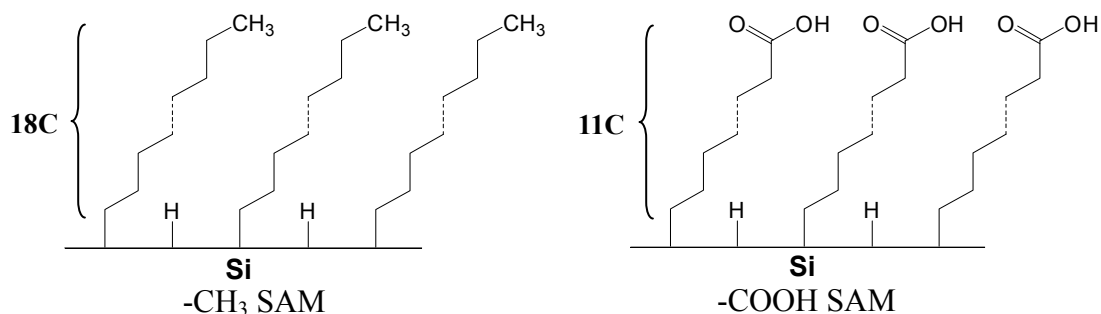
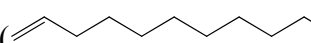


Fig 7.2 The schematic of $-\text{CH}_3$ SAM and $-\text{COOH}$ SAM. The molecules are directly bond to H/Si(111) surface via Si-C bond. The number of carbon atoms is marked on the left of the figure.

Similarly, $-\text{COOH}$ monolayer is formed via thermal hydrosilylation by 1-undecylenic acid () COOH). Fresh H/Si(111) is immersed into distilled neat deoxygenated 1-undecylenic acid under argon or N_2 and heated at 120°C for 2-15h. After the reaction, the derivatized silicon sample is removed, rinsed with ethyl

acetate, then further cleaned by sonication in hot acetic acid followed by immersion in boiling dichloromethane, and dried by N_2 . Then the freshly prepared SAMs are introduced into ALD chamber for further treatment. Note that all the following spectra are taken at incident angle of $\sim 74^\circ$.

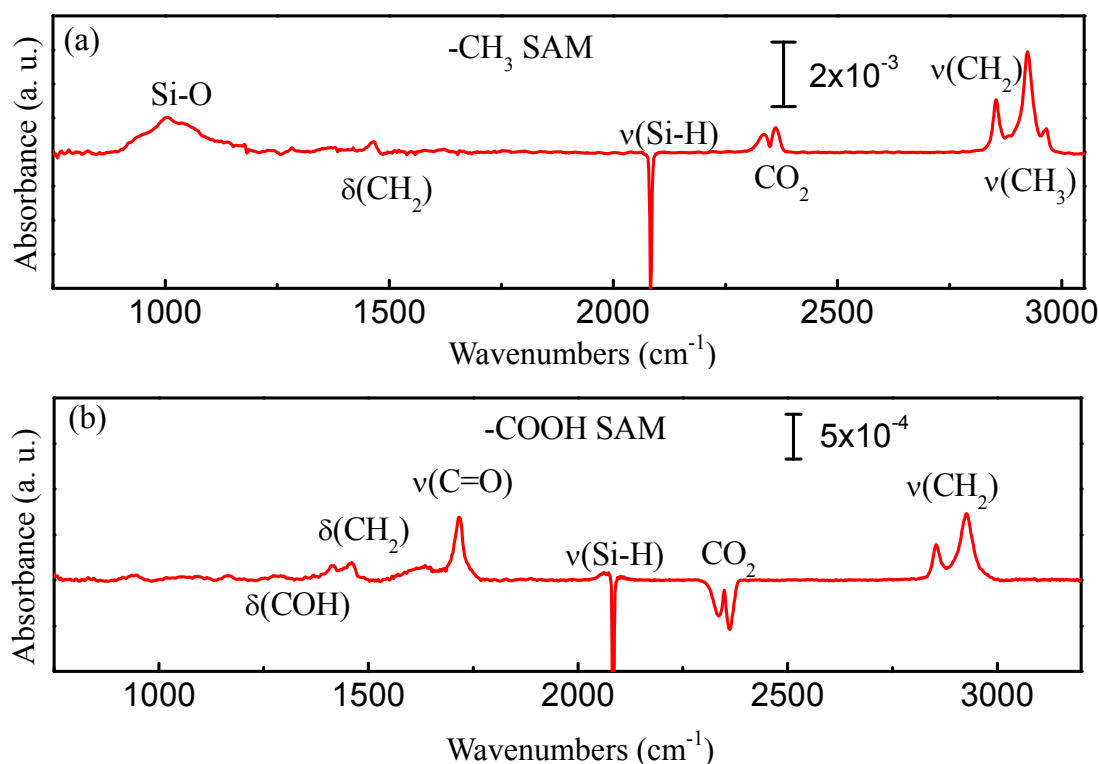


Fig 7.3 Absorption spectra of (a) $-\text{CH}_3$ SAM and (b) $-\text{COOH}$ SAM referenced to H/Si(111). Small amount of Si-O for CH_3 SAM and no oxide for COOH SAM are observed.

The schematic of the two SAMs are shown by Fig 7.2. The $-\text{CH}_3$ SAM has 18 carbon atoms and $-\text{COOH}$ SAM has 11 carbon atoms in total. The IR spectra of $-\text{CH}_3$ SAM and $-\text{COOH}$ SAM are presented in Fig 7.3(a) and (b), which are referenced to the H/Si(111). For both spectra, the loss of Si-H is shown as negative peak around 2083 cm^{-1} [$\nu(\text{Si-H})$], indicating that the desired molecules have been chemically bonded to the Si surface via Si-C by replacing the surface hydrogen. For the $-\text{CH}_3$ SAM, the monolayer is featured by CH_2 scissoring deformation mode at 1465 cm^{-1} , $\nu_{\text{as}}/\nu_{\text{s}}(\text{CH}_2)$ at $2924/2853$

cm^{-1} , $\nu_{\text{as}}/\nu_{\text{s}}(\text{CH}_3)$ at $2966 \text{ cm}^{-1}/2883 \text{ cm}^{-1}$. CH_2 is the dominant part in the hydrocarbon chains. The loss of surface hydrogen is $\sim 83\%$ which is higher than the ideal coverage of alkyl chains on H/Si ($\sim 50\%$) [15]. The extra loss of hydrogen is due to the small amount of oxidation which can be observed around 1000 cm^{-1} (Si-O phonon). According to the integrated area of the Si-O band, the thickness of SiO_2 is $\sim 2 \text{ \AA}$.

As for -COOH SAM in Fig 7.3(b), the loss of Si-H is $\sim 58\%$ according to the negative $\nu(\text{Si-H})$ band at 2083 cm^{-1} after alkylation, indicating the coverage of SAM. It is in good agreement with theoretical predictions for alkyl chains adsorption on H/Si(111) surfaces [15]. The vibration features of the carboxylic acid head group--the strong C=O stretching mode at 1714 cm^{-1} , C-OH stretching mode at 1276 cm^{-1} , and C-O-H bending modes at 1413 cm^{-1} --suggest that the acid end group is intact after the reaction [16]. The interface reaction is dominated by thermal hydrosilylation of surface Si-H with C=C [17, 18]. The absence of any absorption band corresponding to Si-O-C around $\sim 1100 \text{ cm}^{-1}$ confirms the direct bonding of Si-C. It should be note that the free carboxylic acid carbonyl stretching frequency should be $\sim 1760 \text{ cm}^{-1}$. The observed frequency of C=O is at 1714 cm^{-1} , implying that it takes the dimmer form as $\text{O}=\text{CH}-\text{OH} \cdots \text{O}=\text{CH}-\text{OH}$ due to the hydrogen bond which will redshift the frequency to $\sim 1710 \text{ cm}^{-1}$ [19, 20]. In addition, $\delta(\text{CH}_2)$ at 1460 cm^{-1} from the Alkyl chains is observed as well.

The stretching modes of CH_2 at 2926 cm^{-1} (asymmetric) and 2854 cm^{-1} (symmetric), have been correlated to the degree of chain packing [21, 22]. Our observed value of 2926 cm^{-1} is very close to that of the best monolayer with -COOH terminated SAM (2924 cm^{-1}) [23]. For methyl-terminated SAM, the best $\nu_{\text{as}}(\text{CH}_2)$ value has been achieved is $\sim 2918 \text{ cm}^{-1}$. However, as we will show later, the overall quality of the -COOH SAM is good enough to protect the silicon surface from oxidation during the ALD process without

decomposition.

In contrast to the $-\text{CH}_3$ SAM, the absence of absorption bands in the $900\text{--}1200\text{ cm}^{-1}$ region for $-\text{COOH}$ SAM indicates that the surface is essentially oxide free (no SiO_2 , Si-O-C or Si-O-Si bonds). The presence of the carboxylic end group is thought to be responsible for the integrity of the interface by trapping residual water during reaction which prevents water diffusion through the SAM layer.

Thermal stability

Then the fresh SAMs are loaded into our ALD chamber immediately to perform the thermal stability check. Thermal annealing is carried out in purified N_2 (impurity $< 10^{-6}$ ppm) at $\sim 3\text{--}4$ torr for 5 min. All experiments are done by *in situ* method to minimize the interference from the external environment. The annealing results are shown in Fig 7.4(a) and (b) for $-\text{CH}_3$ SAM and $-\text{COOH}$ SAM respectively, which are both referenced to the fresh SAMs.

As in Fig 7.4(a), by observing the evolution of CH_2 and CH_3 stretching bands ($2800\text{--}3000\text{ cm}^{-1}$) as well as the variation in the SiO_2 phone mode ($900\text{--}1200\text{ cm}^{-1}$), the stability is directly obtained. This type of SAM is stable up to 150°C . Upon 200°C , CH_2 and CH_3 start to decompose as shown by negative bands along with the formation of a broad Si-O band around 1000 cm^{-1} , implying the degrading of the SAM and the oxidation of the silicon surface. The degradation strongly occurs at 300°C , $\sim 55\%$ according to the intensity loss of $\nu(\text{CH}_2)$ and $\nu(\text{CH}_3)$, which is in good agreement with the literature measured by ATR [24]. The loss of CH_2 deformation mode at 1465 cm^{-1} is observed above 300°C as well. In addition, the weak feature appearing at 2080 cm^{-1} upon 300°C annealing is attributed to the formation of Si-H bonds on the Si surface. It was previously observed in UHV environment and taken as the evidence for thermal decomposition of

alkyl chains through β -hydride elimination with cleavage of Si-C bonds [25]. Note that the observed Si-O TO/LO frequencies (984 cm^{-1} and 1105 cm^{-1}) is lower than that of typical SiO_2 phonon modes (1060 cm^{-1} and 1250 cm^{-1}) [26], indicating the Si-O-C could be involved which will redshift the Si-O frequency.

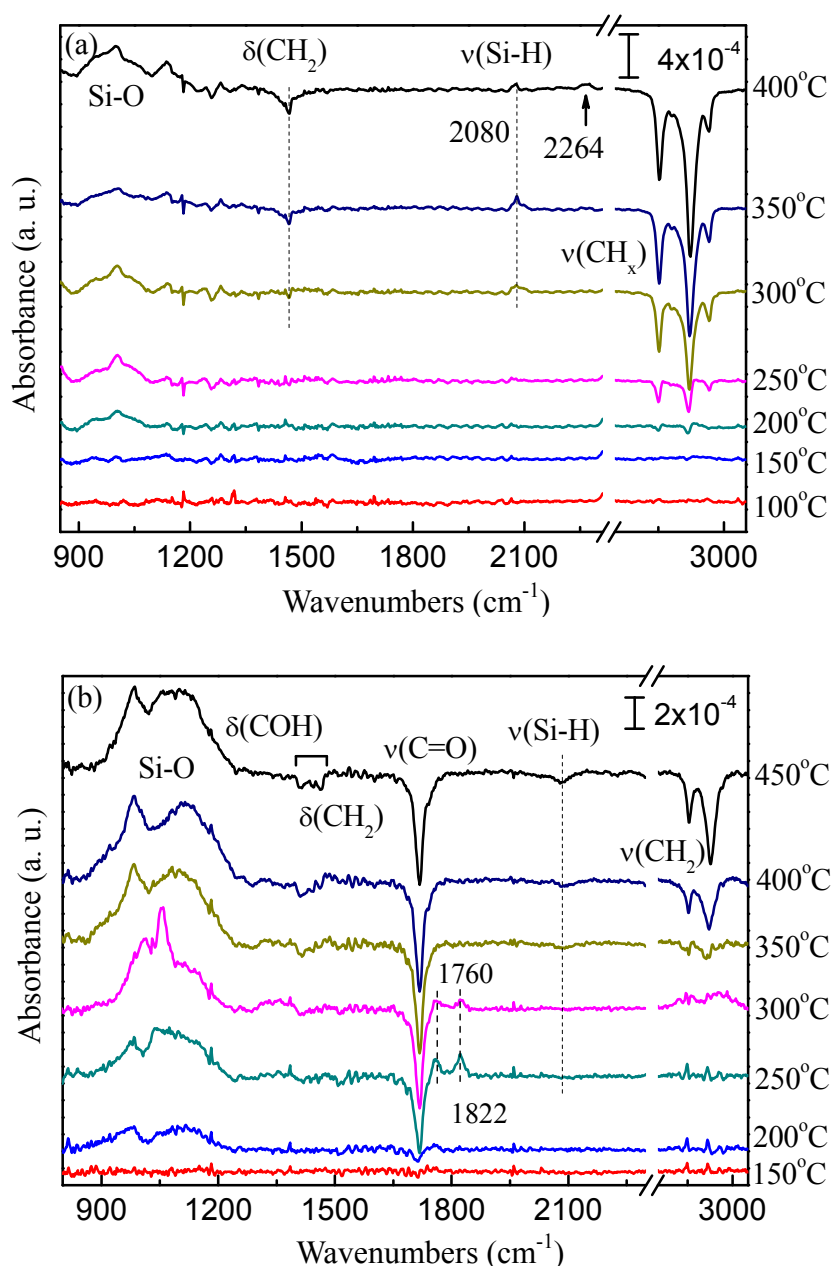


Fig 7.4 The annealing results of (a) -CH₃ SAM and (b)-COOH SAM in N₂ referenced to the fresh SAM surface. COOH SAM is more stable than CH₃ SAM. The stability can be inferred from the loss of CH_x modes and C=O modes.

Shown by Fig 7.4(b), the -COOH terminated SAM exhibits a quite different thermal behavior, where its Alkyl chain is more stable than that of -CH₃ SAM. At 150°C the surface shows no loss for both -CH₂ and -COOH groups. However, the positive spikes appearing at 2916 cm⁻¹ [$\nu_{as}(\text{CH}_2)$] and 2848 cm⁻¹ [$\nu_s(\text{CH}_2)$] may indicate the -CH₂ chain is perturbed such as tilted or reorganized to more ordered status.

Upon 200°C, the SAM starts to degrade evidenced by a little loss of $\nu(\text{C=O})$ at 1714 cm⁻¹ which is the key feature of the -COOH functional group, and $\nu(\text{C=O})$ partly blueshifts to 1758 cm⁻¹ suggesting that $\text{O}=\text{C}-\text{OH} \cdots \text{O}=\text{C}-\text{OH}$ dimers are partially broken and become isolate -COOH due to the degradation. The broad Si-O band at 900-1200 cm⁻¹ indicates the oxidation of Si surface. However, the -CH₂ chain remains intact until 350°C, showing higher stability than that of -CH₃ SAM.

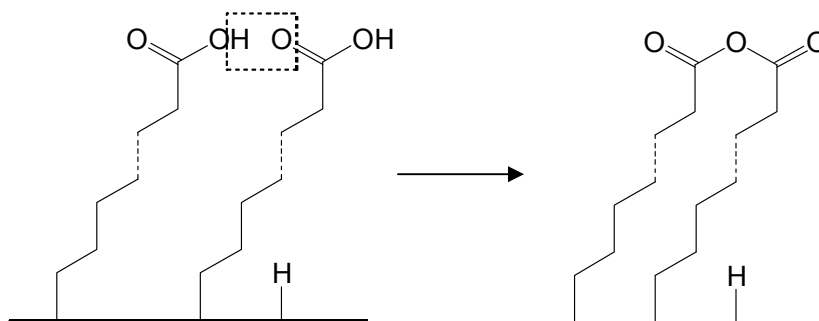


Fig 7.5 The schematic for transformation of carboxyl group to anhydride group. The adjacent COOH groups are combined to anhydride groups during the annealing.

At 250°C, except for the loss of $\nu(\text{C=O})$ at 1714 cm⁻¹, two new bands appear at 1760 cm⁻¹ and 1822 cm⁻¹, which are assigned to $\nu(\text{C=O})$ in anhydride form of $-\text{C}(=\text{O})-\text{O}-\text{C}(=\text{O})-$, as the symmetric mode and asymmetric mode respective [19]. It can be inferred that -COOH is partially transformed into anhydride before the decomposition of -CH₂ chains as shown

by the scheme in Fig 7.5, and this process may result in the higher stability for the -CH_2 chain of -COOH SAM. Our observations are in good agreement with the literature by ATR studies [27].

At 350°C , all -COOH decomposes and -CH_2 starts to degrade featured by the intensity loss of CH_2 stretching modes at 2800 cm^{-1} - 3000 cm^{-1} , C-OH stretching mode at 1276 cm^{-1} and C-O-H bending modes at 1413 cm^{-1} . The Si-O bands (984 cm^{-1} and 1105 cm^{-1}) keep increasing with the raising temperature, indicating the cleavage of Si-C bonds and further oxidation of the surface. At 450°C , the SAM is completely removed from the surface.

The above studies clearly illustrate the thermal stability of the two types of SAMs. Only a moderate thermal annealing below 200°C can be performed without substantial SAM degradation. Based on these, then we can evaluate the ALD application on SAMs.

Stability under ozone exposure

In many cases, ozone is used as oxidant for ALD to minimize the H_2O inside the deposited film to improve its quality. Thus, it is necessary to study the stability of SAMs when exposed to ozone ambient. For this purpose, -CH_3 SAM is exposed to 200 sccm ozone at 60°C for 2s and -COOH SAM is exposed to 100 sccm ozone for 5s from 60°C to 300°C . The spectral results are shown in Fig 7.6(a) and (b) which are referenced to the fresh SAMs.

As shown in Fig 7.6(a), -CH_3 SAM is exposed to ozone at 60°C and the spectrum is referenced to the fresh -CH_3 SAM. It can be seen that the Si is oxidized immediately after the ozone exposure evidenced by the broad Si-O phonon band at 900 cm^{-1} - 1200 cm^{-1} . The intensity loss of $\nu(\text{CH}_2)$ and $\nu(\text{CH}_3)$ (2800 cm^{-1} - 3000 cm^{-1}) as the key features of the alkyl chain confirms the degradation of the SAM by ozone. The data clearly suggests that -CH_3

SAM is very vulnerable to ozone.

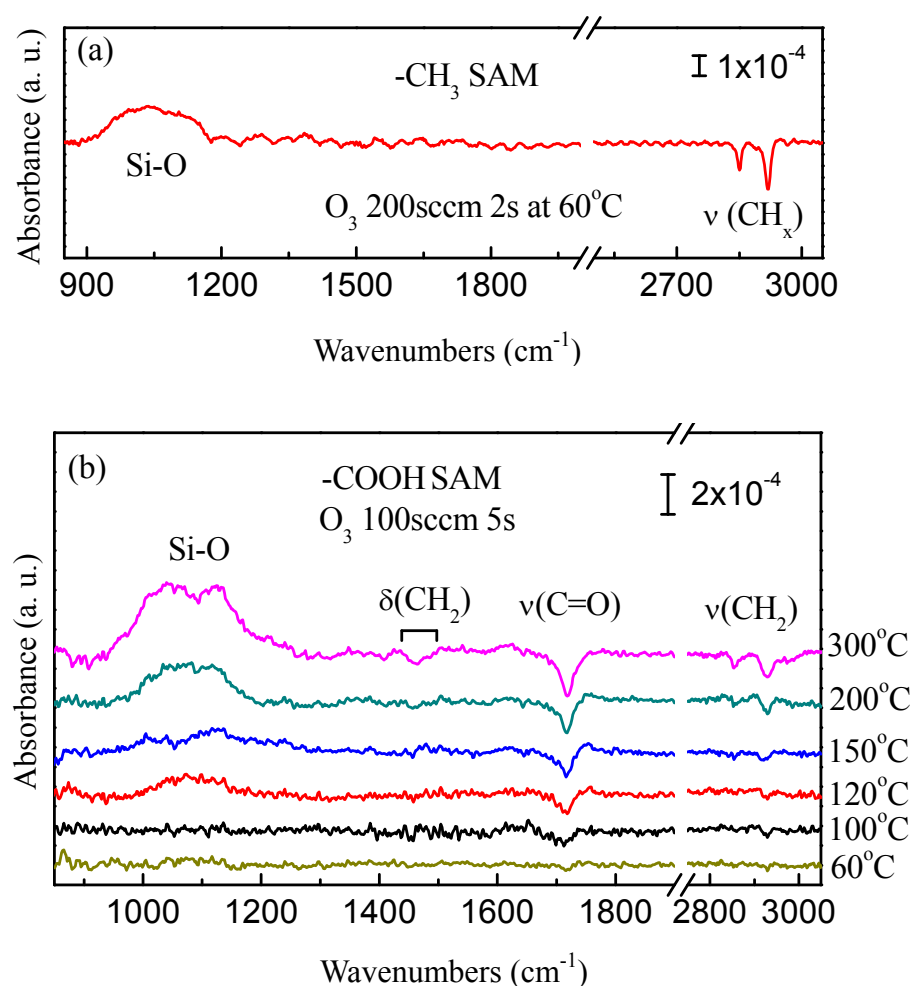


Fig 7.6 The absorption spectra of (a) $-\text{CH}_3$ SAM and (b) $-\text{COOH}$ SAM which are exposed to ozone and referenced to the fresh SAM surface. CH_3 SAM degrades immediate after ozone exposure while COOH SAM is more stable.

Compared with $-\text{CH}_3$ SAM, $-\text{COOH}$ SAM shows higher stability than that of $-\text{CH}_3$ SAM again as indicated by Fig 7.6(b) where all spectra are referenced to $-\text{COOH}$ SAM. There is no change in the spectrum at 60°C , and only a small variation is observed at 100°C for $\nu(\text{C=O})$ at 1714 cm^{-1} , implying no substantial changes for the SAM upon 100°C . At 120°C and 150°C , the intensity loss of $\nu(\text{C=O})$ at 1714 cm^{-1} increases slightly,

and $\nu(\text{C}=\text{O})$ partially blueshifts to 1760 cm^{-1} due to the isolated $-\text{COOH}$ groups after the slight degradation of head groups. The tiny broad band at 900 cm^{-1} - 1200 cm^{-1} may result from base line fluctuation because of no substantial change for $\nu(\text{CH}_2)$ (2800 cm^{-1} - 3000 cm^{-1}), meaning the underlying $-\text{CH}_2$ chain remains intact.

Starting from 150°C , the Si surface is being oxidized according to the increased Si-O band with the loss of $-\text{CH}_2$ according to the negative $\nu(\text{CH}_2)$ bands. These features suggest a slight degradation of CH_2 chains starting from this temperature. As the temperature increases, the intensity of Si-O band keeps increasing and the loss of more $\nu(\text{CH}_2)$ (2800 - 3000 cm^{-1}) confirms further oxidation of Si surface. Note that the loss of CH_2 deformation mode at 1465 cm^{-1} is observed at 300°C as well. Compared with thermal annealing in N_2 , there is about 50°C temperature difference for the stability since ozone is much more chemically reactive which makes the SAM more vulnerable.

$-\text{COOH}$ SAM is a stable surface. Our study shows that the surface remains unchanged with N_2 purge for days. Even after dipping the $-\text{COOH}$ SAM terminated Si into HF or HCl for minutes, the SAM survives. This monolayer shows high quality among organic films.

Thus, we checked the stability of two types of SAMs: one with chemically unreactive methyl functional group, and the other with chemically reactive carboxylic functional group. The $-\text{COOH}$ SAM shows great stability as an ultra thin organic film. It survives after annealing in N_2 or after exposed to ozone at a moderate temperature. It can be used as one of the surface passivation methods to modify Si surface for ALD application due to its active functional group and good stability. Next, we will demonstrate ALD on this surface for both metal and metal oxide, including Al_2O_3 , HfO_2 and Cu.

7.2 ALD of Al_2O_3 on $-\text{COOH}$ SAM

ALD of Al_2O_3 with TMA+ D_2O on $-\text{COOH}$ SAM

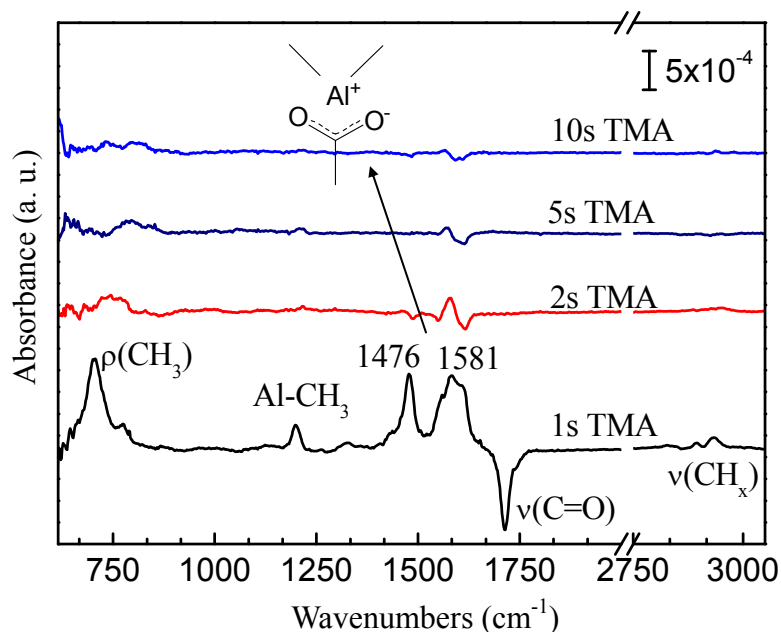


Fig 7.7 Differential FTIR absorption spectra of TMA on $-\text{COOH}$ SAM surface at 100°C . Each spectrum is referenced to the spectrum recorded for the previous treatment.

The spectrum of 1s TMA exposure is referenced to SAM; the spectrum of 2s TMA precursor exposure is referenced to that of 1s TMA exposure; the spectrum of 5s TMA exposure is referenced to that of the 2s TMA exposure, and so on. The inset shows the ionic structure after the reaction between COOH and TMA.

After introduced into the ALD reactor, the $\text{Si}(111)-(\text{CH}_2)_{10}-\text{COOH}$ SAM sample is pre-annealed in N_2 at 120°C for 5min in order to further stabilize the surface and remove physically adsorbed species. *In situ* FTIR measurements are performed in transmission geometry ($\sim 74^\circ$ incidence) at all stages of the process. 10 cycles Al_2O_3 are deposited on SAM using alternative pulses of TMA and D_2O at 100°C . The pressure of both TMA and D_2O pulses is $\sim 3\text{--}4$ torr. Saturation pulse length is used for each precursor dosing. Usually ALD by TMA/ D_2O on H/Si surface is achieved at $\sim 300^\circ\text{C}$ due to the reactivity between TMA and H/Si [28, 29]. Since $-\text{COOH}$ SAM is more reactive than H/Si surface, it

enables us to deposit Al_2O_3 at a much lower temperature. Post-annealing is carried out *in situ* under purified N_2 purge (~ 3 torr) for 5 min after the deposition.

The ALD self-termination nature of TMA on the COOH -SAM surface is checked first, as shown in Fig 7.7 which presents the differential spectra. The differential manner means every spectrum is referenced to the spectrum recorded after the previous treatment, highlighting the chemistry induced by the very last processing step. In the figure, the complete loss of $\text{C}=\text{O}$ stretching mode at 1714 cm^{-1} after 1s TMA exposure at 100°C indicates the reaction between TMA and $-\text{COOH}$, and all surface reactive sites have been reacted. Two strong bands appearing at 1476 cm^{-1} and 1581 cm^{-1} with a shoulder at 1610 cm^{-1} are assigned to the $\text{C}=\text{O}$ symmetric and asymmetric stretching modes in the acid salt structure ($\text{Al}^+-\text{CO}_2^-$) as shown by the inset of Fig 7.7 [19]. The peaks at $\sim 1213\text{ cm}^{-1}$ and 706 cm^{-1} are assigned to $-\text{CH}_3$ symmetric deformation mode and rocking mode of $\text{Al}-\text{CH}_3$, respectively [28, 30, 31]. The additional features at $2800\text{--}3000\text{ cm}^{-1}$ are assigned to $-\text{CH}_3$ stretching modes. All these bands clearly demonstrate that TMA is chemically attached to the SAM surface with intact $-\text{CH}_3$ ligand. Fig 7.8 shows the scheme for the reaction of TMA on the SAM surface.

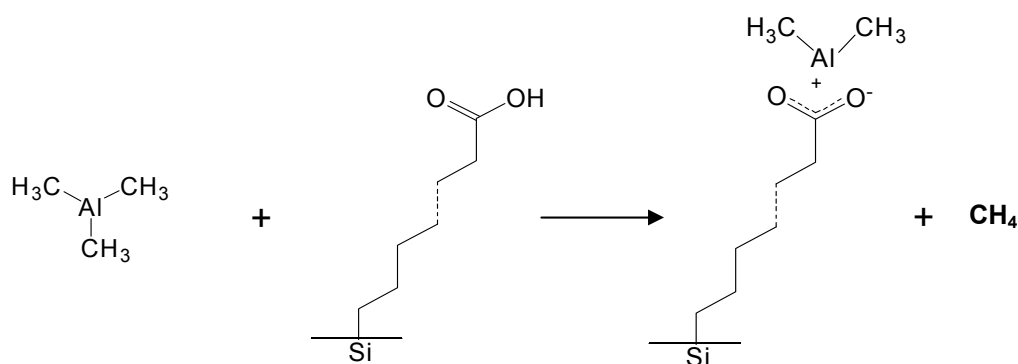


Fig 7.8 Scheme of TMA reacting with the $-\text{COOH}$ SAM surface. TMA will react with COOH to form the COO-Al ionic structure at the interface.

Additional TMA pulses only bring slight fluctuation in the region around 1580 cm^{-1} ,

which could result from the interference of C=O bond in CO₂-Al by the absorbance of non-reacted TMA molecule in the surrounding environment. The spectral stability at $\sim 1213\text{ cm}^{-1}$ confirms that no Al-(CH₃) is adsorbed or desorbed from the surface. In addition, the intensity of the -CH₂ stretching mode of Alkyl chains at 2800-3000 cm⁻¹ remains unchanged after TMA exposure, suggesting that the SAM is intact. Therefore, only the SAM head group is reactive and TMA does show self-terminating nature on it, which is a necessary condition for ALD. Al₂O₃ deposition does not alter the organic monolayer significantly.

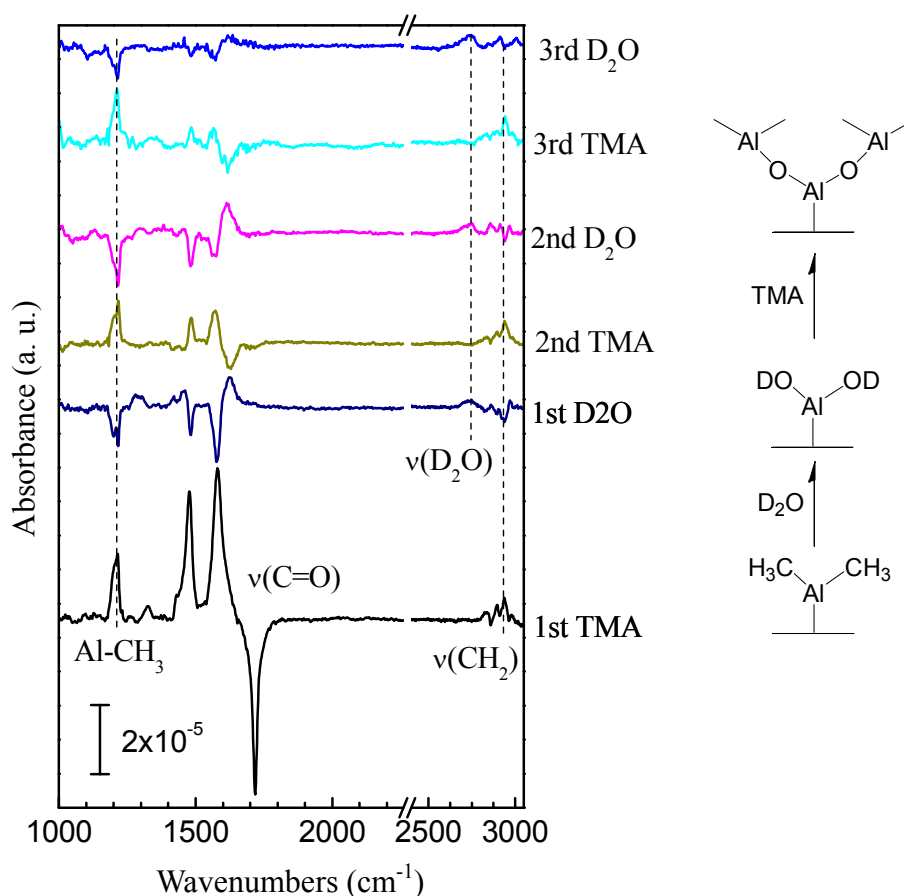


Fig 7.9 Differential FTIR absorption spectra of 10 cycles Al₂O₃ on -COOH SAM surface deposited at 100°C. Each spectrum is referenced to the spectrum recorded for the previous treatment. The bottom spectrum is referenced to SAM. The scheme of the ALD reaction is shown on the right side. ALD ligand exchange is observed by Al-CH₃, OD and CH₃ modes.

The well defined growth of 10 cycles TMA and D₂O at 100 °C is shown in Fig 7.9, where each complete cycle corresponds to one exposure of TMA followed by one exposure of D₂O. The bottom spectrum is referenced to SAM surface and shows the same features as the 1st TMA exposure in Fig 7.7, where the TMA completely consumes the accessible COOH groups on the surface to form a complete layer. After the first D₂O exposure, the peak intensity of the deformation and rocking modes of Al-CH₃ at 1213 and ~706 cm⁻¹ strongly decreases, as expected due to the hydrolysis of Al-CH₃ by D₂O (Al-CH₃ is replaced by Al-OD) [32]. The intensity variation associated with modes at 1476 and 1581 cm⁻¹ (i.e. shift to ~1460 cm⁻¹ and ~1624 cm⁻¹) is tentatively attributed to the environment change of C=O after hydrolysis of Al-CH₃. The weak band centered at 2743 cm⁻¹ (OD stretch) confirms that hydrolysis has taken place.

In contrast to the growth of Al₂O₃ on H/Si (exhibiting interfacial oxidation), there is no interfacial SiO₂ upon water exposure or later on cycles in the ALD process. On the other hand, CH₃ attached to Si (Si-CH₃) is the dominant reaction of initial TMA on H/Si which causes incubation period for ALD growth, while on SAM the Al-CH₃ is the dominant part evidenced by strong and comparable intensity of Al-CH₃ methyl deformation mode (~1213 cm⁻¹) from the 1st TMA to 3rd TMA without any observation of Si-CH₃. This feature indicates less incubation period on SAM and further proves that -COOH SAM is more favorable for TMA than H/Si.

For the following cycles, the periodic ALD ligand exchange behavior is observed, showing the layer by layer growth. After the second TMA exposure, TMA reacts with surface Al-OD groups to form Al-O-Al-CH₃, indicated by the Al-CH₃ characteristic peak at 1213 cm⁻¹ and broad Al₂O₃ band at 700-800cm⁻¹. The subsequent D₂O exposure leading to replacing -CH₃ by -OD is as expected. The reversible intensity variation

(positive/negative) of the features at 1467 cm^{-1} and 1640 cm^{-1} is related to the peak shift induced by the change of C=O bond environment in the interfacial $(\text{CO}_2^-)\text{-Al}^+$ due to the ligand exchange. In subsequent ALD cycles, these changes in the $1400\text{-}1650\text{ cm}^{-1}$ region are still observable but with decreased magnitude as the number of TMA/D₂O cycles increases. This suggests that these features are only associated with the interface between the SAM and Al₂O₃.

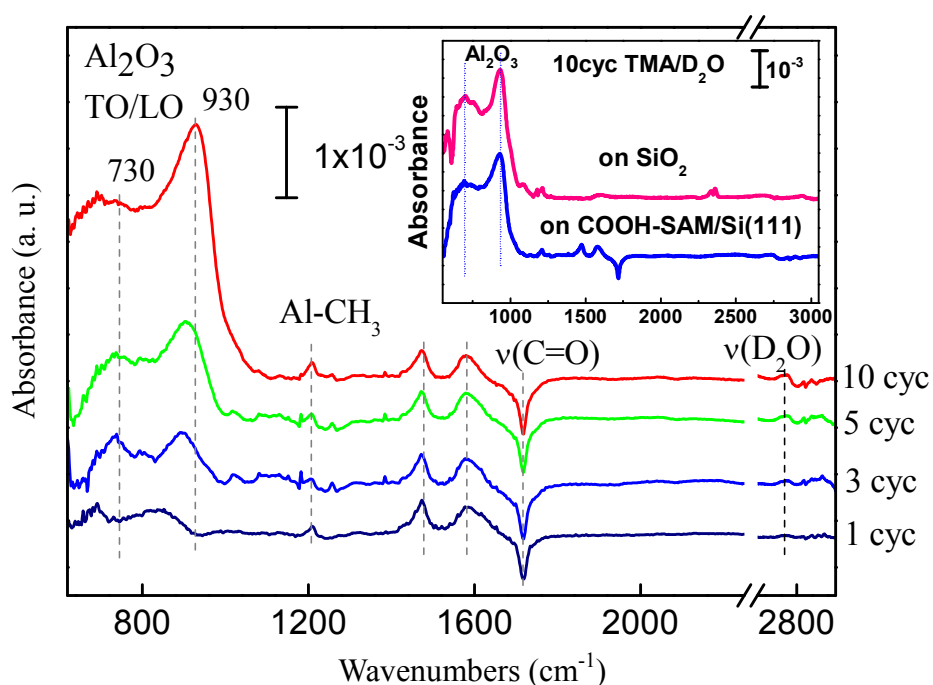


Fig 7.10 Absorption spectra of 10 cycles Al₂O₃ on SAM deposited at 100°C. All referenced to the SAM surface. The inset compares 10 cycles Al₂O₃ on SAM with that on SiO₂ (referenced to SiO₂). The quality of Al₂O₃ is as good as that on SiO₂ surface.

As Fig 7.10 which shows Al₂O₃ growth up to 10 cycles referenced to -COOH SAM, two bands at ~ 730 and $\sim 930\text{ cm}^{-1}$, assigned to the TO and LO phonons of amorphous Al₂O₃, steadily increase in intensity with the number of cycles and blueshift slightly. There are no detectable contributions in the $1000\text{-}1200\text{ cm}^{-1}$ and $\sim 800\text{ cm}^{-1}$ range where the Si-O-C, Al-O-Si, or Si-O-Si stretching modes are located [26, 33]. No Si-CH₃

umbrella mode $\sim 1266\text{ cm}^{-1}$ is observed as well [34]. These results clearly indicate that neither TMA nor oxygen penetrates through the SAM to reach the silicon. All ALD reactions are limited to the top surface of the -COOH functionalized SAM. Therefore, oxygen diffusion to the interface is suppressed due to the protection of SAM as a good barrier. Note that there is some D_2O incorporation in the Al_2O_3 film as the band at 2743 cm^{-1} which has been observed by other studies as well [35]. The overall quality of the Al_2O_3 film is as good as that of aluminum oxide grown on hydrophilic SiO_2 . The inset of Fig 7.10 shows that the TO/LO phonons of Al_2O_3 grown on COOH-SAM and SiO_2 are virtually identical, both much stronger and narrower than those of Al_2O_3 grown on H/Si.

The stability of the Al_2O_3 -coated SAM is investigated by carrying out annealing experiments. Fig 7.11 shows the spectral evolution resulting from post-annealing of a 10-cycle ALD-grown Al_2O_3 film on -COOH SAM, where all spectra are referenced to the SAM surface. The Al_2O_3 -coated SAM is completely stable upon annealing to 300°C . The degradation of the SAM is observed in the range of $300\text{-}400^\circ\text{C}$, as an intensity loss of -CH_2 stretching modes of the Alkyl chains at $2800\text{-}3000\text{ cm}^{-1}$. The biggest loss of -CH_2 occurs in this $300\text{-}400^\circ\text{C}$ range. After annealing to 400°C , a weak feature appears at 2055 cm^{-1} along with the further reduction of -CH_2 mode intensity. This feature, attributed to the formation of Si-H bonds at the surface, was previously observed in UHV environments and taken as the evidence for thermal decomposition of alkyl chains through β -hydride elimination with cleavage of Si-C bonds [25]. The formed Si-H disappears at 500°C , as expected due to its thermal stability. Upon Si-H removal, the TO/LO modes of SiO_2 appear in the $1000\text{-}1200\text{ cm}^{-1}$ spectral region, and the C=O stretching modes ($1400\text{-}1600\text{ cm}^{-1}$) are greatly reduced, suggesting that the whole CH_2 chains are decomposed and oxygen diffuses into the Si substrate. At higher temperatures,

the TO/LO phonon modes of deposited Al_2O_3 film become sharper. The LO mode of the Al_2O_3 blueshifts to $\sim 955\text{ cm}^{-1}$, indicating that Al_2O_3 film becomes denser after annealing. Note that Al_2O_3 film remains after the SAM is thermally decomposed.

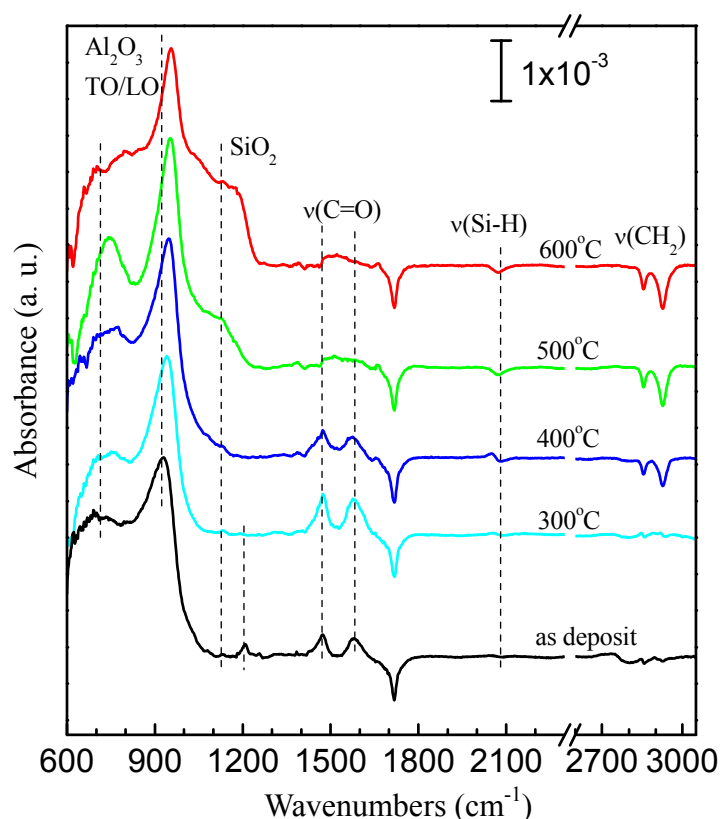


Fig 7.11 Annealing of 10 cycles Al_2O_3 on $-\text{COOH}$ SAM surface in N_2 . All spectra are referenced to SAM surface. The bottom spectrum shows as-deposit Al_2O_3 . SAM decomposes at 400°C featured by the intensity loss of CH_2 modes.

ALD of Al_2O_3 with TMA+ozone on $-\text{COOH}$ SAM

As we have discussed and also observed in the spectra such as in Fig 7.10, visible amount of D_2O exists inside the film, which makes the film an oxygen rich film and substantially affects the quality of the film. Thus, ozone instead of water has also been used to deposit metal oxide films. The problem of ozone ALD is that due to ozone's high reactivity, the organic ligand will react with ozone and leave C-O/C=O related species

inside the film [36, 37]. We have shown that the -COOH SAM is relatively robust when exposed to ozone up to $\sim 150^\circ\text{C}$. The following section will explore the ozone ALD of Al_2O_3 on -COOH SAM at 100°C .

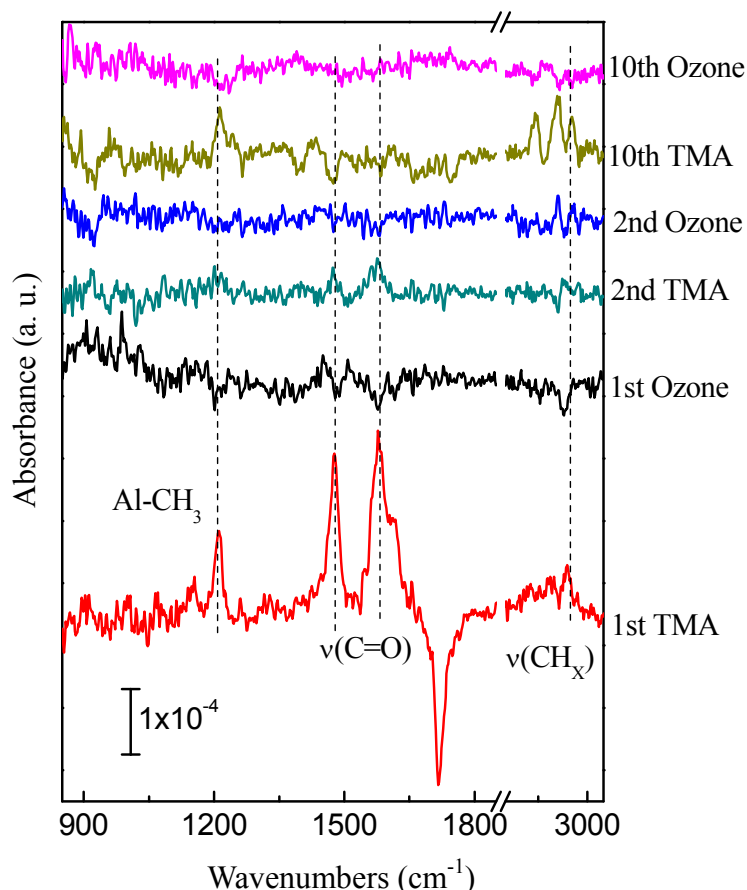


Fig 7.12 Differential FTIR absorption spectra of 20 cycles Al_2O_3 by ozone at 100°C on -COOH SAM surface. Each spectrum is referenced to the spectrum recorded for the previous treatment. The bottom spectrum is referenced to SAM. Weak ALD ligand exchange is observed.

20 cycles Al_2O_3 are deposited by TMA and ozone with saturation pulse length at 100°C . The incident angle of IR beam is $\sim 74^\circ$. Fig 7.12 shows the differential spectral results of the deposition. For the 1st dosing of TMA on SAM, the spectrum is identical to that in the previous discussion, showing the stretching/deformation modes of Al-CH_3 and the variation of C=O stretching mode. These features indicate TMA is chemically bonded to the SAM surface as having been discussed.

Upon the subsequent ozone exposure, the tiny negative band of $\nu(\text{CH}_x)$ at 2800-3000 cm^{-1} shows the reaction of Al-CH_3 methyl ligands with ozone. The weak and reversible intensity variation of the features at 1476 and 1581 cm^{-1} is related to the peak shift induced by the change of C=O bond environment in the interfacial $(\text{CO}_2)\text{-Al}$ from Al-CH_3 to Al-O-Al . The detailed reactions between TMA and ozone have been discussed in the previous chapter for ozone ALD. Shown by the spectra, methyl ligand is not completely removed especially for the 1st cycle, meaning an insufficient ALD ligand exchange which will lower the deposition rate. The following cycles repeat the same scheme: after TMA dosing, Al-CH_3 is adsorbed onto the surface; after ozone dosing, the methyl ligand is partially removed.

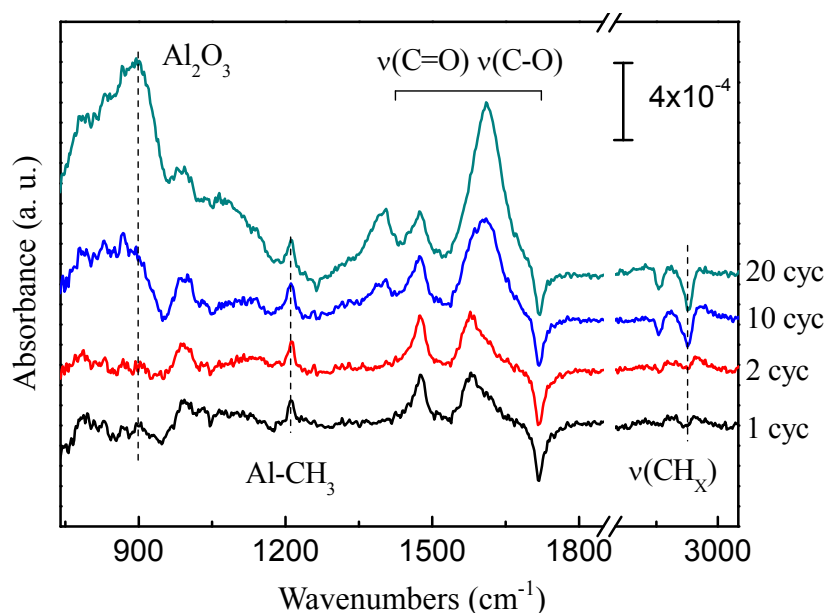


Fig 7.13 Absorption spectra of 20 cycles Al_2O_3 by ozone on SAM. All referenced to the SAM surface. Al_2O_3 and substantial carbonated species are observed. The CH_2 intensity loss indicates the degradation of SAM.

Although tiny changes are observed in the differential spectra, when we reference the spectra to SAM surface as in Fig 7.13, the Al-O phonon mode centered at $\sim 905 \text{ cm}^{-1}$ is observed and indicates the formation of Al_2O_3 . The Al-CH_3 methyl deformation mode

at 1213 cm^{-1} does not increase much after 20 cycles indicating that it is mainly from the 1st TMA dosing and at the Al_2O_3 -SAM interface. In the $1300\text{-}1700\text{ cm}^{-1}$ range, in addition to the interfacial $\nu(\text{C}=\text{O})$ modes (1476 cm^{-1} and 1581 cm^{-1}) due to $(\text{CO}_2)\text{-Al}$, two strong peaks centered at 1609 cm^{-1} and 1409 cm^{-1} are tentatively assigned to $\text{C}=\text{O}/\text{C}-\text{O}$ related modes due to the decomposition of the underlying $-\text{CH}_2$ chains by ozone, with the proof of $\nu(\text{CH}_2)$ intensity loss at 2926 cm^{-1} and 2856 cm^{-1} .

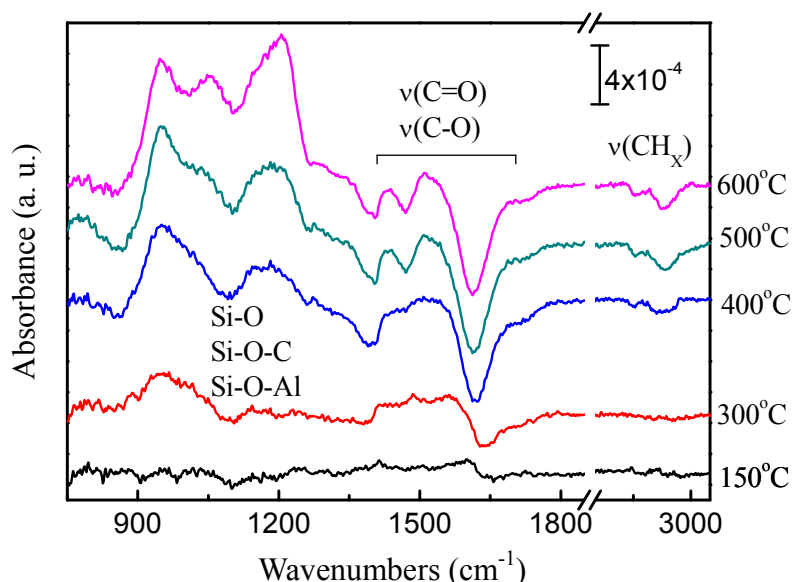


Fig 7.14 Annealing of 20 cycles Al_2O_3 by ozone on $-\text{COOH}$ SAM surface. All spectra are referenced to as deposit Al_2O_3 on SAM. The carbon impurities and SAM are eliminated. But interfacial Si-O modes occur at $900\text{-}1200\text{ cm}^{-1}$ in the spectra.

The presence of formate species [37] in Al_2O_3 , as discussed in Chapter 4, cannot be excluded and may be buried in the two strong peaks centered at 1609 cm^{-1} and 1409 cm^{-1} . Therefore, although $-\text{COOH}$ SAM is stable at this temperature when exposed to ozone, after the reaction of the functional group with TMA, its stability is reduced and the SAM becomes more vulnerable to ozone. So the enhanced stability of $-\text{COOH}$ SAM could result from the big and densely packed $-\text{COOH}$ head group compared with $-\text{CH}_3$ SAM. After the degradation of the SAM, the broad band between $900\text{-}1200\text{ cm}^{-1}$ (Si-O phonon

mode) shows the formation of interfacial SiO₂ as expected, but the thickness is much less than that on H/Si for the long ozone pulse case and comparable to the short pulse case. SAM does protect the surface in spite of the small amount of SiO₂. In contrast to Al₂O₃ on the SAM by TMA/water, the height of the 20-cycle Al₂O₃ phonon mode by ozone based ALD is about 1/2 of that of 10-cycle water based ALD, showing ozone based ALD has lower growth than water ALD possibly due to the absence of trapped water inside the film.

The *in situ* post annealing in N₂ for 5 min is performed afterwards. The results of the annealing from 150°C to 600°C are shown in Fig 7.14 which are referenced to as-deposited 20 cycles Al₂O₃ on SAM. The film is stable at 150°C concluded by the nearly featureless spectrum. Starting from 300°C, C-O/C=O related species in the film decompose shown by the broad negative bands around 1300-1700 cm⁻¹. Upon 400°C, the remnant -CH₂ chains begin to decompose, which is similar to the results of annealing of SAM and Al₂O₃-coated SAM by TMA/water where the initial decomposition of -CH₂ chains start upon 400°C. The expected Si oxidation is observed in the ranged of 900-1200 cm⁻¹, including Si-O-C/Si-O-Al modes at 945 cm⁻¹ and SiO₂ TO/LO modes at 1053 cm⁻¹ and 1206 cm⁻¹. In summary, the -COOH SAM can be used to deposit metal oxide by ozone, but due to ozone's high reactivity Si-O forms during the deposition.

7.3 ALD of HfO₂ on -COOH SAM

As a typical high-κ insulator material, HfO₂ is also deposited on the -COOH SAM surface. 10 cycles HfO₂ are deposited on the SAM by TEMA and D₂O at 100°C. Similarly, saturation pulse length is used for each precursor dosing and the IR incident angle is ~74°. The reaction between TEMA and water has been discussed in the

previous chapter in detail.

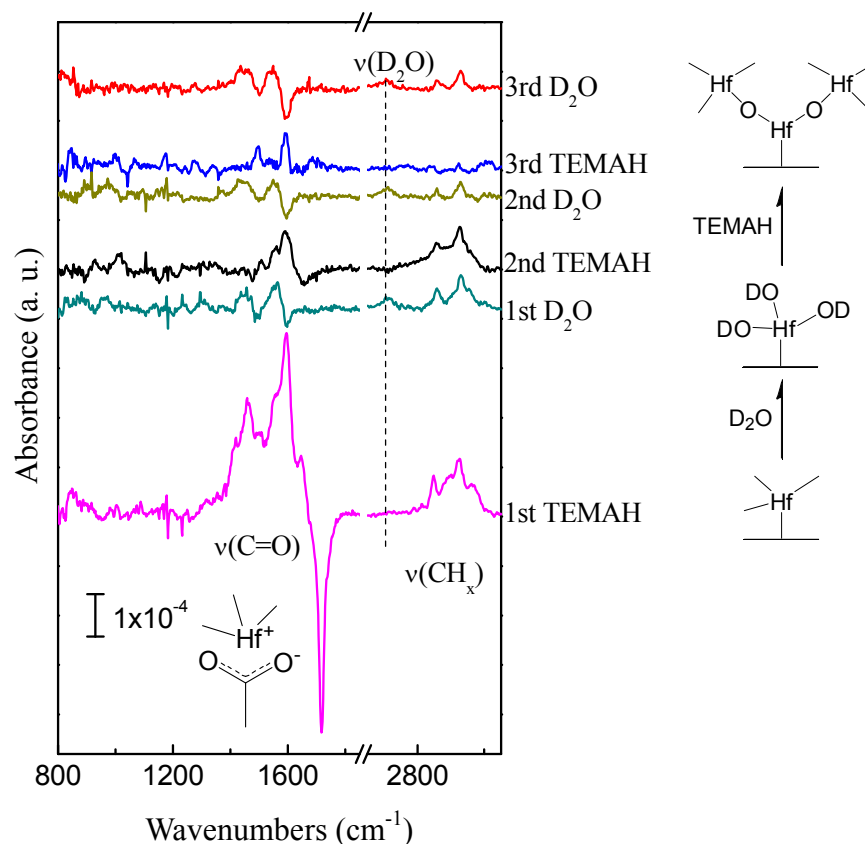


Fig 7.15 Differential FTIR absorption spectra of 10 cycles HfO_2 on $-\text{COOH}$ SAM surface at 100°C . Each spectrum is referenced to the spectrum recorded for the previous treatment. The bottom spectrum is referenced to SAM. The scheme of the ALD reaction is shown on the right side. Weak ALD ligand exchange is observed. The ionic structure after TEMAH reacting with COOH as $\text{COO}-\text{Hf}$ is shown by the inset.

The spectral results are shown in Fig 7.15 which is in the differential form to see the change on the surface after each treatment. For the 1st dosing of TEMAH on SAM, the spectrum is quite similar to that of TMA on SAM. Carboxylic groups on the surface are completely consumed, implying TEMAH is chemically adsorbed on the SAM surface, featured by the intensity loss of $\nu(\text{C}=\text{O})$ at 1714 cm^{-1} , and the positive bands at 1594 cm^{-1} and 1458 cm^{-1} which are assigned to $\nu_{\text{as}}(\text{C}=\text{O})$ and $\nu_{\text{s}}(\text{C}=\text{O})$ in acid salt structures ($\text{Hf}^+-\text{CO}_2^-$) as the small inset in Fig 7.15. Since TEMAH contains C-N bonds, the

broadening of $\nu_{as}/\nu_s(\text{C=O})$ modes is caused by other C, N and O related modes. The intensity increase of $\nu(\text{CH}_x)$ around $2800\text{--}3000\text{ cm}^{-1}$ is attributed to the precursor ligand as well. These bands further confirm that Hf with attached ligands is chemically adsorbed to the SAM surface. Different from TEMAH directly exposed to H/Si, there is no interfacial Hf-O-Si mode observed. Therefore, all ALD reactions are limited to the top surface of the -COOH functionalized SAM.

Upon the subsequent D_2O exposure, there is a positive band for $\nu(\text{CH}_x)$ at $2800\text{--}3000\text{ cm}^{-1}$, which is abnormal because the Hf precursor should be hydrolyzed by D_2O and the ligand should be replaced by -OD. It could be caused by perturbed underlying $-\text{CH}_2$ chains since the bands are mainly of $\nu_s/\nu_{as}(\text{CH}_2)$. The possibility of ligand from hydrolyzed residue TEMAH in the chamber adsorbed to the surface cannot be excluded. The reversible intensity fluctuation of the bands at 1476 and 1581 cm^{-1} is related to the $\nu(\text{C=O})$ shift induced by the change of C=O bond environment in the interfacial $(\text{CO}_2^-)\text{-Hf}^+$ as the Al_2O_3 case. In addition, the D_2O incorporation is observed by -OD stretching mode at 2707 cm^{-1} as the evidence of ALD ligand exchange. The reaction scheme is shown on the right side of Fig 7.15. The following cycles repeat the same scheme: after TEMAH exposures, Hf-ligand is adsorbed on the surface; after D_2O exposures, the chemically adsorbed precursor is reacted to form HfO_2 ,

The spectra in Fig 7.16 are referenced to the SAM surface to show the evolution of HfO_2 film with number of cycles. HfO_2 phonon mode is observed as a broad band centered at $\sim 680\text{ cm}^{-1}$, implying the formation of continuous HfO_2 film. It can be seen that $\nu(\text{D}_2\text{O})$ (2707 cm^{-1}) intensity keeps increasing with the increased number of cycles, indicating trapped D_2O in the film. By $\nu(\text{CH}_x)$ around $2800\text{--}3000\text{ cm}^{-1}$, it can be concluded that some carbon impurities from ligands remain inside HfO_2 . Absence of Si-O

mode around $900\text{--}1200\text{ cm}^{-1}$ and no intensity loss of $\nu(\text{CH}_2)$ suggest that no interfacial SiO_2 exists and the underlying $-\text{CH}_2$ alkyl chains keep intact, which is in good agreement with the result of Al_2O_3 on SAM.

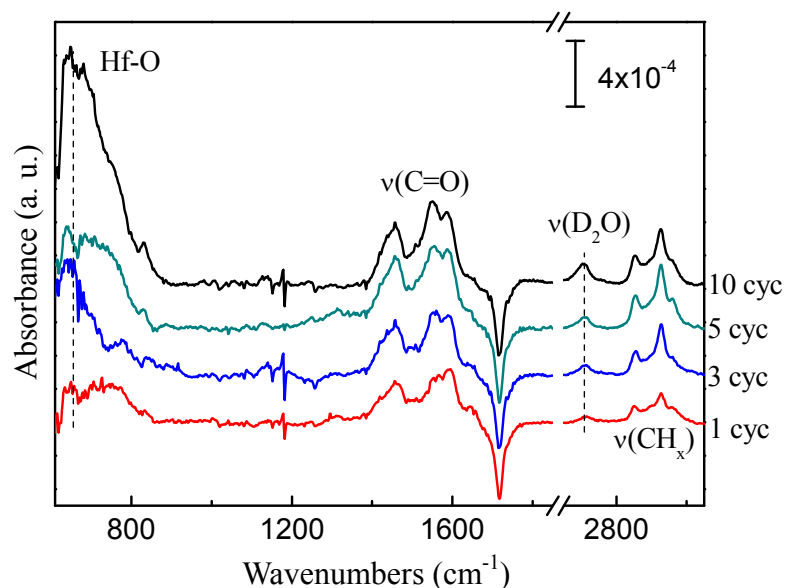


Fig 7.16 Absorption spectra of 10 cycles HfO_2 on SAM. All referenced to the SAM surface. HfO_2 phonon mode is observed. The impurities in the film such as CH_x and D_2O are confirmed by the spectra

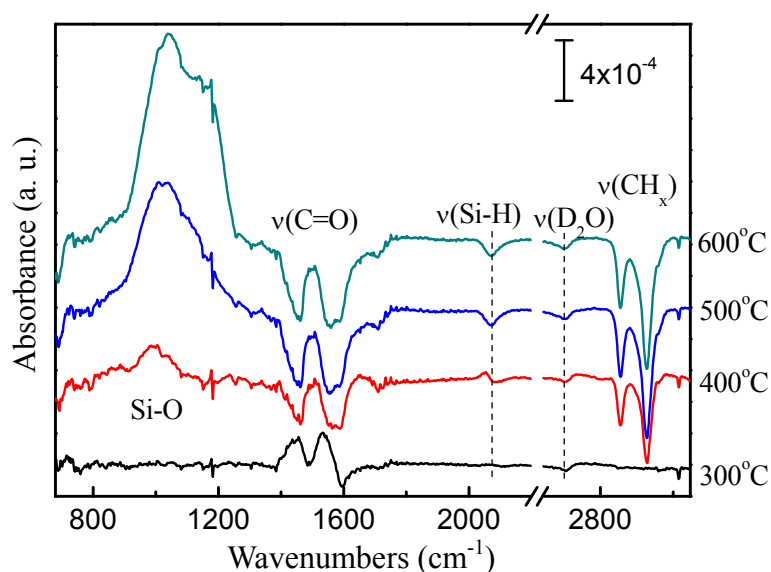


Fig 7.17 Annealing of 10 cycles HfO_2 on $-\text{COOH}$ SAM surface. All spectra are referenced to as-deposit HfO_2 on SAM. The interfacial SiO_2 increases and the COOH SAM degrades above 400°C .

Post annealing of the film is performed in N₂ for 5min *in situ* which is shown by Fig 7.17 (referenced to HfO₂). Upon 300°C, there is no interfacial SiO₂ formation evidenced by the absence of SiO₂ band (900-1200 cm⁻¹). $\nu(\text{C=O})$ redshifts to 1533 cm⁻¹ and 1454 cm⁻¹, suggesting the interface between the SAM and HfO₂ is perturbed. The SAM is intact at this temperature according to the absence of $\nu(\text{CH}_2)$ intensity change. Upon annealing at 400°C, the SAM starts to decompose, shown by the negative $\nu(\text{CH}_2)$ and $\nu(\text{C=O})$ bands around 2800-3000 cm⁻¹ and 1300-1700 cm⁻¹. The expected SiO₂ is observed by the broad band centered at 900 cm⁻¹ and it keeps growing with increased temperature. The removal of residue Si-H and D₂O inside the film is featured by the negative bands of $\nu(\text{Si-H})$ at 2074 cm⁻¹ and $\nu(\text{D}_2\text{O})$ at 2707 cm⁻¹. Note that the same phenomena has been observed as the annealing of Al₂O₃ on SAM at 300°C and 400°C--the formation of Si-H at 2052 cm⁻¹ due to thermal decomposition of alkyl chains through β -hydride elimination with cleavage of Si-C bonds.

7.4 ALD of Cu on -COOH SAM

The deposition of metal electrode on SAM has been an issue for long time [38, 39]. The difficulty is that either the metal deposition may decompose the SAM such as by using sputtering and CVD, or the metal may diffuse through SAM causing short. Since ALD has the advantages of depositing smooth and uniform film at relatively low temperature, ALD of Cu on SAM as electrode or seed layer is very interesting and promising.

For this purpose, 10 cycles Cu are deposited by ALD ([Cu(^sBu-*amd*)]₂ and H₂) [40] on -COOH SAM/HSi(111) at 185°C. The incident angle of IR beam is ~74°. The differential spectra of this deposition are presented in Fig 7.18.

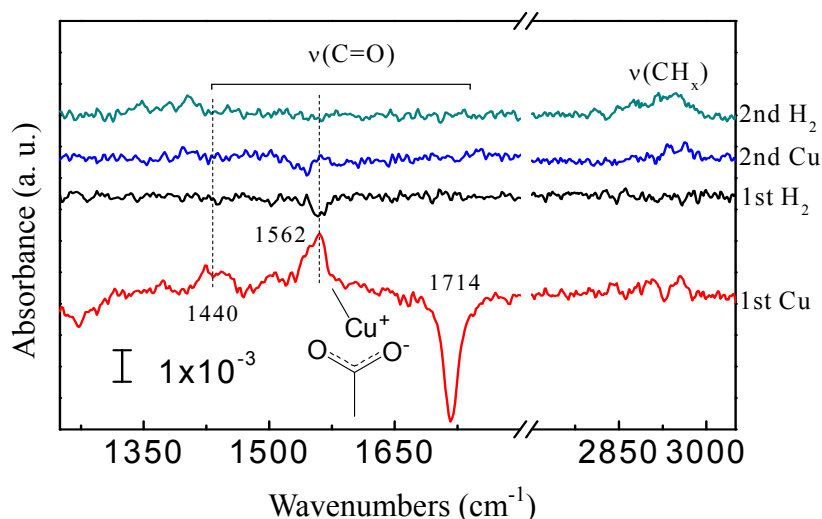


Fig 7.18 Differential FTIR absorption spectra of 10 cycles Cu on -COOH SAM surface at 185°C. Each spectrum is referenced to the spectrum recorded for the previous treatment. The bottom spectrum is referenced to SAM. The scheme of the ALD reaction is shown on the right side. The inset shows the ionic structure formed after the reaction between Cu precursor and the COOH SAM.

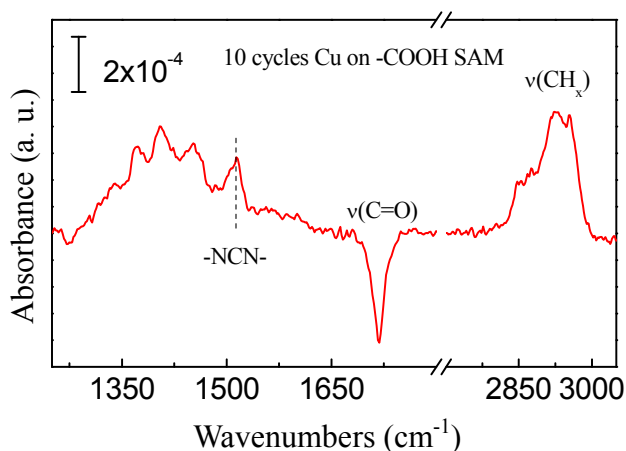


Fig 7.19 Absorption spectra of 10 cycles Cu on SAM referenced to the SAM surface at 185°C. Substantial amount of ligand related impurities are observed in the spectra.

Similarly, the variation of C=O stretching modes after the 1st Cu precursor exposure indicates the Cu precursor is chemically adsorbed to the SAM surface, evidenced by the negative band of -COOH at 1714 cm⁻¹ and the positive bands at 1562 cm⁻¹/1440 cm⁻¹ which are assigned to $\nu_{as}/\nu_s(\text{C=O})$ in acid salt structure (CO₂⁻) as the small inset in Fig 7.18. The coverage can be concluded by the intensity loss of -COOH stretching mode and

is about ~65%, which is less than TMA and TEMAH cases. In addition, the intensity for the shift of $\nu(\text{C}=\text{O})$ is much lower than the TMA and TEMAH cases, along with the lower intensity of $\nu(\text{CH}_x)$ from the ligand, suggesting a lower reactivity of the Cu precursor with -COOH SAM. The subsequent H_2 exposure shows little effect according the spectrum but with tiny variation in the $\text{C}=\text{O}$ stretching modes as having been discussed. The 2nd dosing of Cu precursor add a little CH_x to the surface without observable NCN Cu precursor ligand feature at 1509 cm^{-1} , suggesting a low growth rate. The CH_x introduced by the 2nd H_2 exposure could be caused by the residue Cu precursor in the environment or the perturbed CH_2 chains of the SAM as the HfO_2 case.

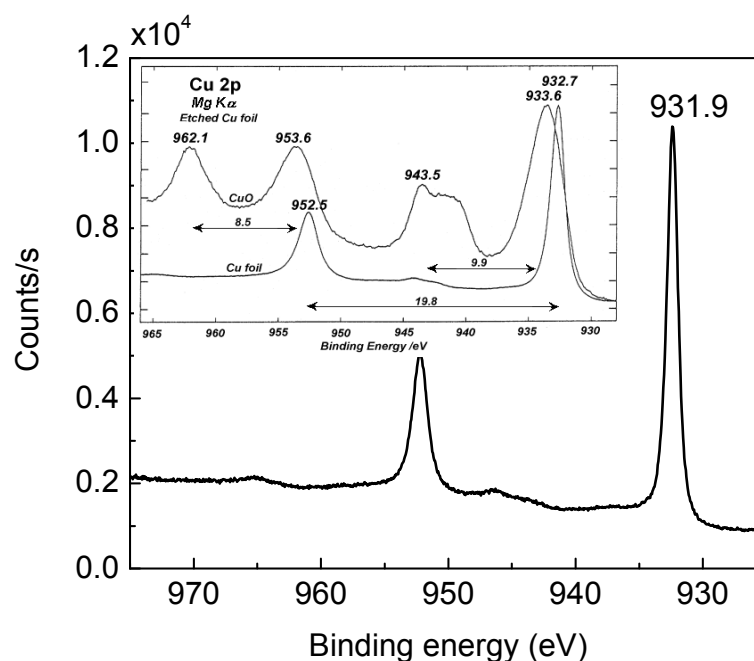


Fig 7.20 XPS Cu 2p of 10 cycles Cu on SAM. The inset [41] shows the spectra of pure Cu and CuO. Compared with the standard spectra, the CuO amount is minimal in the Cu film on COOH SAM.

To determine the species inside the Cu film, the spectrum of 10 cycles Cu is referenced to the starting SAM surface which is shown in Fig 7.19. The strong stretching bands of CH_x are clearly observed at $2800\text{--}3000\text{ cm}^{-1}$. Moreover, the NCN Cu precursor

ligand feature appears at 1513 cm^{-1} , indicating the C and N impurities inside the film. The bands at $1300\text{--}1476\text{ cm}^{-1}$ are related to the C, N and O bonds of impurities inside the film. No evidence of -CH_2 loss indicates that the alkyl chains of the -COOH SAM survive during the ALD process.

To prove the deposition of the Cu, XPS analysis is carried out and Fig 7.20 shows the Cu 2p spectrum. The Cu $2p_{1/2}$ at 931.9 eV [42], compared with the pure Cu and CuO in the inset of Fig 7.20, can be either Cu^0 or Cu^{1+} but believed to be Cu^0 according to the conductivity study done by Gordon's group [40]. The small satellite peak resulting from Cu^{2+} around 945 eV could be caused by the interfacial $(\text{CO}_2)\text{-Cu}$ bond or trace amount of CuO.

7.5 Summary

In this chapter, two types of SAMs on H/Si(111) have been discussed: one with chemically unreactive functional group -CH_3 which is $\text{CH}_3\text{-(CH}_2\text{)}_{17}\text{-H/Si(111)}$, and the other with chemically reactive functional group -COOH which is $\text{COOH-(CH}_2\text{)}_{10}\text{-H/Si(111)}$. The -COOH type SAM is achieved without any Si-O or Si-O-C bond but the -CH_3 type SAM has trace amount of SiO_2 at the interface.

The stability of those two SAMs under thermal annealing and ozone exposure is investigated. The -COOH SAM has higher stability for both cases. The carboxylic head group survives without substantial decomposition up to 200°C for thermal annealing and 100°C for ozone exposure. In both situations, the deterioration of the carboxylic head group starts first, and the -CH_2 chains decompose at a higher temperature. The -CH_3 SAM decomposes above 150°C for annealing and degrades immediately upon ozone exposure at 60°C . Thus, -COOH SAM shows better quality.

ALD of Al_2O_3 , HfO_2 and Cu are deposited on -COOH SAM surface. By using *in situ* FTIR, the reaction mechanism is studied. All the reactions start from the interaction between the precursor and -COOH groups by forming (CO_2) -metal salt structure.

For Al_2O_3 deposition on -COOH SAM at 100°C , both TMA/ D_2O and TMA/ozone are used. For TMA/ D_2O , the quality of Al_2O_3 on SAM is similar to that on SiO_2 . No interfacial SiO_2 is observed and little ALD incubation period is detected, but D_2O impurity is observable inside the film. The SAM remains intact during the ALD process. The post annealing result shows the decomposition of the SAM above 300°C . For TMA/ozone, substantial amount of C-O/C=O impurities are found inside the film due to the decomposition of the underlying SAM and TMA ligands. Its growth rate is about 1/4 of that of water based ALD. Small amount of Si-O is observed by FTIR.

HfO_2 is deposited by TMAH/ D_2O on -COOH SAM at 100°C . Similarly, no interfacial SiO_2 is observed during the deposition and the underlying SAM is intact. However, D_2O is incorporated inside the film. The post annealing shows that coated SAM is stable up to 300°C . Above this temperature, SiO_2 keeps growing with the increased temperature.

Finally, ALD of pure copper on -COOH SAM is demonstrated. It is concluded that the growth rate is low by the intensity of ligand related modes. Residue NCN ligand related carbon impurities are detected inside the film. The alkyl chains survive during the deposition of Cu and XPS Cu 2p spectrum confirms the existence of copper film.

Bibliography

1. J. J. Gooding, F. Mearns, W. Yang and J. Liu, *Self-assembled monolayers into the 21st century: Recent advances and applications*, *Electroanalysis* **15** (2003), 81.
2. S. Onclin, B. J. Ravoo and D. N. Reinhoudt, *Engineering silicon oxide surfaces*

- using self-assembled monolayers, *Angew. Chem. Int. Ed.* **44** (2005), 6282.
3. F. Schreiber, *Structure and growth of self-assembling monolayers*, *Progress in Surface Science* **65** (2000), 151.
 4. ---, *Self-assembled monolayers: From 'simple' model system to biofunctionalized interfaces*, *J. Phys.: Condens. Matter* **16** (2004), R881.
 5. A. Ulman, *Formation and structure of self-assembled monolayers*, *Chem. Rev.* **96** (1996), 1533.
 6. D. D. M. Wayner and R. A. Wolkow, *Organic modification of hydrogen terminated silicon surfaces*, *J. Chem. Soc., Perkin Trans. 2* (2002), 23.
 7. A. B. Sieval, R. Linke, H. Zuilhof and E. J. R. Sudhölter, *High-quality alkyl monolayers on silicon surfaces*, *Adv. Mat.* **12** (2000), 1457.
 8. R. Pool, P. Schapotschnikow and T. J. H. Vlugt, *Solvent effects in the adsorption of alkyl thiols on gold structures: A molecular simulation study* *J. Phys. Chem. C* **111** (2007), 10201.
 9. S. R. Wasserman, Y. T. Tao and G. M. Whitesides, *Structure and reactivity of alkylsiloxane monolayers formed by reaction of alkyltrichlorosilanes on silicon substrates*, *Langmuir* **5** (1989), 1074.
 10. N. A. K. Chaki, M. Aslam, J. Sharma and K. Vijayamohanan, *Applications of self-assembled monolayers in materials chemistry*, *Proc. Indian Acad. Sci. (Chem. Sci.)* **113** (2001), 659.
 11. R. Chen, H. Kim, P. C. McIntyre, D. W. Porter and S. F. Bent, *Achieving area-selective atomic layer deposition on patterned substrates by selective surface modification*, *Appl. Phys. Lett.* **86** (2005), 191910.
 12. R. Chen and S. F. Bent, *Chemistry for positive pattern transfer using area-selective atomic layer deposition*, *Adv. Mat.* **18** (2006), 1086.
 13. O. Seitz, T. Böcking, A. Salomon, J. J. Gooding and D. Cahen, *Importance of monolayer quality for interpreting current transport through organic molecules: Alkyls on oxide-free Si*, *Langmuir* **22** (2006), 6915.
 14. N. P. Kobayashia, C. L. Donleya, S.-Y. Wanga and R. S. Williamsa, *Atomic layer deposition of aluminum oxide on hydrophobic and hydrophilic surfaces* *Journal of Crystal Growth* **299** (2007), 218.
 15. A. B. Sieval, B. v. d. Hout, H. Zuilhof and E. J. R. Sudhölter, *Molecular modeling of covalently attached alkyl monolayers on the hydrogen-terminated Si(111) surface*, *Langmuir* **17** (2001), 2172.
 16. D. M. Byler, W. V. Gerasimowicz, H. Susi and M. Schnitzer, *FT-IR spectra of soil constituents: Fulvic acid and fulvic acid complex with ferric ions*, *Applied Spectroscopy* **41** (1987), 1428.
 17. R. Boukherroub, J. T. C. Wojtyk, D. D. M. Wayner and D. J. Lockwood, *Thermal hydrosilylation of undecylenic acid with porous silicon*, *J. Electrochem. Soc.* **149** (2002), H59.
 18. H. Asanuma, G. P. Lopinsk and H.-Z. Yu, *Kinetic control of the photochemical*

- reactivity of hydrogen-terminated silicon with bifunctional molecules*, Langmuir **21** (2005), 5013.
19. R. T. Conley, *Infrared spectroscopy*, Allyn and Bacon, Inc. (1972).
 20. O. Gershevitz and C. N. Sukenik, *In situ FTIR-ATR analysis and titration of carboxylic acid-terminated sams*, J. Am. Chem. Soc **126** (2003), 482.
 21. R. G. Snyder, H. L. Strauss and C. A. Elliger, *Carbon-hydrogen stretching modes and the structure of n-alkyl chains. 1. Long, disordered chains*, J. Phys. Chem **86**, 5145 - 5150.
 22. M. D. Porter, T. B. Bright, D. L. Allara and C. E. D. Chidsey, *Spontaneously organized molecular assemblies. 4. Structural characterization of n-alkyl thiol monolayers on gold by optical ellipsometry, infrared spectroscopy, and electrochemistry*, J. Am. Chem. Soc. **109** (1987), 3559-3568.
 23. S. Lenfant, D. Guerin, F. TranVan, C. Chevrot, S. Palacin, J. P. Bourgoin, O. Bouloussa, F. Rondelez and D. Vuillaume, *Electron transport through rectifying self-assembled monolayer diodes on silicon: Fermi level pinning at the molecule-metal interface*, J. Phys. Chem. B (2006), 13947.
 24. A. Faucheux, F. Yang, P. Allongue, C. H. d. Villeneuve, F. Ozanam and J.-N. Chazalviel, *Thermal decomposition of alkyl monolayers covalently grafted on (111) silicon*, Appl. Phys. Lett. **88** (2006), 193123.
 25. M. M. Sung, G. J. Kluth, O. W. Yauw and R. Maboudian, *Thermal behavior of alkyl monolayers on silicon surfaces*, Langmuir **13** (1997), 6164.
 26. K. T. Queeney, N. Herbots, J. M. Shaw, V. Atluri and Y. J. Chabal, *Infrared spectroscopic analysis of an ordered Si/SiO₂ interface*, Appl. Phys. Lett. **84** (2004), 493.
 27. A. Faucheux, A. C. Gouget-Laemmel, C. H. d. Villeneuve, R. Boukherroub, F. Ozanam, P. Allongue and e.-N. Chazalviel, *Well-defined carboxyl-terminated alkyl monolayers grafted onto H-Si(111): Packing density from a combined AFM and quantitative IR study*, Langmuir **22** (2006), 153.
 28. M. M. Frank, Y. J. Chabal and G. D. Wilk, *Nucleation and interface formation mechanisms in atomic layer deposition of gate oxides*, Appl. Phys. Lett. **82** (2003), 4758.
 29. M. M. Frank, Y. J. Chabal, M. L. Green, A. Delabie, B. Brijs, G. D. Wilk, M. Y. Ho, E. B. O. d. Rosa, I. J. R. Baumvol and F. C. Stedile, *Enhanced initial growth of atomic-layer-deposited metal oxides on hydrogen-terminated silicon*, **83** (2003), 740.
 30. J. D. Ferguson, A. W. Weimer and S. M. George, *Atomic layer deposition of Al₂O₃ films on polyethylene particles*, Chem. Mat. **16** (2004), 5602.
 31. T. R. Gow, R. Lin, L. A. Cadwell, F. Lee, A. L. Backman and R. I. Masel, *Decomposition of trimethylaluminum on silicon(100)*, Chem. Mat. **1** (1989), 406.
 32. A. W. Ott, J. W. Klaus, J. M. Johnson and S. M. George, *Al₂O₃ thin film growth on Si(100) using binary reaction sequence chemistry*, Thin Solid Film **292** (1997), 135.

33. W. Mozgawa, M. Sitarz and M. Rokita, *Spectroscopic studies of different aluminosilicate structures*, Journal of Molecular Structure **512** (1999), 251.
34. A. Fidelis, F. Ozanam and J.-N. Chazalviel, *Fully methylated, atomically flat (111) silicon surface*, Surf. Sci. **44** (2000), L7.
35. M.-T. Ho, Y. Wang, R. T. Brewer, L. S. Wielunski and Y. J. Chabal, *In situ infrared spectroscopy of hafnium oxide growth on hydrogen-terminated silicon surfaces by atomic layer deposition*, Appl. Phys. Lett. **87** (2005), 133103.
36. X. Liu, S. Ramanathan, A. Longdergan, A. Srivastava, E. Lee, T. E. Seidel, J. T. Barton, b. Dawen Pang and R. G. Gordonb, *ALD of hafnium oxide thin films from tetrakis(ethylmethylamino) hafnium and ozone*, J. Electrochem. Soc. (2005), 2005.
37. J. Kwon, M. Dai, M. D. Halls and Y. J. Chabal, *Detection of a formate surface intermediate in the atomic layer deposition of high- κ dielectrics using ozone*, Chem. Mat. **20** (2008), 3248.
38. B. d. Boer, A. Hadipour, M. M. Mandoc, T. v. Woudenberg and P. W. M. Blom, *Tuning of metal work functions with self-assembled monolayers*, Advanced Materials **17** (2005), no. 5, 621-625.
39. B. d. Boer, H. Meng, D. F. Perepichka, J. Zheng, M. M. Frank, Y. J. Chabal and Z. N. Bao, *Synthesis and characterization of conjugated mono- and dithiol oligomers and characterization of their self-assembled monolayers*, Langmuir **19** (2003), 4272.
40. Z. Li, A. Rahtu and R. G. Gordon, *Atomic layer deposition of ultrathin copper metal films from a liquid copper(I) amidinate precursor*, Journal of Electrochemical Society **153** (2006), C787-C794.
41. <http://www.lasurface.com/database/spectrexp.php>.
42. J. F. Moulder, N. F. Stickle, P. E. Sobol and K. D. B. I. J. Chastain, *Handbook of X-ray photoelectron spectroscopy*, Perkin-Elmer Corporation (1995).

Chapter 8: Summary

The main contribution of the work described in this thesis is the fundamental understanding of the ALD process for a variety of important systems, derived from *in-situ* FTIR studies. This technique was essential to characterize the properties of both starting surfaces and precursors, and to study the essential elements of ALD. The mechanistic aspects of ALD are investigated including the side reactions taking place during ALD growth, which provides the necessary insight to suggest possible optimization schemes for future ALD applications, as summarized below.

1) Two types of starting surfaces are discussed in detail: nitrided Si surface and SAMs modified H/Si surface. In this dissertation, SiN_x is used as an oxygen barrier to suppress interfacial SiO_2 for ALD of high- κ metal oxides, and SAMs are for area-selective ALD. But both have many other applications as well.

For the nitrided surfaces, we studied the mechanism of thermal NH_3 nitridation of flat H/Si(111) surface and vicinal H/Si(111) surfaces including monohydride and dihydride stepped surfaces. By varying the temperature from 150°C to 600°C at a small temperature step of 25°C, the surface interaction with NH_3 is investigated to conclude the whole picture of NH_3 nitridation. Flat H/Si(111) surface and monohydride stepped H/Si(111) surface show the same nitridation behavior due to their structural similarity. The nitridation starts from NH_3 dissociation by replacing the surface Si-H with Si-NH₂ at 350°C. The nitrogen insertion to Si-Si network and formation of SiN_x layer take place above 400°C. Dihydride stepped H/Si(111) shows a very different nitridation mechanism, where desorption of Si-H begins at 325°C accompanied by the forming an unexpected H-Si-NH-Si bridging structure at the step edge. DFT calculation perfectly confirms our

vibrational mode assignments and assumed nitridation model. Upon 400°C, nitrogen insertion to Si-Si back bond is evidenced. This information is helpful to determine condition for initial interaction between NH_3 and surface Si-H and we understand how NH_3 attacks the surface and is bonded to the surface. By varying the temperature, the termination of the Si surface can be changed.

For the SAM-terminated surfaces, the stability of two types of SAMs is studied including -COOH terminated SAM (reactive) and -CH₃ terminated SAM (unreactive) grafted on H/Si(111) surface via direct Si-C bond. -COOH SAM has higher stability under thermal annealing in N₂ and ozone exposure. The carboxylic head group survives without substantial decomposition up to 200°C for thermal annealing and 100°C for ozone exposure, while the CH₂ chains decompose at a higher temperature. The -CH₃ SAM decomposes above 150°C for annealing and degrades immediately upon ozone exposure at 60°C. Thus, -COOH SAM shows much better quality and it is a very reactive surface for ALD which can be utilized for selective growth.

2) ALD of high- κ metal oxides and pure metal are studied, including HfO₂, Al₂O₃, La₂O₃ and pure Cu on various surface:

HfO₂ is deposited by TEMA/ozone at 100°C, and it is compared with the deposition by TEMA/D₂O. On H/Si surface, ozone based HfO₂ shows substantial interfacial Si oxide and carbonyl/nitro derivatives as impurities in the film without trapped water/OH. By using SiN_x and -COOH SAM surfaces, the interfacial SiO₂ is suppressed for ozone based ALD.

Al₂O₃ is deposited by TMA/ozone on H/Si(111) at 300°C. When excessive ozone exposure is used, an unpredicted formate surface intermediate is detected and studied assisted by DFT calculations. Substantial interfacial SiO₂ is observed during the ALD

process. When the ozone pulse length is shortened, the film quality is improved evidenced by the absence of formate species and minimal interfacial SiO_2 which is comparable to water based ALD but with lower growth rate. The gas phase reaction of TMA/ D_2O is straightforward and CH_4/CD_4 are the only byproducts, while the reaction of TMA/ozone is much more complicated. C_2H_4 is not the only byproduct and the oxidation of the methyl terminal group/ Al-O-CH_3 may prevail which needs further study. The reaction pathway could be determined by ozone amount. By using -COOH SAM surface, high quality Al_2O_3 is achieved by TMA/ D_2O at 100°C without interfacial SiO_2 due to the high reactivity and protection of -COOH SAM.

In short, ozone based ALD can improve the film quality but the reaction is much more complicated due to ozone's high reactivity. The amount of ozone significantly alters the reaction pathway and the film quality. By using SiN_x and SAMs surfaces, the surface properties are modified and interfacial SiO_2 is suppressed which are very good starting surfaces for ALD.

La_2O_3 is deposited by using a brand new precursor, $\text{La}(\text{}^i\text{Pr-MeAMD})_3$, and D_2O . By checking the La precursor gas phase, all ligand features are observed. Partial hydroxylation of the precursor is detected in the gas phase by the unexpected stretching vibrational modes resulting from C=N and N-H in free hydrogenated ligands. The gas phase reaction of $\text{La}(\text{}^i\text{Pr-MeAMD})_3$ and D_2O confirms this finding. The growth of La_2O_3 on H/Si(111) surface shows that $\text{La}(\text{}^i\text{Pr-MeAMD})_3$ is highly reactive with H/Si and involves the formation of a Si-O-La bond due to the partially hydrolyzed precursor, where the free hydrogenated ligand is unreactive with the surface. For the deposition at 200°C , substantial acetate/carbonate impurities are detected, while for the deposition at 300°C , acetate/carbonate impurities are reduced but cyanamide (or carbodiimide)

intermediate species are observed with increased interfacial SiO₂. The highly hygroscopic nature of La₂O₃ results in CVD-like deposition and thickness non-uniformities on a macroscopic scale. The deposition of La_xAl_yO nanolaminate by alternating TMA/D₂O and La(ⁱPr-MeAMD)₃/D₂O ALD cycles successfully suppresses CVD-like reactions and minimizes the acetate/carbonate incorporation while remains the high dielectric constant.

Thus, the properties and reactions of the new La precursor are studied in detail. The intrinsic of La₂O₃ makes the ALD process difficult. With the understanding of the its mechanism, the ALD process can be optimized such as by using Al₂O₃ incorporated La₂O₃.

Finally, pure copper is deposited by using a novel liquid copper precursor--copper(I) di-sec-butylacetamidinate ([Cu(^sBu-amd)]₂) and molecular hydrogen on SiO₂ surface. The evolution of SiO₂ phonon modes in the IR spectra clearly shows the agglomeration and the diffusion of Cu on/into SiO₂ during the initial 10 cycles. Cu agglomeration and diffusion increase when the deposition temperature is raised. The H₂ reduction of the precursor ligand and ligand hydrogenation are observed by the vibrational modes attributed to CH_x and NCN bonds. *Ex situ* XPS results confirm the deposition of copper on the SiO₂ surface. Both FTIR and XPS results show residue ligand impurities inside the Cu film with small amount of N (< 2%) and substantial amount of C for the initial cycles due to incomplete ALD reactions. RBS indicates that the growth rate on SiO₂ is temperature dependent and the maximum growth rate is found in the range of 185-250°C based on one ALD cycle. At 185°C, the thickness of 10 cycles Cu is 1.04-1.18 nm with uniform distribution.

The Cu deposition at 185°C on other surfaces is studied as well, such as H/Si, SiN_x, Al₂O₃ and SAM surfaces. FTIR and XPS show the similar film contents and growth

mechanism as on SiO_2 . However, much lower growth rate is found for all those surfaces than that of SiO_2 surface. Cu_3N is deposited on SiO_2 at 160°C successfully. After annealing at 225°C in forming gas, the Cu_3N is partially reduced to Cu with little Cu agglomeration.

Therefore, the properties and the initial interactions of the new precursor with SiO_2 and other surfaces are addressed and Cu agglomeration/diffusion is observed as well for the initial ALD cycles. This information is critical for the subsequent processes of Cu ALD. In addition, ALD of metal on SAMs may resolve the problem of making metal electrode on SAMs as the application for organic devices.

Appendix: ALD of HfO_2 on Trenched H/Si

With the fast development of modern microelectronics, structures have evolved from planar dimensions to three dimensions, which greatly decrease surface area and cost per bit [1]. For example, deep trenches are used for trench capacitors in DRAM (Dynamic Random Access Memory) which can have much larger capacitance than that of planar capacitors due the increased surface area without increasing the wafer area [2, 3, 4]. The schematic diagram of a trench capacitor is shown by Fig A.1.

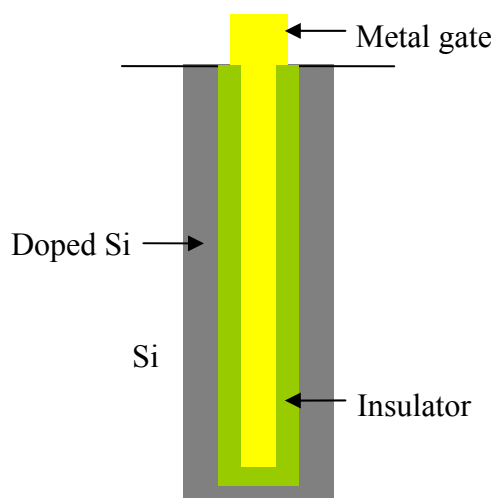


Fig A.1 Diagram of a trench capacitor in silicon. (yellow-metal gate, green-insulator, gray-doped silicon)

Normally the trench is quite deep to increase the surface area with high aspect ratio. High- κ metal oxide is utilized as insulator to further improve the capacitance. How to deposit highly conformal and uniform high- κ metal oxide and metal into the deep trench as insulator layer and metal gate is challenging [5].

Due to the great advantages of ALD to deposit homogeneous and high quality film, it is becoming the major method for those applications. Trenched surfaces are very

different from flat surfaces due to its artificial roughness, and it is very important to study the behavior of ALD precursor on it. In this chapter, we will perform *in situ* FTIR measurements of trenched surfaces and compare the results with those obtained on flat surfaces. This work is put in an appendix because the interpretation of the data is beyond the scope of this thesis. The results/interpretation are therefore to be considered as preliminary.

A.1 Thermal stability of H/Si surfaces

Before we go on to HfO₂ deposition on H-terminated trenched samples, the thermal stability of different H/Si including flat H/Si(111), flat H/Si(100) and trenched H/Si(100) is studied. The annealing is performed in purified N₂ at ~3-4 torr for 5min.

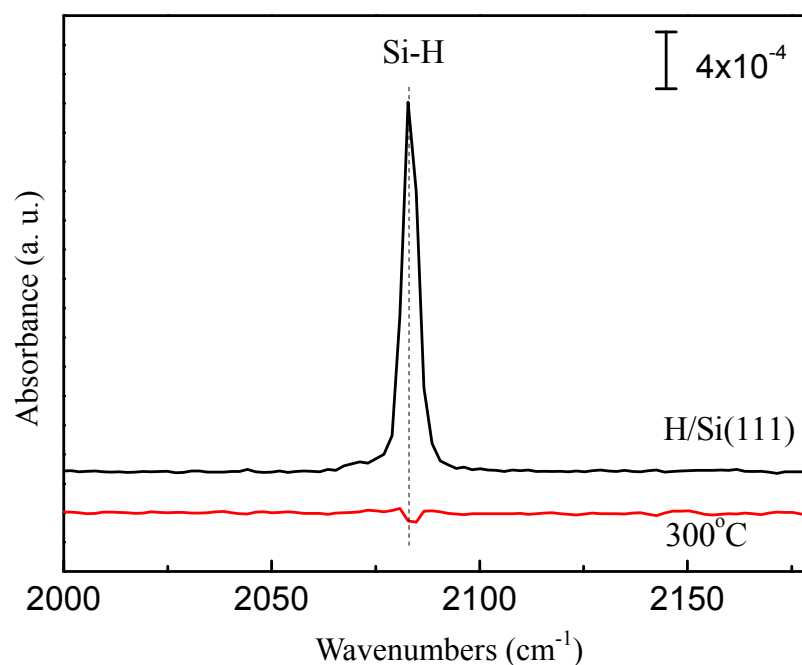


Fig A.2 Absorption spectra of annealing of flat H/Si(111) at 300°C referenced to initial H/Si(111) which is at the bottom in red and the initial H/Si(111) referenced to oxide which is on the top in black. The incident angle is ~74°. The H/Si(111) is stable at 300°C.

Annealing of flat H/Si(111) at 300°C is shown in Fig A.2. The black curve is the initial H/Si(111) spectrum referenced to an oxide surface and the bottom red curve shows the difference due to annealing, using the initial H/Si(111) as reference. The Si-H stretching mode is at 2083 cm^{-1} as discussed in chapter 2 [6]. The single Si-H peak in the spectrum is due to the monohydride structure on H/Si(111). After annealing at 300°C, the surface remains almost unchanged (no net loss of integrated area). It can be concluded that the Si-H is stable at this temperature. Normally Si-H is much more stable in UHV environment and can survive at higher temperature. Our ALD reactor is not maintained as UHV environment, thus residue water and other contaminants existing in the chamber reduce the stability of Si-H.

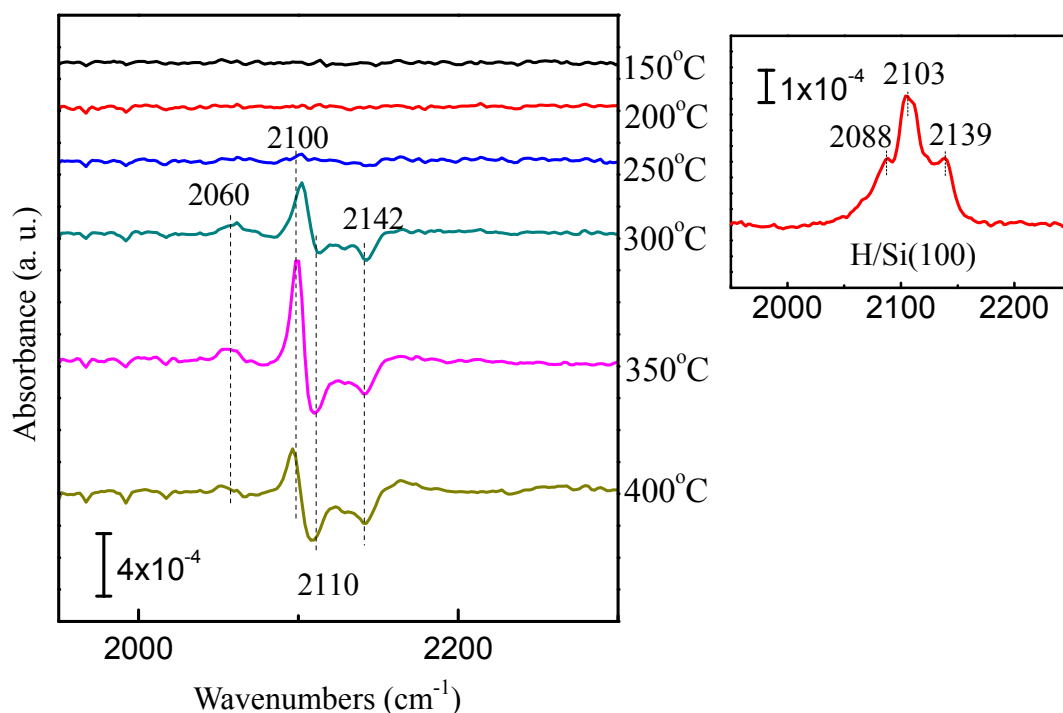


Fig A.3 Absorption spectra of annealing of flat H/Si(100) which is referenced to initial H/Si(100) and the inset is the initial H/Si(100) which is reference to oxide surface. The incident angle is $\sim 74^\circ$. The surface is stable up to 250°C

Flat H/Si(100) surfaces are then annealed in N₂ as shown by Fig A.3, where the spectra are referenced to the initial H/Si(100). The inset shows the initial H/Si(100) referenced to oxide. The peaks at 2088 cm⁻¹, 2103 cm⁻¹ and 2139 cm⁻¹ are attributed to Si-H monohydride, dihydride and trihydride modes, respectively [7]. The H/Si(100) is stable up to 250°C. Upon 300°C, the Si-H begins to desorb starting with the loss of dihydride and trihydride stretching modes at 2110 cm⁻¹ and 2142 cm⁻¹. The positive peak at 2100 cm⁻¹ corresponds to an increased concentration of dihydride, most likely resulting from the partial decomposition of trihydride. The band at 2060 cm⁻¹ is caused by the isolated monohydride stretching mode due to the decomposition of surface Si-H. Therefore, it is clear that H/Si(111) is more stable than H/Si(100) because there are more reactive dihydrides and trihydrides and more defects on H/Si(100) surfaces.

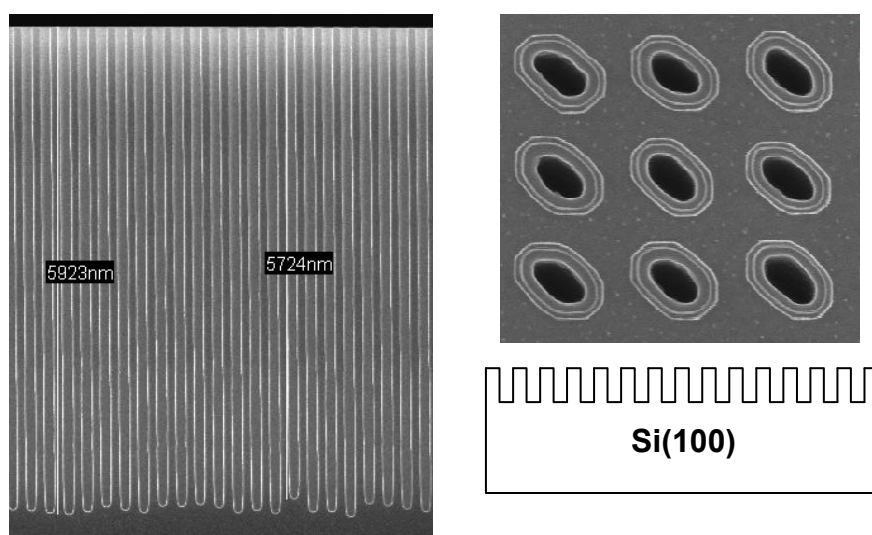


Fig A.4 The structure of trenched sample, including the cross section and top views. The typical size of the trench is ~0.1-0.2μm wide and ~6-8μm deep (provided by Dr. Uwe Schroeder).

The structure of the trenched sample we used is shown by Fig A.4. The trenches are on one side and the other side is flat. The substrate is (100) oriented and CZ grown. The

typical size of the trenches is $\sim 0.1\text{-}0.2\mu\text{m}$ wide and $\sim 6\text{-}8\mu\text{m}$ deep. The surface is artificially rough. The hydrogen-terminated trenched Si(100) is measured by IR with the IR facing the trenched side, as the inset in Fig A.5. The spectrum is presented in Fig A.5 which is taken at normal incidence. The stretching modes of Si-H are around 2100 cm^{-1} and the bending mode of Si-H are observed $\sim 620\text{ cm}^{-1}$. The broad negative band at $900\text{-}1300\text{ cm}^{-1}$ corresponds to SiO_2 TO/LO modes due to the etching of HF [8].

Note that to fully remove the SiO_2 , 10 min HF etching is used in this case. The prolonged etching time will not rough the surface once the surface is fully passivated by hydrogen [9]. As in the inset of Fig A.5, three strong modes are observed at 2087 cm^{-1} , 2104 cm^{-1} and 2139 cm^{-1} , which are tentatively assigned to monohydride, dihydride and trihydride modes. Due to the roughness of the surface, more coupled modes may appear and overlap within this range. The spectrum taking at $\sim 74^\circ$ shows little difference from that of normal incidence resulting from the surface roughness. So it can be concluded that trenches dominate the contribution.

The sine-wave like baseline oscillation in Fig A.5 is caused by the trenched surface [10]. There is an interference due to the change of index of refraction between the trench area and the solid Si region. The oscillation frequency depends on the depth of the trenches. The effective refractive index of the surface is related to the trench top width since the increased top void fraction will make it closer to that of the air lowering the reflectivity. Although an accurate model is difficult, we use a highly simplified mode according to Fabry-Pérot interferometer [11]:

$$\Delta\lambda \approx \frac{\lambda_0^2}{2nd \cos\theta} \quad \text{Eq A.1}$$

where n is the refractive index, d is the trench depth and $n \approx n_{\text{Si}} = 4$, to get an estimate of the

trench depth and find that d is around 1-5 μm .

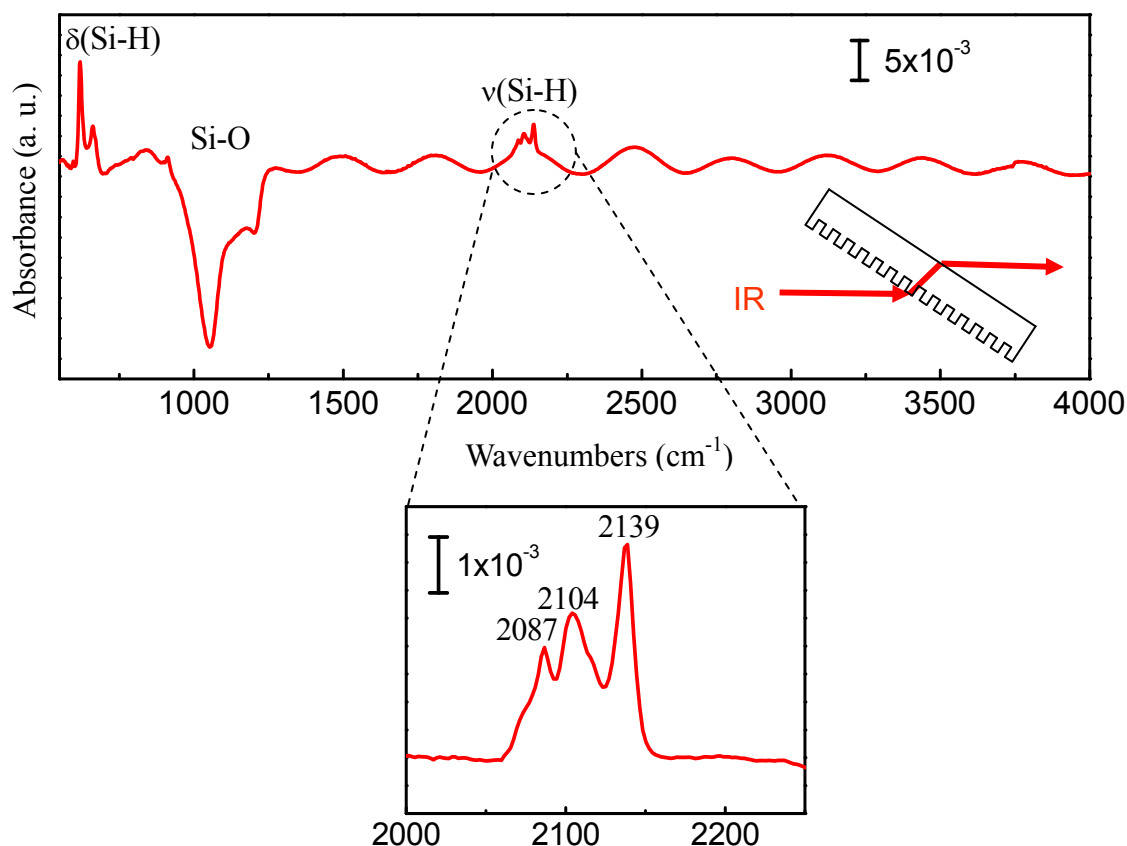


Fig A.5 The absorption spectrum of hydrogen terminated trenched Si(100). The inset shows the magnified Si-H stretches. The incident angle of IR is $\sim 0^\circ$. The curved baseline is due to the trenches. And the small schematic shows the IR transmission geometry.

Thermal annealing is carried on for H-terminated trenched Si as well with the same condition. The spectral results are shown in Fig A.6. Upon 250°C , the surface Si-H starts to decompose featured by the negative bands corresponded to monohydride, dihydride and trihydride stretches which are centered at 2085 cm^{-1} , 2108 cm^{-1} , and 2137 cm^{-1} , respectively. The band appearing at 2061 cm^{-1} is due to the decoupled Si-H resulting from thermal decomposition. At 350°C , the surface is being oxidized evidenced by the broad Si-O band center $\sim 998\text{ cm}^{-1}$. The modes appearing at 2175 cm^{-1} and 2264 cm^{-1} are caused by the oxygen insertion into Si-Si bond. The 2175 cm^{-1} mode is assigned to Si-H shifted

by insertion of two oxygen atoms ($\text{O}_2\text{-Si-H}$) and 2262 cm^{-1} mode is assigned to Si-H shifted by insertion of three oxygen atoms ($\text{O}_3\text{-Si-H}$) [12], which are getting stronger with more Si-O formation.

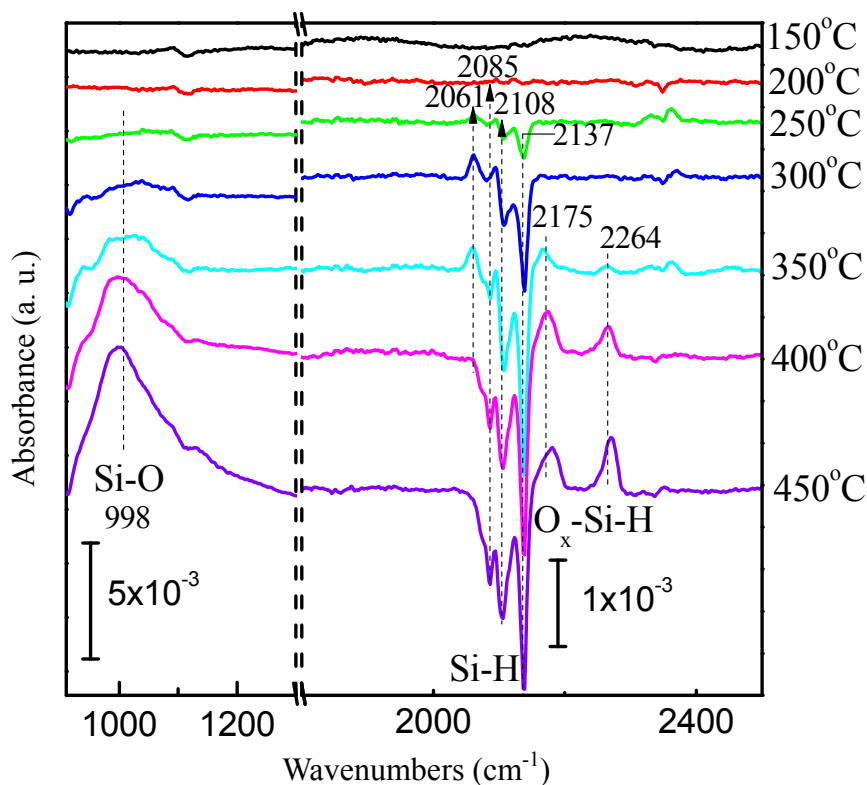


Fig A.6 Absorption spectra of annealing of H-terminated trench Si surface which are referenced to H/Si. The surface is not as stable as the flat surface and Si-H starts to desorb from the surface upon 250°C annealing.

By comparing above results, it is found that H/Si(111) is the most stable surface and remains unchanged at 300°C annealing. Due to the presence of more defects, H-terminated trench Si(100) is the least stable surface and its Si-H decomposes at 250°C while flat H/Si(100) is stable up to 250°C. However, when the ALD reactor is contaminated such as by large amount of residue metal precursor and hydroxyl group, the stability of H/Si will be further decreased.

A.2 HfO₂ deposition on trenched H/Si(100)

Based on the thermal stability study of H/Si we have discussed above, HfO₂ is deposited on them by TEMAH and D₂O. The comparison of HfO₂ deposition on flat H/Si(100) surface and on trenched H/Si(100) will be presented in the following part.

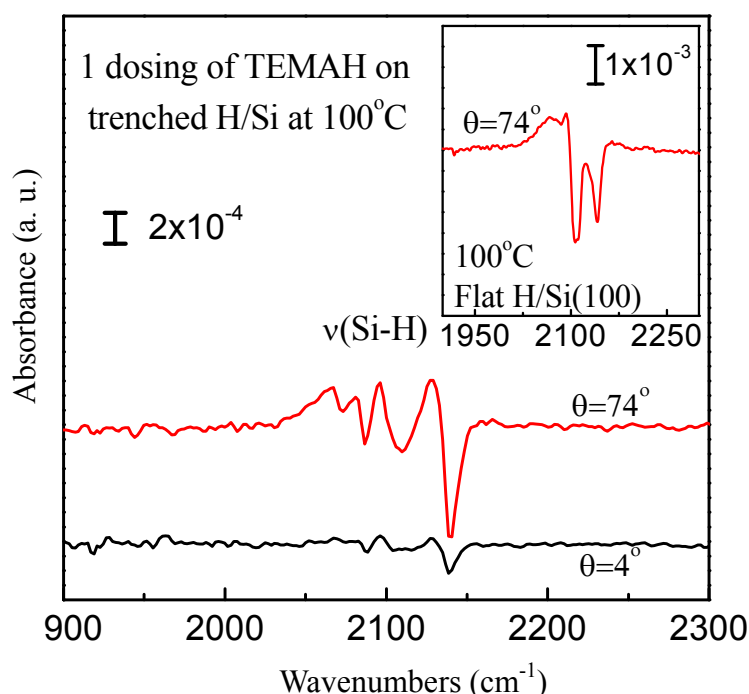


Fig A.7 Absorption spectra of trenched H/Si(100) exposed to TEMAH at 100°C which are referenced to H/Si. The bottom spectrum in black is taken at normal incidence and the top spectrum in red is taken at 74°. The inset shows the spectrum of flat H/Si(100) exposed to TEMAH at 100°C and taken at 74°. The loss of Si-H indicates the interaction.

First the trenched H/Si surface is exposed to TEMAH at 100°C as shown by the spectra in Fig A.7 which are referenced to H/Si and show the range of Si-H stretching modes. The spectrum for the trenched sample taken at 74° has a substantial change in the Si-H stretching modes, indicating the TEMAH is interacting with the surface Si-H and the flat H/Si(100) exhibits similar feature after TEMAH dosing at 74° (the inset of Fig A.7).

However, the spectrum of the trenched sample taken at normal incidence only shows

small changes (Si-H loss less than 2%) in the range of the Si-H stretches. Since the 74° spectrum gives the information (dipoles vertical and parallel to the surface) of both flat surface and trenches (the side of the hole), and normal incidence gives mostly the information (bonds parallel to the surface) of trenches, the spectral results may indicate that at 100°C, TEMAH precursor doesn't enter the trenches to have sufficient reaction with Si-H. But due to the complexity of the surface geometry, it cannot be simply explained.

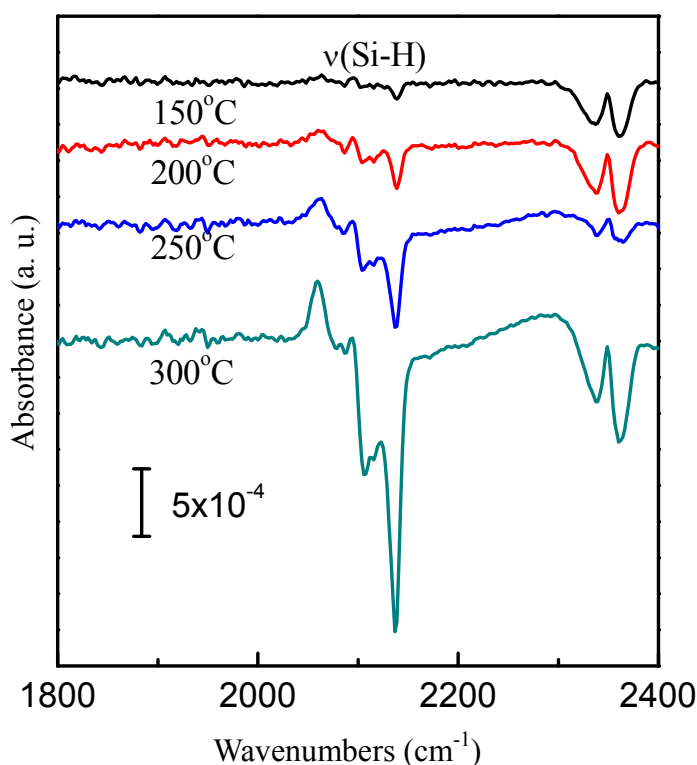


Fig A.8 Absorption spectra of trenched H/Si(100) exposed to TEMAH at various temperatures which are referenced to H/Si and taken at normal incidence. Little change is observed at 150°C, and at higher temperature, more Si-H loss is observed.

When the temperature is increased to 200°C, the loss of Si-H becomes more intense as shown by Fig A.8, where the surface is thermally stable in N₂ as studied in the previous section, possibly indicating that the precursor has sufficient kinetic energy to be

driven into the trenches. With further increased temperature, although much more loss of Si-H is observed, the contribution of the precursor interaction cannot be distinguished from the thermal effect.

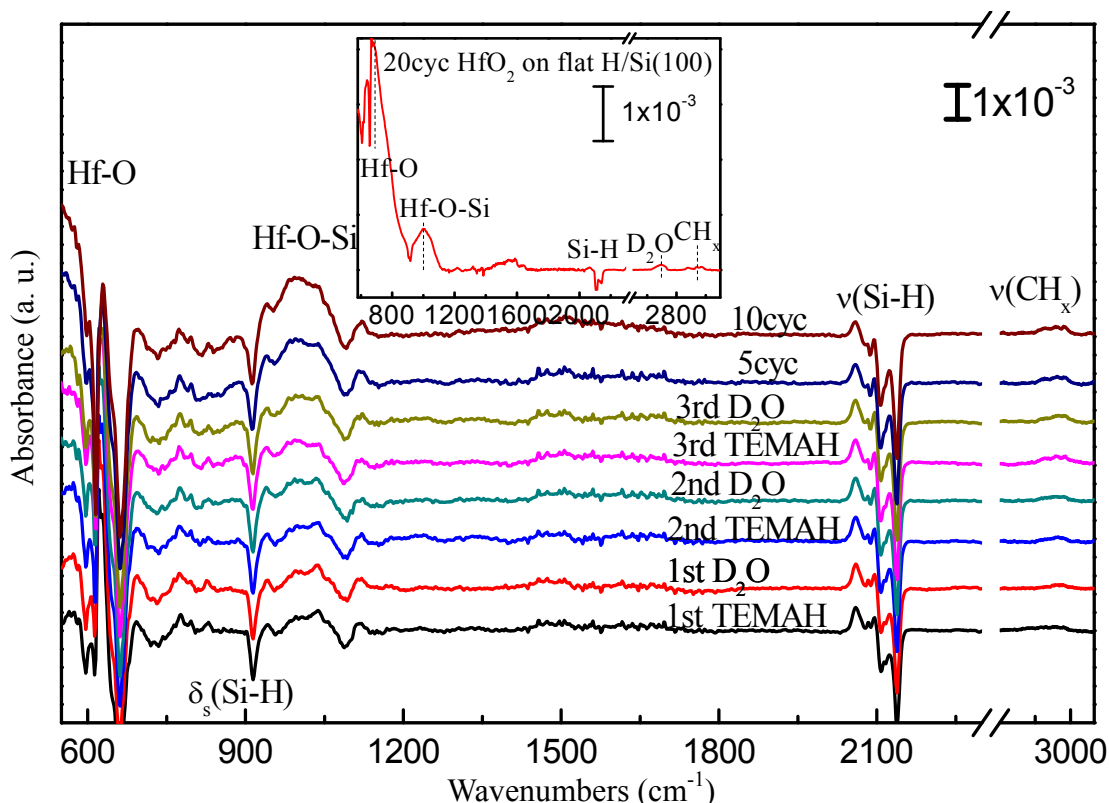


Fig A.9 Absorption spectra of 10 cycles HfO_2 on H/Si(100) at 300°C which are referenced to H/Si taken at normal incidence. The inset shows 20 cycles HfO_2 on flat H/Si(100) at 100°C which is referenced to H/Si and taken at 74° . Small amount of Hf-O-Si and impurities is observed. Compared to the deposition on flat H/Si, there is no significant difference.

Further, 10-cycle HfO_2 is deposited on H/Si(100) at 300°C (Fig A.9). The inset of Fig A.9 shows the spectrum of 20 cycles HfO_2 deposited on flat H/Si(100) surface at 100°C . Hf-O mode observed $\sim 680\text{ cm}^{-1}$ indicates the formation of continuous HfO_2 layer. The broad band around 990 cm^{-1} is due to the interfacial Hf-O-Si bond [13]. Less amount of impurities (C, N and O) for the deposition at 300°C are observed by the region at $1300\text{--}1700\text{ cm}^{-1}$ than that at 100°C as well as the reduced D_2O amount. The

interfacial SiO_2 is not obvious in both cases. There is no significant difference between the flat surface and trenched surface according to the spectral features.

However, due to the complicated surface geometry of trenched H/Si(100) surfaces, the RBS spectrum of 10 cycles HfO_2 on it has a large tail for the Hf peak as shown by Fig A. 10. Thus, it is very difficult to get the Hf atom areal density through RBS measurement as we relied on before.

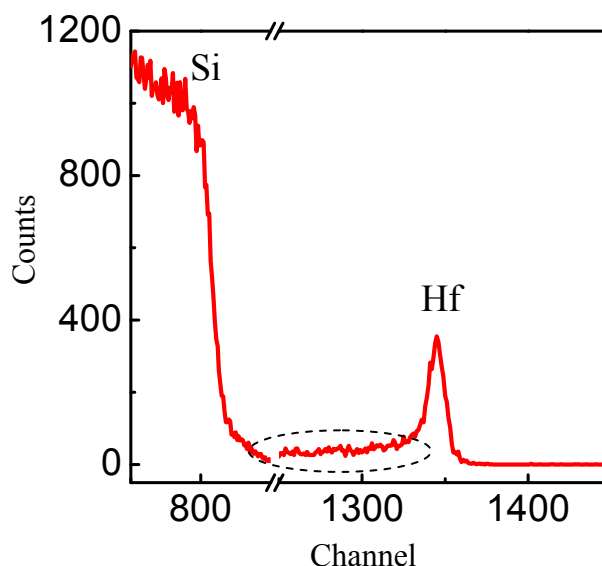


Fig A.10 RBS spectrum of 10 cycles HfO_2 on trenched H/Si(100) at 300°C . There is a big tail for the Hf peak because of the trenches which makes the analysis difficult.

A.3 Summary

In this chapter, the thermal stability of flat H/Si(111), H/Si(100) and trenched H/Si(100) in N_2 is studied by *in situ* FTIR. Flat H/Si(111) shows the highest stability and trenched H/Si(100) shows the lowest. Due to the surface roughness of trenched H/Si(100) samples, little direct information can be obtained by using normal and $\sim 74^\circ$ incidence for the IR measurements. The interference resulting from the trenches can be used to estimate the trench depth with a simple model.

The deposition of HfO_2 by using TEMAH and D_2O is carried out at various temperatures. Compared with the deposition on flat $\text{H}/\text{Si}(100)$, higher temperature (above 200°C) is needed to drive the TEMAH precursor into the trench, as determined from the results of normal incidence and $\sim 74^\circ$ IR absorption spectra. The RBS spectrum shows a large tail resulting from the trenches which makes the analysis difficult. As a result, the interpretation is only qualitative.

Bibliography

1. A. W. Topol, J. D. C. La Tulipe, L. Shi, D. J. Frank, K. Bernstein, S. E. Steen, A. Kumar, G. U. Singco, A. M. Young, K. W. Guarini and M. Jeong, *Three-dimensional integrated circuits*, IBM Journal of Research and Development **50** (2006), 491.
2. K. Yamada, K. Yamabe, Tsunashima, Y. Imai, K. Kashio and H. T. Tango, *A deep-trenched capacitor technology for 4 mega bit dynamic RAM*, Elect. Dev. Meeting **31** (1985), 702.
3. J. Lutzen, A. Birner, M. Goldbach and e. al., *Integration of capacitor for sub-100-nm DRAM trench technology*, VLSI Technology, 2002. Digest of Technical Papers. 2002 Symposium on (2002), 178.
4. E. Gerritsena, N. Emonetb, C. Caillatb, N. Jourdanb, M. Piazzab, D. Frabouletd, B. Boeckc, A. Berthelota, t. Smitha and P. Mazoyerb, *Evolution of materials technology for stacked-capacitors in 65 nm embedded-DRAM* Solid-State Electronics **49** (2005), 1767.
5. L. Pinzellia, M. Gros-Jeana, Y. Bréchetb, F. Volpib, A. Bajoleta and J.-C. Giraudina, *High-k dielectric deposition in 3D architectures: The case of Ta_2O_5 deposited with metal-organic precursor TBTDET* Microelectronics Reliability **47** (2007), 700.
6. P. Dumas, Y. J. Chabal and G. S. Higashi, *Coupling of an adsorbate vibration to a substrate surface phonon: H on Si(111)*, Physical Review Letters **65** (1990), 1124.
7. Y. J. Chabal, G. S. Higashi, K. Raghavachari and V. A. Burrows, *Infrared spectroscopy of Si(111) and Si(100) surfaces after HF treatment: Hydrogen termination and surface morphology*, J. Vac. Sci. Technol. A **7**(3) (1989), 2104.
8. K. T. Queeney, Y. J. Chabal, M. K. Weldon and K. Raghavachari, *Silicon oxidation and ultra-thin oxide formation on silicon studied by infrared absorption spectroscopy*, Phys. Stat. Sol. (a) **175** (1999), 77.
9. G. W. Trucks, K. Raghavachari, G. S. Higashi and Y. J. Chabal, *Mechanism of HF etching of silicon surface: A theoretical understanding of hydrogen passivation*, Phys. Rev. Lett. **65** (1990), no. 4, 504.
10. P. Weidner, A. Kasic, T. Hingst and T. Lindner, *Deep trench metrology challenges for*

75nm DRAM technology, Semiconductor Fabtech (2006), no. Edition 32, Wafer Processing, 115.

11. E. Hecht, *Optics (Addison-Wesley series in physics)*, Addison Wesley (1987).

12. X. Zhang, Y. J. Chabal, S. B. Christman, E. E. Chaban and E. Garfunkel, *Oxidation of H-covered flat and vicinal Si(111)-1x1 surfaces*, J. Vac. Sci. Technol. A **19(4)** (2000), 1725.

13. M.-T. Ho, Y. Wang, R. T. Brewer, L. S. Wielunski and Y. J. Chabal, *In situ infrared spectroscopy of hafnium oxide growth on hydrogen-terminated silicon surfaces by atomic layer deposition*, Appl. Phys. Lett. **87** (2005), 133103.

Acknowledgment of Previous Publications

1. Atomic Layer Deposition of Aluminum Oxide on Carboxylic Acid-terminated Self-Assembled Monolayers

M. Li, **M. Dai**, and Y. J. Chabal

Submitted to *Appl. Phys. Lett.*

2. In-situ Infrared Characterization during Atomic Layer Deposition of Lanthanum Oxide

Jinhee Kwon, **Min Dai**, Mathew D. Halls, Yves J. Chabal and Roy G. Gordon

Submitted to *J. Phys. Chem.*

3. Detection of a Formate Surface Intermediate in the Atomic Layer Deposition of High-K Dielectrics Using Ozone

Jinhee Kwon, **Min Dai**, Mathew D. Halls, and Yves J. Chabal

Chem. Mater., 20, 3248-3250, 2008

4. In-situ FTIR Study of Atomic Layer Deposition (ALD) of Copper Metal Films

Dai, Min; Kwon, Jinhee; Langereis, Erik; Wielunski, Leszek; Chabal, Yves J.; Li, Zhengwen; Gordon, Roy G.

ECS Transactions, 11, 91-101, 2007

5. In-situ Infrared Absorption Monitoring of Atomic Layer Deposition of Metal Oxides on Functionalized Si and Ge Surfaces

Min Dai, Jinhee Kwon, Ming-Tsung Ho, Yu Wang, Sandrine Rivillon, Meng Li, Yves Jean Chabal, Marek Boleslawski

Mater. Res. Soc. Symp. Proc., 996E, 0996-H07-04, 2007

6. Infrared Characterization of Hafnium oxide grown by Atomic Layer Deposition using Ozone as the oxygen precursor

Y. Wang, **M. Dai**, M-T. Ho, L.S. Wielunski, and Y. J. Chabal

Applied Physics Letter, 90, 022906, 2007

7. In-situ Infrared Absorption Spectroscopy for Thin Film Growth by Atomic Layer Deposition

Y. Wang, **M. Dai**, S. Rivillon, M-T. Ho, and Y.J. Chabal

SPIE Proceedings, p.63250G, 2006

Curriculum Vita

Min Dai

■ Educations

2004. 9-2008. 10	Ph. D in Physics (Surface Science) Department of Physics, Rutgers University
2001. 9-2004. 6	Master of Science in Microelectronics and Solid State Electronics Department of Physics, Nanjing University, P. R. China
1997. 9-2001. 6	Bachelor of Science in Microelectronics and Solid State Electronics Department of Physics, Nanjing University, P. R. China

■ Research Experiences (Research Assistant)

2005-Present	Mechanistic study of Atomic Layer Deposition (ALD) of High- κ materials and metals Advisor: Prof. Yves J. Chabal, Rutgers University
2000-2004	Fabrication, characterization and electrical properties of nano-crystalline silicon (nc-Si) Advisor: Prof. Kunji Chen and Prof. Xinfan Huang, Nanjing University, P. R. China

■ Publications

-
- Atomic Layer Deposition of Aluminum Oxide on Carboxylic Acid-terminated Self-Assembled Monolayers
M. Li, **M. Dai**, and Y. J. Chabal
Submitted to *Appl. Phys. Lett.*
 - In-situ Infrared Characterization during Atomic Layer Deposition of Lanthanum Oxide
Jinhee Kwon, **Min Dai**, Mathew D. Halls, Yves J. Chabal and Roy G. Gordon
Submitted to *J. Phys. Chem.*
 - Detection of a Formate Surface Intermediate in the Atomic Layer Deposition of High-K Dielectrics Using Ozone
Jinhee Kwon, **Min Dai**, Mathew D. Halls, and Yves J. Chabal
Chem. Mater., 20, 3248-3250, 2008
 - In-situ FTIR Study of Atomic Layer Deposition (ALD) of Copper Metal Films
Dai, Min; Kwon, Jinhee; Langereis, Erik; Wielunski, Leszek; Chabal, Yves J.; Li, Zhengwen; Gordon, Roy G.
ECS Transactions, 11, 91-101, 2007
 - In-situ Infrared Absorption Monitoring of Atomic Layer Deposition of Metal Oxides on Functionalized Si and Ge Surfaces

- Min Dai**, Jinhee Kwon, Ming-Tsung Ho, Yu Wang, Sandrine Rivillon, Meng Li, Yves Jean Chabal, Marek Boleslawski
Mater. Res. Soc. Symp. Proc., 996E, 0996-H07-04, 2007
6. Infrared Characterization of Hafnium oxide grown by Atomic Layer Deposition using Ozone as the oxygen precursor
 Y. Wang, **M. Dai**, M-T. Ho, L.S. Wielunski, and Y. J. Chabal
Applied Physics Letter, 90, 022906, 2007
7. In-situ Infrared Absorption Spectroscopy for Thin Film Growth by Atomic Layer Deposition
 Y. Wang, **M. Dai**, S. Rivillon, M-T. Ho, and Y.J. Chabal
SPIE Proceedings, p.63250G, 2006
8. Charging and Coulomb blockade effects of the nc-Si embedded in SiN_x double-barrier structures
 Xinfan Huang, Liangcai Wu, **Min Dai**, Peigao Han, Linwei Yu, Zhongyuan Ma, Yansong Liu, Wei Li, Kunji Chen
Journal of Non-Crystalline Solids, 352, 126-1129, 2006
9. Structural characterization and Coulomb blockade of a-SiN_x/ nanocrystalline Si/ a-SiN_x asymmetric double-barrier structures
 L. C. Wu, **M. Dai**, X. F. Huang, P. G. Han, L. W. Yu, H. C. Zou, W. Li, and K. J. Chen
Mater. Res. Soc. Symp. Proc., 832, F3. 6. 1, 2005
10. Collective behavior of single electron effects in a single layer Si quantum dot array at room temperature
 Linwei Yu, Kunji Chen, Liangcai Wu, **Min Dai**, Wei Li, Xinfan Huang
Physical Review B, 71, 24305, 2005
11. Electronic properties of nanocrystalline-Si embedded in asymmetric ultrathin SiO₂ by in-situ fabrication technique
 L. C. Wu, K. J. Chen, L. W. Yu, **M. Dai**, Z. Y Ma, P. G. Han, W. Li, X. F. Huang
Chinese Physics Letter, 22, 733-736, 2005
12. Formation and charging effect of Si nanocrystals in a-SiN_x /a-Si /a-SiN_x structures
Min Dai, Kai Chen, Xinfan Huang, Liangcai Wu, Lin Zhang, Feng Qiao, Wei Li, Kunji Chen
Journal of Applied Physics, 95, 640-645, 2004
13. Room temperature electron tunneling and storing in nanocrystalline silicon floating gate structure
 Liangcai Wu, **Min Dai**, Xinfan Huang, Yongjun Zhang, Wei Li, Jun Xu, Kunji Chen
Journal of Non-Crystalline Solids, 338-40, 318-321, 2004
14. Size dependent resonant tunneling and storing of electron in nanocrystalline silicon floating gate double-barrier structure
 Liangcai Wu, **Min Dai**, Xinfan Huang, Wei Li, Kunji Chen
The Journal of Vacuum Science and Technology B, 22, 678-681, 2004
15. Room temperature resonant tunneling and Coulomb blockade in nanocrystalline Si with

double SiO₂ barriers

L. C. Wu, K. J. Chen, **M. Dai**, W. Li, L. W. Yu, X. F. Huang

Mat. Res. Soc. Symp. Proc., 794, T3. 42. 1, 2004

16. Charging and Coulomb blockade effects in nanocrystalline Si dots embedded in SiO₂ matrix

Liangcai Wu, Kunji Chen, **Min Dai**, Linwei Yu, Peigao Han, Da Zhu, Wei Li, Xinfan Huang

Solid-State and Integrated Circuits Technology, Proceedings. 7th International Conference on, 2 (18-21), 898 – 901, 2004

17. A mechanism for the self-organization of colloidal gold nanoparticles

Zhang Y J, Han G Q, Li W, **Dai M**, Zhang Y, Huang X F, Chen K J

Chinese Physics Letters, 21, 2486-2488, 2004

18. Capacitance-voltage study of SiO₂/nanocrystalline silicon/SiO₂ double barrier structures

Liangcai Wu, Xinfan Huang, Jianjun Shi, **Min Dai**, Feng Qiao, Wei Li, Jun Xu, Kunji Chen

Thin Solid Film, 425, 221-224, 2003

19. Coulomb blockade effect of carriers in nc-Si embedded in ultrathin SiO₂ films

Shi Jianjun, Wu Liangcai, Bao Yun, Liu Jiayu, Ma Zhongyuan, **Dai Min**, Huang Xinfan, Li Wei, Xu Jun, and Kunji Chen.

Chinese Journal of Semiconductors, 24, 29-32, 2003

20. New nanocrystalline Si floating gate structure for nonvolatile memory application

L. C. Wu, J. J. Shi, K. J. Chen, J. Xu, W. Li, Z. Y. Ma, **M. Dai**, D. Wu, A.D. Li, X.F. Huang

Mat. Res. Soc. Symp. Proc., 737, 2003

21. The charge storage of the nc-Si layer

Dai Min, Zhang Lin, Bao Yun, Shi Jian-jun, Chen Kai, Li Wei, Huang Xin-fan and Chen Kun-ji

Chinese Physics, 11, 944-947, 2002

22. The charge storage effect of a-SiN_x/nc-Si/a-SiN_x sandwich structure

Dai Min, Bao Yun, Shi Jianjun, Zhang Lin, Li Wei, Chen Kai, Wang Li, Huang Xinfan, Chen Kunji

Research & Progress of SSE, 22, 445-448, 2002 (in Chinese)